REPORT DOCUMENTATION PAGE

1a. REPORT SECURITY CLASSIFICATION UNCLASSIFIED	1b.

2a. SECURITY CLASSIFICATION AUTHORITY	3. Di
2b. DECLASSIFICATION / DOWNGRADING SCHEDULE	pu

DTIC SELECTED FEB 6 1989

AD-A204 260

4. PERFORMING ORGANIZATION REPORT NUMBER(S)	5. MONITORING ORGANIZATION REPORT NUMBER(S)
	AFOSR·TR· 89·0090

6a. NAME OF PERFORMING ORGANIZATION Massachusetts Institute of Technology	6b. OFFICE SYMBOL (If applicable)	7a. NAME OF MONITORING ORGANIZATION AFOSR/NA

6c. ADDRESS (City, State, and ZIP Code) 77 Massachusetts Avenue Cambridge, MA 02139	7b. ADDRESS (City, State, and ZIP Code) Bolling Air Force Base, Building 410 Washington, DC 20332-6448

8a. NAME OF FUNDING/SPONSORING ORGANIZATION AFOSR	8b. OFFICE SYMBOL (If applicable) AFOSR/NA	9. PROCUREMENT INSTRUMENT IDENTIFICATION NUMBER AFOSR 84-0356

8c. ADDRESS (City, State, and ZIP Code) Bolling Air Force Base, Building 410 Washington, DC 20332-6448	10. SOURCE OF FUNDING NUMBERS			
	PROGRAM ELEMENT NO. 61102F	PROJECT NO. 2308	TASK NO. A2	WORK UNIT ACCESSION N

11. TITLE (Include Security Classification)

"Numerical Simulation of Turbulent Combustion Using Vortex Methods"

12. PERSONAL AUTHOR(S)

Ahmed F. Ghoniem

13a. TYPE OF REPORT Annual Technical	13b. TIME COVERED FROM 9-1-87 TO 8-31-88	14. DATE OF REPORT (Year, Month, Day) 88, Sept, 27	15. PAGE COUNT 181

16. SUPPLEMENTARY NOTATION

17. COSATI CODES			18. SUBJECT TERMS (Continue on reverse if necessary and identify by block number)
FIELD	GROUP	SUB-GROUP	Numerical Simulation, Turbulent Combustion, Vortex Methods

19. ABSTRACT (Continue on reverse if necessary and identify by block number) During the course of this year, we have concentrated on the validation of the transport element method in two dimensions and its extension to: three dimensional flow, to reacting flow with finite Arrhenius rates, and to variable-density flow including the effect of gravity. Comparisons with experimental data on a reacting shear layer with low heat release show that the numerical results agree very closely with the measurements of the velocity statistics, the passive scalar statistics, the product formation rate and the product thickness. Numerical studies are used to establish the dependence of the product formation rate on the Reynolds number, the Lewis number and the Damkohler number. Studies of a variable-density flow focused on the effects of density gradients on the structure of turbulence in both the momentum driven and gravity-driven reacting flow. In particular, how does heat release change the rates of growth and mixing within the layer via the impact of the expansion field and the baroclinic vorticity generation due to the density gradients. For this purpose, examples of a horizontal premixed reacting shear layer and a vertical jet diffusion flame are analyzed.

20. DISTRIBUTION/AVAILABILITY OF ABSTRACT ☐ UNCLASSIFIED/UNLIMITED ☒ SAME AS RPT ☒ DTIC USERS	21. ABSTRACT SECURITY CLASSIFICATION UNCLASSIFIED
22a. NAME OF RESPONSIBLE INDIVIDUAL Julian M. Tishkoff	22b. TELEPHONE (Include Area Code) 202-767-0465	22c. OFFICE SYMBOL AFOSR/NA

DD FORM 1473, 84 MAR 83 APR edition may be used until exhausted.
All other editions are obsolete.

Original contains color plates: All DTIC reproductions will be in black and white

"CONTROLLING COMBUSTION: NUMERICAL SIMULATION OF REACTING FLOW"
"TRUBULENCE-COMBUSTION INTERACTIONS IN A REACTING SHEAR LAYER"
"ON MIXING, BAROCLINICITY AND THE EFFECT OF STRAIN IN CHEMICALLY REACTING SHEAR LAYER"
"DEVELOPMENT AND APPLICATION OF VORTEX METHODS: A REVIEW AND SOME EXTENSIONS"
"ORIGIN AND MANIFESTATION OF FLOW-COMBUSTION INTERACTIONS IN A PREMIXED SHEAR LAYER"
"ON THE FORMATION OS STREAMWISE VORTICITY IN TURBULENT SHEAR FLOWS"
"NUMERICAL STUDY OF A THREE-DIMENSIONAL VORTEX METHOD"

FOURTH ANNUAL TECHNICAL PROGRESS REPORT
ON

NUMERICAL SIMULATION OF TURBULENT COMBUSTION USING VORTEX METHODS

(AFOSR Grant No. 84-0356)

Principal Investigator:

Ahmed F. Ghoniem

Department of Mechanical Engineering
Massachusetts Institute of Technology
Cambridge, MA   02139

SUMMARY

During the course of this year, we have concentrated on the validation of the transport element method in two dimensions and its extension to: three dimensional flow, to reacting flow with finite Arrhenius rates, and to variable-density flow including the effect of gravity. Comparisons with experimental data on a reacting shear layer with low heat release show that the numerical results agree very closely with the measurements of the velocity statistics, the passive scalar statistics, the product formation rate and the product thickness. Numerical studies are used to establish the dependence of the product formation rate on the Reynolds number, the Lewis number and the Damkohler number. Studies of a variable-density flow focused on the effects of density gradients on the structure of turbulence in both the momentum driven and gravity-driven reacting flow. In particular, how does heat release change the rates of growth and mixing within the layer via the impact of the expansion field and the baroclinic vorticity generation due to the density gradients. For this purpose, examples of a horizontal premixed reacting shear layer and a vertical jet diffusion flame are analyzed.

Accesion For		
NTIS CRA&I	☑	
DTIC TAB	☐	
Unannounced	☐	
Justification		
By		
Distribution /		
Availability Codes		
Dist	Avail and / or Special	
A-1		

DTIC
COPY
INSPECTED
1

OBJECTIVES

The objectives of this research are:

I. The development of accurate numerical methods which can be utilized for the integration of the time-dependent, three-dimensional Navier-Stokes equations and the energy and species conservation equations at high values of the Reynolds and Peclet numbers and moderate values of the Damkohler number, and when the heat release is large with respect to the internal energy of the flow.

II. The investigation of the mechanisms of turbulence-combustion interactions on the basis of the solutions obtained from the numerical simulations, and the study of how these interactions can be manipulated to provide more control over the burning process in turbulent shear flows.

We have been working on the development of grid-free, Lagrangian schemes: the vortex element and the transport element methods, which can be used to simulate fields that develop large velocity and scalar gradients. For the purpose of validating these schemes and analyzing turbulence-combustion interactions, we are using simulations of the reacting shear layers in two and three dimensions and in cases when the fuel and oxidizer are initially flowing in separate streams, and when the premixed reactants and products are initially flowing in separate streams. Attention has been focused on the low Mach number compressible flow limit in which spatial pressure variations are neglected in the thermodynamics of the problem. Effort is underway to extend the formulation to high Mach number flow in which this restriction is relaxed.

PERSONNEL

Six graduate students are currently working on projects related to the subject of this research. Their names, Ph.D. thesis titles and expected dates of completion are listed below in order of seniority. These students have been partially or totally supported by this grant. Copies of these theses will be forwarded as soon as they are ready.

1. Heidarinejad, Ghassem, Numerical Simulation of a Reacting Shear Layer Using The Transport Element Method, December 1988.

2. Najm, Habib, Numerical Study of the Convective Instability of Turbulent Flames in a Confined Combustor with Sudden Expansion, December 1988.

3. Knio, Omar, Spanwise Structure of a Turbulent Mixing Layer: Solutions Using 3-D Vortex Methods, September 1989.

4. Krishnar., Anantha, The Formulation of Compressible Vortex Methods for the Simulation of Turbulent Reacting Flow, September 1989.

5. Martins, Luis-Filippe, A Hybrid Finite Element, Vortex Method for Simulation of Internal Flow, December 1989.

6. Soteriou, Marios, started September 1988.

WORK STATUS

The research has been divided into several tasks: formulation of the numerical schemes, validation of the codes in which these schemes are implemented, and study of physics of turbulent–combustion interactions in reacting flow. In the following, a briefing on each project is given.

I. Numerical Simulation of a Reacting Shear Layer

Numerical simulation is applied to study mixing of a passive scalar in a spatially–developing shear layer, and to investigate the enhancement of the rate of chemical reaction in a mixing layer formed of separate fuel and oxidizer streams. The numerical simulations are performed using the transport element method, which we have developed as an extension of the vortex element method for the solution of the species and the energy conservation equations at high heat and mass transfer Peclet numbers. The method is Lagrangian and grid–free, and is based on the accurate discretization of flow gradients among finite elements which are transported along particle paths. The core functions of the elements are chosen to guarantee high spatial accuracy, and may be deformed to capture mild strain field. Computational elements are only utilized in areas of large flow gradients, i.e. shear layers or flames, and are redistributed whenever the flow map becomes severely distorted. The strengths of the elements are updated according to the source terms in the conservation equations [A1,A2].[*]

In the spatially–developing, non–reacting mixing layer, we found that

---

[*] References are listed in the Sections on New Publications [A] and Publications Under Preparation [B].

instantaneous scalar profiles exhibit mixing asymmetry and that the concentration fractions within the cores are skewed in favor of the high

speed stream due to the asymmetry in the dynamic field. The velocity statistics and mixing statistics of a passive scalar agree well with the experimental measurements of Masutani and Bowman in a two-dimensional shear layer. The rms of the passive scalar and the computed scalar PDF, which can be used as measures of the mixedness, emphasize the effect of molecular diffusion on mixing for Peclet numbers in the range of 1000-10000 [A3].

We have extended the computations to a chemically-reacting, spatially-developing layer assuming that the heat release does not change the density of the flow (the extension to a variable-density flow is described in the next section). Results of these simulations are compared with the experimental measurements of Mungal, Dimotakis and Broadwell. The agreement is very favorable [B1]. In particular, we obtain the same values for the rate of product formation and the product thickness as was measured in these experiments. We are in the process of analyzing the dependence of the rate of product formation on the Reynolds number, the Lewis number and the Damkohler.

II. Flow-Combustion Interactions in Premixed Combustion

The interactions between the flow field and the combustion process in a premixed shear layer are investigated by analyzing the results of numerical simulation using the transport element method [A6]. The reaction is governed by finite-rate Arrhenius kinetics for a single reactant, the density of the flow is allowed to vary with the temperature, and the Reynolds number is high. Heat release is moderate and molecular heat and mass diffusivities are finite, while the Mach number is small. The thickness of the reaction zone and that of the vorticity layer are of the

same order of magnitude, i.e. turbulence scales are relatively small. Attention is focused on a single, or two eddies in a temporal shear layer to limit the computational time. Extension to a spatially developing layer is discussed in the previous section.

Results indicate that at the early stages, a reacting layer behaves like a laminar flame. During the growth phase of the eddy, the rate of burning is strongly enhanced by the entrainment fluxes that lead to the swelling of the reaction zone. During this phase, the total rate of product formation can be approximated by the unstrained laminar burning velocity times the flame length measured along the line of maximum reaction rate. Following the burning of the eddy core, the strain field along the eddy boundaries causes a noticeable thinning of the reaction zone, thus curbing the rise in the rate of burning. During this phase, the rate of burning expression in the wrinkled laminar flame theory should be modified to account for the change of the laminar burning velocity with strain.

Baroclinic vorticity generation, due to the acceleration of fluid elements in the density gradient of the flame, is found to be the most important mechanism by which combustion alters the flow field in the low Mach number limit. The baroclinic torque augments the vorticity within the core while it reduces the vorticity on its outer edges. This enhances the overall volumetric entrainment into the eddy core, and causes entrainment asymmetry with a bias towards the products stream. The modified vorticity field extends the growth, or entrainment period of the eddy and imparts on it an extra mean convective motion in the direction of the reactants stream.

In all steps of development, the numerical methods are validated by comparing the numerical solutions with the results of the linear stability theory of shear layer during the initial stages of development. This

strategy is used to ensure that the physical model utilized in the numerical solution matches that used in the analytical, or semi-analytical study. Results for the late, non-linear stages are compared with idealized experimental data or results of conceptual models.

We are currently working on: (1) extending these computations to a spatially-developing shear layer with premixed reactants for which experimental results exist; and, (2) adding the effects of gravity, which acts an another vorticity generation mechanism, to these computations [B2,B3]. This is particularly important in the case of momentum/gravity flame as the jet flame of Roquemore [B4]. We are also looking into extending the transport element scheme to high Mach number flows in which spatial pressure variations play an important role.

III. Three-Dimensional Structure of a Stratified Shear Flow

The main goal of this project is the extension of vortex methods to three-dimensional flows. The numerical scheme is based on the accurate discretization of the vorticity field into a number of finite-core, spherical vortex elements, and the transport of these elements along particle paths. The vortex scheme is then used to study the formation of streamwise vorticity which is known to be a precursor to self-turbulization and mixing transition in shear flows. To validate the scheme, and understand the underlying physics of the transition process, two examples are analyzed: an isolated finite-core vortex ring perturbed in the azimuthal direction, and a periodic shear layer simultaneously perturbed in its streamwise and spanwise directions.

Results obtained for both cases show the innate tendency of vorticity, initially aligned in the direction normal to the stream, to form coherent streamwise structures which have alternating vorticity signs in the spanwise

direction. The formation of streamwise vorticity follows the "maturation" of the spanwise structure and the evolution of the former is energized by the strain field of the latter. While the streamwise vorticity is responsible for the added "turbulization" of the flow, leading to further mixing enhancement, it does not seem to lead to the disintegration of the two-dimensional basic structure. Results compare favorably with the conclusions of the linear stability theory and the available experimental results [A7,A8].

We are using the three-dimensional vortex method to simulate a shear layer and a jet flow. The transport element method has also been extended to three dimensions to allow the investigation of the effect of streamwise vorticity on the mixing of scalars within this flow [B6]. Next, we will implement the Arrhenius reaction mechanism used in the two dimensional computations to study a three-dimensional reacting shear layer.

NEW PUBLICATIONS DURING 1987-1988:

A1. Ghoniem, A.F., Heidarinejad, G. and Krishnan, A. "Numerical simulation of A Thermally-stratified Shear Layer Using the Vortex Element Method ," J. Comput. Phys., 75, 1988, in press.

A2. Ghoniem, A.F., Heidarinejad, G. and Krishnan, A. "On Mixing, Baroclinicity and the Effect of Strain in A Chemically Reacting Shear layer," the AIAA 26th Aerospace Sciences Meeting, January 11-14, Reno, Nevada AIAA-88-0729.

A3. Ghoniem, A.F., Heidarinejad, G. and Krishnan, A. "Turbulence-combustion Interactions in A Reacting Shear Layer," Lecture Notes in Engineering, Proceedings of the France-U.S.A. Joint Workshop on Turbulent Reactive Flows, July 1987, Rouen, France, Springer-Verlag, 1988, in press.

A4. Ghoniem, A.F., and Givi, P., "Lagrangian Simulation of A Reacting Shear Layer at Low Heat Release," AIAA Journal, 26, 1988, in press.

A5. Ghoniem, A.F., "Vortex Methods in Two and Three Dimensions with Application to Turbulent Shear Flows," Invited paper, Proceedings of the AIAA/ASME/SIAM/APS 1st National Fluid Dynamics Congress, Cincinnati, OH, July 24-28, 1988, p. 658.

A6. Krishnan, A. and Ghoniem, A.F. "Origin and Manifestation of Flow-Combustion Interaction in A Premixed Shear Layer," Proceedings of the 22nd Symposium (International) on Combustion, 8-13 August, 1988, Seattle, Washington, the Combustion Institute, Pittsburg, PA, in press.

A7. Knio, O. M. and Ghoniem, A. F. "On the Formation of Streamwise Vorticity in Turbulent Shear Flows," the AIAA 26th Aerospace Sciences Meeting, January 11-14, 1988/ Reno, Nevada, AIAA-88-0728.

A8. Knio, O.M. and Ghoniem, A.F. "Numerical Study of A Three-dimensional vortex method," submitted for publication at J. Comput. Phys., April 1988.

PUBLICATIONS UNDER PREPARATION:

B1. Heidarinejad, G. and Ghoniem, A.F., "Vortex Simulation of the Reacting Shear Layer; Investigation of the Limits on the Rate of Burning," for presentation at the 27th AIAA Aerospace Sciences Meeting, Reno, Nevada, January 9-12, 1989.

B2. Ghoniem, A.F. and Krishnan, A, "Baroclinic Effects in Density-stratified Flows; Part I: A Shear-Driven Flow, Part II: A Gravity-Driven Flow," to be submitted for publication, J. Fluid Mech, 1988.

B3. Ghoniem, A.F. and Krishnan, A. "Mixing Patterns and the Generation of Vorticity in Density Stratified Flow," for presentation at the International Workshop on The Physics of Compressible Turbulent Mixing, Princeton University, Princeton, N.J., October 24-27, 1988.

B4. Krishnan, A. and Ghoniem, A.F., "Numerical Simulation of the Structure of A Momentum/Gravity Driven Diffusion Flame," for presentation at the 27th AIAA Aerospace Sciences Meeting, Reno, Nevada, January 9-12, 1989.

B5. Ghoniem, A.F., Vortex Methods in Turbulent Reacting Flow, in Numerical Approaches to Combustion Modeling, ed by E. S. Oran and J. P. Boris, to be published by the AIAA, 1989.

B6. Knio, O.M. and Ghoniem, A.F. "Three-dimensional Simulation of the Entrainment Augmentation Due to Streamwise Vortex Structures," for presentation at the 27th AIAA Aerospace Sciences Meeting, Reno, Nevada, January 9-12, 1989.

B7. Ghoniem, A.F., Najm, H. and Martins, L.F., "Shear Flow Instability Behind A Bluff-body, Numerical Simulation and Potential for Control," the AIAA 2nd Shear Flow Control Conference, Tempe, Arizona, March 13-16, 1989.

INTERACTIONS WITH INDUSTRY AND GOVERNMENT LABORATORIES DURING 1987-1988:

During the course of last year, we have started and/or cemented collaborative working relations with the following industrial or governmental laboratories:

1. Wright-Patterson Laboratory; with Dr. M. Roquemore on the modeling of the jet diffusion flame.

2. General Electric Research Center; with Dr. Sanjay Corea on the study of turbulent premixed flames and their instability.

3. Sandia National Laboratory; with Drs. R. Lucht and John Kelly and their associates on the study of bluff-body diffusion flames.

4. Gas Research Institute; with Dr. J. Kezerle.

5. Ford Motor Company.

APPENDIX

Copies of the following articles are included:

1. Ghoniem, A.F., "Controlling Combustion: Numerical Simulation of Reacting Flow," The John von Neumann National SuperComputer Center Annual Research Report, 1987, pp. 67-72, the John von Neumann National Supercomputer Center, Princeton, NJ.

2. Ghoniem., A.F., Heidarinejad, G. and Krishnan, A. "Turbulence-combustion Interactions in A Reacting Shear Layer," Lecture Notes in Engineering, Proceedings of the France-U.S.A. Joint Workshop on Turbulent Reactive Flows, July 1987, Rouen, France, Springer-Verlag, 1988, in press.

3. Ghoniem, A.F., Heidarinejad, G. and Krishnan, A. "On Mixing, Baroclinicity and the Effect of Strain in A Chemically Reacting Shear Layer," the AIAA 26th Aerospace Sciences Meeting, January 11-14, Reno, Nevada AIAA-88-0729.

4. Ghoniem, A.F., "Vortex Methods in Two and Three Dimensions with Application to Turbulent Shear Flows," Invited paper, Proceedings of the AIAA/ASME/SIAM/APS 1st National Fluid Dynamics Congress, Cincinnati, OH, July 24-28, 1988, p. 658.

5. Krishnan, A. and Ghoniem, A.F. "Origin and Manifestation of Flow-Combustion Interaction in A Premixed Shear Layer," Proceedings of the 22nd Symposium (International) on Combustion, 8-13 August, 1988, Seattle, Washington, the Combustion Institute, Pittsburg, PA, in press.

6. Knio, O. M. and Ghoniem, A. F. "On the Formation of Streamwise Vorticity in Turbulent Shear Flows," the AIAA 26th Aerospace Sciences Meeting, January 11-14, 1988/ Reno, Nevada, AIAA-88-0728.

7. Knio, O.M. and Ghoniem, A.F. "Numerical Study of A Three-dimensional Vortex Method," submitted for publication at J. Comput. Phys., April 1988.

Controlling Combustion: Numerical Simulation of Reacting Flow

Ahmed F. Ghoniem
Department of Mechanical Engineering
Massachusetts Institute of Technology
Cambridge, MA 02139

Background

Reacting flow is a complex process in which turbulent fluid motion enhances the mixing between reactants, and chemical kinetics determines the rate of reaction in the mixture. The heat release associated with the reaction supplies the energy to the flow, and therefore changes its nature. The study of reacting flow is made more difficult by the strong coupling between these processes. Consequently, it requires sophisticated instrumentation or elaborate numerical methods and powerful computers. Experimental investigations of the physics of reacting flow depends heavily on the application of such modern measuring techniques as laser flourescence methods. These methods are expensive and sometimes difficult to apply due to the hostile conditions dominated by high pressure and temperature within a chemically reacting flow. Reacting flow plays a critical role in energy conversion and propulsion systems, in air pollution and waste incineration phenomena, in fire spread and in some areas of manufacturing.

Applications: Propulsion Systems, Air Pollution, Toxic Waste Control and Fire Control

The performance of a propulsion system, such as an automobile or an airplane, is often measured by the efficiency of energy conversion, the environmental impact in terms of noise and pollution, and the size and durability of the hardware. The operation of the system is directly related to the physics of the reacting flow in which chemical energy is converted into heat and mechanical force. In some cases, as in automobile engines, the challenge is to design the smallest possible engine that will achieve efficient and fast combustion using a variety of fuels and without producing harmful pollutants. In other cases, as in the engine of the proposed National Aerospace Plane, the challenge is to burn large quantities of fuel in the uncooperative environment of high pressure and very high, supersonic or hypersonic speeds. Considerations of stability of operation, noise and cost are also important if the plane is to become viable commercially.

Another set of applications involves air pollution control. Air pollution is governed by the transport of active gases from the source and their chemical reaction with air and water in the atmosphere. The interaction between the wind pattern, the earth terrain, the sunlight and the source of pollutants; which form the components of a typical reacting flow, ultimately determines the impact of this source on the environment. The location and orientation of the source of pollutants can be optimally determined when the results of these interactions are analyzed in advance.

In a related topic, toxic waste incineration, which is proposed as a solution to the national problem of how to deal with waste generation, represents another application of reacting flow analysis. In waste incineration, the thorough mixing of toxic by-products with hot gases is necessary if the destruction of these mutagins by chemical reaction is to be successfully accomplished. One hopes that the products of this combustion process will be less harmful than the toxicants being burnt in the incinerator, and that the energy produced from the burning of these toxics will be a useful source of heat or power.

> Reacting flow plays a critical role in energy conversion and propulsion systems, in air pollution and waste incineration phenomena, in fire spread and in some manufacturing processes.

Fire, whether it be a forest fire or the result of an explosion in a nuclear reactor or supertanker, spreads by the action of the fluid flow and the burning of combustible material. In these systems, fluid motion is determined by the design of the enclosures, the size and locations of the connecting passages and the obstacles inside the enclosures. The combustibility of the material de-
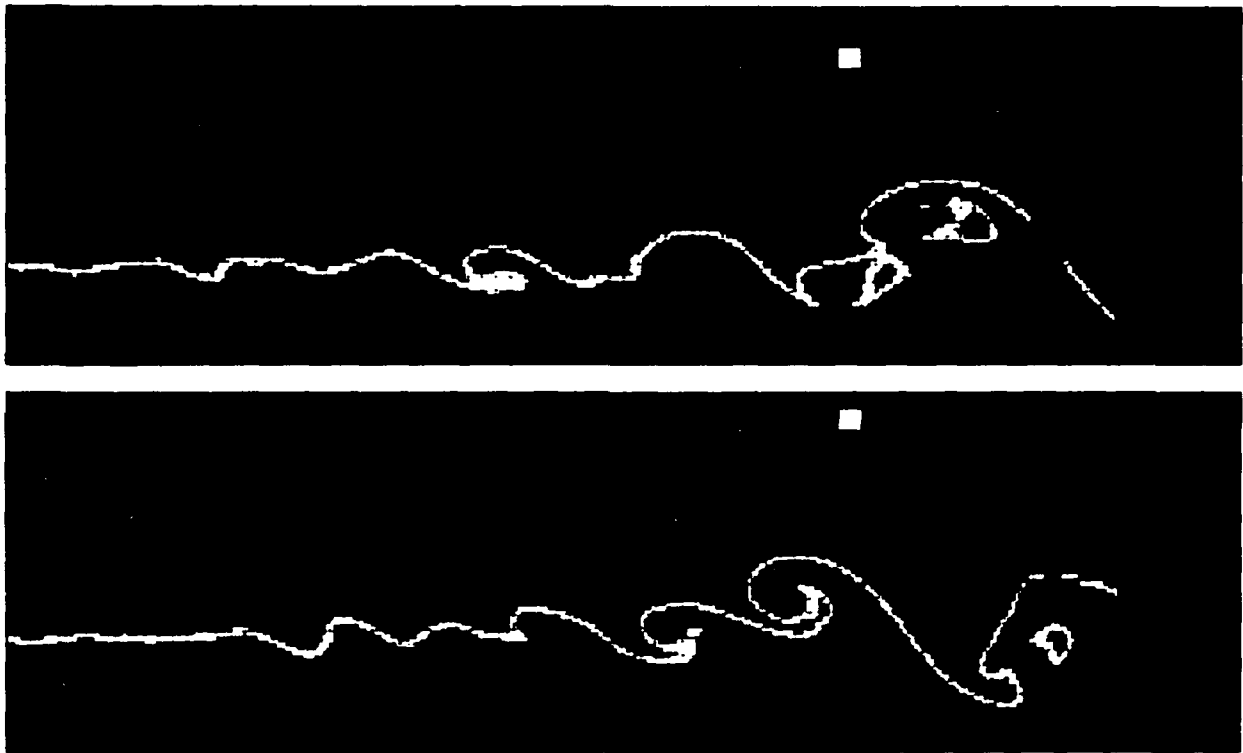
Figure 1: How Turbulence Enhances Combustion in a Fuel Mixture

pends on the kinetic rates of reactions between the gases and solids present in these enclosures and the oxidizing air. Understanding the mechanisms of fire spread and the contribution of each one of these factors will lead to a better control of fire spread via the redesign of the passages and employment of fire retarding material in construction.

The Problem

It is the objective of this research to develop accurate and efficient numerical methods for the prediction of reacting flow, and to apply these methods to gain better insight into their fundamental physics. Predictive methods will provide "computer-aided engineering" tools that can be used to speed up, simplify and reduce the cost of design. While the design criteria may change according to the application described, the fundamental issues involved are strongly related to the physics of the flow which we hope to reveal using the results of numerical experiments.

Mathematical modeling of reacting flow results in a set of three-dimensional, time-dependent partial differential equations which govern the flow within regions of complex geometry. These equations are impossible to integrate analytically except for very simple cases. The numerical integration of the governing equations requires high spatial and temporal resolution to capture all the phenomena that arise during the development of chemical reaction in a turbulent flow. Thus, very large numbers of grid points or particles must be used for large numbers of time steps, requiring the computing power and the memory size available only on a supercomputer.

In the next section, we present results which have been obtained for a number of fundamentally and practically important cases: the flow and combustion in a mixing layer, the flow in a ramjet engine, the flow inside an internal combustion engine, and the turbulent flow in a pulsed jet.

Results

I. Mixing and Combustion in Turbulent Flow

It is well known that turbulence enhances the mixing between species in a reacting flow. However, the mechanisms involved are not yet well-understood. Moreover, turbulent fluid motion may promote, and at times suppress the rate of reaction. In this work, and by using "numerical experiments," we are trying to understand the fundamental role of turbulence in reacting flows which are commonly encountered in practice. Turbulence is modeled by a concentrated zone of vorticity, or rotational flow, that initially separates the cold reactants (blue) and the hot

68
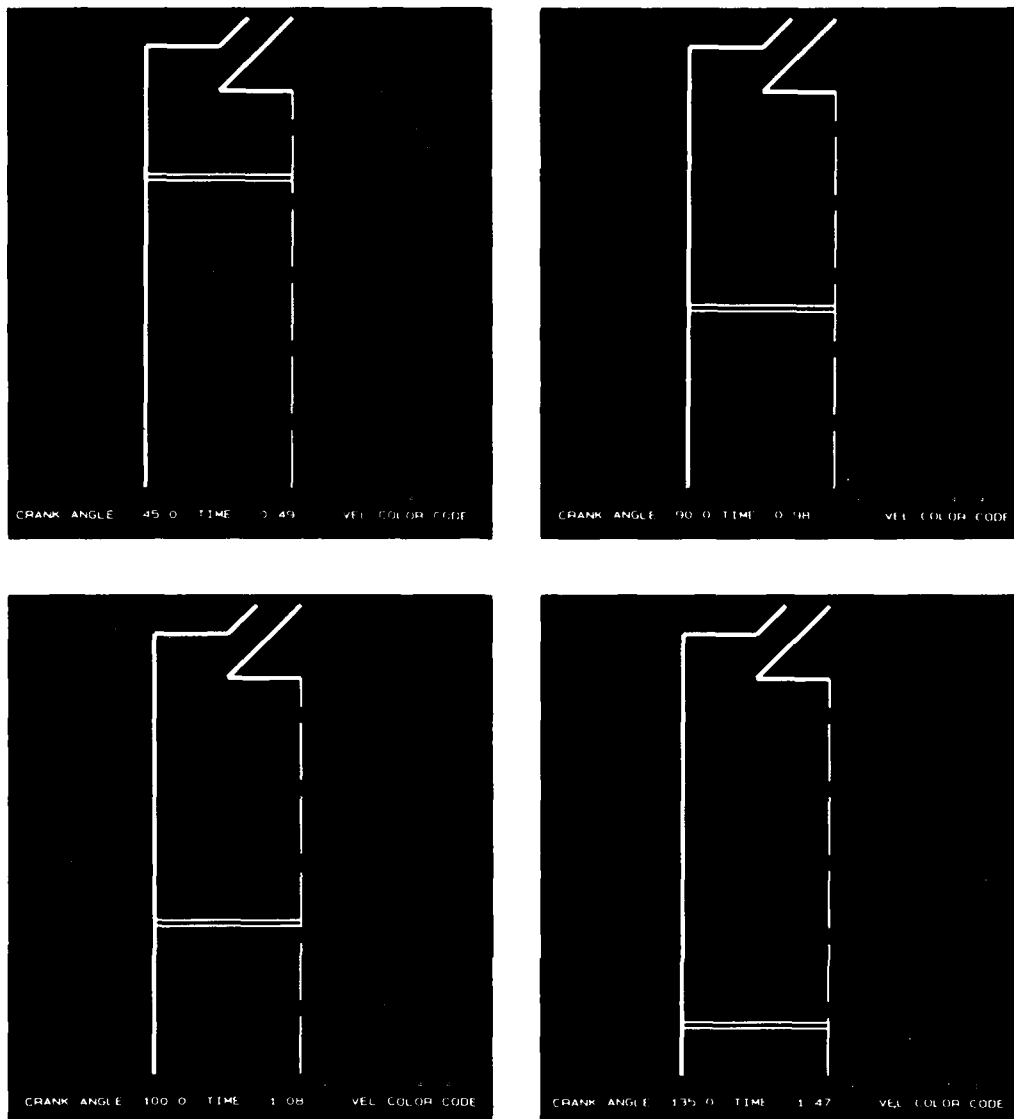
Figure 2: Induction Eddies Inside a Reciprocating Engine

products of combustion (red). As time progresses, an eddy, or a set of eddies emerge within the vorticity zone. Figure 1 shows that the swirling motion produced by these eddies leads to the entrainment of fluids from both sides of the eddies into their cores where they get mixed (yellow and green).

II. Flow in an Internal Combustion Engine

The fluid flow during the intake stroke of an internal combustion engine determines its performance. The power output of the engine is controlled by the total amount of air that enters the cylinder. Its efficiency is determined by the residual turbulent fluid motion at the end of the compression stroke. Both depend on the design parameters of the engine configuration and its

speed. In this project, we are developing methods of numerical simulation to study the effect of both piston, cylinder and inlet valve geometry, and the engine speed on the structure of this flow.

Figure 2, shows that the flow inside the cylinder, as the piston moves to charge the engine, consists of a jet that penetrates a system of eddies. These eddies maintain the flow inside the cylinder in a state of coherent rotation throughout the entire length of the stroke.

III. Combustion in a Model of a Jet Engine

The mechanism of stabilization of combustion in the high speed flow inside an ordinary jet engine, or a ramjet engine, is analyzed in terms of the interaction between the the fluid flow, the
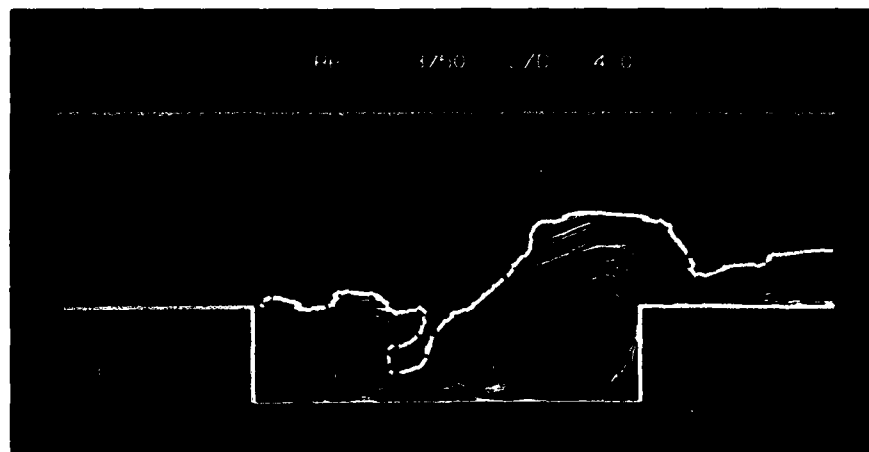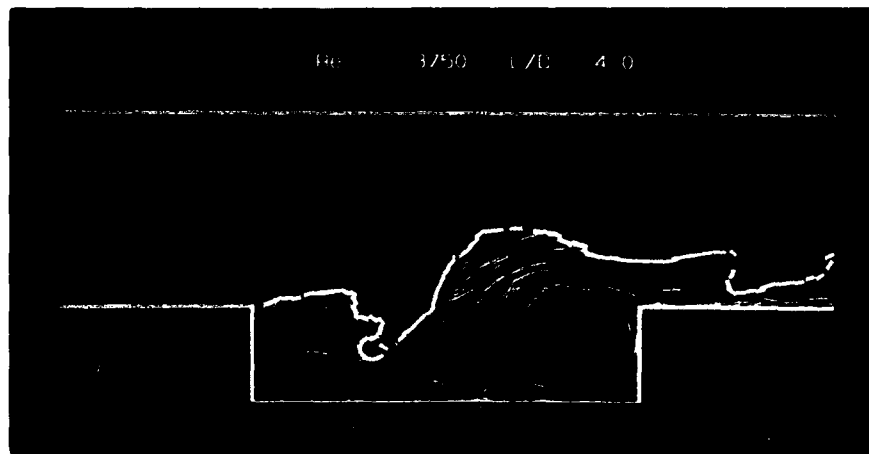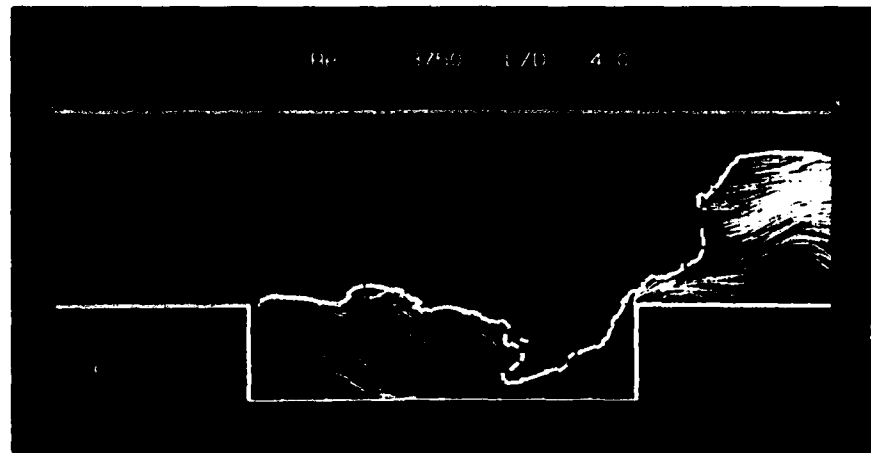
Figure 3: Stabilization by Recirculation of Combustion Products

flame and the geometry of the combustion chamber. Results, shown in Figure 3, reveal that the flame (white interface) is stabilized by the recirculation of the hot products (red) behind the sudden expansion, as shown by the velocity arrows. The flow-induced oscillations cause a periodic motion of the flame front into the reactant stream (blue). The underlying flow structure is composed of a cluster of large eddies, as indicated by the velocity of the vortex particles (yellow).

IV. Mechanisms of Turbulence

The transition of an initially well organized flow to a fully-developed turbulent flow is encountered in all the applications listed above. Whether it

70
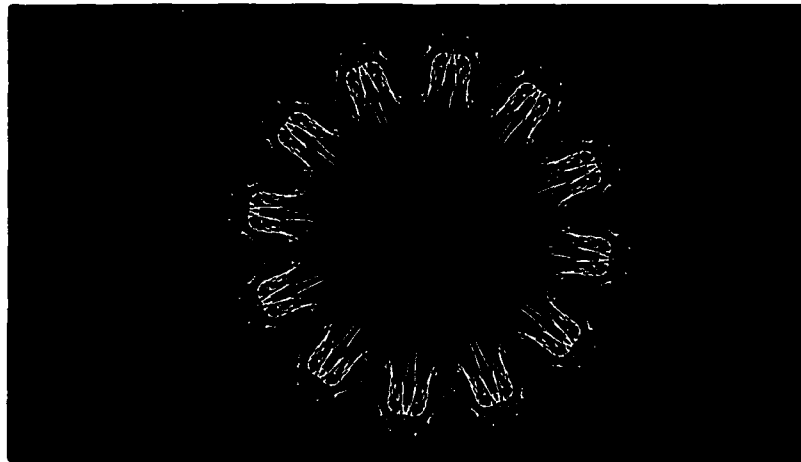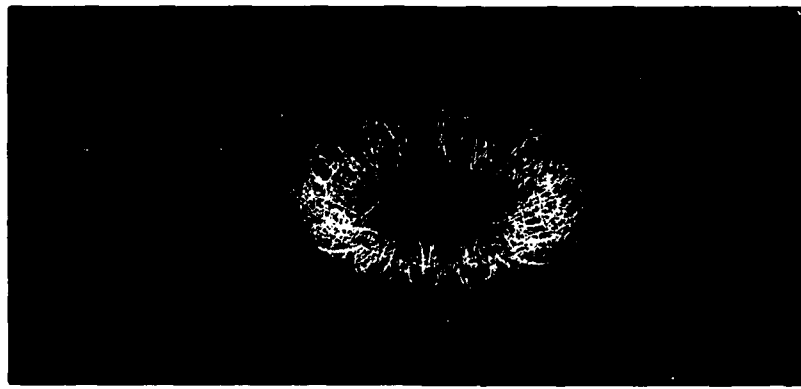
Figure 4: Development of a Vortex Ring Created by a Laminar Jet

is a welcomed event, as in a mixing device, or it is a problem to be avoided, as in aerodynamic flows, transition to turbulence occurs in the majority of applications. In this work, this phenomenon is analyzed in terms of the generation of small scales in a three dimensional motion due to the growth of flow instabilities. As an example, we show in Figure 4 the evolution of a vortex ring generated by the impulsive motion of a laminar jet towards the turbulent state. This structure is formed of a bundle of "vortex" lines that start as concentric circles and evolve to become a highly convoluted structure of severely stretched "worms."

Methodology

The numerical algorithms are designed to integrate the time-dependent, multi-dimensional partial differential equations that govern react-

ing flow. The algorithms are based on vortex-particle methods. The methods are employed in the solution of unsteady, multi-dimensional Navier-Stokes equations and the energy and species conservation equations. The fundamental scheme is Lagrangian. In other words, it is based on following a set of elementary fluid particles and their properties in space and time. To improve the accuracy of the computations, this algorithm is used to transport flow gradients by employing a large number of field particles distributed according to the magnitude of the gradient. The mutual interactions between the fields of these moving particles determine the evolution of the flow variables such as velocity, concentrations, temperature and pressure.

This methodology offers very high spatial resolution since the particles can be distributed arbitrarily in space to resolve regions of strong varia-

71

tions and high concentrations. Particle tracking allows one to observe the physical phenomena in a very similar way to that which have been used in experimental investigations. Moreover, the unsteady form of the calculations emphasizes the dynamic nature of turbulent reacting flows and helps shed light on the fundamental mechanisms of these flows. The methods can also accommodate complex geometrical configurations.

The computations are time consuming since they require the evaluation of mutual interactions between N particles at each time step. This amounts to $O(NxN)$ operations for each flow variable. For high spatial resolutions, N = 1000-10000 and more if the physical extent of the computational domain is wide. Moreover, the calculations must be performed for 1000-10000 time steps to capture the temporal evolution of the flow. The algorithms are readily vectorizable, thus requiring CPU time on the order of magnitude of one to five hours on the CYBER 205, depending on the dimensionality of the geometry and the complexity of the chemical reaction.

The algorithms are suitable for the implementation of parallel processing technology and should benefit from the installation of the ETA10. Preliminary studies on currently available parallel processors have confirmed that the parallel efficiency of our algorithm is high. Using the ETA10, we plan to simulate three dimensional reacting flows in practical configurations.

References

Ghoniem, A.F., Aly, H.F. and Knio, O.M., "Three-dimensional Vortex Simulation with Application to an Axisymmetric Shear Layer," The 25th AIAA Aerospace Sciences Meeting, January 1987, Reno, Nevada, AIAA-87-0379.

Ghoniem, A.F. and Givi, P., "Vortex-scalar Element Calculations of a Turbulent Diffusion Flame stabilized on a Shear Layer," The 25th AIAA Aerospace Sciences Meeting, January 1987, Reno, Nevada, AIAA-87-0225.

Ghoniem, A.F., and Givi, P., "Lagrangian Simulation of a Reacting Mixing Layer at Low Heat Release," AIAA Journal, 26, July 1988 (in press).

Ghoniem, A.F., Heidarinejad, G. and Krishnan, A., "Numerical Simulation of a Reacting Shear Layer Using the Transport Element Method," The AIAA/SAE/SAME/ASEE Joint Propulsion Meeting, June 29-July 1, 1987, La Jolla, California, AIAA-87-1718.

Ghoniem, A.F., Heidarinejad, G. and Krishnan, A., "Turbulence-combustion Interactions in a Reacting Shear Layer," Lecture Notes in Engineering, Proceedings of the United States-France Joint Workshop on Turbulent Reactive Flows, pp 6-10, July, 1987, Rouen, France, ed by Murthy and Bourghi, Springer-Verlag, in press (invited lecture).

Ghoniem, A.F., Heidarinejad, G. and Krishnan, A., "Numerical Simulation of a Thermally Stratified Shear Layer Using the Vortex Element method," Jounrnal Computational Physics, 74, 1988 (in press).

Ghoniem, A.F., Heidarinejad, G. and Krishnan, A., "On Mixing, Baroclinicity and the Effect of Strain in a Chemically Reacting Shear Layer," The AIAA 26th Aerospace Sciences Meetings, January 11-14, 1988/Reno, Nevada, AIAA-88-0729.

Najm, H. and Ghoniem, A.F., "Vortex Simulation of the Convective Instability in a Dump," The AIAA/SAE/SAME/ASEE Joint Propulsion Meeting, June 29-July 1, 1987, La Jolla, California, AIAA-87-1874.

Martins, L.-F. and Ghoniem, A.F., "Vortex Simulation of the Induction and Compression Processes in a Model Engine," SAE International Fuels and Lubricants Meeting and Exposition, November 2-5, 1987, Toronto, Ontario, Canada, 872102.

TURBULENCE-COMBUSTION INTERACTIONS IN A REACTING SHEAR LAYER

Ahmed F. Ghoniem, Ghassem Heidarinejad, and Anantha Krishnan

Department of Mechanical Engineering
Massachusetts Institute of Technology
Cambridge, MA 02139

ABSTRACT

Turbulence-combustion interactions are analyzed using results of a numerical simulation of a reacting shear layer. Premixed combustion at finite activation energy, moderate chemical kinetic rates and finite diffusivities is considered. The transport element method, a numerical scheme based on the accurate discretization of the vorticity and the scalar gradient fields into Lagrangian finite elements, is used to perform the numerical simulation. Processes that lead to burning enhancement or flame deceleration or possible extinction are analyzed. We find that the rollup of the shear layer accelerates burning by stretching the reaction surface. However, by comparing the local burning velocities within the shear layer to that of a laminar flame, we find that stretch, which accompanies the rollup, decelerates the rate of burning per unit area. This is due to the local cooling effects associated with the enhanced heat flux out and mass flux into the reaction zone. Both phenomena are strong functions of the turbulence field and the Damkohler number.

I. INTRODUCTION

Turbulent combustion is governed by complex interactions between convective and diffusive transport processes on the one hand, and chemical reaction and heat release on the other hand. Chemical reactions are strong nonlinear functions of temperature and species concentrations, and thus their rates are critically dependent on the transport fluxes which determine these variables. Meanwhile, rates and magnitudes of heat release, associated with the chemical oxidation of practical fuels, are large enough to affect the dynamics of the flow, and hence the transport phenomena. Understanding the outcome of these interactions is an important leap on the way to achieve better control of burning processes in combustion systems. It is the objectives of this work to: (1) develop numerical models capable of predicting turbulent combustion processes; (2) identify the most important modes of turbulence-combustion interactions; and (3) elucidate the subtle outcome of some of these interactions. We confine our attention to shear layers since they are relatively simple to analyze, and since they represent a generic model for many reacting flows.

Turbulent combustion has been the subject of extensive experimental, theoretical and numerical investigations over the years.[1] However, many of its fundamental mechanisms remain unclear.[2] Progress in phenomenological turbulent combustion models, based on the closure of a system of averaged transport equations which describe the statistical behavior of the aerothermodynamic variables, has made it possible to produce results which agree with experimental measurements. However, since some of the interesting dynamics of turbulence—combustion interactions are hypothesized a priori in these models, solutions do not provide a better understanding of the phenomena and are limited by the modelling assumptions.

Two problems have been identified as most challenging in the study of turbulence in reacting flows: the origin of the statistical correlations between fluctuating quantities; and the nature of the source terms in the energy and species conservation equations. In turbulent shear layers, the first problem is complicated by the presence of large scale structures that cannot be modelled by gradient diffusion terms. The second problem stems from the fact that chemical reactions are strongly affected by fluctuations in local variables in a nonlinear way, e.g., the Arrhenius form. In the following, the two issues are discussed in more detail.

Time-resolved flow visualization and instantaneous point measurements in nonreacting and reacting shear layers have revealed the existence of large scale periodic turbulent structures for a long distance downstream the separation point.[3,4,5,6] It has been shown experimentally, and supported by numerical studies, that these structures appear via the Kelvin—Helmholtz instability of the vorticity layer which forms between two initially-separate streams.[7] By a different mechanism, the subharmonic instability, these structures persist through successive pairings, thus maintaining the periodicity downstream though at different frequencies. Qualitatively, it is known that the role played by these structures in the mixing process is to engulf, then stretch layers of fluids to scales where molecular diffusion is most effective. The two processes, which have been called

entrainment, may create a bottleneck impeding mixing if the rate of molecular diffusion is high due to small scale turbulence.[8] However, analytical results that support, or reproduce these effects are not yet available.

The importance of these results in the context of investigating turbulence-combustion interactions is how the existence of different scales can be properly represented. Even though gradient diffusion models, which assume that only local conditions can affect turbulence, may provide an adequate description of the small diffusive scales, they do not contain enough information to identify the large convective scales. The latter is a feature of the unsteady flow field and depends strongly on the initial and boundary conditions. Thus, it must be resolved by solving the unsteady unaveraged equations using accurate schemes, while the effect of the small scales, for the sake of economy, may be modelled based on an understanding of the "substructural phenomena."

Since chemical reaction depends on the rate of molecular mixing which, as previously described, is a consequence of entrainment by the large scales and diffusion at the small scales, it is important that these two processes be represented accurately. Overestimating the rate of mixing by turbulence models, which do not account for the effect of the large scales on the entrainment process, results in erroneous prediction of combustion.[8,9,10] The solution algorithm must, therefore, be able to resolve large scale convective structures as well as small scale diffusive eddies. It should also give careful consideration to their continuous interactions. Since a typical size of a large scale eddy is on the order of magnitude of the thin, but finite vorticity layers, they can only be resolved if the unsteady unaveraged equations are integrated using accurate numerical methods. These methods must be non-diffusive, i.e. they should not dissipate the flow energy by distributing it on large cells.

Resolving the unsteadiness of the flows is particularly important in combustion modelling since chemical source terms are strong nonlinear functions of the instantaneous values of the temperature and species concentrations, as exemplified by the Arrhenius form. The magnitudes of the source terms depend on the fluctuations of the aerothermodynamic variables and, to a lesser extent, on the mean values. Moreover, since a chemical reaction, which is a time-dependent process, occurs on the molecular level, using averaged and modelled equations in which mixing is described by mean fluctuations is not expected to properly describe it. An important aspect of combustion is that the chemistry is a Lagrangian process which proceeds as fluid elements move. Averaging this intrinsically unsteady process removes information that cannot be recovered using few moments.

A better description of chemical reaction in an unsteady flow field may be based on the Lagrangian formulation of the conservation equations. A numerical scheme, which employs the Lagrangian description of the flow field, should then lead to more accurate results if fine resolution is achieved. In this work, we describe such numerical simulation algorithms. Mathematical theories constructed to address issues of accuracy and convergence are exemplified in [11,12,13].

Numerical simulation of turbulent combustion attempts to minimize the use of phenomenological modelling. Thus, their results can be used to investigate some of the mechanisms of turbulence–chemistry interactions. Furthermore, since the instantaneous behavior of the variables are known at all points and at all times, accurate simulations offer a method of probing the flow when experimental techniques are not available. Ultimately, and after validating and verifying the results against experimental measurements, ab initio predictions can be possible. Finite difference methods,[14,15] spectral methods,[16] and vortex methods[17] have been utilized in numerical simulation of nonreacting shear layers. Some have also been extended to reacting shear layers.[18,19] The first two methods are based on Eulerian description of the flow field, using grids to discretize derivatives of the aerothermodynamic variables, or to expand these variables in harmonic functions, respectively. Vortex methods are grid free, Lagrangian schemes, which have been used to obtain solutions at high Reynolds number.

Vortex methods optimize the computational efforts by distributing computational elements around regions of high vorticity.[20,24] However, five factors have limited their utilization to study combustion problems: (1) Eulerian methods, which were used to solve the energy and species conservation equations in thin flame sheet models, seemed, in some sense, to defeat the purpose of using vortex methods to simulate the hydrodynamic field;[25] (2) the limit of fast chemistry, which was used in thin flame sheet models, did not allow realistic finite rate chemical kinetics to be part of the model;[26] (3) vortex methods, while maintaining reasonable accuracy in the majority of the field, lost resolution within the part of the field where the strain field is very strong;[27] (4) vortex methods were limited to handling incompressible flows, thus the models neglected the distributed expansion and the baroclinic torque generated during combustion; and (5) three–dimensional effects were only included in specific cases,[28,29] and no attempt has been made yet to represent small scale dissipation in two–dimensional methods.

In this article, we introduce the transport element method. When applied to obtain a solution of the vorticity transport equation, the method becomes the vortex element method in which particles are treated as finite elements that accurately discretize the vorticity field and change their shape, configuration or distribution to accommodate distortions of the vorticity field caused by the development of strong strain fields. The transport element method, moreover, extends the concepts of the vortex element method to obtain solutions of the scalar conservation equations, which govern reacting flows, in terms of moving Lagrangian gradients. Both schemes are formulated to preserve the effect of compressibility at low Mach number. The transport element method is applied to study the evolution of combustion in a reacting shear layer in premixed gases. Results are used to investigate different modes of turbulence–combustion interactions in a shear layer, and to study the outcome of these interactions in different regimes of the governing parameters. Processes of burning enhancement and flame deceleration or complete extinction via the effect of stretch which develops within the rolling shear layer are analyzed in light of the numerical results.

In Section II, the formulation of the model equations governing a reacting shear layer at low Mach number is described. In Section III, we give a summary of the vortex element method, and a comprehensive development of the transport element method. Emphasis is placed on the latter since it clarifies some subtle issues regarding the effect of the strain field on the local scalar gradients. In Section IV, results of the application of these methods to a spatially developing, thermally stratified mixing layer are described. In Section V, results for a reacting, temporally developing mixing layer are analyzed. In Section VI, conclusions and future work are summarized.

II. FORMULATION

The non–dimensional form of the conservation equations governing a two-dimensional, unsteady reacting flow is summarized in Table I. We assume that initially, and at all times at the inlet section, a premixed reactant R and a product P are present at given concentrations c_{Ro} and c_{P0} in the top high–speed and bottom low–speed streams, U1 and U2, respectively. For computational simplicity, chemistry is assumed to be governed by a single–step, irreversible, Arrhenius reaction of order n. Adding more steps to the chemical kinetics scheme will require integrating more species conservation equations. The Mach number is assumed to be small, which leads to the following simplifications in the governing equations: (1) pressure variation due to the flow field is small compared with the total pressure, and hence neglected in the equation of state; (2) spatial variations of pressure, and energy dissipation due to viscosity are neglected in the energy equation; and (3) acoustic interactions are removed. This isobaric approximation allows partial decoupling of continuity, momentum and energy equations so that they can be integrated sequentially instead of simultaneously.[30,31] We assume that the reactant and product behave as perfect gases with equal molecular weights and specific heats, and that thermal and mass diffusivities are constants, but not necessarily equal. The Reynolds number is high and the effect of viscosity is neglected.

The definition of the symbols is as follows: $d/dt = \partial/\partial t + u \cdot \nabla$ is the Lagrangian derivative along a particle path. $u = (u,v)$ is velocity, $x = (x,y)$ and x and y are the streamwise and the cross-stream directions, respectively. t is time, ϕ is a velocity potential, $\psi = \psi e_z$ is a stream function defined such that $u_\omega = \nabla \times \psi = (\partial\psi/\partial y, -\partial\psi/\partial x)$, and $\omega = \nabla \times u$ is vorticity. e_z is the unit vector normal to the x-y plane. u_p is a potential velocity, $\nabla \cdot u_p = 0$, added to satisfy the normal boundary condition across the boundary of the domain. c is the concentration per unit mass, T is temperature. ∇ and ∇^2 are the gradient and Laplacian operators, respectively. $A_f W$ is the rate of formation of products per unit mass per unit time, $W = c_R^n \exp(-T_a/T)$, and n is th ereaction order. Variables are non-dimensionalized with respect to the appropriate combination of the velocity of the high–speed stream U1, the channel height H, the free–stream concentration of R, c_{Ro}, and the free– stream temperature of the reactants at $x = 0$, T_o. T_a is the

activation energy, non-dimensionalized with respect to $(R_g \ T_o)$, R_g being the gas constant. Q is the enthalpy of reaction, non-dimensionalized with respect to $C_p \ T_o$, where C_p is the specific heat at constant pressure. $P_e = U1 \ H/\alpha$ is the Peclet number, where $\alpha = k/(\rho C_p)$ is the thermal diffusivity, taken as a constant. $A_f = A \ H/U1$ is the non-dimensional frequency factor of the chemical reaction-rate constant. The Damkohler number $D_a = A_f \ W(c_m, T_m)$, c_m and T_m corresponding to conditions of maximum reaction rate, is the ratio of flow time to chemical time. $L_e = \alpha/D$ is the Lewis number, and D is the mass diffusivity.

Equation (2) is the decomposition of the velocity field into irrotational, solenoidal and potential components. Equation (3) is obtained by substituting u into the continuity equation and using $p = \rho \ T = $ constant since the flow is unconfined and is at low Mach number. Equation (5) is obtained by taking the curl of the momentum equation of an inviscid flow and using $\nabla p = - \rho \ du/dt$ to substitute for the pressure gradient in the baroclinic torque term to allow the integration of the equations without explicitly computing the pressure distribution. Equations (6-8) are the conservation of energy and species, respectively, for a reacting mixture at finite heat and mass diffusivities. Equation (9) is the equation of state at low Mach number in an unconfined flow.

The equations form a five-parameter system: P_e, L_e, D_a, Q and T_a. The properties of the solution and the characteristics of the interaction between the flow field and the chemical reaction depend on the values, or the combination of values, of the individual parameters. If the system is not adiabatic, i.e., $T_R = T_o$ while $T_P - T_R \neq Q$, one more parameter, such as T_P/T_R, must be specified in the formulation. The equations identify four different processes of turbulence-combustion interactions: (1) the generation of an irrotational velocity due to volumetric expansion as the temperature rises during heat release, $\nabla\phi$, in Eqs. (2,3); (2) the generation of baroclinic vorticity due to pressure gradient-density gradient interactions during heat release, $\nabla\rho \times \nabla p$ in Eq. (5); (3) the advection and straining of the flame structure in Eqs. (6,7 and 8); and, (4) the inhomogeniety in the diffusive fluxes due to non-unity Lewis number in Eqs. (6) and (7).

TABLE I GOVERNING EQUATIONS

REACTION
$$R \ \xrightarrow{k} \ P \tag{1}$$

VELOCITY
$$u = \nabla\phi + \nabla\times\psi + u_p \tag{2}$$

EXPANSION
$$\nabla^2\phi = \frac{1}{T} \frac{dT}{dt} \tag{3}$$

ROTATION
$$\nabla^2\psi = - \omega(x,t) \tag{4}$$

VORTICITY
$$\frac{d}{dt}(\frac{\omega}{\rho}) = - \frac{1}{\rho^2} \nabla\rho \times (\frac{du}{dt}) \tag{5}$$

ENERGY $\qquad \dfrac{dT}{dt} = \dfrac{1}{P_e} \nabla^2 T + A_f Q W$ $\qquad\qquad$ (6)

REACTANTS $\qquad \dfrac{dc_R}{dt} = \dfrac{1}{P_e L_e} \nabla^2 c_R - A_f W$ $\qquad\qquad$ (7)

PRODUCTS $\qquad \dfrac{dc_P}{dt} = \dfrac{1}{P_e L_e} \nabla^2 c_P + A_f W$ $\qquad\qquad$ (8)

STATE $\qquad \rho T$ = constant $\qquad\qquad$ (9)

III. NUMERICAL METHOD

III.1. THE VORTEX ELEMENT METHOD

An important step in improving the accuracy and extending the application of vortex schemes to flow fields that develop large strain rates, such as shear layers, is the formulation of the vortex element method.[27] In this method, the vorticity field is accurately discretized among finite elements that move along particle paths, or particles that transport finite elements of vorticity. The strain field is used to redistribute the vorticity among the computational elements as time progresses so that small scales generated by planar stretch can be captured. This allows accurate long-time computation of the vorticity field after the strain field has developed. Capturing the strain field accurately is very important in computing turbulent flames since: (1) it governs the mixing process, which occurs after the original fluid layers have been stretched to very small scales, since it defines the diffusive flux; and (2) it may lead to flame quenching, or to burning enhancement, due to the generation of strong gradients as will be shown later. Below, we summarize the method and show how it can be extended to compute a compressible non-barotropic flow at low Mach number.

The vorticity field is initially discretized among vortex elements of finite structure. The distribution of vorticity associated with each element is described by a radially symmetric function, f_δ, with a characteristic radius, δ, such that most, or all of the vorticity is concentrated within $|x-X_i| < \delta$. X_i denotes the center of a vortex element at time $t = 0$. Vortex elements are initially distributed within the area where $|\omega| > 0$ such that the distance between neighboring elements is h in the two principal directions. The accuracy of the discretization depends on the choice of f_δ, the value of h, and the ratio δ/h. The strength of the vortex element located at X_i, which is denoted by ω_i, is obtained from the solution of the system of equations:

$$\omega(X_i, 0) = \sum_{j=1}^{N} \omega_j h^2 f_\delta(X_i - X_j) \qquad\qquad (10)$$

where $\omega(\mathbf{X},0)$ is the vorticity distribution at $t = 0$. It can be shown that $f_\delta(r) = (1/\pi \delta^2) \exp(-r^2/\delta^2)$ leads to a second-order discretization. We found that for accurate representation of the vorticity distribution, δ must be slightly larger than h, i.e., $\delta/h \sim 1.1-1.3$, and that h must be varied until $||\Gamma - \Sigma\Gamma_i|| < \epsilon$ and $|| \omega(x,0) - \Sigma \omega_i h^2 f_\delta(x-X_i) || < \epsilon$. Γ is the total circulation of the vorticity field, $\Gamma(x) = \Sigma \Gamma_j \kappa(x - X_j)$, $\kappa(r) = {}_0\int^r r' f(r')dr'$ and $r = |x|$. $\Gamma_i = \omega_i h^2$ is the total circulation of each individual vortex element. $||$ denotes the second norm and ϵ is a small number which determines the accuracy.

For an incompressible flow, Eq. (5) leads to the Helmholtz theorem, which states that vorticity is constant along particle paths, i.e.

$$\omega(x,t) = \sum_{i=1}^{N} \Gamma_i \, f_\delta(x-X_i(X_i,t)) \tag{11}$$

and

$$\frac{dX_i}{dt} = u(X_i(X_i,t),t) \tag{12}$$

where X_i is the particle path $X_i(X_i,0) = X_i$. To obtain the velocity field of a collection of vortex elements in the form of Eq. (11), we note that the stream function of a single vortex element is obtained by integrating Eq. (4). Using polar coordinates to integrate this equation for a vortex element placed at x=0, we get $\partial\psi_\delta/\partial r = -\kappa(r/\delta)/r$. The velocity field of a single element is thus radially symmetric since $u_\theta = -\partial\psi_\delta/\partial r$. The velocity field induced by a distribution of finite-core vortex elements, of shape f_δ and strength Γ_i located at $X_i(X_i,t)$ is:

$$u_\omega(x,t) = \sum_{i=1}^{N} \Gamma_i \, K_\delta(x-X_i(X_i,t)) \tag{13}$$

where $\qquad K_\delta(x) = - \frac{(y, -x)}{r^2} \kappa(\frac{r}{\delta}) \tag{14}$

Vortex elements move at the local velocity computed at their centers. As time progresses, the distance between neighboring elements increases in the direction of maximum strain such that $\Delta X > h$, where ΔX is the distance in the direction of maximum strain defined as $\Delta X = \Delta X.\Delta u/|\Delta u|$ and Δ is the difference operator. This leads to a deterioration of the discretization accuracy, which requires that $\delta > \Delta X$. Thus, an algorithm must be used such that when $\Delta X > \beta h$, where $\beta \sim 1.5$, a computational element is inserted at the midpoint between the original elements and $\Delta X' = \Delta X/2$. The circulation of the new element, and that of the original two neighboring elements, is one third the sum of the circulation of the original two elements.[27]

For compressible barotropic flow, Eq. (5) shows that $d(\omega/\rho)/dt = 0$. Moreover, $\Gamma = \int \omega \, dA$, where A is the area, while $\int \rho \, dA = $ constant. Thus, the circulation is constant along a particle path — Kelvin theorem — and Eqs. (11-14) can be used to compute the evolution of the vorticity and velocity field provided that Eq. (3) is

used to compute the irrotational component of the velocity due to volumetric expansion, as will be shown in the next section. When $\nabla\rho \times \nabla p \neq 0$, the circulation of each vortex element must be updated each time step. Using the definition of the circulation in Eq. (5), we get:

$$\frac{d\Gamma}{dt} = - \int \frac{\nabla\rho}{\rho} \times (\frac{du}{dt}) \, dx \tag{15}$$

Since $\Gamma = \Sigma \, \Gamma_i \, \kappa(x-\chi_i)$, $\nabla\rho = \Sigma \, \Delta\rho_i \, f_\delta(x-\chi_i)$, and $\Delta\rho_i = \nabla\rho_i \, h^2$ as will be shown in the next section, Eq. (15) can be written as:

$$\frac{d\Gamma_i}{dt} = \frac{\Delta T_i}{T_i} \times (\frac{du}{dt})_i \tag{16}$$

where, according to the low Mach number approximation, $\nabla\rho/\rho = - \nabla T/T$, while $\nabla T = \Sigma \, \Delta T_i \, f_\delta(x-\chi_i)$ and $\Delta T_i = \nabla T_i \, h_i^2$. In the next section, we will show how to compute $\nabla\rho$, ρ, ∇T and T. Moreover, $(du/dt)_i$ is computed by numerically differentiating the velocity of the vortex element using a high-order formula. Equations (11) and (15) are integrated using a fourth order Runge-Kutta-Merson method with variable time step for error control.

III.2. THE TRANSPORT ELEMENT METHOD

Another important development in the application of particle methods to reacting flows is the formulation of the transport element method to compute the temperature and species concentration distributions in a Lagrangian form.[27] In this scheme, the gradient of the scalar field is discretized into a number of finite elements using Eq. (10) with ω replaced by $g = \nabla s$, where s is a generalized scalar, being either T or c. Like vortex elements, transport elements are distributed where $|\nabla s| > 0$ and are moved with the local velocity field with time. Particles are used to transport scalar gradients, however, contrary to vorticity, scalar gradients are not conserved along particle paths, and should be modified according to the local straining and tilting of the material elements. The extension of this method to reacting flow will require changing the gradient transported by each element according to the reaction source term in Eqs. (6,7,8) in a way similar to changing the circulation with the non-baroclinic torque. Thus, the evolution of the chemical reaction with time will be computed in a Lagrangian frame of reference as the interacting species flow. In the following, we describe the conservative form of the transport element scheme and its extension to solve Eqs. (6,7,8).

Initially, the scalar gradient g is discretized on a square mesh h x h according to

$$g(X_j,0) = \sum_{i=1}^{N} g_i \, h^2 \, f_\delta(X_j - X_i) \tag{17}$$

where f_δ, δ and h have been defined before, and should be chosen to satisfy the same requirements. Note that the values of g_i depend on the choice of h and δ, and are obtained by solving the system of linear algebraic equation formed by applying Eq. (17) to all mesh points. To see how to transport the scalar gradient in a Lagrangian form, we start by the incompressible, non-diffusive, non-reactive case. If s is a passive, non-diffusive scalar, the conservation equations for s and $g = \nabla s$ are:

$$\frac{ds}{dt} = 0 \tag{18}$$

and

$$\frac{dg}{dt} = - g \cdot \nabla u - g \times \omega \tag{19}$$

where $\omega = \omega\, e_z$. Thus, s remains constant along a particle path, while g changes due to the straining and rotation of the material line by the local strain field and vorticity. If the material is exposed to a strong strain in the direction normal to the gradient, the value of g must increase by the same amount as the stretch in the material element. This can be seen by expanding of g in terms of n and g, where $g = |g|$ and $n = g/g$, noting that $dn/dt = - n \times \omega / 2$ (see Batchelor[30]):

$$\frac{dg}{dt} n = - g (n \cdot \nabla u + \frac{1}{2} n \times \omega) \tag{20}$$

Moreover, $g = (ds/dn)\, n \sim (\delta s/\delta n)\, n$, where δs is the variation of s across a small material line δn. The variation of a material vector element δn is given by $d(\delta n)/dt = \delta n \cdot \nabla u$, where $\delta n = \delta n\, n$.[30] Furthermore, for an incompressible flow, $\delta l.\delta n = $ constant along a particle path defined by $d\chi/dt = u(\chi(X,t),t)$. From these kinematic ralations, the variation of the material line δl along a particle path can be written as:

$$\frac{d\delta l}{dt} n = - \delta l (n \cdot \nabla u + \frac{1}{2} n \times \omega) \tag{21i}$$

From Eqs. (20) and (21i), it follows that $g/\delta l = $ constant along a particle path. For a graphical representation of this concept, see Fig. 1. Thus, the flux initialized by Eq. (17) evolves according to:

$$g(x,t) = \sum_{i=1}^{N} g_i(t)\, h^2\, f_\delta(x - \chi_i(X_i,t)) \tag{22i}$$

where

$$g_i(t) = \frac{\delta s_i\, \delta l_i(t)}{h^2}\, n_i(t) \tag{23i}$$

while

$$\frac{d\chi_i}{dt} = u(\chi_i(X_i,t),t)$$

where $\chi_i(X_i,0)=X_i$. δl_i is updated using Eq. (21i) and $n_i \cdot \delta l_i/\delta l_i = 0$. While using Eq. (23) is equivalent to updating $g_i(t)$ according to Eq. (19), applying the expression in Eq. (23i) guarantees the conservation of δs_i. Moreover, instead of integrating Eq. (21i) to update δl_i, one can save computational effort by recalling that $\delta l_i(t) = (X_{i+1} - X_{i-1})/2$. Thus, it suffices to move the centers of the transport elements, while remembering the neighboring elements at $t = 0$ in order to compute the scalar flux. Moreover, when an element is inserted between two neighboring elements, in the direction of maximum strain, the values of δl_i are redistributed between the three elements. This also requires changing h^2 in Eqs. (22) and (23) to h_i^2 so that the total material area is conserved. In this case, Eq. (22) becomes

$$g(x,t) = \sum_{i=1}^{N} g_i(t) \, h_i^2 \, f_\delta(x - \chi_i(X_i,t)) \tag{22s}$$

where

$$g_i(t) = \frac{\delta s_i \, \delta l_i(t)}{h_i^2} \, n_i(t) \tag{23s}$$

For a compressible flow, the above analysis should be modified to reflect the fact that $\rho \, \delta l . \delta n = $ constant along a particle path. Using the kinematic relations listed above, Eq. (21i) becomes:

$$\frac{d}{dt}(\rho \, \delta l) \, n = - \rho \, \delta l \, (\, n \, . \, \nabla u + \frac{1}{2} \, n \times \omega \,) \tag{21c}$$

Thus, $g/(\rho \, \delta l) = $ constant along a particle path. In terms of the variational change in s, δs_i, across a material element δl_i, Eq. (23i) is modified as follows:

$$g_i(t) = \frac{\delta s_i \, \delta l_i(t) \, \rho_i(t)}{\rho_i(0) \, h_i^2(0)} \, n_i(t) \tag{23c}$$

The value of ρ is computed using the relation $\rho \, T = $ constant, in accordance with the low Mach number approximation, $T = \sum \nabla T_i \, h^2 \, f_\delta(x - X_i)$. Note that the area of the material element is expanding such that $\rho_i(t) \, h_i^2(t) = $ constant. Thus,

$$g_i(t) = \frac{\delta s_i \, \delta l_i(t)}{h_i^2(t)} \, n_i(t) \tag{23c}$$

and

$$g(x,t) = \sum_{i=1}^{N} g_i(t) \, h_i^2(t) \, f_\delta(x - \chi_i(X_i,t)) \tag{22c}$$

Given the location and strength of the transport elements, the scalar concentration can be computed as follows. By taking the gradient of $\nabla s = g$, we get $\nabla^2 s = \nabla . g$. The solution of this equation in an infinite domain can be written as:

$s = \int \nabla.g \, G \, dx$, where $G = -1/2\pi \, \ln r$ is the Green function of the Poisson equation. This last equation shows that the transport elements act as sources of strength equal to the divergence of the scalar flux, $\nabla.g$. Integrating by parts, one gets $s = \int g \cdot \nabla G \, dx$. Using Eqs. (22) and (23) for g, we get:

$$s(x,t) = \sum_{i=1}^{N} g_i(t) \, h_i^2(t) \cdot \nabla G_\delta(x-\chi_i(X_i,t)) \tag{24}$$

where

$$\nabla G_\delta = \frac{(x,y)}{r^2} \, \kappa(\frac{r}{\delta}) \tag{25}$$

where $\kappa(r) = \int r' \, f(r') \, dr'$, as defined before. If the distance between neighboring elements in the direction of principal strains exceeds a maximum distance βh, one element is inserted halfway between the two elements and the value of δl_i and h_i^2 are adjusted for the three elements. A recombination procedure can also be implemented to curb the growth in the number of computational elements. The need for this insertion-recombination procedure is more apparent here since the magnitude of the gradient increases where the strain field is high; and to maintain accuracy, more elements must be used to transport this gradient.

With finite diffusivity, the first term on the right hand side of Eqs. (6-9) should be simulated in the solution. In gradient form, the conservation equation can be written as:

$$\frac{dg}{dt} = -g.\nabla u - g \times \omega + \alpha \nabla^2 g \tag{26}$$

where α is the molecular diffusivity, or the inverse of the Peclet number. At high speed, this is typically 10^2-10^5. To solve Eq. (26) using the scheme that we have developed so far, each element g_i must be updated according to the diffusion equation:

$$\frac{\partial g_i}{\partial t} = \alpha \nabla^2 g_i \tag{27}$$

without changing the shape of the core function or the value of g_i. Taking $\delta = \delta(t)$, and substituting Eq. (17) into Eq. (27), we obtain $d\delta^2/dt = 4\alpha$. Thus, to simulate the effect of diffusion, the core radius must grow according to:

$$\delta^2 = \delta_o^2 + 4 \alpha t \tag{28}$$

where δ_o is the core radius at $t = 0$. If the diffusivities of momentum, heat and mass are different, the core of the vortex elements and of different scalar transport elements become different as time progresses. At high diffusivities, or small Peclet numbers, the cores of the elements will experience rapid growth and $\delta \gg \beta h$. In this case, transport elements must be subdivided into elements with

smaller cores while preserving their total strength. However, this will not be used here since we are interested in cases where the Peclet number is large. Values typical to this study are: $\delta_o = h = 0.3$, $t_{max} = 20$, $\alpha = 0.001$, and $\delta_{max} = 0.41$.

If the chemical source term is non-zero, then Eq. (26) is modified to become:

$$\frac{dg}{dt} = -g \cdot \nabla u - g \times \omega + \alpha \nabla^2 g + \sum_{j=1}^{k+1} \frac{dW}{ds_j} g_j \tag{29}$$

where k is the number of chemical species. Using the definitions of g, the gradient transported by each element must be modified according to:

$$\frac{d}{dt} \delta s_i = \sum_{j=1}^{k+1} \frac{dW}{ds_j} \delta s_j \tag{30}$$

In this case, the element strength should be modified as:

$$g_i(t) = \frac{\delta s_i(t) \, \delta l_i(t)}{h_i^2(t)} n_i(t) \tag{23r}$$

while all the kinematic relations, and Eq. (22c) hold as before.

Recognizing the fact that $h_i^2(t)$ appears in the numerators of Eqs. (22i), (22s) and (22c); while it appears in the denominator of Eqs. (23i), (23is), (23c), and (23r), we will define a new quantity $\Delta g_i = g_i h_i^2$ and rewrite these equations as:

$$g(x,t) = \sum_{i=1}^{N} \Delta g_i(t) \, f_\delta(x - \chi_i(X_i,t)) \tag{31}$$

$$\Delta g_i = \delta s_i(t) \, \delta l_i(t) \, n_i(t) \tag{32}$$

$$s(x,t) = \sum_{i=1}^{N} \Delta g_i(t) \cdot \nabla G_\delta(x - \chi_i(X_i,t)) \tag{33}$$

Equations (31), (32) and (33) apply for the most general case. The transport elements generate an expansion field as their temperatures change, according to Eq. (3). The velocity field associated with this expansion within each element at the low Mach number limit can be written as:

$$\nabla^2 \phi_i = \frac{1}{T_i} \left(\frac{dT}{dt}\right)_i \tag{34}$$

The total velocity produced by the expansion field is:

$$\nabla \phi(x,t) = \sum_{i=1}^{N} \frac{1}{T_i} \left(\frac{dT}{dt}\right)_i h_i^2(t) \, \nabla G_\delta(x - \chi_i(X_i,t)) \tag{35}$$

where h_i^2 is the area of the material element which is divided every time one element is inserted due to stretch and is varied according to mass conservation, and $\rho_i(t)$ $h_i^2(t)$ = constant.

The algorithm of the transport element method proceeds as follows: (1) update the locations of the elements χ_i according to the velocity at their centers using Eq. (12); (2) update the values of δl_i and n_i either according to the integration of Eq. (21) or by keeping track of the neighboring elements; (3) update the core radii of different elements according to the corresponding Peclet number using Eq. (28); and (4) compute the concentrations of all the scalars using Eq. (24); and (5) update the value of δs_i according to Eq. (30). In most cases, it is possible to use the same set of particles to transport elements of different scalars, as well as the vortex elements, resulting in substantial savings in the transport step.

IV. THE SPATIALLY-DEVELOPING, NON-REACTING SHEAR LAYER

The vortex element and the transport element methods are applied to simulate the initial stages of development of a spatially-developing, thermally-stratified, two-stream shear layer. On the left boundary of the domain, it is assumed that the wake region behind the splitter plate, where the two incoming boundary layers merge to form the shear layer, is negligibly small. Thus, at x = 0; for y > Δ_s: u → U1 = 1 , T → T1* = 1, and for y < - Δ_s, u → U2 = 0.333, and T → T2* = 0, where → means "approaches asymptotically". Δ_s^2 = 2 σ^2, while σ is the standard deviation of the Gaussian distribution that describes the vorticity and the scalar gradients and 2 Δ_s is the nominal shear layer thickness at x = 0. The normalized temperature is defined as T* = (T-T2)/(T1-T2). For the results in Figure 2, Δ_s = 1/26.4. The corresponding most unstable wavelength, as predicted by the linear theory, is 0.5. Within the shear layer, the velocity and temperature distributions are represented by error functions.

The rate at which vorticity is convected into the upstream side of computational domain, at x = 0, is $d\Gamma/dt$ = $\Delta U.Um$, where Um = (U1 + U2)/2. At each time step, five elements, arranged vertically, are used to discretize this vorticity according to Eq. (10). The potential velocity component, u_p, is computed by adding two source flows at x = - ∞ and y = + 0 and y = - 0 to the velocity field in Eq. (2) to satisfy the boundary condition at x =0. The no-flow boundary condition across the solid walls is implemented by using conformal mapping and image vortices with the opposite sign of vorticity in the transformed plane.[7]

In the solution of the energy equation, the walls are considered insulated, dT/dn = 0 where n is the unit vector normal to the wall. To satisfy this boundary condition, the images of the temperature transport elements in the transformed plane must have the opposite of the signs of the elements. Energy sources are utilized to impose the boundary condition at x = 0. At the downstream side of the computational window, x = 5, vortex and transport elements are deleted. This induces a perturbation which ensures that the rollup and first pairing will always take place

within the computational window. Since this perturbation is not applied in an organized manner, the resulting shear layer will be considered as an unforced layer.

Figure 2 shows the location and velocity of all vortex elements used in the computations at four different time steps. The time step of the computations is Δt = 0.15. The plots exhibit a very clear and accurate portrait of the rollup. During rollup, the vorticity within the shear layer is attracted towards the center of a large eddy, entraining fluid from both sides, and forming what appears to be a moving focal point of a spiral. Between neighboring large eddies, a zone of strong strain is developing where the vorticity is depleted and the scalar gradients are growing. This "braid" zone can be described as a moving saddle point where locally the fluid flow experiences a separation into two streams; one moving towards the left and the other moving towards the right with respect to the saddle stagnation point. Downstream, the process of rollup continues until a stronger perturbation forces two neighboring eddies to interact in a pairing process. It is important to stress that the algorithm of inserting elements as the strain field develops is responsible for maintaining the organization of the calculation for a long time.

The natural frequency of shedding can be defined as $f_n = U_m/\lambda$, where λ is the wavelength of the large eddy. The corresponding average Strouhal number, as computed from the computational results, is $S_t = 1/f_n = 0.033$. This is the same value as the frequency of the most unstable mode computed from the linear stability theory of a spatially developing shear layer under the conditions described above. Results for the growth rate, average velocity and turbulent statistics were presented in the study of Ghoniem and Ng[7] for the forced shear layer. Comparison with the corresponding analytical and experimental data were also performed in the same reference.

If the layer is forced at a frequency close to the most unstable mode by oscillating the incoming vorticity layer according to $\Delta y = a_f \sin (2 \pi \Omega_f t)$, where Δy is displacement of the center of the vortex element due to forcing and a_f and Ω_f are the amplitude and frequency of forcing, the evolution is expected to be more organized.[7] In Fig. 3, we plot the results of such a case with $a_f = 0.025$ and $\Omega_f = (\lambda_f/U_m) = 1.33$, where λ_f is the wavelength of forcing. The evolution of the eddy which has the forcing frequency through the various stages of rollup is shown clearly at each time step when moving downstream, or with time when observed from the same location.

The effect of rollup on the temperature distribution within the eddy is shown in Fig 4. Here, we plot the temperature distribution across several sections downstream, superimposed on the distribution of vortex elements at the same location. In these plots, we assume that the thermal diffusivity is negligibly small, and we concentrate on the effect of the convection field on the entrainment of hot and cold fluid within the large eddies. Note that the temperature profiles become more rugged as the core spins further, and that the temperature distribution is not symmetric around the midsection of the eddy.

The high resolution of the transport element method demands the use of a large number of computational elements. Moreover, the number of elements grows rapidly

with time due to the severe stretch produced in the shear layer. This makes the computation of a wide window, which contains a number of successive eddies, rather expensive. In the next section, we direct attention towards a model of this problem that requires less effort computationally while essentially preserving all the physical processes involved in the spatially developing layer. This is the temporal shear layer model in which a computational window that moves at the average speed of the flow is imposed on a single wavelength while the eddy is growing.

V. TEMPORALLY-DEVELOPING, REACTING SHEAR LAYER

Computational results showing the evolution of a large eddy in a temporal shear layer are presented in Figure 5. In this case, the boundary conditions are periodic, i.e., $\omega(x,y,t) = \omega(x+\lambda,y,t)$ and $u(x,y,t) = u(x+\lambda,y,t)$, where λ in the wavelength of the perturbation. Since detailed analysis of the evolution of the temporal, thermally stratified shear layer was presented in Ghoniem et al.[27], it will not be repeated here. The qualitative resemblance between the development of large eddies in a spatial and a temporal shear layer is clearly seen by comparing Figs. 3 and 5. Moreover, the shedding frequency, i.e. the frequency of the most amplified mode, is almost the same in both cases. However, the growth rate of the perturbation is different since it depends on the velocity ratio across the layer; a parameter that does not appear in the analysis of the temporal layer. Moreover, the asymmetric growth of the eddies, which is observed in the spatially-growing case, Fig. 3, is not present in the temporally-developing layer results, Fig. 5.

In the computation of the temporal layer, the window is limited to one wavelength and one can afford to use more elements within the domain to improve the resolution. One can also conduct, inexpensively, parametric studies on the effect of various physical parameters that appear in the model, Eqs.(1-9). Thus, the temporal layer will be used as a model for the spatial layer to study turbulence-combustion interactions in shear flow. Since the flow is unconfined, the wavelength Δ_s is used instead of H to non-dimensionalize the length.

The temperature profile across the midsection of the eddy is exhibited in Fig. 6. The rollup brings fluid from one side to the opposite side, while stretch increases the gradient across each layer. Thus, the rollup of the shear layer is the mechanism of entrainment that leads to strong mixing enhancement as the two fluids diffuse across the stretched interface. The temperature profiles show that after the relaxation of the first rollup, a secondary instability develops which forces the core through another turn, creating a more ragged temperature distribution. It is also noticed, by comparing Figs. 4 and 6, that the asymmetric growth of the spatially-developing layer is responsible for creating asymmetric temperature profiles across the midsection of the eddies. The relationship between these temperature profiles and the asymmetric entrainment observed in experimental measurements[32,33] will be explored in detail in future studies.[34]

Since rollup is associated with strong stretch that reduces the thickness of the material layers, it increases the gradients across these intertwining layers, thus enhancing the diffusion fluxes. Quantitatively, the rate of mixing can be expressed as $\dot{M} = \int q \cdot n \, da$, where q is the diffusion flux, n is the unit vector normal to the material surface, and da is the surface area element. Moreover, for two-dimensional flow, $da = dl$, and since $q / \delta l = $ constant, then $\dot{M}$ is proportional to $(\delta l)^2$. The net result is that stretch by a factor ζ enhances mixing by a factor ζ^2. The quadratic rise in mixing during rollup is expected to have a significant effect on the rate of reaction.

In the reacting layer calculations, the full system of equations is integrated using particles which transport vortex elements, temperature gradient elements, and reactant and product gradients elements. At time $t = 0$, the vorticity layer and the flame front coincide, and the thickness of the vorticity layer as well as the flame thickness are equal. A small sinusoidal perturbation with amplitude $\varepsilon = 0.05 \lambda$ is imposed on both distributions. The first case to be computed corresponds to the following set of parameters: $P_e = 200$, $L_e = 1$, $A_f = 1$, $Q = 4$, $T_a = 10$ and $n = 1$. The corresponding Damkohler number, measured at the conditions of maximum reaction rate, is around 0.02, and the temperature ratio across the layer is $T_P/T_R = 5$.[*1]

Figure 7 shows the results for the reacting shear as the rollup and the chemical reaction porceed simultaneously. At the early stages, the reacting eddy strongly resembles the nonreacting eddy shown in Fig. 5. However, as rollup starts, the following is observed: (1) a swelling, due to the increase in the rate of heat release, continues as more reactants are entrained into the burning core; (2) the growth of the instability, as measured by the angle between the major axis of the elliptical structure and the main stream direction, is encumbered because the volumetric expansion causes the vorticity intensity to decrease and the eddy to become weaker and less coherent; and (3) the eddy loses its symmetry and becomes eccentric due to the asymmetric expansion, and due to the generation of a baroclinic torque associated with density gradients. As more of the initial core is burnt, the fluid inside the eddy ceases to spin, contrary to the nonreacting case in which the secondary instabilities force the core to continue its spinning. Meanwhile reactants move through the side to enter the reaction region.

These numerical results agree qualitatively with the experimental results of Keller and Daily[5] on the reacting premixed shear layer at intermediate values of the equivalence ratios. The Schlieren photographs of the experiment show that as the equivalence ratio is increased, the rate of growth of both the individual eddies as well as the entire shear layer, increase due to heat release. In the meantime, the rollup of individual eddies slows down, leading to the formation of elliptical

---

1*In the following results, the value of h in Eq. (23c) was taken as a constant for all elements and for all times. In more recent computations, when we varied h with stretch and expansion, while all the trends were the same, the rate of reaction was found to be less than what was obtained with constant h. Thus, the results will only be interpreted qualitatively.

eddies. The major axes of the eddies remain at a finite angle with respect to the streamwise direction. Moreover, at low equivalence ratios, most burning occured within the cores of the eddies, and the flame did not leave the shear layer.

On the same figure, a solid line is plotted through points of maximum reaction rate. The line indicates where the flame front, or the maximum heat release rate, is within the shear layer. Below this line, the product concentration approaches unity and the temperature reaches T_p. During the early stages of rollup, the line of maximum reaction rate follows one of the material lines closely, i.e., the growth of perturbation merely changes the topology of the flame front. At later stages, this line, while staying close to another material line, forms a boundary of the products across which the reactants are entrained into the burning core. Below this line, where products form, the core almost ceases to rotate. At the last stage of burning of the eddy, the two sides of the flame within the core burn to close this entry way, and the flame moves out of the eddy and becomes an ordinary laminar flame.

The effect of heat release on the structure of the eddy, which is generated by the rollup of the shear layer, can be seen from the temperature profiles across the midsection of the wavelength, shown in Fig. 8. Since the Lewis number is one, $c_R = 1 - (T - T_R)/Q$. As reactants are entrained into the core of the growing eddy from the right side, a Z-shaped flame is formed. At the initial stages where the rate of entrainment is faster than the rate of burning, the flame extends deeper into the lower stream. As the reactants within this zone burn, heat is released within the core of the rotating eddy, causing the eddy to swell, while maintaining its elliptical shape. The baroclinic vorticity generated around this zone causes the observed eccentricity of the large eddy. The temperature profiles show that the higher order instabilities observed in the nonreacting case are suppressed by the heat release, and that the core of the eddy stops its rotation. As the reactants within the eddy burn, the flame leaves the structure and moves into the reactants. This results in the formation of a temperature profile which is very similar to the temperature profile at t=0.

Figure 7 also shows the effect of rollup on the shape of the flame front, which, as will be shown in the next paragraph, has a strong effect on the overall rate of burning and the local burning velocity. In the early stages, and until t ~ 7, the flame front maintains its sinusoidal shape and its length is approximately the same as the flame length at t = 0. In the second stage, and as the eddy starts to roll up, the flame front forms a fold within the eddy. Within this fold, reactants are trapped, and a situation in which two flames are burning towards each other is created. Rollup increases the length of flame front and exposes the flame to a strong strain. The extent of the fold within the eddy is limited by the consumption of the reactants trapped between the two sides of the flame front. It is also limited by the fact that burning inhibits the spinning of the core. The consumption of reactants and the continuous stretch of the flame reduces the distance between the two folds around t ~ 15, and the two flames become much closer to each other than before.

To study the effect of the shear layer on the chemical reaction, we plot the total mass of products, M_p, formed since the rollup starts at $t = 0$ on Fig. 9. At the early stages, when the flame stretch is negligibly small, the rate of burning is linear and identical to that of a laminar flame. As the layer starts to roll up, the area of the reaction surface increases and the flame is convoluted around the growing eddy. The increase in the flame area, or length in a two-dimensional sense, L_f, due to its folding within the eddy is shown in Fig. 10. The rate of product formation, $\dot{M}_p$, which is the slope of the curve in Fig. 9, can be approximated by the product of the flame length times the average burning velocity along the flame, S_u. Since $\dot{M}_p$ is almost constant in the second stage, then the value of S_u must be decreasing with increasing L. Thus, as the flame stretches, its burning velocity decreases. This is in accordance with the previous results on stretched laminar flames at high strain rates.[35,36] In both studies, a drop in the flame burning velocity and partial extinction was observed as the strain rate was increased.

The drop of the local burning velocity when a strain rate develops along the flame can be explained as follows. As the strain rate along the flame front becomes finite and positive, the local gradients normal to the front increase, enhancing the diffusion fluxes of heat from and of reactants into the flame. This can lead to flame cooling if the chemical time scale is relatively large, i.e., if the reaction is not fast enough to produce heat that could balance the cooling effect of the diffusion fluxes. Moreover, cooler flames burn slower than adiabatic flames. Thus, strong strain may lead to slower flames at moderate value of the reaction rate.

In Fig. 11, we plot the temperature T, the strain rate $\dot{s}$, and the rate of expansion $\dot{e}$, along one particular layer of fluid within the reacting eddy. The rate of expansion is an indication of the rate of temperature rise due to the combined effect of diffusion and chemical reaction, as seen from Eq. (6). The layer along which these parameters are plotted is shown in Fig. 12. Figure 11 shows that within the fold of the flame, the temperature is very close to the temperature of maximum reaction rate, indicating that most of the burning occurs within the eddy core. This is in agreement with the experimental results.[5] On the other hand, the temperature at the side of the eddy which is exposed to the reactants is relatively low, and burning is not expected to proceed at an appreciable rate there.

When we decrease the frequency factor to $A_f = 0.5$, which reduces the Damkohler number by the same ratio, we see a stronger effect of stretch and a better disctinction between the different stages of development. For this case the large eddy is shown in Fig. 13 at $t = 17.57$, while the total mass of products is shown in Fig. 14. The swelling of the eddy is reduced since the rate of chemical reaction is one half of its value in the first case. Figure 14 shows that at the early stages, the reaction proceeds in the same way as before: a laminar flame followed by a stretched laminar flame. Around time $t = 14$, the slope of the curve of M_p vs. t, i.e. $\dot{M}_p = S_u L_f$, increases. While the value of S_u is still decreasing as the flame length increases, its value is somewhat higher than before. A possible explanation for this phenomenon can be found by observing that the two sides of the flame fold become much closer around $t = 14$, as seen in Fig. 7. As the two sides of the flame

fold approach each other, the temperature of the reactants trapped between the two sides rises. This leads to an increase in the burning velocity.

At t = 17.57, the reaction slows down approaching a state of total extinction, as shown by the total mass of products exhibited in Fig. 14. To explain what happens around extinction, we refer to Fig. 15. In this figure, plots of T, $\dot{s}$, and $\dot{e}$ are shown along one particular layer at t = 17.57. The geometry of the same layer is shown in Fig. 16. Plots for $\dot{e}$ show that the temperature is falling and the layer is experiencing cooling. This is in spite of the fact that T corresponds to maximum reaction rate along most of the layer. Moreover, the values of T and $\dot{s}$ are now negatively correlated, i.e. temperature maxima correspond to minima in $\dot{s}$, and $\dot{s}$ and $\dot{e}$ are also negatively correlated. The strain thus cools the flame leading to its eventual extinction

When the frequency factor is lowered further to A_f = 0.25, extinction occurs earlier at around t = 10, as shown in Fig. 17. A laminar flame at the same condition shows the expected linear rise in M_p. These results confirm that the local burning velocity decreases with stretch, and that this phenomena is caused by the imbalance between the rates of diffusion and the rate of the chemical reaction.

VI CONCLUSIONS

Numerical methods enable one to: (1) integrate elaborate and detailed models, which cannot be done analytically, so that complex mechanisms may be revealed and analyzed; and (2) provide detailed information about the flow field which may not be possible using traditional experimental techniques. Computer output, rich in data, offers the challenge of extracting and presenting valuable information about the phenomena under investigation. Finding the appropriate diagnostics to probe computational results represents half the journey to reaching the conclusions.

In this article, we have introduced the transport element method; a Lagrangian particle scheme based on the discretization of the vorticity and the gradients of the scalars into finite elements. The particles move along material lines, in accordance with their transport equations. As strong strains develop in the dynamic field, the finite elements may change their shape or configuration to accommodate the distortion which is produced by these strain fields. In case of chemical reaction: (1) the strength of the elements, i.e. the source strength, changes according to the rate of reaction; and (2) the chemical heat release induces volumetric expansion and non-baroclinic vorticity into the dynamic field.

The simplest model which can be proposed to study turbulence-combustion interactions contain five parameters: (1) the Peclet number which defines the ratio between the rate of convective and diffusive heating; (2) the Lewis number which represent the ratio between the rate of heat and mass diffusion; (3) the frequency factor which defines the ratio between the rate of chemical reaction and mass convection; (4) the activation energy of the reaction; and (5) the enthalpy of reaction. The outcome of these interactions can, thus, be presented on a five-

dimension space where one can identify several subdomains for burning enhancement, flame extinction, flame oscillations, etc. To accomplish this goal, computations must be performed for a matrix of parameters. The compiled data can then be plotted on this space. Under the idealization of high activation energy and thin flame structure, results of the asymptotic analysis can be used to fill some parts of this space and show the limiting trends[38,39,40].

In this article, we presented results for the effect of changing the frequency factor, which leads to changing the Damkohler number, at fixed values of the rest of the parameters. We showed that for $P_e = 200$, $L_e = 1$, $T_a = 10$ and $Q = 4$, at $A_f = 1.0$, the stretch associated with the rollup of large eddies in the mixing layer enhances the rate of reaction by extending the flame surface area within the large eddies, in spite of the fact that the local burning velocity decreases as the flame surface is stretched. At lower values of A_f, combustion is interrupted under strong stretch, and the lower the values of A_f become, the earlier the flame is extinguished. This is due to the fact that the rise in the mass flux into the reaction zone and the heat flux out of the flame is not balanced by an increase in heat release by chemical reaction within this zone. The reaction zone is thus cooled, followed by the extinction of the flame. Work is underway to vary the rest of the controlling parameters and study their effect on flame stability.

REFERENCES

1. Libby, P.A. and Williams, F.A., eds., Turbulent Reacting Flows, Springer-Verlage, Berlin, 1980, xiii + 243 p.

2. Chigier, N.A., ed., Progress in Energy and Combustion Science, special issue on Turbulent Reacting Flows, 12, (1986).

3. Brown, G.L. and Roshko, A., J. Fluid Mech., 64, 775 (1974).

4. Ho, C.-H., and Huerre, P., Ann. Rev. Fluid Mech., 16, 365, (1985).

5. Keller, J.O. and Daily, J.W., AIAA J., 23, 1937, (1985).

6. Mungal, M.G., and Dimotakis, P.E., J. Fluid Mech., 148, 349, (1984).

7. Ghoniem, A.F. and Ng, K.K., Phys. Fluids, 30, 706, (1987).

8. Broadwell, J.E. and Breidenthal, R.E., J. Fluid Mech., 125, 397, (1982).

9. Driscoll, J.F., Tangirala, V. and Chen, R.H., Combust. Sci. Tech., 51, 75, (1986).

10. Kelly, J. private communications.

11. Hald, O., SIAM J. Num. Anal., 16, 726, (1979).

12. Beale, J.T. & Majda, A., Math. Comp., 39, 28, (1982).

13. Anderson, C., J. Comput. Phys., 61, 417, (1985).

14. Corcos, G.M. and Sherman, F.S., J. Fluid Mech., 139, 29, (1984).

15. Grinstein, F.F., Oran, E.S. and Boris, J.P., J. Fluid Mech., 165, 201, (1986).

16. Riley, J.J., and Metcalfe, R.W., AIAA paper 80.0274.

17. Ashurst, W.T., in Turbulent Shear Flows, ed. Durst et al. (Springer-Verlag, Berlin, 1979), p. 402.

18. McMurtry, P.A., Jou, W.A., Riley, J.J., and Metcalfe, R.W., AIAA Journal, 24, 962 (1986).

19. Ghoniem, A.F. and Givi, P., AIAA paper 87-0225.

20. Chorin, A.J., J. Fluid Mech., 57, 785 (1973).

21. Chorin, A.J., "Vortex models and boundary layer instability." SIAM J. Sci. Stat. Comput., 1, 1980, pp. 1-24.

22. Leonard, A., J. Comput. Phys., 37, 289 (1980).

23. Ghoniem, A.F. and Gagnon, Y., J. Comput. Phys., 68, 342, (1987).

24. Sethian, J.A. and Ghoniem, A.F., "Validation of the vortex method," J. Comput. Phys., to appear.

25. Ashurst, W.T. and Barr, P.K., "Lagrangian-Eulerian calculation of turbulent diffusion flame propagation," Sandia Report SAND80-9950, Sandia National Laboratories, 1982.

26. Ghoniem, A.F., Chorin, A.J. and Oppenheim, A.K., Phil. Trans. Roy. Soc. Lond., A304, 303, (1982).

27. Ghoniem, A.F., Heidarinejad, G. and Krishnan, A. "Vortex element simulation of the rollup and mixing in a thermally stratified shear layer," J. Comput. Phys., submitted for publication.

28. Leonard, A. Ann. Rev. Fluid Mech., 17, 523, (1985).

29. Ghoniem, A.F., Knio, O.M., and Aly, H.F., AIAA Paper 87-0379.

30. Majda, A., and Sethian, J.A., Combust. Sci. Tech., 42, 185, (1987).

31. Ghoniem, A.F., Lectures in Applied Mathematics, 24, ed. by A. Ludford, 199, (Amer. Math. Soc., 1986), p. 199.

32. Koochesfahani, M.M., Dimotakis, P.,E. and Braodwell, J. E., AIAA Journal, 23, 1985, pp. 1191-1194.

33. Dimotakis, P.E., AIAA Journal, 24, 1986, pp. 1791-1796.

34. Krishnan, A., and Ghoniem, A.F., "Baroclinic effect of a density stratified shear layer," for presentation at the 1st National Congress on Fluid Dynamics, Cincinati, OH, July 1988.

35. Darabiha, N., Candel, S.N. and Marble, F.E., Combust. Flame, 64, 1986, pp. 203-217.

36. Giovangigli, V. and Smooke, M.D., J. Comput. Phys., 68, 1987, pp. 327-345.

37. Rogg, B., "Response and flamelet structure of stretched premixed methane-air flames," Combust. Flame, 1987, in print.

38. Clavin, P., Prof. Energy Combust. Sci., 11, 1 (1985).

39. Williams, F.A., Combustion Theory, 2nd ed., Benjamin/Cummings, 1985, xxiii + 680 p.

40. Buckmaster, J.D. and Ludford, G.S.S., Lectures on Mathematical Combustion, SIAM, 1983, V + 126 p.

$$\vec{g} = \frac{\delta s}{\delta n} = \frac{S_2 - S_1}{\delta n}$$

(a)

(b)
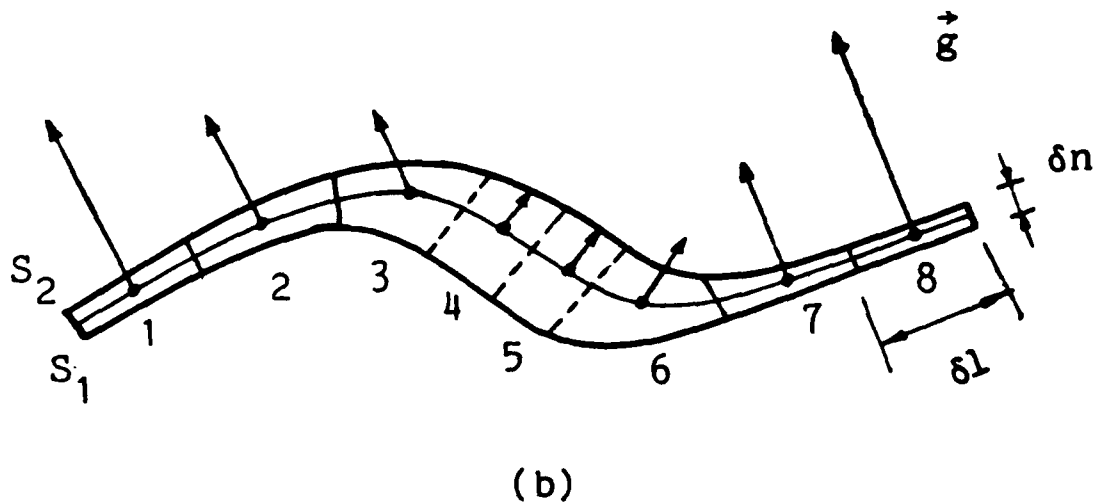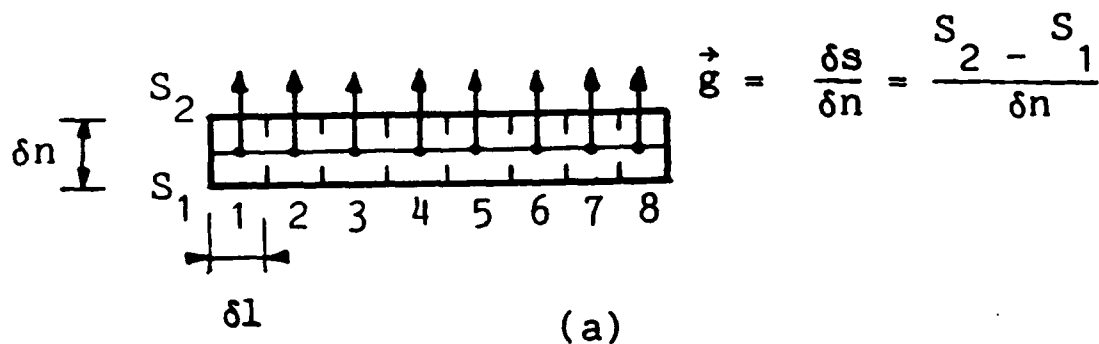
Figure 1. Schematic sketch showing the evolution of a material layer separating two values of the conserved scalar, s, and the associated scalar gradient, g, under the effect of stretch.

STEP= 78   TIME=11.40   ELEMENTS= 5892(5892)
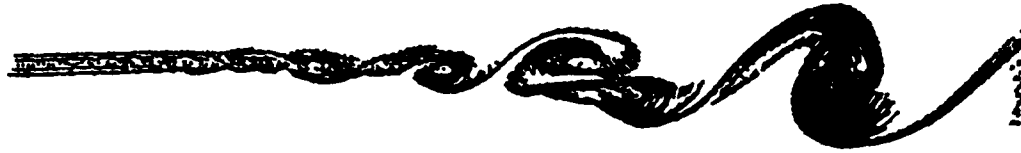
STEP= 78   TIME=11.70   ELEMENTS= 6498(6498)

STEP= 80   TIME=12.00   ELEMENTS= 7304(7304)

STEP= 82   TIME=12.30   ELEMENTS= 8199(8199)
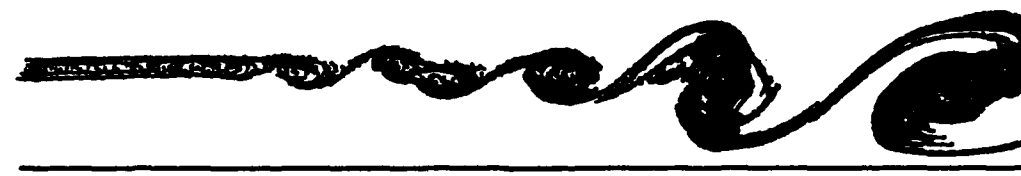
Figure 2. The development of large scale vortex structures in an unforced,
spatial shear layer. Each point in the figure represents a vortex element
and the line attached to it is the velocity vector. The velocity ratio
across the layer is 3:1.

STEP=186   TIME=27.90   ELEMENTS=13393(13393)

STEP=188   TIME=28.20   ELEMENTS=12441(12441)

STEP=190   TIME=28.50   ELEMENTS=11134(11134)

STEP=192   TIME=28.80   ELEMENTS=10657(10657)

Figure 3. The development of large scale vortex structures in a forced, spatial shear layer with the same velocity ratio as in Fig. 2. The forcing frequency is 1.333.

X=1.650
TIME=28.80
ALPHA=.000E+00

X=3.840
TIME=28.80
ALPHA=.000E+00

X=1.150
TIME=28.80
ALPHA=.000E+00

X=3.075
TIME=28.80
ALPHA=.000E+00

X=0.680
TIME=28.80
ALPHA=.000E+00

X=2.510
TIME=28.80
ALPHA=.000E+00
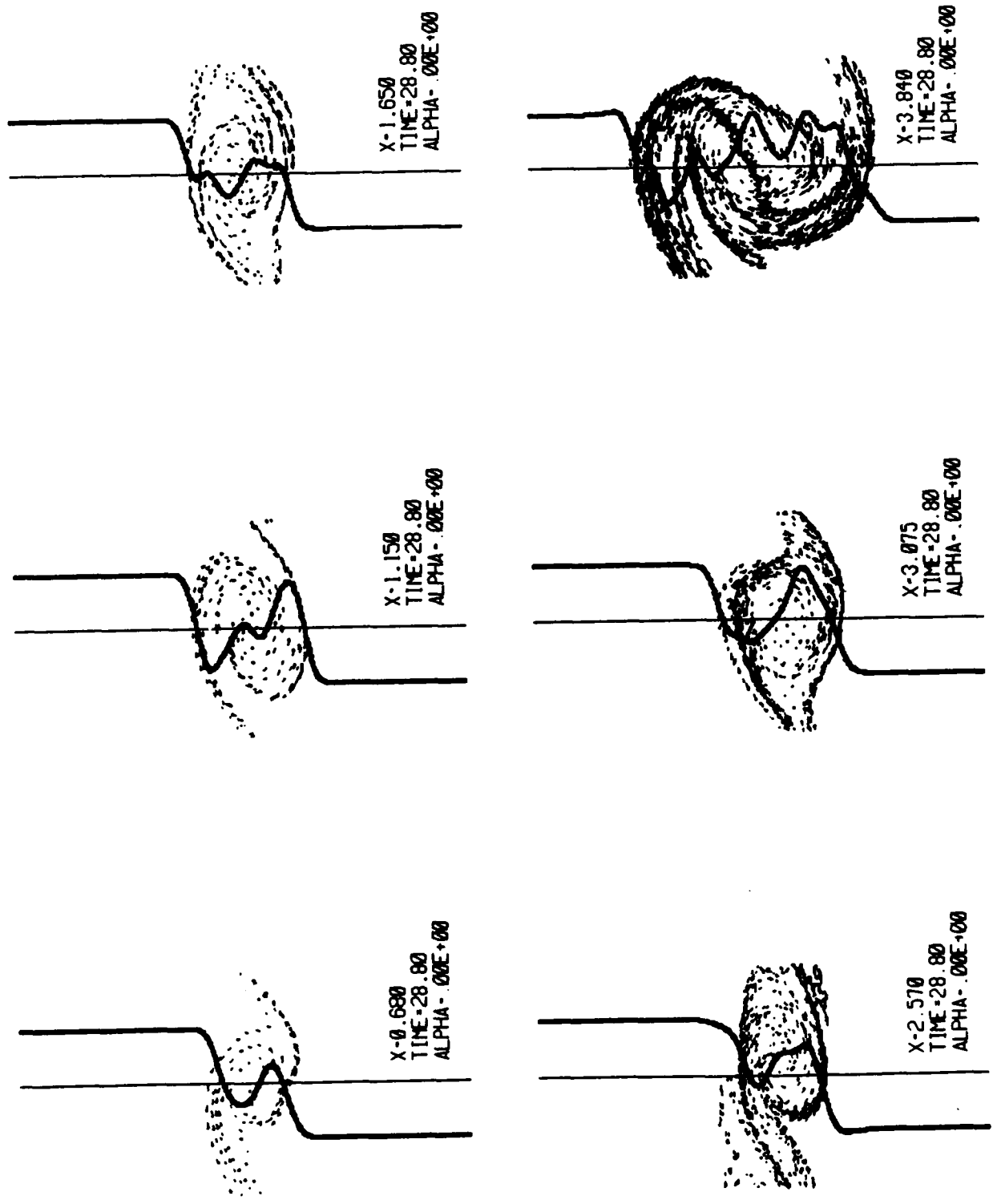
Figure 4. The temperature distribution across selected cross sections for the layer in Fig. 3.

TIME = 0.00   ELEMENTS = 270

TIME = 12.00   ELEMENTS = 604

TIME = 4.00   ELEMENTS = 310

TIME = 16.00   ELEMENTS = 902

TIME = 8.00   ELEMENTS = 428

TIME = 20.00   ELEMENTS = 1263
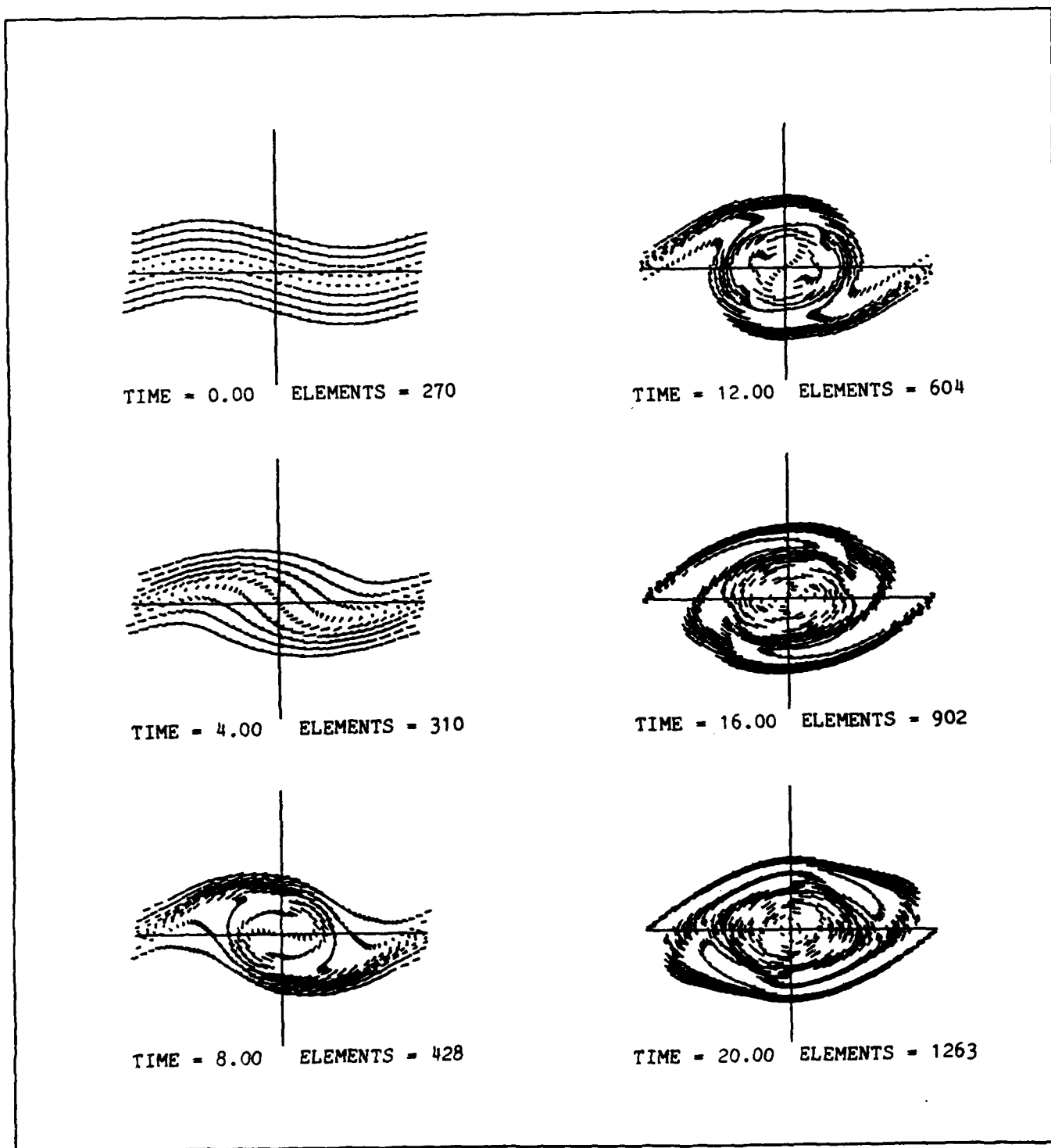
Figure 5. The development of a large eddy in a temporally growing shear layer.
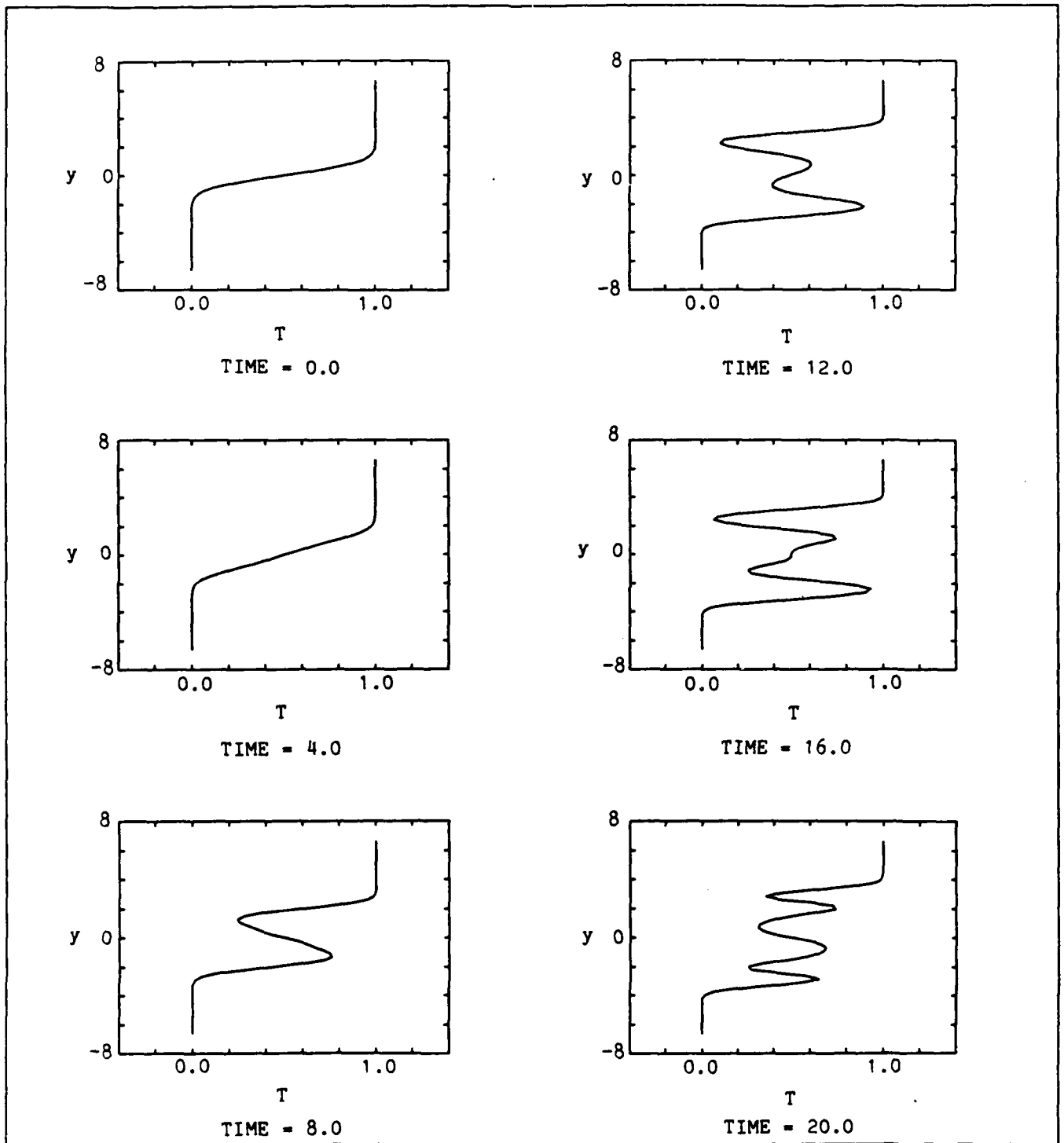
Figure 6. Temperature distribution across the midsection of the large eddy shown in Fig. 5.
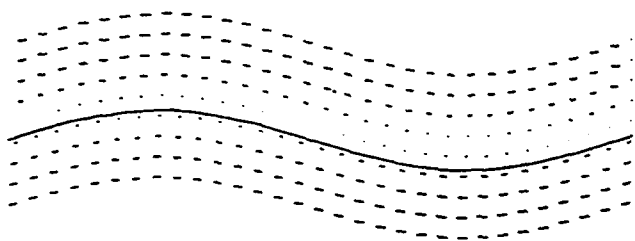
Time = 0.0
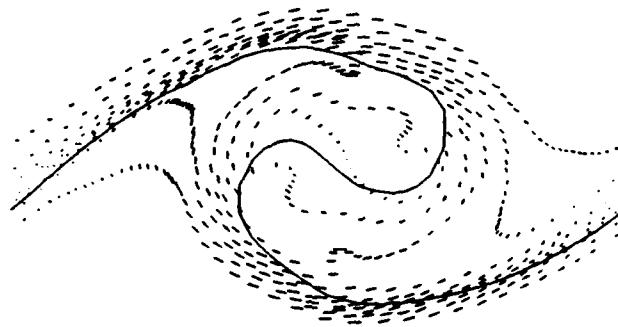
Time = 10.53
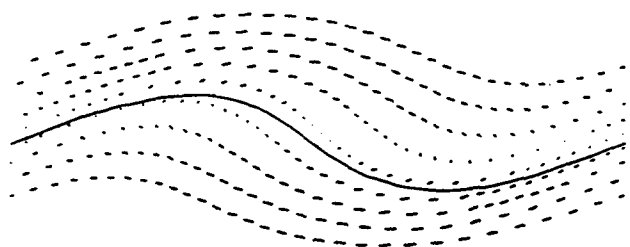
Time = 3.50
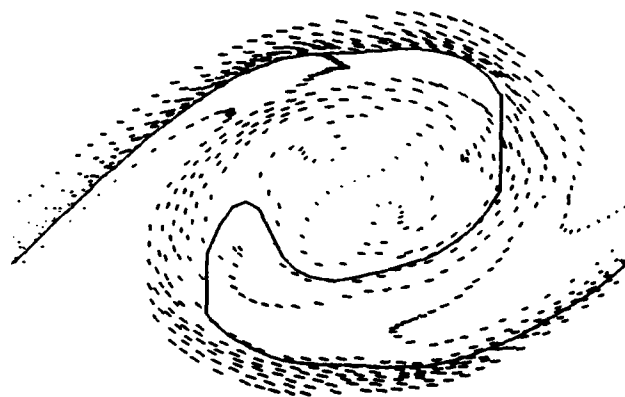
Time = 14.06
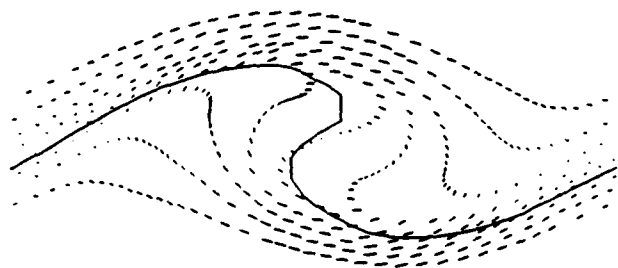
Time = 7.03
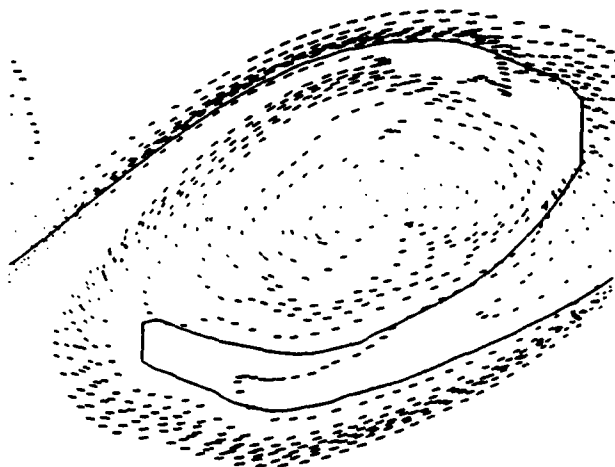
Time = 17.54

Figure 7. The development of a large eddy in a reacting temporal shear layer at the same conditions as in Fig. 5. The solid line defines the flame front.
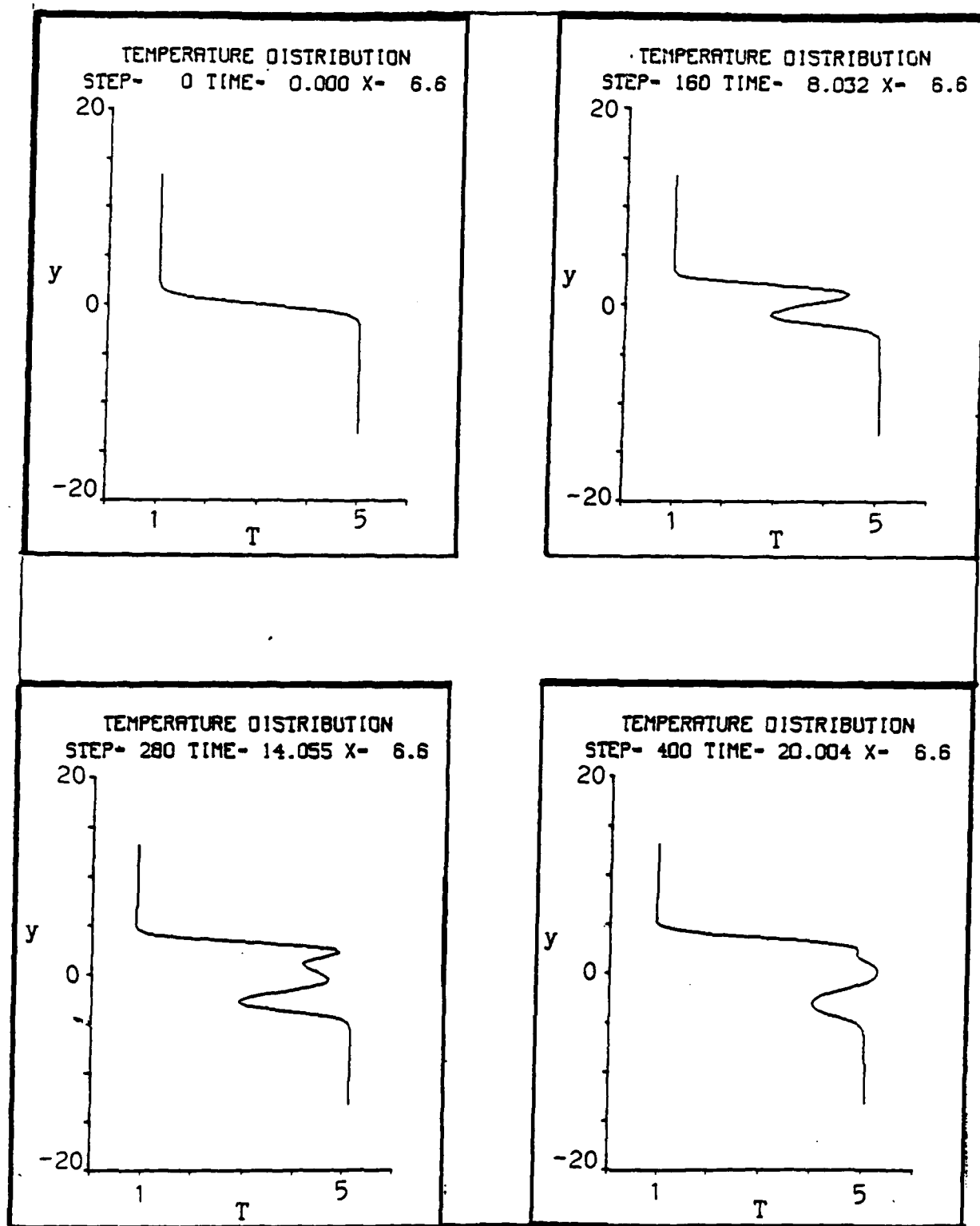
Figure 8. Temperature distribution across the midsection of the reacting large eddy shown in Fig. 7.
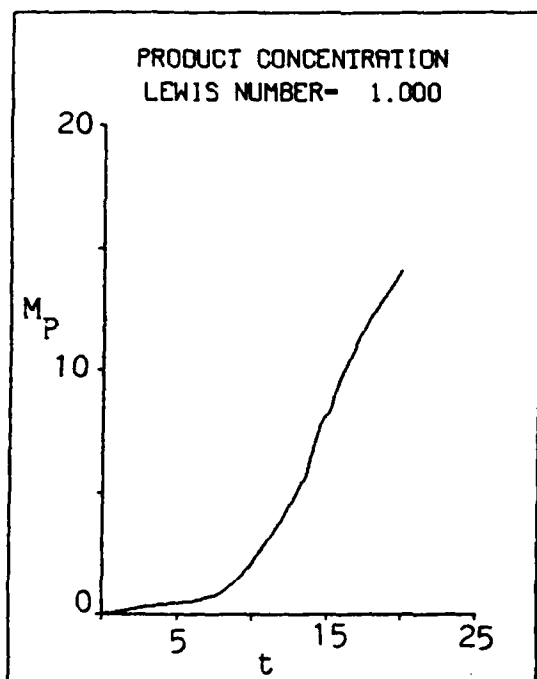
Figure 9. Total mass of products M_p formed since t = 0, in the reacting mixing layer with A_f = 1.0.
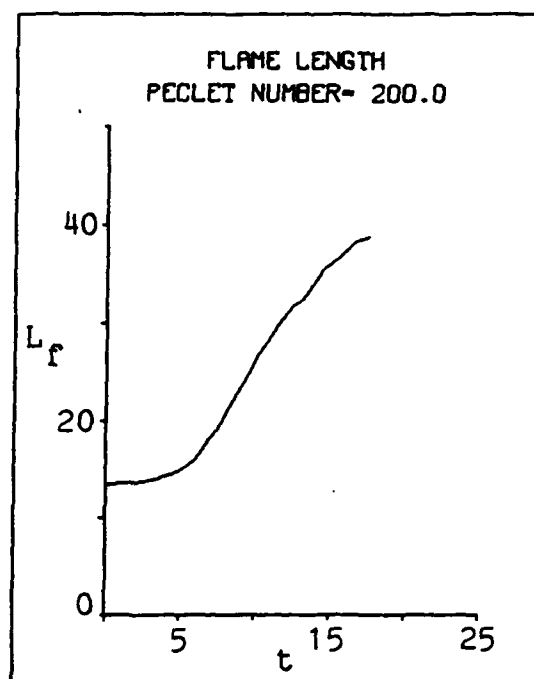
Figure 10. The total length of the flame in the reacting shear layer of figure 7.
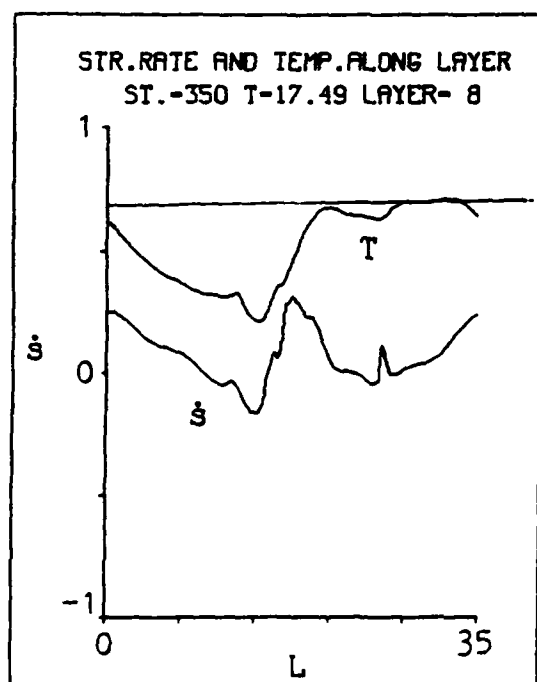
(a)
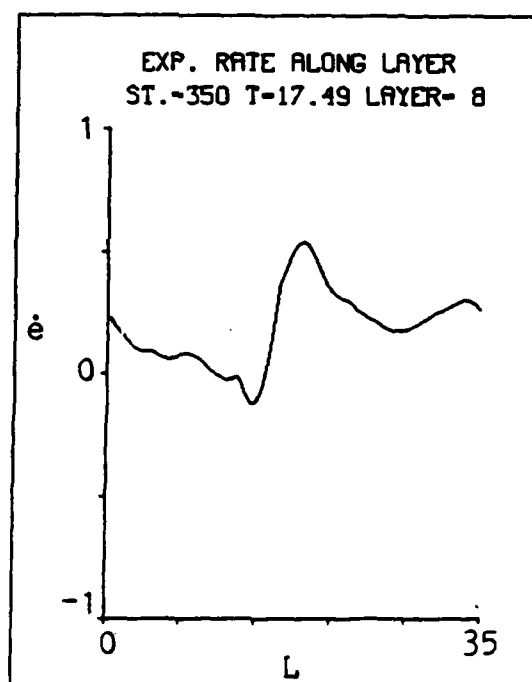
(b)

Figure 11. (a) the temperature T and the strain rate $\dot{s}$, (b) the expansion rate $\dot{e}$ along layer 8 in the reacting eddy shown in Fig. 7.

LAYER LOCATION
ST.- 350 T- 17.49 LAYER- 8
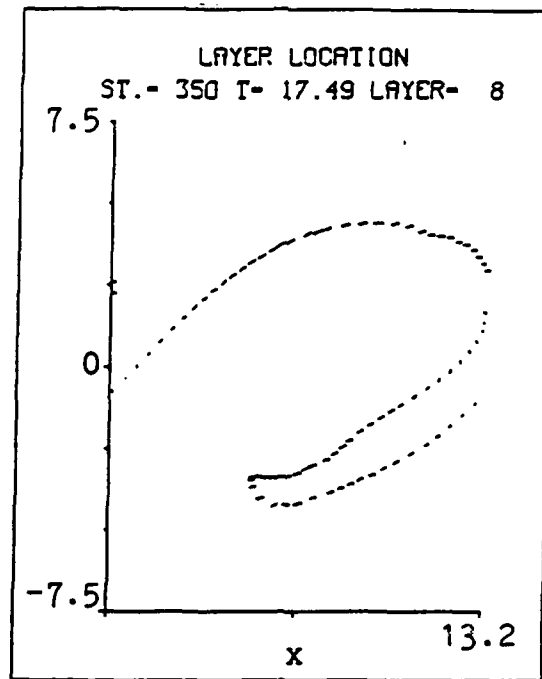
Figure 12. Layer 8 in the reacting eddy of Fig. 7.

VORTICITY LOCATION
STEP- 350 TIME- 17.57 LE- 1.0
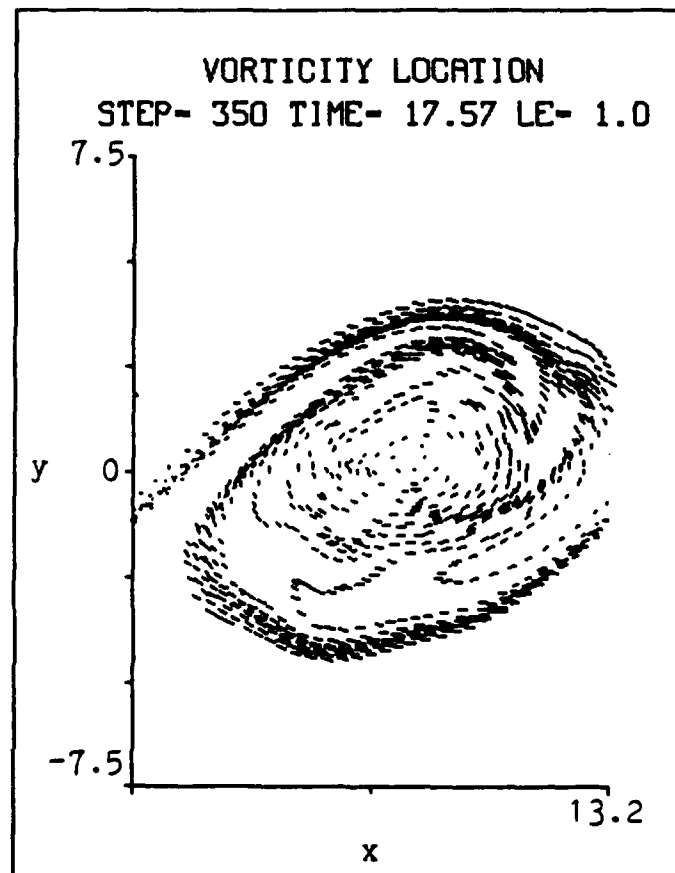
Figure 13. The large eddy in a reacting temporal shear layer at the same conditions as in Fig. 7 but with A_f = 0.5 at t = 17.57.

PRODUCT CONCENTRATION
LEWIS NUMBER= 1.000
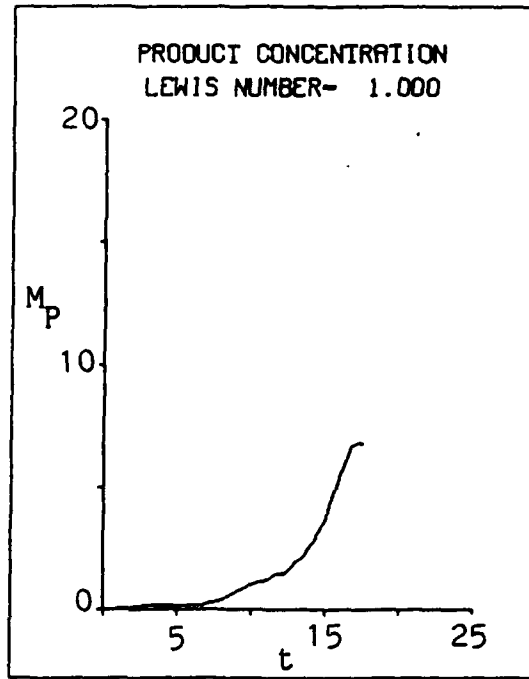
Figure 14. The total mass of products M_p formed since $t = 0$ for a reacting shear layer with $A_f = 0.5$.

STRAIN RATE ALONG LAYER
ST.=350 T=17.57 LAYER= 3

(a)

EXP. RATE ALONG LAYER
ST.=350 T=17.57 LAYER= 3
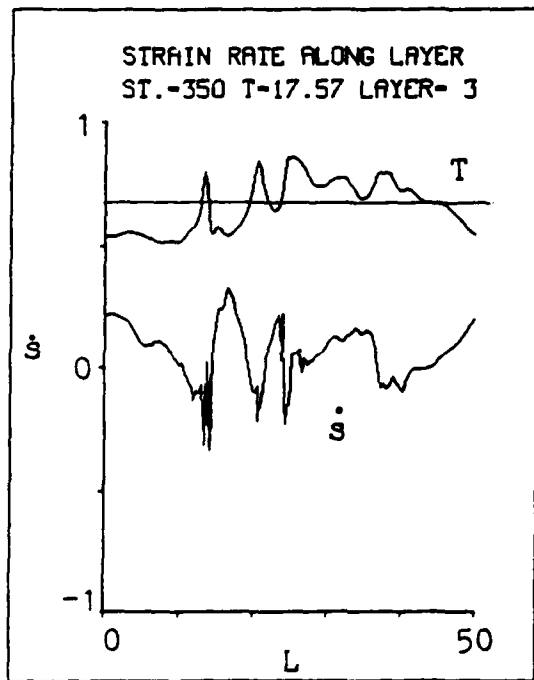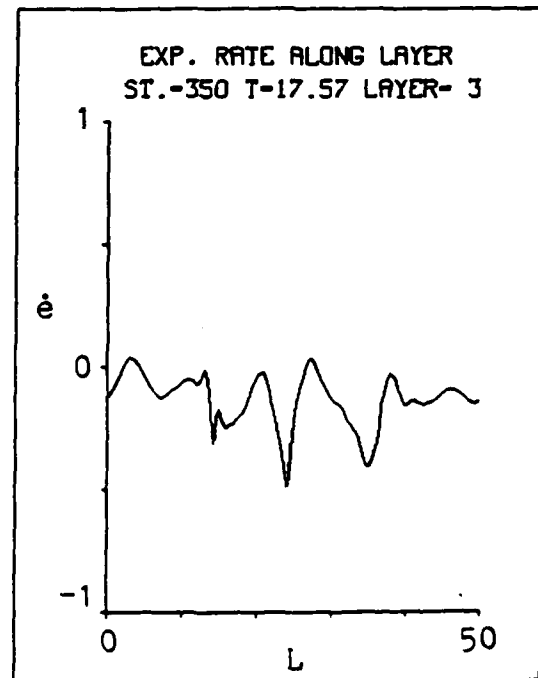
(b)

Figure 15. (a) the temperature T and the strain rate $\dot{s}$, and (b) the expansion rate $\dot{e}$ along layer 3 in the reacting eddy of Fig. 13.
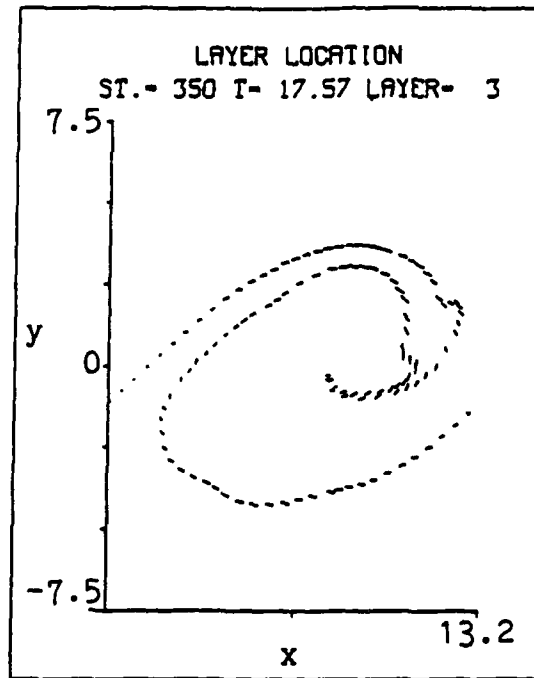
Figure 16. Layer 3 in the reacting eddy of Fig. 13.
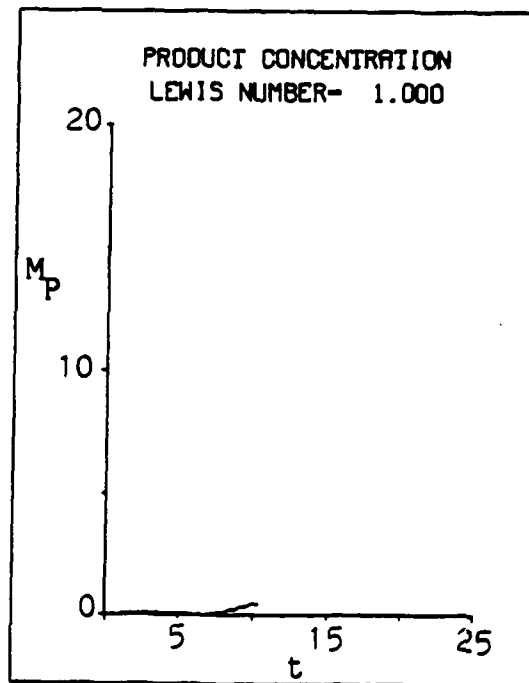
Figure 17. The total mass of products M_p formed since t = 0 for a reacting shear layer with A_f = 0.25.

AIAA-88-0729
On Mixing, Baroclinicity and the
Effect of Strain in a Chemically-
Reacting Shear Layer

A.F. Ghoniem, G. Heidarinejad & A. Krishnan
Massachusetts Institute of Technology
Cambridge, MA 02139

AIAA 26th Aerospace Sciences Meeting
January 11-14, 1988/Reno, Nevada

ON MIXING, BAROCLINICITY, AND THE EFFECT OF STRAIN
IN A CHEMICALLY-REACTING SHEAR LAYER

Ahmed F. Ghoniem[1], Ghassem Heidarinejad[2] and Anantha Krishnan[3]
Department of Mechanical Engineering
Massachusetts Institute of Technology
Cambridge, MA 02139

ABSTRACT

Numerical simulation, using the transport element method, is applied to study mixing of a passive scalar in a spatially-developing shear layer, and to investigate the interaction between the flow and the chemical reaction in a temporally-growing, premixed shear layer. In the first case, instantaneous scalar profiles exhibits mixing asymmetry and the skewness of concentration fractions within the cores in favor of the high-speed stream. Mixing statistics of a passive scalar agree well with the experimental measurements of Masutani and Bowman in a two-dimensional shear layer, and emphasize the effect of molecular diffusion on mixing. In the second case, two processes are identified as most important in flow-chemistry interactions: the production of vorticity due to baroclinicity, and the generation of strong entrainment fluxes due to roll-up. Baroclinic vorticity imparts a finite velocity on the growing eddy, delays its transition into the non-linear stages, and results in asymmetric entrainment. Results on the variation of the eddy velocity with density stratification agree with Dimotakis formula. Entrainment, leading to the extension of the apparent flame length, augments the rate of combustion during the formation of the eddy. At later stages, flow strain reduces the rate of burning measured along the line of maximum reaction rate.

I. INTRODUCTION

Reacting shear layers have been the subject of extensive investigation as models of turbulent diffusion and premixed flames (see, e.g., Mungal and Dimotakis [1], Masutani and Bowman [2], Keller and Daily [3] and Jou and Riley [4].) The flow configuration, which represents a generic model of many mixing and combustion systems, is used to improve the mixing and to stabilize the chemical reaction at high speeds. It is also simple enough to allow accurate and detailed experimental measurement employing modern diagnostic techniques. The experimental maps can then be used as data bases in the validation of the

numerical modelling and simulation of the same flow field. In this work, we utilize numerical simulation to develop a predictive capability for, and to study the dominant physical processes in a reacting shear layer.

The extension of the material interface between the two streams due to the roll-up of the vorticity layer, and the associated growth of scalar gradients, lead to the augmentation of mixing between the two streams. During the course of the study of mixing in a shear layer, it was found that mixing dynamics depends, to varying degrees, on: the velocity ratio across the layer, the molecular diffusivity of the transported species, the size and frequency of the perturbation at the upstream boundary, the density ratio across the layer, and the amount and rate of heat release. The mechanism governing mixing and, in particular, how each of these parameters can quantitatively affect the rate of mixing, has been under investigation. The influence of some parameters, such as the velocity ratio and the properties of the perturbations, have been elaborated. However, that of other parameters are still not fully understood.

Improving mixing is one mechanism by which turbulence can affect combustion. Another mechanism involves the development of a strong strain field within the combustion zone and along the reaction fronts. The interaction between a premixed combustion zone and a strain field can be particularly important under non-adiabatic conditions and when the Lewis number of the species that controls the rate of chemical reaction is different from unity (Libby and Williams [5,6] and Darabiha et al. [7]). Changing the mixture stoichiometry may emphasize the effect of strain on the combustion process (Keller et al. [8] and Peters and Williams [9].)

In the mean time, heat release due to combustion is expected to influence the dynamic field in at least two ways: volumetric expansion and baroclinic vorticity generation. Thus, and depending on the amount and rate of heat release, turbulent reacting shear layers may have different dynamics than that of a non-reacting layer. The processes of interaction between turbulence and combustion form a closed feedback loop since the vorticity field, which is perturbed by heat release, controls mixing dynamics.

Lagrangian calculations of mixing of a passive scalar in a shear layer was first performed by Ghoniem and Givi [10], using the scalar element method. This stochastic method is based on the representation of the mixing species by a number of "particles" that move with the local convective velocity and diffuse by random walk. The method, while lacking resolution within the areas of strong strain field, was able to predict the shape of the profiles describing the mixing statistics. However, some of the numerical

---

1 Associate professor, associate fellow, AIAA.
2 Graduate research assistant.
3 Graduate research assistant.

values did not match the experimental measurements. Because it lost resolution around the areas of strong strain, the method could not be used in the reacting flow calculations. Moreover, the method could not be extended to handle compressibility effects.

In a continuing effort to develop accurate numerical methods for reacting flows, we formulated the vortex element method and the transport element method (Ghoniem et al. [11,12,13]). Both methods are based on the accurate discretization of flow gradients, which may be the vorticity or the scalar gradients, into finite elements which are transported along particle paths. The distortion of the flow map due to the development of strong strain is accommodated by rediscretizing the field of the transport elements among a larger number of elements distributed in areas of strong strain. The strength of the vortex elements change with baroclinicity, and that of the scalar gradient elements vary with strain and chemical reaction.

In this paper, we present results for the application of these methods to mixing and chemical reaction in a shear layer. In Section II, the physical model governing a reacting, premixed shear layer is formulated. The dynamic effect of heat release, associated with volumetric expansion and the establishment of density and pressure gradients, are emphasized. The numerical schemes applied to obtain solutions for the model equations, the vortex element method and the transport element method are summarized in Section III. Results for mixing in an incompressible, spatially-growing shear layer are presented and analyzed in Section IV. Experimental data of Masutani and Bowman [2], which we will call M&B [2], are used to establish the accuracy of the numerical solution. In Section V, we study solutions of a reacting, temporally-growing shear layer. Mechanisms of entrainment asymmetry due to density stratification, and augmentation of reaction due to entrainment are investigated in detail. The paper is concluded in Section VI.

II. FORMULATION

The model is formulated on the basis of the following assumptions:
(1) at the inlet section, the reactant, R, and product, P, with concentrations c_{Ro} and c_{Po} in the top high-speed and bottom low-speed streams, flow at velocities U1 and U2, respectively;
(2) chemistry is governed by a single-step, first-order, irreversible, Arrhenius reaction, R --> P;
(3) the Mach number is small, and hence, pressure is taken as a constant in the equation of state and the energy equation;
(4) both the reactant and product behave as perfect gases with equal molecular weights and specific heats; and
(5) the thermal and mass diffusivities are constants, but not necessarily equal, while the effect of viscosity is neglected.

Under these conditions, the non-dimensional form of the conservation equations governing a two-dimensional, unsteady, reacting flow are:

$$\nabla^2 \phi = \frac{1}{T} \frac{dT}{dt} \tag{1}$$

$$\nabla^2 \psi = - \omega(\mathbf{x}, t) \tag{2}$$

$$\frac{d}{dt}\left(\frac{\omega}{\rho}\right) = -\frac{1}{\rho^2} \nabla\rho \times \left(\frac{d\mathbf{u}}{dt}\right) \tag{3}$$

$$\frac{dT}{dt} = \frac{1}{P_e} \nabla^2 T + A_f Q W \tag{4}$$

$$\frac{ds}{dt} = \frac{1}{P_e L_e} \nabla^2 s \pm A_f W \tag{5}$$

where the velocity is decomposed as: $\mathbf{u} = \nabla\phi + \nabla\times\psi + \mathbf{u}_p$, and the equation of state is: $p = \rho T$. The definition of the symbols is: $d/dt = \partial/\partial t + \mathbf{u}.\nabla$, $\mathbf{u} = (u,v)$ is the velocity, $\mathbf{x} = (x,y)$ where x is the streamwise direction and y is the cross-stream direction. t is time, ϕ is a velocity potential, $\boldsymbol{\psi} = \psi\,\mathbf{e}_z$ is a stream function defined such that $\mathbf{u}_\omega = \nabla\times\boldsymbol{\psi} = (\partial\psi/\partial y, -\partial\psi/\partial x)$, and $\omega\,\mathbf{e}_z = \nabla\times\mathbf{u}$ is vorticity. $\mathbf{u}_p$ is a potential velocity, $\nabla.\mathbf{u}_p = 0$, added to satisfy the normal boundary condition across the boundary of the domain. c is the concentration per unit mass, T is temperature. ∇ and ∇^2 are the gradient and Laplacian operators, respectively. $A_f W$ is the rate of product formation per unit mass per unit time, and $W = c_R \exp(-T_a/T)$.

Variables are non-dimensionalized with respect to the appropriate combination of the velocity of the high speed stream U1, the channel height H, the free stream reactant concentration, c_{Ro}, and the free stream reactant temperature at x $= 0$, T_o. $T_a = E_a/(R_g T_o)$, where E_a is the activation energy and R_g is the gas constant. $Q = Q_h/(C_p T_o)$, where Q_h is the enthalpy of reaction and C_p is the specific heat at constant pressure. $P_e = U1\,H/\alpha$ is the Peclet number, where $\alpha = k/(\rho C_p)$ is the thermal diffusivity. $A_f = A\,H/U1$, where A is the frequency factor of the chemical reaction rate constant. $L_e = \alpha/D$ is the Lewis number.

Equation (1) is obtained by substituting the decomposition of $\mathbf{u}$ into the continuity equation and using $p = \rho T = $ constant since the flow is unconfined and is at low Mach number. Equation (3) is obtained by taking the curl of the momentum equation of an inviscid flow and using $\nabla p = -\rho\, d\mathbf{u}/dt$ to substitute for the pressure gradient. This allows the integration of the equations without explicitly computing the pressure distribution. Equations (4) and (5) are the conservation of energy and species, respectively, for a reacting mixture at finite thermal and mass diffusivities. For the reactant, $s = c_R$, the source term is negative; for the product, $s = c_p$, the source term is positive. For more detail on the development of the model, see Ghoniem et al. [12,13].

III. NUMERICAL METHODS
III.1. THE VORTEX ELEMENT METHOD
In this Lagrangian, grid-free scheme, the vorticity field is discretized among finite elements that move along particle paths:

$$\omega(x,t) = \sum_{i=1}^{N} \Gamma_i \; f_\delta(x-\chi_i(t)) \qquad (6)$$

The distribution of vorticity associated with each element is described by a radially-symmetric core function, f_δ, with a characteristic radius, δ, such that most, or all of the vorticity is concentrated within $r < \delta$, where $r^2 = x^2 + y^2$. Vortex elements are initially distributed in the area where $|\omega| > 0$ such that the distance between neighboring elements is h in the two principal directions. The accuracy of the discretization depends on the choice of f_δ, the value of h, and the ratio δ/h. A Gaussian distribution, $f_\delta(r) = (1/\delta^2) \exp(-r^2/\delta^2)$, leads to a second-order discretization. We found that for accurate representation of the vorticity distribution, δ must be slightly larger than h, i.e., $\delta/h = 1.3$.

The equations describing the vortex scheme are summarized as follows:

$$\frac{d\chi_i}{dt} = u(\chi_i(t),t) \qquad (7)$$

$$u_\omega(x,t) = \sum_{i=1}^{N} \Gamma_i \; K_\delta(x-\chi_i(t)) \qquad (8)$$

$$K_\delta(x) = - \frac{(y,\,-x)}{r^2} \; \kappa(\frac{r}{\delta}) \qquad (9)$$

where $\chi_i(0)=X_i$, and $\kappa(r) = {}_0\!\int^r r' \, f(r') \, dr'$.

According to Eq. (7), vortex elements move at the local velocity evaluated at their centers. As time progresses, the distance between neighboring elements increases in the direction of maximum strain rate such that $\Delta\chi > h$, where $\Delta\chi$ is the distance in the direction of maximum strain defined as $\Delta\chi = (\Delta u.\Delta\chi)/|\Delta u|$ and Δ is the difference operator between neighboring elements. This leads to a deterioration of the discretization accuracy since the latter requires that $\delta > \Delta\chi$. Thus, an algorithm must be used such that when $\Delta\chi > h_{max}$, where $h_{max}/h = 1.5$, a computational element is inserted at the midpoint between the original elements. The circulation of the new element, and that of the original two neighboring elements, is one third the sum of the circulation of the original two elements. for more detail on the vortex element method, see Ghoniem et al. [11].

When $\nabla\rho \times \nabla p \neq 0$, the circulation of the vortex element must be updated each time step. Since $\Gamma = \Sigma \; \Gamma_i \; \kappa(x-\chi_i)$ and, and $\nabla\rho/\rho = -\nabla T/T$, while as will be shown in the next section, $\nabla T = \Sigma \; \Delta T_i \; f_\delta(x-\chi_i)$, then:

$$\frac{d\Gamma_i}{dt} = \frac{\Delta T_i}{T_i} \times (\frac{du}{dt})_i \qquad (10)$$

In the next section, we will show how to compute ΔT and T. $(du/dt)_i$ is computed by numerically differentiating the velocity of the vortex element using a high order formula. Equation (10) is integrated using a fourth order Runge-Kutta-Merson method with variable time step for error control.

The velocity field produced by the volumetric expansion due to combustion is described by the solution of Eq. (1). Written in terms of Lagrangian transport elements, the expansion velocity is:

$$\nabla\phi(x,t) = \sum_{i=1}^{N} \frac{1}{T_i} (\frac{dT}{dt})_i \; h_i^2(t) \; \nabla G_\delta(x-\chi_i(t)) \qquad (11)$$

$$\nabla G_\delta = \frac{(x,y)}{r^2} \; \kappa(\frac{r}{\delta}) \qquad (12)$$

where h_i^2 is the material area associated with the transport element i.

III.2. THE TRANSPORT ELEMENT METHOD

In this scheme, the gradient of the scalar field is discretized into a number of finite elements using Eq. (6) with ω replaced by $g = \nabla s$, where s is a generalized scalar, being either T or c:

$$g(x,t) = \sum_{i=1}^{N} \Delta g_i(t) \; f_\delta(x - \chi_i(t)) \qquad (13)$$

Similar to vortex elements, transport elements are distributed where $|\nabla s| > 0$ and are transported at the local velocity field. However, contrary to vorticity, scalar gradients are not conserved along particle paths, and should be modified according to the local strain and the tilting of the material elements. Moreover, the evolution of the chemical reaction with time will be computed in a Lagrangian frame of reference as the interacting species flow. In the following, we *summarize the equations describing the transport element scheme:*

$$\Delta g_i(t) = \delta s_i(t) \; \delta l_i(t) \; n_i(t) \qquad (14)$$

$$\delta^2 = \delta_0^2 + 4 \, \alpha \, t \qquad (15)$$

$$\frac{d}{dt} \delta s_i = \sum_{j=1}^{k+1} D_s \; \frac{dW}{ds_j}(s_j) \; \delta s_j \qquad (16)$$

$$s(x,t) = \sum_{i=1}^{N} \Delta g_i(t) \, . \, \nabla G_\delta(x-\chi_i(t)) \qquad (17)$$

where δ_0 is the core radius at $t = 0$, k is the number of reacting species, $D_s = \pm A_f$ for c_P/c_R, and $D_s = A_f \, Q$ for T. δl_i is updated according to $\delta l_i(t) = (\chi_{i+1}(t)-\chi_{i-1}(t))/2$, i and i+1 are neighboring transport elements in the direction of maximum strain, n_i is the unit vector normal to δl_i, while $\delta l_i = |\delta l_i|$. If the distance between neighboring elements in the direction of principal strain exceeds a maximum distance, h_{max}, one element is inserted half-way between the two elements and the values of δl_i and h_i are adjusted for the three elements. A recombination procedure is implemented to curb the growth of the number of computational elements at areas of negative

stretch. The core of the vortex elements and of different scalar transport elements become different as time progresses. At high diffusivities, or small Peclet numbers, the cores of the elements will experience rapid growth and δ $>>$ h. In this case, transport elements must be subdivided into elements with smaller cores while preserving their total strength. However, this will not be used here since we are interested in cases where the Peclet number is large. For more detail on the transport element method, see Ghoniem et al. [12,13].

IV. RESULTS: A SPATIALLY-DEVELOPING SHEAR LAYER

IV.1. VORTICITY, AND VELOCITY STATISTICS

Results showing the development of the vorticity field of a shear layer, obtained using the vortex method, are depicted in Fig. 1 (see also Ghoniem and Ng [14,15] and Ghoniem et al [11,12,13]). The plots show the roll-up and pairing of large vortical structures due to the growth of "random" perturbations. These plots were obtained for a shear layer which starts at x = 0.0 with a Gaussian vorticity distribution. The velocity ratio across the layer is 2:1, and the momentum thickness at x = 0.0 is θ = 0.0148. All the vortex elements used in the computations are shown, along with their instantaneous velocity vectors measured with respect to the mean velocity. The plots show that the growth of the layer can be divided into two ranges: the linear range in which the "random" perturbations organize the vorticity into "lumps" that concentrate the vorticity into semi-round structures, and a non-linear range in which the vorticity field is formed of large eddies that move downstream while they interact by pairing.

Detailed analysis of the results indicate that the most-probable shedding frequency of these eddies correspond to the frequency of the fastest growing mode predicted by the linear theory of a spatially-developing shear layer. Smaller eddies with higher frequencies have been observed, but infrequently. Pairing starts, most often, as soon as the eddies reach their maximum growth, and proceeds to join two eddies into a larger structure. Few eddies escape pairing and, occasionally, multiple pairing of more than two eddies is seen. We also found that forcing at a frequency close to that of the fundamental mode organizes the shedding at the forcing frequency. Forcing at subharmonics of the fastest growing mode accelerates the spread of the layer by promoting earlier pairing. Multiple-eddy pairing occurs more frequently under these circumstances [15].

Predicted velocity statistics: averaged streamwise velocity, root-mean-square of the streamwise and cross-stream fluctuations, and Reynolds shear stress are shown in Figs. 2, 3, 4, and 5 (see also [14,15].) Figure 6 shows the mean momentum thickness of the layer. The growth rate within the non-linear range is $d\theta/dx$ = 0.0165. Note that what we called the linear range (following the definitions of the linear theory of stability) exhibits a plateau, followed by a small but exponential rise in θ. In the non-linear range, the value of θ increases linearly. The predicted value of $d\theta/dx$, while smaller than the value measured by M&B [2], falls in the middle of the scatter of the experimental data documented by Ho and Huerre [16]. It should noted that M&B [2] remarked that the growth rate of their layer is about 15-20 % larger than the value measured by the majority of other experiments. The effect of difference in the growth rate will appear in all the comparisons: the experimental profiles are
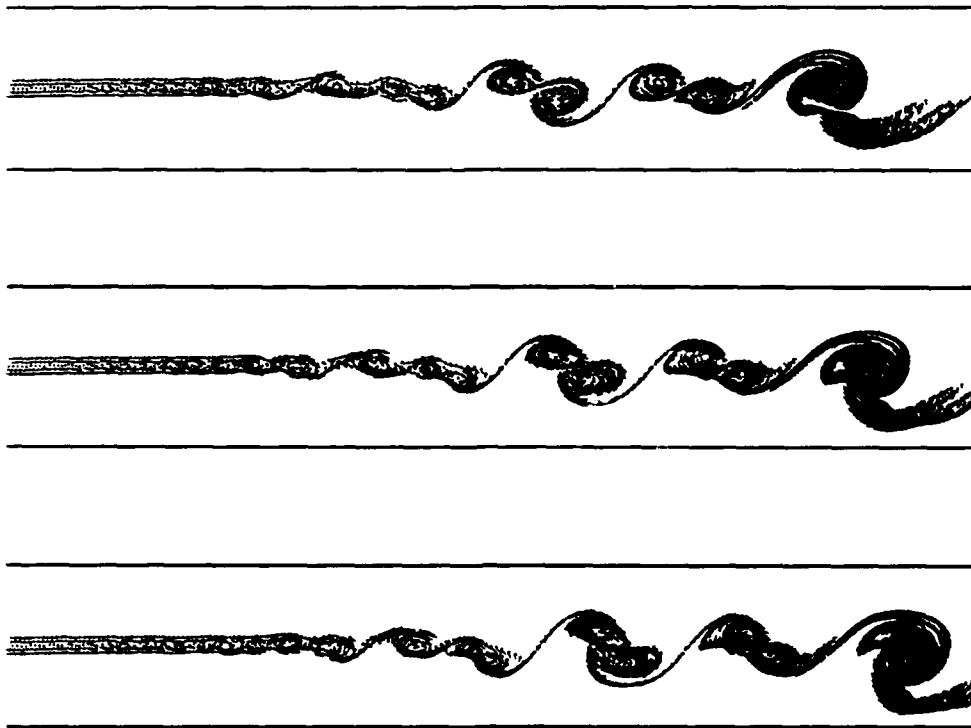
Figure 1. Locations and velocity vectors of all the vortex elements in an unforced shear layer, U1/U2 = 2.0. t = 50.70, 51.00 and 51.30.
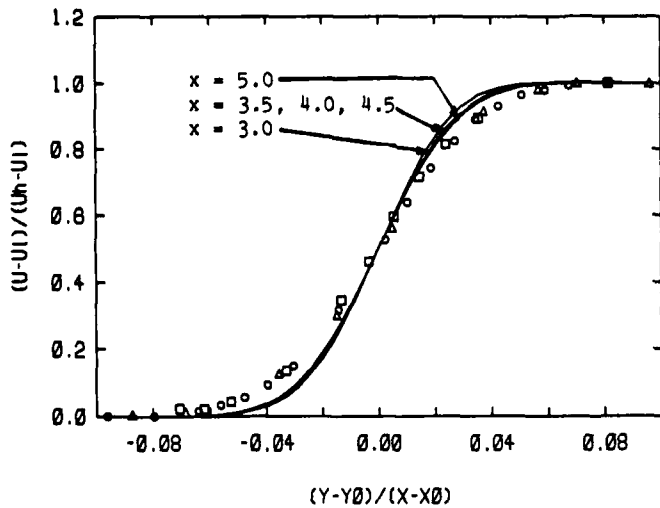
Figure 2. Time-averaged streamwise velocity profiles at x = 3.0, 3.5, 4.0, 4.5 and 5.0. The experimental results of Masutani and Bowman [2] are shown by symbols.
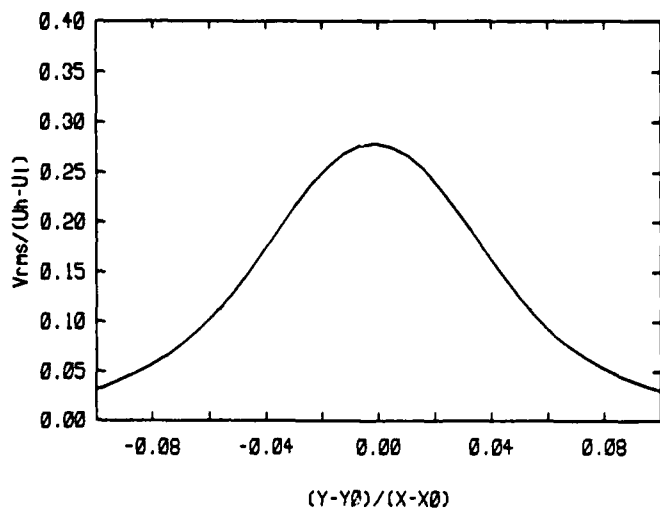
Figure 4. Time-averaged cross-streamwise velocity fluctuations at x = 3.5.
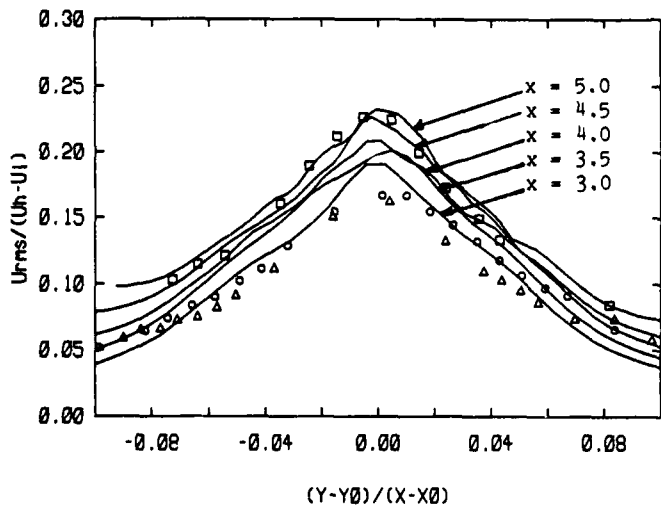
Figure 3. Time-averaged streamwise velocity fluctuations at x = 3.0, 3.5, 4.0, 4.5 and 5.0. The experimental results of Masutani and Bowman [2] are shown by symbols.
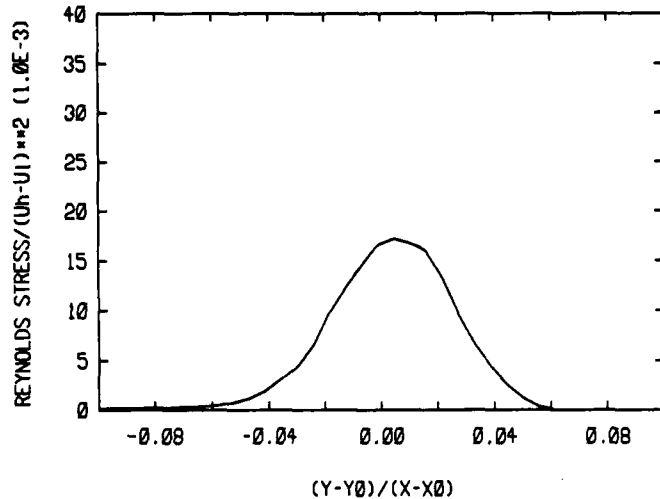


Figure 5. Time-averaged Reynolds shear stress at x = 3.5.
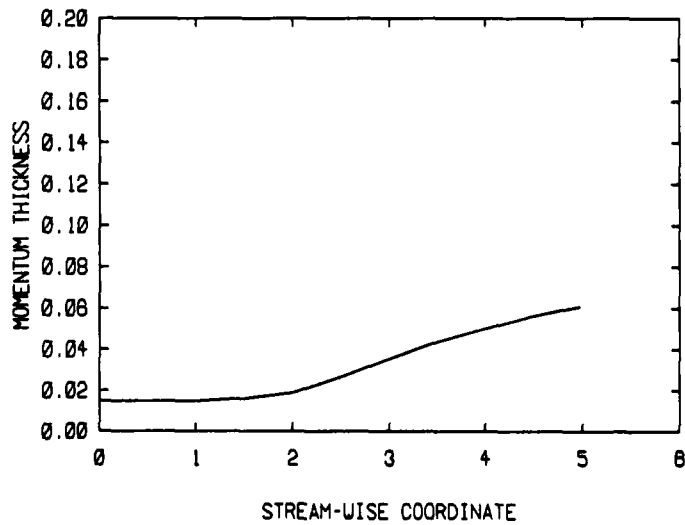
Figure 6. Average momentum thickness for the shear layer.

expected to spread into the free streams faster than the predicted profiles.

The plots show that the averaged streamwise velocity reaches a self-similar distribution early downstream, which also resembles the initial error function velocity distribution of the vorticity layer. On the other hand, velocity fluctuation statistics reach a self-similar state some distance downstream. The transition region for the development of the velocity fluctuation is most likely within the region of growth of the initial perturbation and before a "mature" eddy has formed.

As shown in Figs. 2 and 3, the numerical results agree well with the measurements of M&B [2] in a two-dimensional shear layer. The agreement will improve substantially if $(y-y_o)$ is normalized with respect to the local momentum thickness $\theta(x)$ instead of $(x-x_o)$ since this will absorb the difference between the spread rates of the two layers. This experiment was selected for comparison because the two-dimensionality of the flow was carefully maintained and verified, and because of the availability of experimental measurements on mixing statistics before mixing transition. Some differences between the numerical predictions and the experimental data, which may have resultsd in different growth rates, may be attributed to the relative amplitude of noise in the numerical and experimental studies, and to the expected scatter in experimental results.

It is important to emphasize that the velocity fluctuations are due to flow unsteadiness imposed by the formation and interactions of the large eddies. The unsteadiness arise due to flow instability, regardless of the boundary conditions which are steady, and lead to the augmentation of interaction between the two streams via the fluctuation fluxes. The order of magnitude of these fluctuations, in each direction, is about 20% of the velocity jump across the layer. The fluctuations are, thus, almost isotropic.

IV.2. MIXING, AND SCALAR STATISTICS

We have used the transport element method to compute the mixing of a passive scalar in the same flow. The distribution of the concentration immediately downstream of the splitter plate is described by an error function, similar to the velocity profile. The corresponding scalar gradient is a Gaussian, similar to the vorticity distribution. The concentration is $c = 1$ in the bottom low-speed stream, and is $c = 0$ in the top high-speed stream. Computations were performed for different values of the Peclet number to show the effect of molecular diffusion on mixing dynamics at high Reynolds numbers.

Figure 7 shows the instantaneous profiles of c at different sections downstream the channel, superimposed on the instantaneous distribution of the vortex, or transport elements for the case of $P_e = \infty$. The sections are chosen at the centers of the vortex eddies in Fig. 7a, and across the braids in Fig. 7b. The distributions reveal that, even at sections far downstream of the splitter plate, zones of completely unmixed fluid still exist within the layer (unmixedness). These zones correspond to the gulfs, or "tongues", of pure fluid brought into the layer from either sides by the inviscid mechanism of entrainment, i.e., the convective transport of fluid across the

(a)

(b)
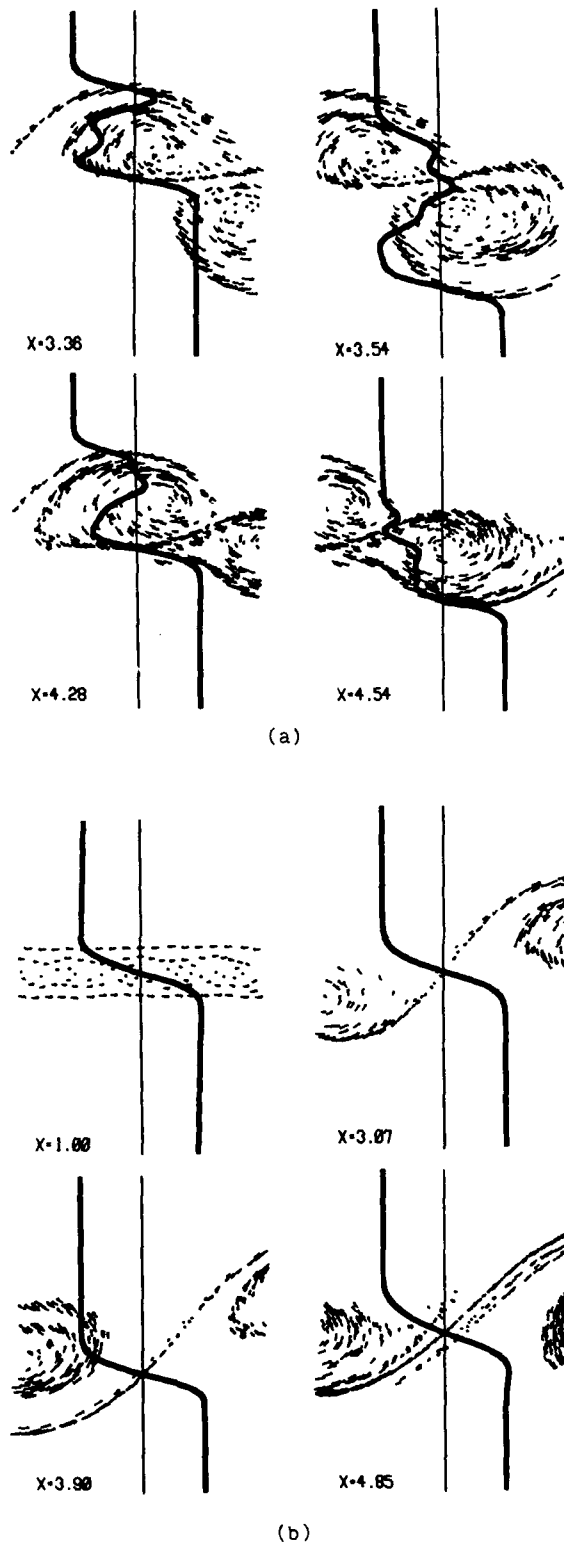
Figure 7. Instantaneous concentration profiles superimposed on the vortex elements: (a) across the mid-sections of the eddies; and (b) across the braids.

centerline of the layer by the roll-up of the vorticity layer.

Instantaneous concentration profiles show the mechanisms of asymmetric mixing, which leads to the establishement of a preferred-mean concentrations, c_p, different than 0.5 (M&B [2].)

Mixing asymmetry, which arises due to the asymmetric growth of the eddies during the initial stages of roll-up, is indicated by the fact that the profiles are not symmetric around the line c = 0.5 (computations of a temporally-growing mixing layer, in which flow boundary conditions are symmetric, show that the concentration profiles are perfectly symmetric around the line c = 0.5 at all times.) Asymmetric mixing is thus due to the asymmetric flow field in a spatially-growing layer. The preferred mean concentration is the value of c most likely to be found within the cores of the structures. As the c-profiles indicate, under the conditions simulated by our computations, c_p ~ 0.35. Across the braids, the concentration changes between the free stream values within a distance on the order of magnitude the initial shear layer thickness.

Figure 8 shows the averaged concentration profiles (a) for different values of the Peclet number at the same streamwise location; and (b) at different streamwise locations for the same Peclet number, both compared with the data of M&B [2]. The mean concentration profiles differ substantially from the initial error function profile, and develop downstream to form a zone of almost constant value, between two inflection points, around the midsection of the shear layer and towards the high-speed side. This constant value is close to the preferred-mean concentration within the cores. Diffusion, which generates strong fluxes around areas of sharp gradients, tends to make the profiles smoother. However, as shown by Fig. 8a, diffusion effect on the mean concentration is minor.

Comparison between the mean concentration profiles and the mean velocity profile indicates that the former penetrates further into the free streams than the latter. This supports the hypothesis that, in these shear flows, mixing is entrainment dominated and that entrainment, while it is a consequence of the vorticity-induced field, acts on the vorticity-free part of the flow by the Biot-Savart effect. Mixing enhancement by the roll-up of the shear layer, due to its intrinsic instability, is thus not limited to the neighborhood of the area where $|\omega| \neq 0$. Instead, the mixing zone extends further into the free streams as we move downstream. The numerical results predict the experiment very accurately (the effect of the faster growth of the experimental layer, which was indicated earlier, shows around the free streams especially on the high-speed side).

The root-mean-squared concentration fluctuations are shown in Fig. 9 for (a) different values of the Peclet number at the same streamwise location; and (b) at different streamwise locations for the same Peclet number, both with the experimental measurements of M&B [2]. As expected, at zero molecular diffusion, the maximum value of c' approaches 0.5, the unmixed state, indicating that the concentration in the fluid passing by the measurement point is alternating between the two extreme states. With increasing levels of molecular diffusion, the maximum value of c' decreases, and the whole profile attains smaller values, showing that the limits between
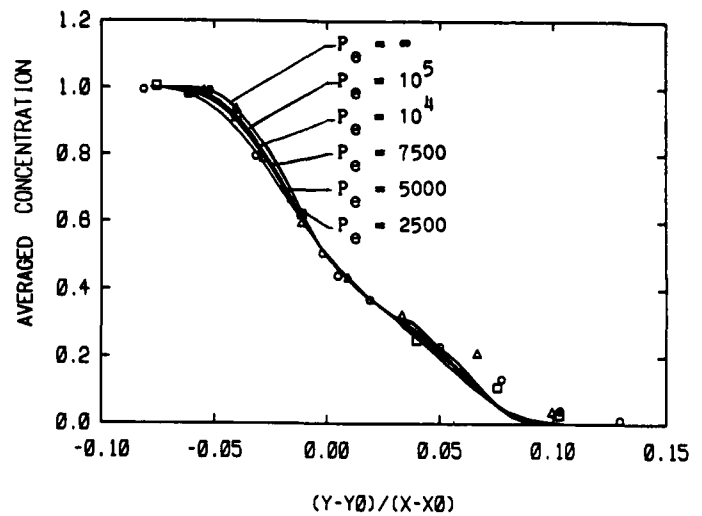
(a)
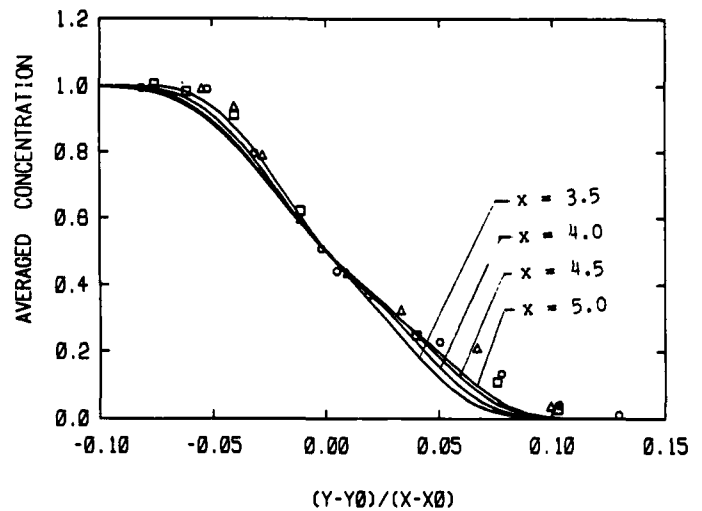
(b)

Figure 8. Time-averaged concentration profiles: (a) at x = 5.0 for P_e = ∞, 10^5, 10^4, 7500, 5000 and 2500; and (b) at x = 3.5, 4.0, 4.5 and 5.0 for P_e = 2500. Symbols correspond to the experimental data [2].

which the value of c is oscillating decreases. The peak and the wide plateau which are observed in this distribution correspond roughly to the transition between the slow stream in which c = 1, and the mixing core of the eddy.

Figure 9a shows that molecular diffusion has a pronounced effect on the concentration fluctuations, emphasizing the influence of diffusion on the instantaneous profiles and on the outcome of time-dependent processes which may take place within the shear layer, such as chemical reactions. Figure 9b shows that the concentration fluctuations reach self-similarity downstream of the station at which the mean profiles reach self-similarity, similar to the velocity profiles. This is not surprising since the controlling transport mechanism here is convection. The figure also shows that the penetration of the transported species cannot be measures by its mean values only. The deviation between the numerical

7

(a)

(b)
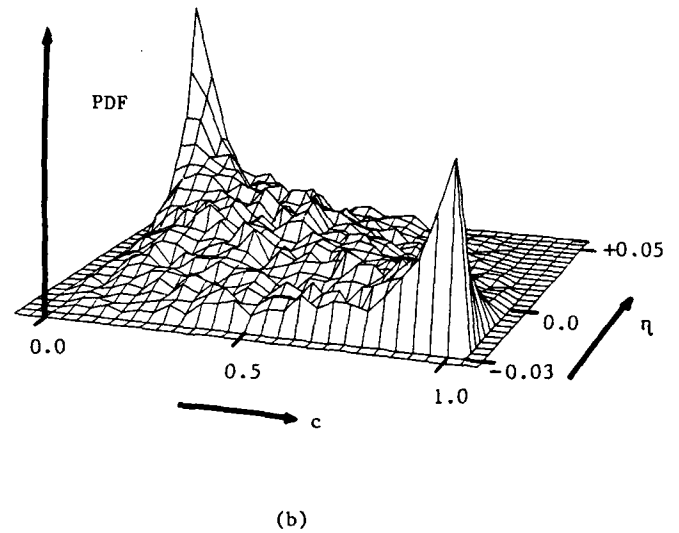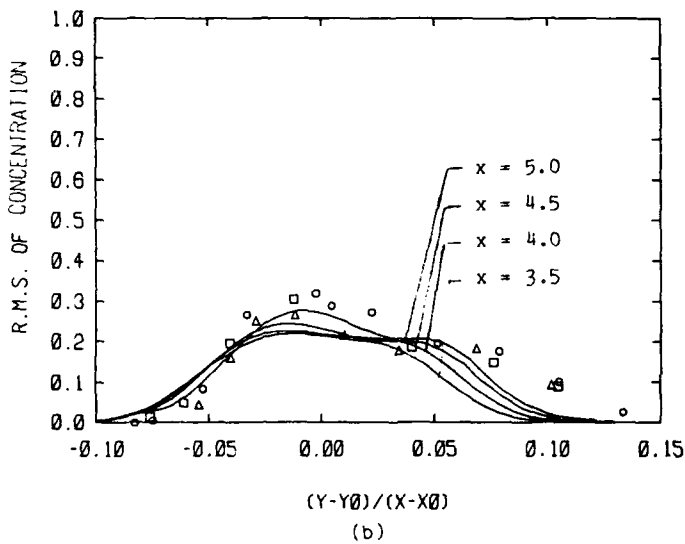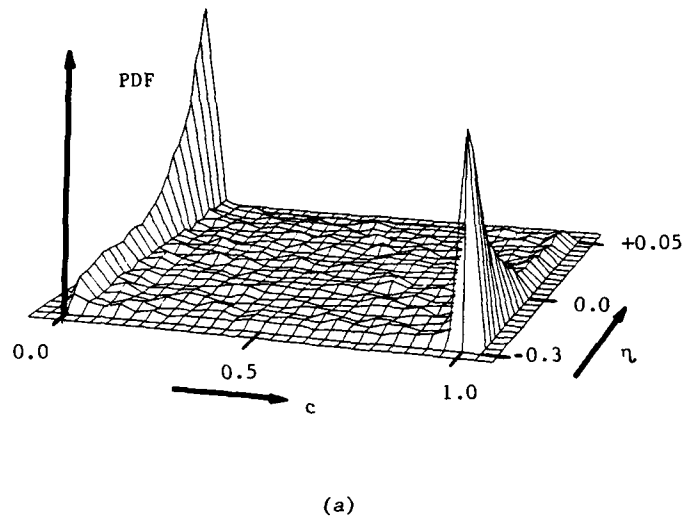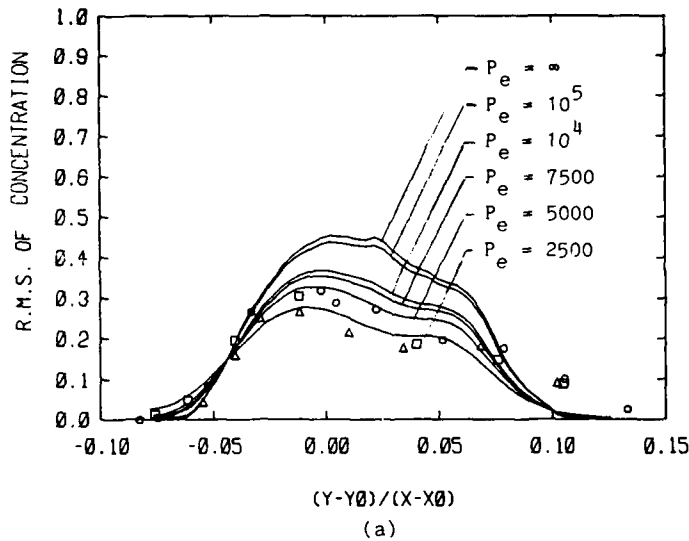
Figure 9. Time-averaged concentration fluctuations: (a) at $x = 5.0$ for $P_e = \infty$, 10^5, 10^4, 7500, 5000 and 2500; and (b) at $x = 3.5$, 4., 4.5 and 5.0 for $P_e = 2500$. Symbols correspond to the experimental data [2].


(a)

(b)

Figure 10. Probability-density function of concentration at $x = 5.0$ for: (a) $P_e = \infty$; and (b) $P_e = 2500$. $\eta = (y-y_0)/(x-x_0)$.

results and the experimental data near the high-speed stream is due to the difference between the growth rates in the experiment and the numerical solution. Concentration fluctuation of almost 20% of the concentration difference between the two streams accompanies a velocity fluctuation of almost 20% of the velocity difference between the two streams (turbulent Prandtl number = 1!).

The probability-density function of the concentration across the cross section $x = 5$ is shown in Fig. 10 for two values of Peclet number: $P_e = \infty$ and $P_e = 2500$. The bimodal shape, characteristic of non-diffusive entrainment, is clearly exhibited by the plot, and is indicative of the absence of numerical diffusion even at such distance downstream. At $P_e = 2500$, concentrations at intermediate values of c appear, with higher probability, close to the high-speed side where $c \sim$

0. Evidence for the existence of a preferred concentration within the cores is given in Fig. 9b. An intermediate peak appears between the two peaks at $c = 0$ and $c = 1$, at a value around $c_p \sim$ 0.4. M&B [2] show that the value of $c_p(x)$ is displaced towards higher values of c, and with slightly higher probability, as we move downstream, appearing more prominently at values of $x/\theta \sim 100$. The value identified by the numerical simulations at $x = 5.0$ is $c \sim 0.4$.

Results in this section show that the transport element method can be used to accurately predict the two-dimensional dynamics and mixing in a spatially-developing shear layer prior to "mixing transition." It is also capable of providing uniform spatial resolution throughout the domain and for a long time, as seen by the c-profiles across the braids. This is an important step towards computing a reacting shear layer.

8

V. RESULTS: A CHEMICALL-REACTING, TEMPORALLY-GROWING LAYER

V.1. FLOW AND TEMPERATURE FIELDS

Computations of a reacting mixing layer have been performed for an idealized model, a temporally-growing shear layer. While this is not a necessary idealization in either the physical model or the numerical scheme, it facilitates the long-time, high-resolution calculation of a reacting flow at low cost. The choice of the physical parameters that describe the combustion process was limited to cases for which the computer-time and memory requirements could be economically met. High Damkohler number, at which the chemical reaction proceeds much faster than the flow, requires a small time step and stiff integration routines. High activation energy, at which the flame thickness is very small, generates sharp gradients, and needs a large number of transport elements to resolve these gradients. Large heat release extends the temperature variation in the field and demands a large number of transport elements. Therefore, the results presented here were obtained for moderate values of all of these parameters and were used to study the different modes of interaction between the fluid flow and the chemical reaction.

In the temporally-growing layer, the normalizing velocity is $\Delta U/2$, where $\Delta U = U1-U2$, and the normalizing length is $\Delta_\omega/2$, where Δ_ω is the total vorticity thickness of the layer at $x = 0.0$.

To start, we present the vortex elements and their velocity vectors for the development of a non-reacting, uniform-density flow in Fig. 11, as a base state. For the reacting flow, we show the vortex elements and their velocity vectors for the following parameters: $T_a = 5.0$, $P_e = 200$, $L_e = 1.0$, $Q = 1.0$ and $A_f = 2.0$, in Fig. 12. In both cases, the initial perturbation is a sinewave with an amplitude $\varepsilon = 0.05\,\lambda$, where $\lambda = 6.6\,\Delta_\omega$ is the wavelength. The perturbation is chosen so that its initial growth rate is small enough to allow a slow increase in the length of a typical material layer until $t = 5$. It is important to point out that the initial vorticity thickness and flame thickness are not the same. While the former is chosen to correspond to the most unstable linear mode, the latter is the steady-state laminar flame thickness as defined by the diffusion and chemical parameters of the problem. In the second stage, $t > 5$, an eddy, which corresponds to a localized accumulation of the layer vorticity, forms and grows to its maximum size. Within this range, the primary mechanism of growth is the entrainment of fluid from both sides into the core of the eddy. In the final stage, starting around $t = 12$ and 15 for the non-reacting and reacting eddies, respectively, entrainment ceases and the eddy flattens in the streamwise direction.

Compared with the non-reacting eddy, the reacting eddy expands due to heat release, it moves to the right, it exhibits a definite asymmetry, and it starts flattening at later times. The expansion of the eddy due to heat release, which was limited to small values, occurs primarily in the second stage and within the core. This indicates that most of the burning occurs during this stage and inside the eddy core. The growth rate of the reacting eddy, measured by the integral of the perturbation velocity over the vorticity layer thickness, shown in Fig. 13, is
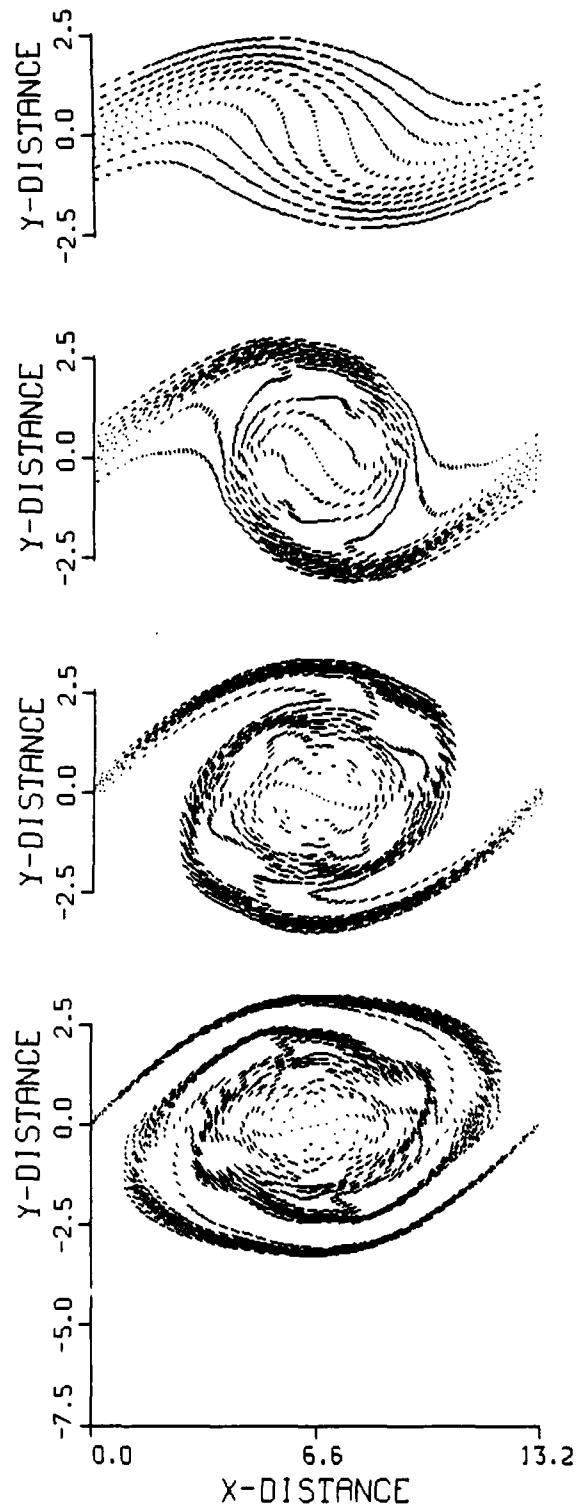

Figure 11. Locations and velocity vectors of all the vortex elements for a uniform-density, non-reacting layer at t = 5, 10, 15 and 20.

9
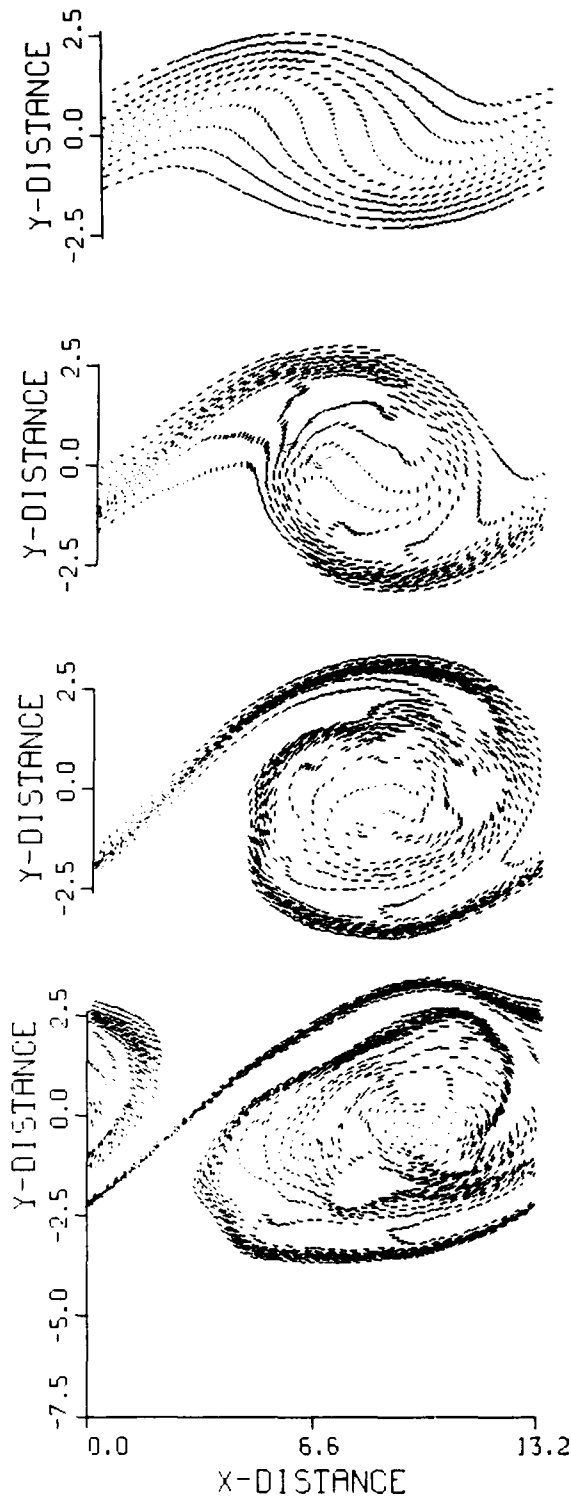
Figure 12. Locations and velocity vectors of all the vortex elements for a reacting layer at t = 5, 10, 15 and 20. Reaction parameters are: A_f = 2.0, T_a = 5.0, Q = 1.0, P_e = 200.0 and L_e = 1.0.
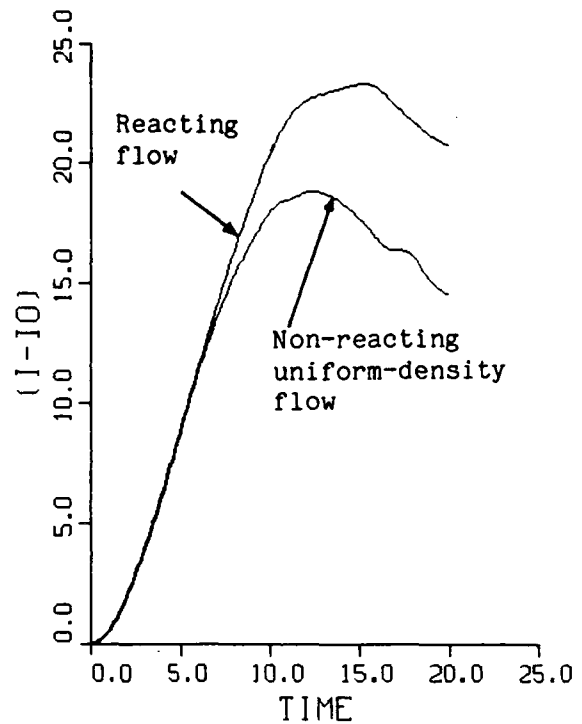

Figure 13. Integral of the perturbation velocity for the uniform-density, non-reacting flow and the reacting flow. (I-I0) = $\int (u(x,t)-u(x,0))$ dx.

the same as that of the non-reacting, uniform-density eddy. However, the reaction prolongs the growth phase and delays the start of the flattening or collapse phase. This explains why the angle between the major axis of the eddy and the positive streamwise direction, assuming that the eddy can be modelled by an ellipse, is smaller in the non-reacting, uniform-density case than in the reacting case (for experimental verification, see Keller and Daily [3].)

Figure 13 also indicates that the total fluctuations is larger for the reacting eddy than for the uniform-density, non-reacting eddy, suggesting that the total volumetric entrainment is also larger in the former case. Figures 11 and 12 show that in the reacting case, volumetric entrainment is asymmetric with a bias towards the hot fluid. Clearly, the gulf, or tongue, of hot fluid reaches deeper into the eddy than that of cold fluid. Moreover, the free-stream gulfs reach deeper/shallower, respectively, than their counterparts in the non-reacting, uniform-density case. The origin of the asymmetry will be investigated in detail in the next section.

The temperature contours for both the non-reacting, uniform-density and the reacting cases are plotted in Figs. 14 and 15, respectively. Figure 14 shows the symmetric development of the scalar field, accompanying the symmetric evolution of the dynamic field in this case. Although the Peclet number is finite and moderate, the temperature distribution remains non-uniform and steep gradients are still noticeable even near the center of the core. As time progresses, more mixed fluid, at T = 1.5 is entrained into the
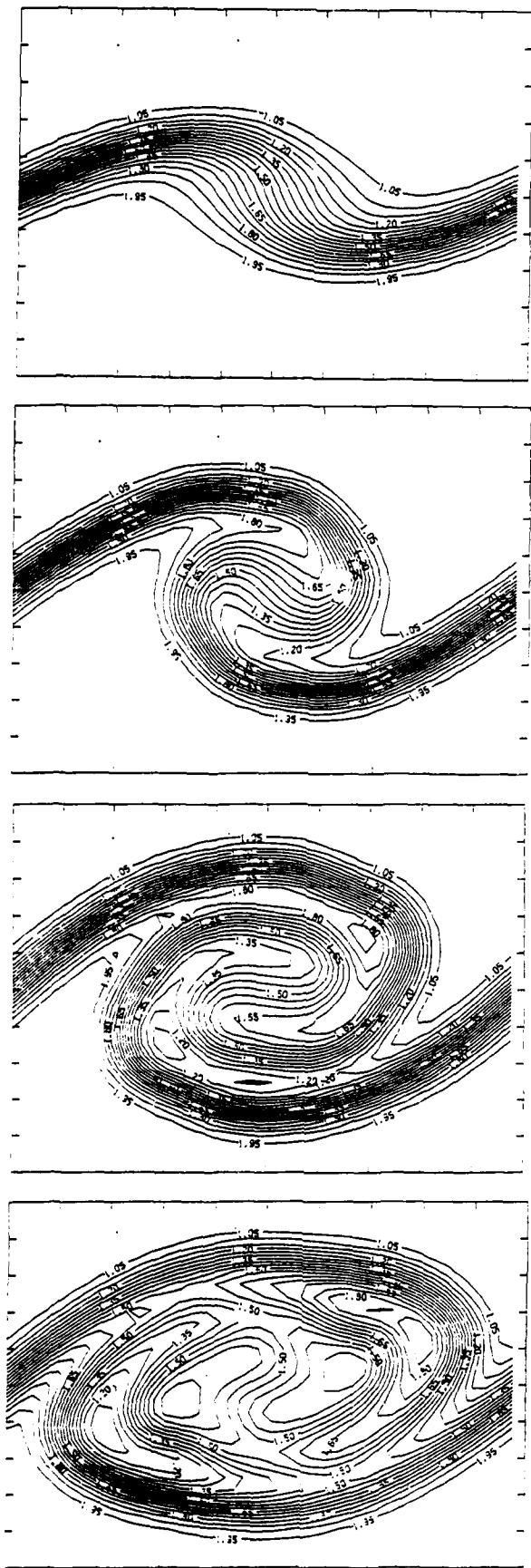
Figure 14. Temperature contours for the uniform density, non-reacting flow, T1/T2 = 0.5, at t = 5, 10, 15 and 20.
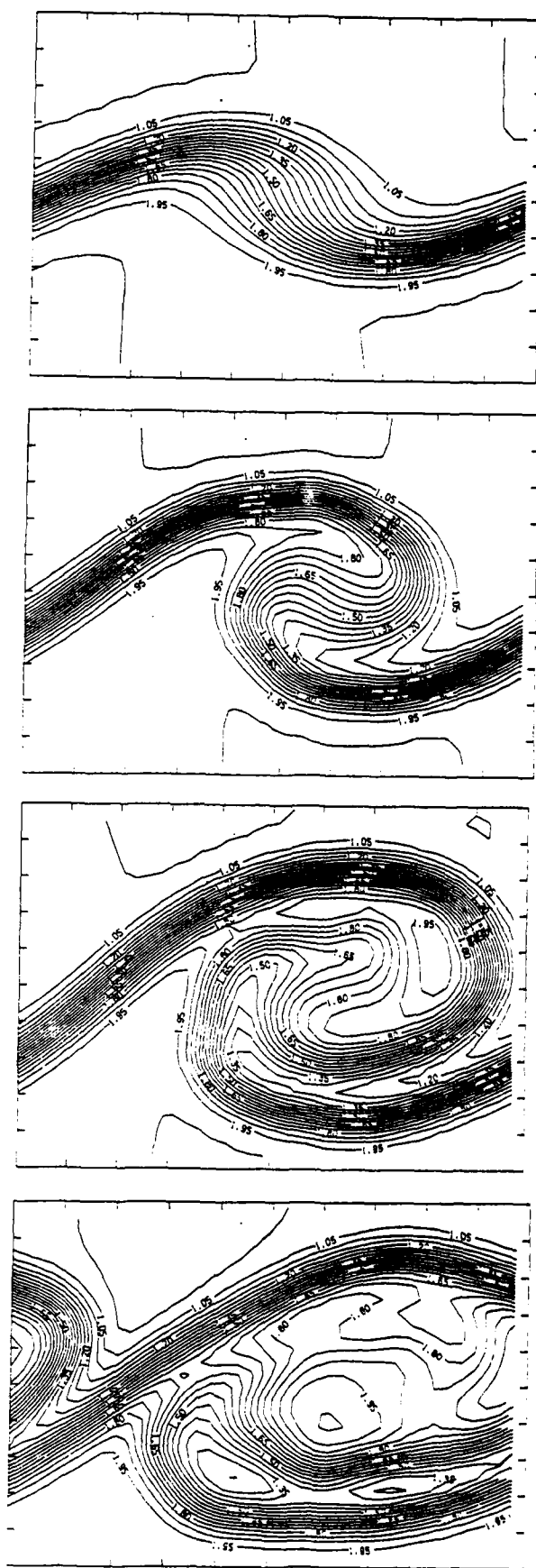
Figure 15. Temperature contours for the reacting flow, t = 5, 10, 15 and 20.

core. The mixed fluid forms along the convoluted interface by the diffusion across the concentration surfaces, and is entrained along the interface towards the core. It also shows that fluid in an unmixed state has penetrated deep into the eddy from both sides, similar to the spatially-developing case in Fig. 7. The final state of the shear layer can be characterized as follows: a semi-homogeneous core separated from the free streams by two strained zones of sharp gradients.

In the analysis of the results of the reacting case, it is helpful to note that the maximum reaction rate occurs at T = 1.53, and that the reaction rate reaches one third of its maximum at T = 1.0 and 1.90. Because the activation energy is moderate, leading to a thick reaction zone, we expect that the interaction between the flow field and the flame cannot be approximated by a wrinkled laminar flame model. Figure 15 shows that within the growth stage, $5 < t < 15$, the flame zone is slightly thinner around the braids and is substantially thicker in the core zone, both with respect to the flame thickness at $t = 0$. The first is due to the strong strain, while the second is due to the enhanced entrainment, both associated with the roll-up of the layer and the formation of a vortex core. Flame thinning due to the strain along the braids is almost unnoticeable since the reduction of the flame thickness due to the strain is balanced by the increase in the flame thickness due to the enhanced diffusion. Flame thickening is due to negative strain in the vicinity of the center of the core and the strong entrainment currents accompanying the roll-up. It is thus expected that the total reaction rate must increase within this range since the reaction zone has grown beyond its area (or volume in a three-dimensional world) at $t = 0$.

Another factor which is expected to contribute to the increase in the reaction rate for $10 < t < 15$ is the formation of a flame fold, or gulf of reactant that penetrates into the burning core. Within this range, there is a burning core at the center of the eddy, formed by the entrainment of reactant at the early stages of roll-up, surrounded by one flame zone on the top side and two flame zones on the bottom side. The two flame zones are approaching each other and trapping a gulf of reactant in-between. By the end of the growth stage, $t = 15$, the core is almost fully burnt and the flame is on the outer boundaries of the eddy. Figure 15 shows that for $t > 15$, the flame is aligned with the streamlines of the flow, and is exposed to a strong strain along its own direction.

V.2. RATE OF BURNING

The total mass of products, M_p, formed since $t = 0$ is shown in Fig. 16. The total flame length, L_f, approximated by the line of maximum reaction rate, is depicted on the same plot. As a reference case, we also plot the total mass of products formed due to the propagation of a laminar flame which has the same initial conditions and whose length is λ. For $t = 5.0$, the rate of product formation is the same as that of a laminar flame and L_f is almost constant. Within the growth range, the flame length increases due to the roll-up of the layer. The slope of the M_p-curve, which is the rate of product formation, $\dot{M}_p = dM_p/dt$, exhibits a similar increase in the range of $5 < t < 15$. The rise in
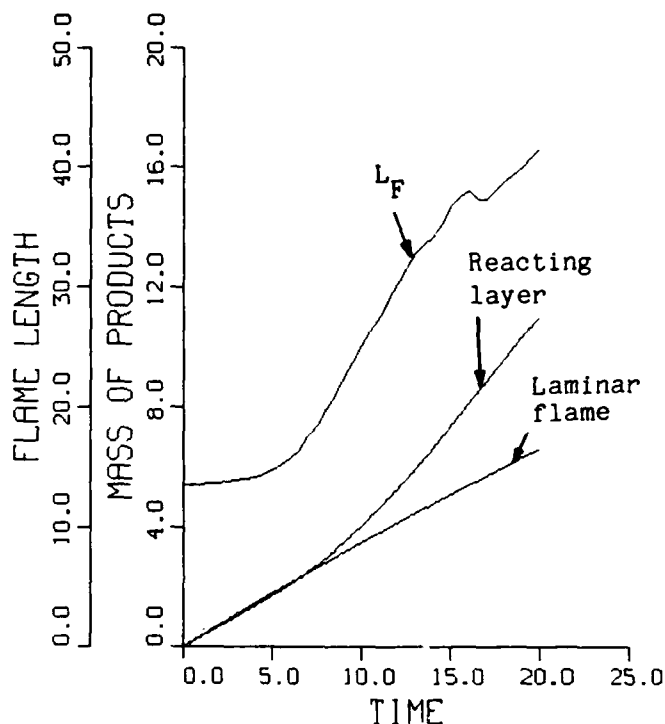

Figure 16. Total mass of product formed since $t = 0$ for a laminar flame and a reacting layer, and the apparent flame length in the latter case.

$\dot{M}_p$ is the same as that in L_f, indicating that the rate of burning per unit length of the flame, the burning velocity, remains constant. Beyond $t = 15$, $\dot{M}_p$ stays constant while L_f continues to increase (the slight decrease in L_f around $t = 17$ shows that a piece of the fold has been consumed.) Since $\dot{M}_p = S_{ua} L_f$, where S_{ua} is the average laminar burning velocity of a strained flame convoluted within the eddy, the average burning velocity decreases after $t = 15$. The reason for this drop will be investigated in Section V.4.

It is important to point out that the L_f-curve is used only to characterize the stage of growth of the eddy and not to define a unique relationship between $\dot{M}_p$ and L_f. The flame under investigation is a "thick" flame in which the flame thickness is of the same order of magnitude as the flow gradients. Thus, it is the area of reaction (or the volume of reaction in a three-dimensional world) which determines the total rate of burning. Results in Fig. 15 indicate that within the second stage of roll-up, the entrainment stage, the total rate of burning can be well approximated by the product of the laminar burning velocity of the unstrained flame times the apparent flame length. Beyond that, the strain field and the geometry of the streamlines associated with roll-up play important roles in determining the local laminar burning velocity.

12

V.3. VORTICITY GENERATION BY BAROCLINIC TORQUE

The asymmetric growth of the reacting eddy is accompanied by: (1) its displacement to the right; and, (2) the volumetric entrainment of more hot fluid than cold fluid. The reacting eddy and the uniform-density, non-reacting eddy are dynamically different in two aspects: the volumetric expansion associated with heat release, and the stratified density field. The former is kept small by taking $Q = 1$, and it is of interest to isolate the effect of the latter. Figures 17 and 18 show the vortex

Figure 18. Temperature contours for the density-stratifies, non-reacting flow, $\rho1/\rho2 = 2.0$, at $t = 10$, 15 and 20.

Figure 17. Locations and velocity vectors of all the vortex elements for a density-stratified, non-reacting layer, $\rho1/\rho2 = 2.0$, at $t = 10$, 15 and 20.

elements and their velocity, and the temperature contours of a density-stratified, non-reacting shear layer eddy. These results resemble those of the reacting eddy in Figs. 12 and 15 (the values of the temperature are, however, different). The similarity suggests that the mechanism leading to the asymmetry in the hydrodynamic field is active in both cases, and that this mechanism depends on the density gradient within the field.

13

Referring to Eq. (3), the density field can, when coupled with a pressure field, produce vorticity that will perturb the initial vorticity field and thus affect the roll-up of the eddy. Figures 19, 20 and 21 show the vorticity contours for the uniform-density, non-reacting case, the non-reacting density-stratified case and the reacting case. Here also, Figs. 20 and 21 exhibit a strong similarity, although some of the numerical values are different, indicating that the mechanism of vorticity generation by the baroclinic torque, $\nabla\rho\times\nabla p$, is responsible for the change in the structure of the eddy. Volumetric expansion in the reacting case, however, weakens the vorticity locally by increasing the area of the eddy core.

Figures 20 and 21 show that in a layer formed of negative vorticity, positive vorticity generated on the high-density side of the layer due to baroclinic effects forms a secondary eddy above the primary eddy. The secondary eddy, having positive vorticity, produces a velocity field which propels the primary eddy towards the right, as seen in Figs. 12 and 17. The positive secondary eddy on the top side of the primary eddy reduces the entrainment velocities into the eddy from this side, resulting in less entrainment of the top, cold fluid than that of the bottom, hot fluid, as shown in Figs. 12 and 17.

Thus, we have been able to identify the two observations, the motion to the right and the asymmetric entrainment, with the formation of a positive secondary eddy above the negative primary eddy. The convective velocity of the eddy in a density stratified flow and the asymmetric entrainment have been observed experimentally. Dimotakis [16] suggested the following expression for this velocity: $U_c = (1 + r_u\sqrt{s_\rho})/(1 + \sqrt{s_\rho})$, where r_u is the velocity ratio across the layer and s_ρ is the density ratio. In a temporal frame of reference, this expression can be rewritten as: $u_t = u_c - u_m = 1 - 2\sqrt{s_\rho}/(1 + \sqrt{s_\rho})$ (Krishnan and Ghoniem [17]). Figure 22 shows a comparison between the numerical predictions of u_t and the values evaluated using the modified Dimotakis formula. The close agreement shows that the baroclinic vorticity generation is indeed responsible for this asymmetric dynamics. It also validates our numerical results.

V.4. FLAME-STRETCH EFFECTS

Figures 15 and 16 show that after the burning of the core, $t > 15$, the rate of product formation, $\dot{M}_p$, is constant while the apparent length of the flame measured along the line of maximum reaction rate, L_f, is increasing. Thus, the burning velocity, averaged over the length of this flame length is decreasing. As shown in Fig. 15, the flame during this period exists on the outer edges of the large eddy and its length cannot be easily approximated by the line of maximum strain.

To analyze this phenomenon further, we plot the strain rate in the direction of the local streamlines in Fig. 23. The figure indicates that, while during the growth stage, $5 < t < 15$, most of the burning zone lies on areas where the strain is negative, at the later stages, $t > 15$, most of the burning zone coincides with areas of strong positive strain. Strong strain reduces the
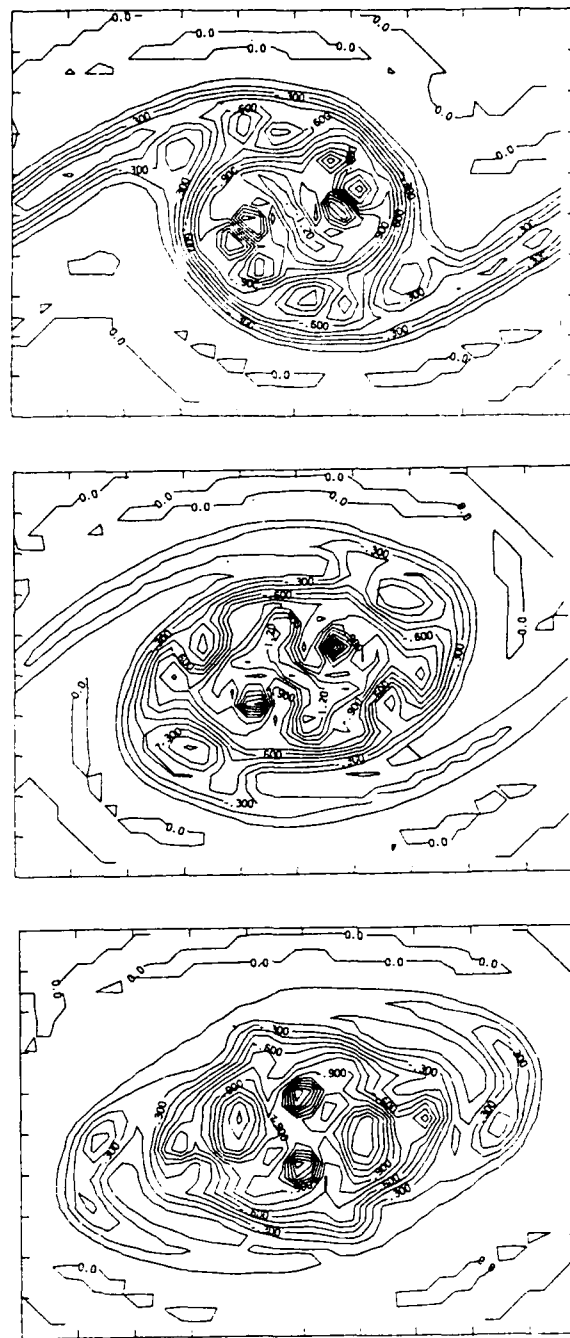

Figure 19. Vorticity contours for the uniform-density, non-reacting flow at t = 5, 10, 15 and 20.

flame thickness, causing some reduction in the total rate of burning. A more important effect, associated with the convoluted nature of the streamlines at this stage, is that the flame does not exist on a simply-connected region any more, and that gulfs, islands and intersecting flame fronts exist simultaneously. Thus, the simple definition of a flame length is not applicable and the definition of a local burning velocity may not be unique.
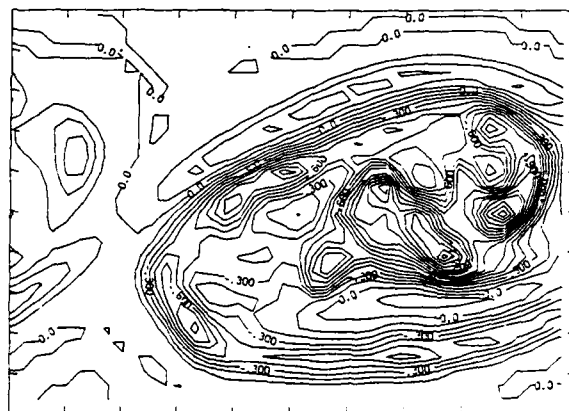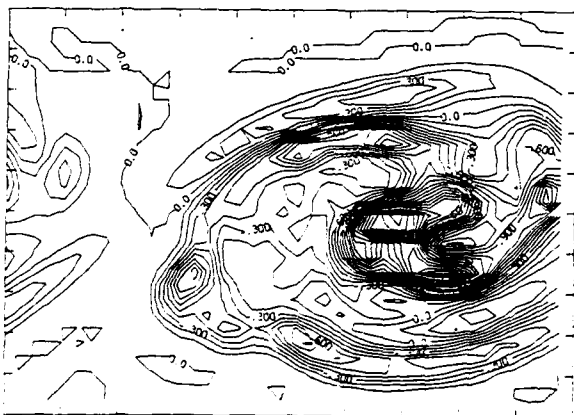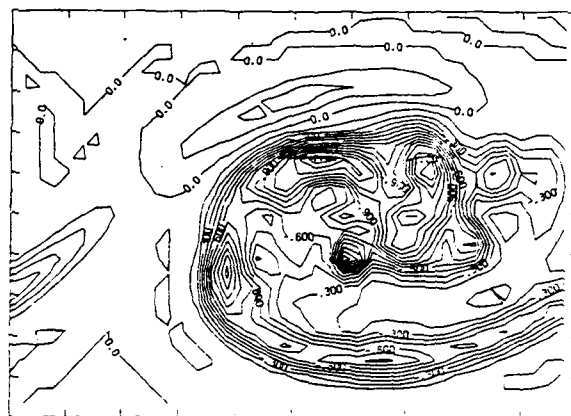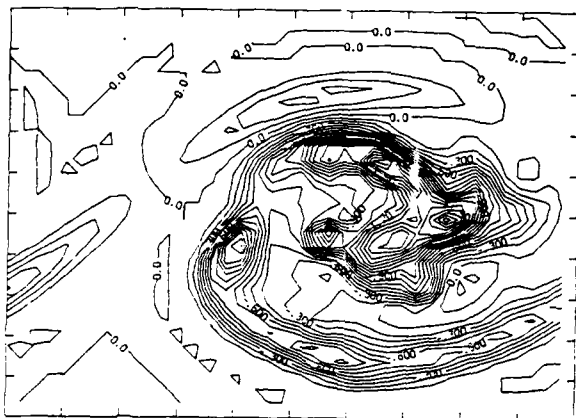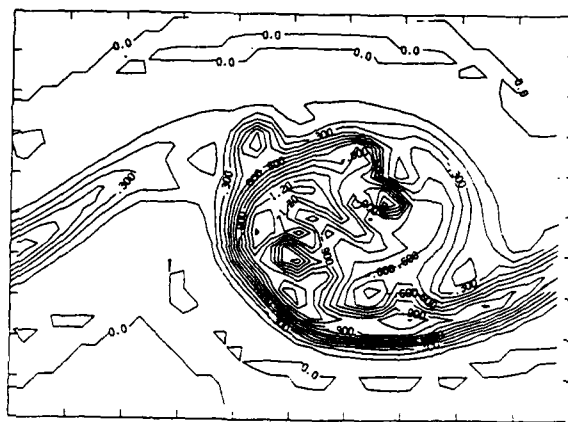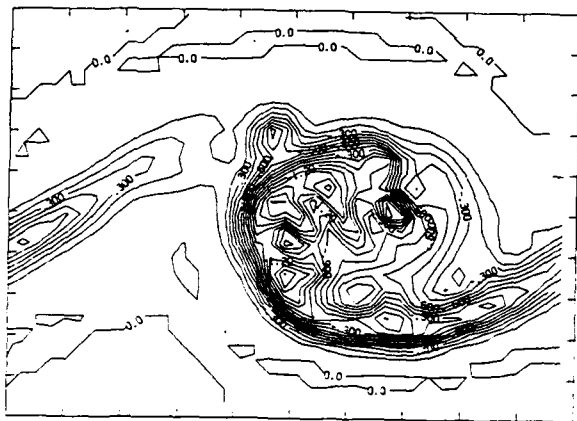
Figure 20. Vorticity contours for the density-stratified, non-reacting flow at t = 10, 15 and 20.

Figure 21. Vorticity contours for the reacting flow at t = 10, 15 and 20.
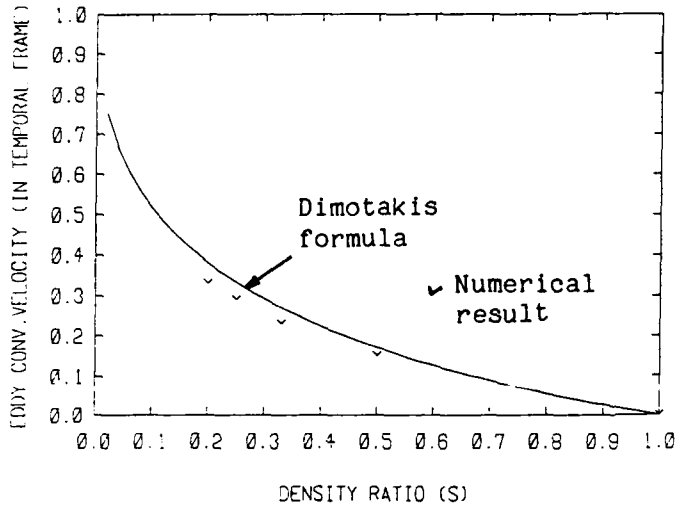
Figure 22. Convective velocity of the eddy in a temporal frame of reference for different values of the density ratio.
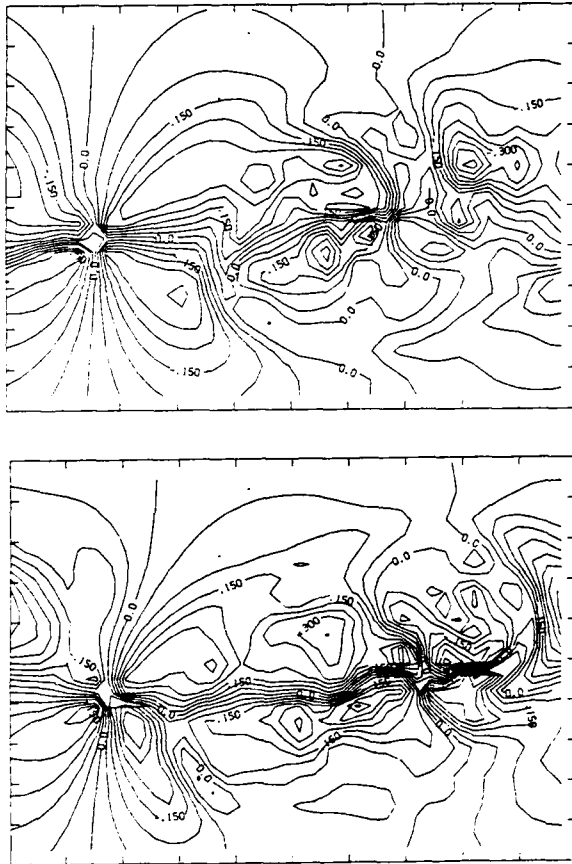
Figure 23. Strain rate along the streamline direction for the reacting shear layer at t = 15 and 20.

VI. CONCLUSIONS

Numerical simulation of mixing and chemical reaction in a two-dimensional, shear layer has been performed using the transport element method. Results have been obtained for a non-reacting, uniform-density, spatially-growing confined shear layer, and a reacting, premixed, variable-density, temporally-growing shear layer. For the first case, comparisons with the experimental measurements of M&B [2] were conducted to validate the results. For the second case, processes of turbulence-combustion interactions, especially the effect of vorticity generation by baroclinicity, of entrainment fluxes and of flame stretch, were investigated. Major conclusions are:

(1) Velocity and mixing statistics agree well with the experimental measurements of a two-dimensional shear layer before mixing transition;

(2) Processes leading to mixing asymmetry and the establishment of a preferred mixture fraction in a spatially-growing layer are illustrated;

(3) Mixing asymmetry in a variable-density layer is found to be due to the generation of vorticity due to baroclinic torque;

(4) Entrainment associated with roll-up augments the rate of burning. However, strong strain reduces the local burning rate at later stages.

Work is underway to extend the simulation of the spatially-growing shear layer to a reacting, diffusion flame, and to study the effect of different chemical parameters on turbulence-combustion interactions.

16

REFERENCES

1. Mungal, M.G. and Dimotakis, P.E. "Mixing and combustion with low heat release in a turbulent shear layer," J. Fluid Mech., Vol. 148, pp. 349-382, 1984.

2. Masutani, S.M. and Bowman, C.T., "The structure of a chemically reacting plane mixing layer," J. Fluid Mech., Vol. 172, pp. 93-126, 1986.

3. Keller, J. and Daily, J.W., "The effect of highly exothermic reaction on a two-dimensional mixing layer," AIAA Journal, Vol. 23, pp. 1937-1945, 1985.

4. Jou, W.H-. and Riley, J.J., "On direct numerical simulations of turbulent reacting flows," AIAA 19th Fluid Dynamics, Plasma Dynamics and Laser Conference, June 6-10, 1987/Honolulu, Hawaii, AIAA-87-1324.

5. Libby, P.A. and Williams, F.A., " Structure of laminar flamelets in premixed turbulent flames," Combust. Flame, Vol. 44, pp. 287-303, 1982.

6. Libby, P.A. and Williams, F.A., " Strained premixed laminar flames under nonadiabatic conditions," Combust. Sci. Tech., Vol. 31, pp. 1-42, 1983.

7. Darabiha, N., Candel, S.M. and Marble, F.E. "The effect of strain rate on a premixed laminar flame," Combust. Flame, Vol. 64, pp. 203-217, 1986.

8. Keller, J. O., Vaneveld, L., Krochlet, D., Hubbard, G. L., Ghoniem, A. F., Daily, J. W., and Oppenheim, A. K., "Mechanisms of instabilities leading to flash back," AIAA Journal, Vol. 20, pp. 254-262, 1982.

9. Peters, N. and Williams, F.A., "Coherent structures in turbulent combustion," in The role of Coherent Structures in Modelling Turbulence and Mixing, ed. by J. Jimenez, Springer-Verlag, Berlin, 1983, pp. 364-393.

10. Ghoniem, A.F. and Givi, P. "Lagrangian simulation of a reacting shear layer," AIAA Journal, to appear, 1988. Also AIAA-87-0225

11. Ghoniem, A.F., Heidarinejad, G., Krishnan, A. "Numerical simulation of a thermally stratified shear layer using the vortex element method," J. Comput. Phys., to appear, 1988.

12. Ghoniem, A.F., Heidarinejad, G., Krishnan, A. "Numerical simulation of a reacting shear layer using the transport element method," AIAA/SAE/ASME/ASEE Joint Propulsion Conference, San Diago, CA, July 1987, AIAA-87-1718.

13. Ghoniem, A.F., Heidarinejad, G., Krishnan, A. "Turbulence-combustion interactions in reacting shear layer," Proceedings of the Joint France-U.S.A. Workshop on Turbulent Reactive Flows, Rouen, France, 6-10 July 1987.

14. Ng, K.K. and Ghoniem, A.F. "Numerical simulation of a confined shear layer," Dynamics of Reactive Systems, Part II: Modeling and Heterogeneous Combustion, Vol. 105 of Prog. Astro. Aero, pp. 18-49, 1986.

15. Ghoniem, A.F. and Ng, K.K. "Numerical study of the dynamics of a forced shear layer," Phys. Fluids, Vol. 30, No. 3, pp. 706-721, 1987.

16. Dimotakis, P., "Two-dimensional shear layer entrainment," AIAA Journal, Vol. 24, pp. 1791-1796, 1986.

17. Krishnan, A. and Ghoniem, A.F., "Baroclinic effects on a thermally stratified shear layer," to be presented at the 1st National Fluid Dynamics Conference, July 1988.

DEVELOPMENT AND APPLICATION OF VORTEX METHODS: A REVIEW AND SOME EXTENSIONS
(Invited paper)

Ahmed F. Ghoniem

Department of Mechanical Engineering
Massachusetts Institute of Technology
Cambridge, MA 02139

ABSTRACT

Recent developments in vortex methods in two and three dimensions are reviewed. Extension to the solution of scalar conservation equations using the transport element method is included. A formulation of a compressible flow simulations is presented. Attention is focused on the construction of the numerical schemes and their convergence to the solutions of the fluid flow equations. The numerical accuracy of these methods is investigated by comparing results of numerical simulations of incompressible flows at high Reynolds numbers to analytical and experimental results. Information revealed by the numerical solutions are discussed.

I. INTRODUCTION

The desire to study high Reynolds flows, in which molecular diffusion plays an important role in a relatively small but finite zones of the flow, motivates the continued development of computational schemes in which numerical stability is not limited to low Reynolds numbers, and in which numerical diffusion is minimized to values smaller than those of physical diffusion. The class of flows of interest to this work is shear flows at high Reynolds number, including shear layers, jets, wakes, recirculating flows and boundary layers. In these flows, one can define a major streamwise direction that represents the mean primary flow. At high Reynolds numbers, the dominant transport mechanism of momentum and scalars, such as species concentration and energy, is convection in both the streamwise and cross-stream directions. The cross-stream convection is increased substantially with the growth of flow natural instabilities and their maturation into fully-developed secondary and higher-order flows.

In spite of the fact that convection transport dominates these flows, transport by molecular diffusion cannot be ignored especially in the cross-stream direction. Molecular diffusion is responsible for the diffusion of vorticity form solid walls, where it is generated due to the no-slip condition, into the interior of the flow through the boundary layer. Molecular diffusion also plays a primary role in the mixing of streams which are initially heterogeneous, in terms of species concentration or temperature, when they are brought into contact by the action

of convection. This is particularly important in reacting flows where mixing must be accomplished before chemical reaction. Thus, molecular diffusion cannot be ignored at high Reynolds numbers without sacrificing an important part of the physics od turbulence and mixing.

The numerical simulation of turbulent shear flows must be based on accurate representations of both mechanisms at value of the Reynolds number, and the Peclect number, in the order of magnitude of 1000-10000. Although the relative contribution of both transport mechanisms is determined by the square root of the Reynolds number, the absolute contributions of either mechanisms may also be important in many problems. Excessive numerical diffusion can lead to stabilization of flow instabilities in the case of momentum diffusion, or to overestimation of the rate of mixing or reaction in the case of scalar transport. In both cases, the local flow gradients are determined by convective mechanisms that distort the flow map, but actual diffusion fluxes are proportional to the molecular diffusivity. The extreme case of infinite Reynolds number flow in which no mixing, or vorticity diffusion away from the walls can occur independent of how strong are the convective currents illustrates this point.

One more challenge which is encountered in the numerical simulation of shear flow is the severe distortion of the flow map as the natural instabilities of these flows grow into their non-linear stages. The maturation of these instabilities in the "primary flow," which can normally be characterized by almost parallel streamlines, results in the establishment of a "secondary flow" with strongly curved streamlines. Due to the non-linearity of these problems, continuous interaction is expected between these two artificially-separated components of the flow. To capture these changes accurately, one must relay on numerical schemes with a very high spatial accuracy, i.e. very large number of fixed grid points, or schemes with moving grids in which the mesh points follow the distortion of the flow field. The latter class can be categorized as Lagrangian schemes.

In particular, if the grid points are used to represent discrete values of the functions of interest, i.e., Lagrangian finite-difference of finite-element methods, solutions can be obtained for long times after the initial phase of instability growth. These methods tend to loose accuracy after strong distortion has been encountered due to the growth of the discretization error on a non-uniform mesh. In

1

this case, regularization and remeshing become important (for a review, see Clark [1].) On the other hand, Lagrangian particle methods, of the type described in this paper, avoid using approximation formulae to determine spatial derivatives on the non-uniform mesh. This is accomplished by using particles that transport finite values of the spatial gradients of the functions of interest, i.e., transport of vorticity or scalar gradients instead of velocity of scalar concentrations. This allows longer time computations to be performed without substantial loss of accuracy due to the distortion of the underlying grid. These methods, including vortex methods, are reviewed in this article.

Vortex methods, a particular class of Lagrangian particle methods, are used to solve the momentum transport equation. They are based on the discretization of the vorticity into finite vortex elements and the transport of these elements along particle path. The fact that vorticity is conserved along the particle path in a two-dimensional, uniform-density flow has made these method particularly simple for this class of problems. However, we show that other accuracy requirements may necessitate the application of more elaborate vorticity-updating schemes as vortex elements are moved along particle path. The extension and application of vortex methods to three dimensions where the conservation of vorticity along particle path is not satisfied is also described.

The application of vortex methods to reacting and compressible flows requires the development of compatible schemes to compute the transport of scalars in Largrangian forms. For this purpose, we have developed the transport element method, a generalized Lagrangian particle scheme which is constructed to compute solutions of a convective-diffusive-reactive scalar transport equation. The formulation of the method is summarized and its application to a mixing flow at low Mach number where the momentum and energy equations can be partially decoupled is presented.

A formulation to extend the applicability of the transport element method to flows high Mach number where strong pressure variations are expected to arise is briefly described. In this case, the system of conservation equations must be solved simultaneously, and the spatial variation of the pressure must be taken into account in computing the aerothermodynamic variables.

II. VORTEX METHODS IN TWO DIMENSIONS

For a two-dimensional, incompressible, inviscid flow, the vorticity transport equation is:

$$\frac{\partial \omega}{\partial t} + u \cdot \nabla \omega = 0 \qquad (1)$$

where $\nabla \times u = \omega$ and $\nabla \cdot u = 0$. In the above, $u = (u,v)$ is the velocity, ω is the vorticity, $x = (x,y)$, t is time and $\nabla = (\partial/\partial x, \partial/\partial y)$. If $\chi(X,t)$ is a particle path, where X is the Lagrangian coordinate of χ, i.e. $\chi(X,0) = X$, then Eq. (1) states that $\omega(\chi(X,t),t) = \omega(X,0)$. Morever, $u(x,t) = \int K(x-x') \omega(x') dx'$, $K(x) = -1/2\pi r^2 (-y,x)$ and $r^2 = x^2+y^2$. This Lagrangian formulation of vorticity transport is the basis for the construction of vortex methods.

In vortex methods, the vorticity field is discretized into a number of vortex elements of finite and overlapping cores:

$$\omega(x,t) = \sum_{i=1}^{N} \omega_i h^2 f_\delta(x-\chi_i(X_i,t)) \qquad (2)$$

where ω_i is the vorticity at the center of an element, N is the total number of vortex elements, h is the average distance between the centers of neighboring elements in two principal directions, $h^2 = h_x h_y$, δ is the core radius of a vortex element, and $f_\delta = 1/\delta^2 f(r/\delta)$ is the core function describing the distribution of vorticity associated with an element. The importance of the core function in stabilizing vortex computations was realized by Chorin and Bernard [2].

Equation (2) is equivalent to expanding a function $\omega(x,t)$ in terms a number N of kernel functions, f_δ, located at X_i and with weights $\omega_i h^2$. The accuracy of the discretization depends on the choice of f, the initial distribution of the particles, the determination of the values of ω_i, $i = 1, 2, \ldots, N$, and the ratio of δ/h. The selection of the core function for a particular accuracy was extensively discussed in the work of Hald, e.g. in [3], and Beale and Majda, e.g in [4]. For the initialization of the values of ω_i, we found that collocation on a uniform grid provides the best long time accuracy (it is conceivable that collocation on a non uniform grid may be a better choice, but we have not computationally pursued this scheme). For more detail, see Ghoniem et al. [5].

We also found, using extensive numerical experimentation, that accurate discretization and long time accuracy of the computed flow field require that $\delta > h$, in agreement with all the known convergence theories of vortex methods (for a recent review, see Anderson and Greengard [6].) We found that for an initially smooth distribution of vorticity, $\delta/h = 1.1-1.5$ is an optimum choice. Note that although the core function is constructed as a fast decaying function, such as an nth order Gaussian, the fields of individual vortex elements are strongly overlapping due to the choice of δ. Thus, the local value of the vorticity at a point is determined by the

2

contributions of many surrounding elements. For more detail, see Ghoniem et al. [7].

Moreover, the velocity field of a distribution of vortex elements is given by:

$$u(x,t) = \sum_{i=1}^{N} \omega_i \, h^2 \, K_\delta(x - \chi_i(X_i, t)) \qquad (3)$$

where

$$\frac{d\chi_i}{dt} = u(\chi_i(X_i, t), t) \qquad (4)$$

where $K_\delta(x) = K(x) \, \kappa(r/\delta)$, and $\kappa(r) = 2\pi \int_0^r f(r') \, r' \, dr'$.

The generation of strong strain fields, associated with the growth of perturbations into the non-linear stages, increases the distance between neighboring elements, $\delta\chi$, beyond the "target" value of h. Thus, the accuracy of spatial discretization, which is governed by δ/h, is negatively affected. In actual computations, deterioration of accuracy is observed as the generation of unorganized, random motion on the scale of h which grow as time progresses. To avoid this problem, more elements are introduced in areas where $\delta\chi > \beta h$ where $\beta \sim 1.5$, and the circulation of the original elements is locally redistributed among the newly introduced elements. Since the circulation of each element is $\omega_i h^2$, and since the vorticity is conserved along a particle path, the redistribution of circulation is accomplished by dividing the value of h^2 of the original element equally among the newly generated elements.

For consistency, and to satisfy the condition of conservation of vorticity, $d\omega/dt = 0$, the value of δ^2 should also be adjusted so that the ratio of δ^2/h^2 is maintained constant in Eq. (1). Thus, the core radius of an element is effectively decreased as the element is exposed to strong positive strain. Note that this could also be accomplished by replacing a circular element by an elliptical element whose major axis is aligned with the direction of maximum positive strain and whose area is the same as the area of the original circular element. For an elliptical element, the major axis stretches and the minor axis is shortened so that the total area remains constant as a strain field is applied. In the extreme limit of this process, a circular vortex element becomes a flat vortex sheet with a velocity jump across its length equal to the local value of the vorticity ω_i (Note the similarity with the vortex sheet algorithm, Chorin [8].) For computational convenience, however, we chose to use more circular elements along the major axis instead of fewer elliptical elements. Elliptical elements were used by Ting [9] to solve the boundary layer equations.

The redistribution of vorticity in the direction of maximum tensile strain requires maintaining a list of near neighbors in the direction of maximum strain, and updating this list each time step according to the changes in the vorticity distribution along the layer. This process is equivalent to utilizing a one-dimensional Lagrangian grid along each individual layer of vortex elements to preserve the

organization of the computations. It can also be used to provide information about the flow map at any time step since, according to the condition of incompressibility, one can compute the changes in the length of the material elements normal to the layer of vortex elements associated with the extension of the elements in the direction of maximum strain.

As was mentioned earlier, employing more elements to discretize the vorticity in the direction of maximum strain is equivalent, in some sense, to distorting the original elements from their circular shape to elliptical shapes due to the generation of the strain field. By increasing the number of vortex elements, we insure that the underlying grid of computational elements can capture the instantaneous vorticity distribution as it evolves with the motion of the flow. The need to increase the number of elements becomes clear when realizing that as the flow develops strong strains and curvature, the streamlines become strongly convoluted and require more particles to describe their geometry accurately. On the other hand, reducing the size of the cores of vortex elements help minimizing the numerical diffusion which may accumulate to unacceptable levels if the area on which the vorticity exists is alloed to grow beyond its original size.

A careful numerical investigation of the accuracy of this scheme was conducted by Ghoniem et al. [5]. The growth of a stationary sinusoidal perturbation on an infinite shear layer was used as a case study. For a sample results, see Fig. 1. This problem, besides its obvious relevance fundamentally and practically, is ideally suited for a study aimed at checking the accuracy of the computation and the response of the scheme to the generation of a strong strain field. Numerical results for the growth rate of linear perturbations, whose amplitudes are O(0.01) of the wavelength, vs. the wavelength of the perturbation was found to agree with the results of the linear theory over a wide range of perturbation wavelengths. Another test, done by Ghoniem and Ng [10], was performed for a spatially-developing shear layer in which the flow was assumed to be semi-infinite and the growth of the perturbation was observed in the mean flow direction. Results agreed with the linear theory of stability of a spatially growing layer.

In the non-linear regime, which is characterized by the formation of large scale structures due to the roll-up of the vorticity layer associated with the growth and saturation of the instability, no theory exists and results must be checked for self consistency and against experimental data. Self consistency refers to numerical convergence and the approximate satisfaction of differential and integral constraints. Numerical convergence is achieved when, as the numerical parameters are refined, one obtains solutions that become independent of the numerical parameters. An example for a differential constraint, which should approximately be satisfied by the numerical solution, is the conservation of vorticity along a particle path, $d\omega/dt = 0$. This implies that an accurate solution is one in which if the total vorticity at the center of each element is computed, then $\omega_i(\chi_i, t)$ should remain constant.
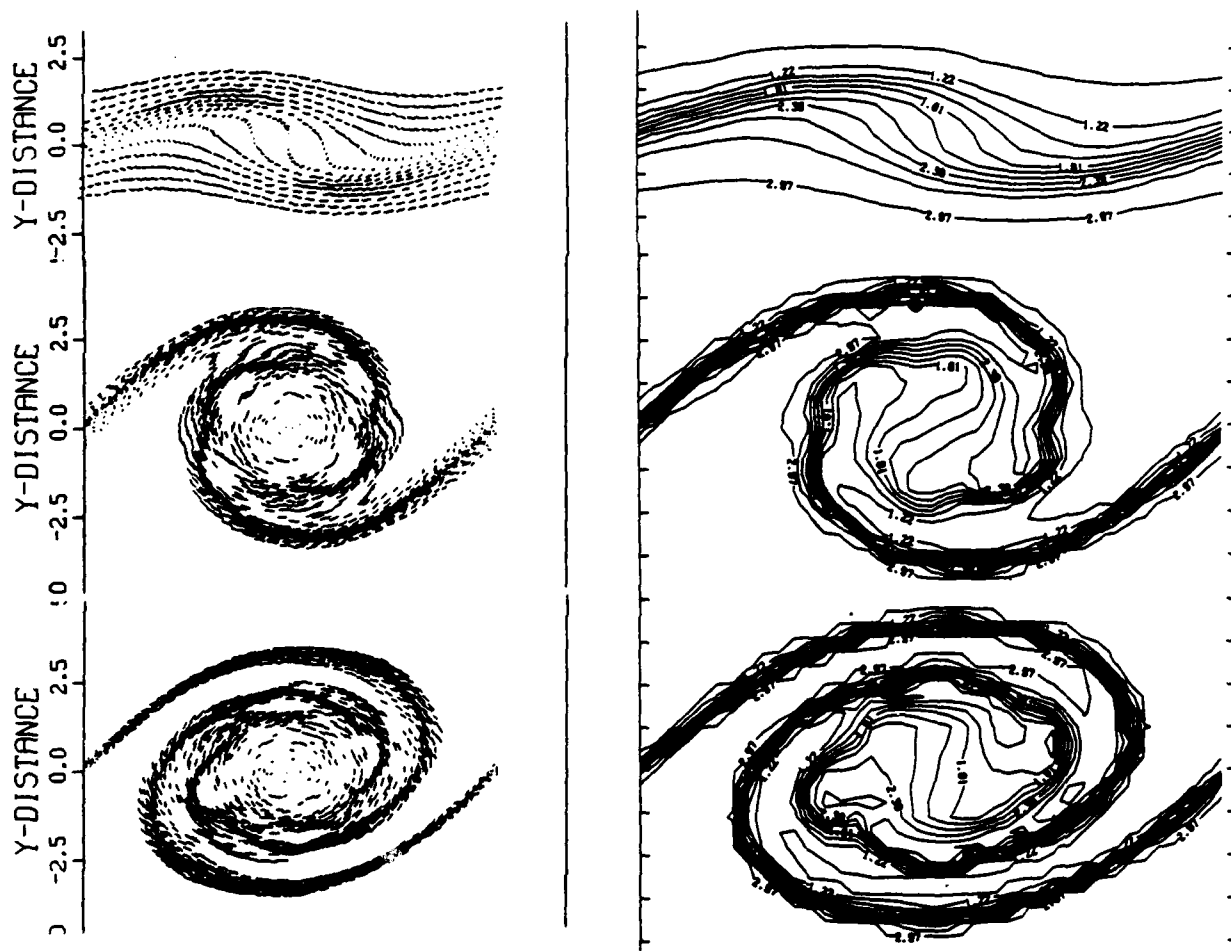
Figure 1. The location and velocity of the vortex element, left, and the temperature contour, right, in a temporal mixing layer at time t = 10, 20 and 25. Initial perturbation is 0.01 of the wavelength. Temperature ration across the layer is 1:3, with cold fluid on top.

To validate the numerical scheme, numerical results were used to compute the flow statistics which can be compared with experimental data. For example, the frequency of shedding in a spatially-developing shear layer was found to match the most unstable frequency evaluated from the linear stability theory for spatially growing waves in a vorticity layer. The mean growth the momentum thickness of the layer as it develops downstream, which reaches a constant value beyond the linear range of the instability (where the growth is exponential) was found to agree closely with experimental data on shear layers. To study the response of the layer to time-dependent boundary conditions, the inlet flow was assumed to be harmonically modulated at frequencies different from the natural shedding frequency, and the response of the layer was found to correspond closely to the experimental data. Results were used to establish how the shear layer growth, and the accompanying rate of mixing, can be enhanced or reduced by applying external forcing. For a sample of the results, see Fig.2.

The mean flow velocity, root mean square and cross correlations of velocities were shown to agree closely with experimental results on two-dimensional shear layers in both the unforced and the forced cases, Fig. 3. Results show that in the two-dimensional flow, the source of the fluctuation is the formation of the "secondary" flow associated with the growth of the large scale vortex structures due to the natural flow instability, and their subsequent pairing due to the subharmonic instability. Forcing, which can be used to either promote or suppress these instabilities, was shown to have a direct impact on the values and signs of these fluctuations, suggesting that by employing carefully-designed forcing functions, one can control the interactions between the mean flow and the shear layer flow (Ghoniem and Ng [10]).
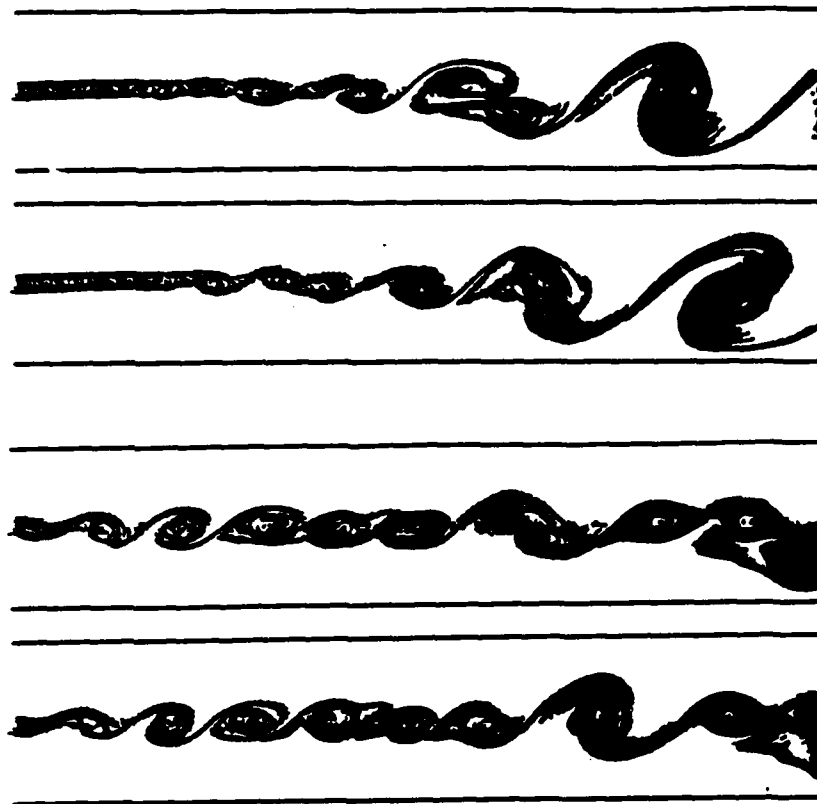
Figure 2. The location and velocity of vortex elements for an unforced shear layer at two time steps, top, and a forced shear layer at two time steps, bottom, showing the organization of large scale vortex shedding under the influence of forcing. In both cases, the velocity ratio is 3:1 with the high speed fluid on top.
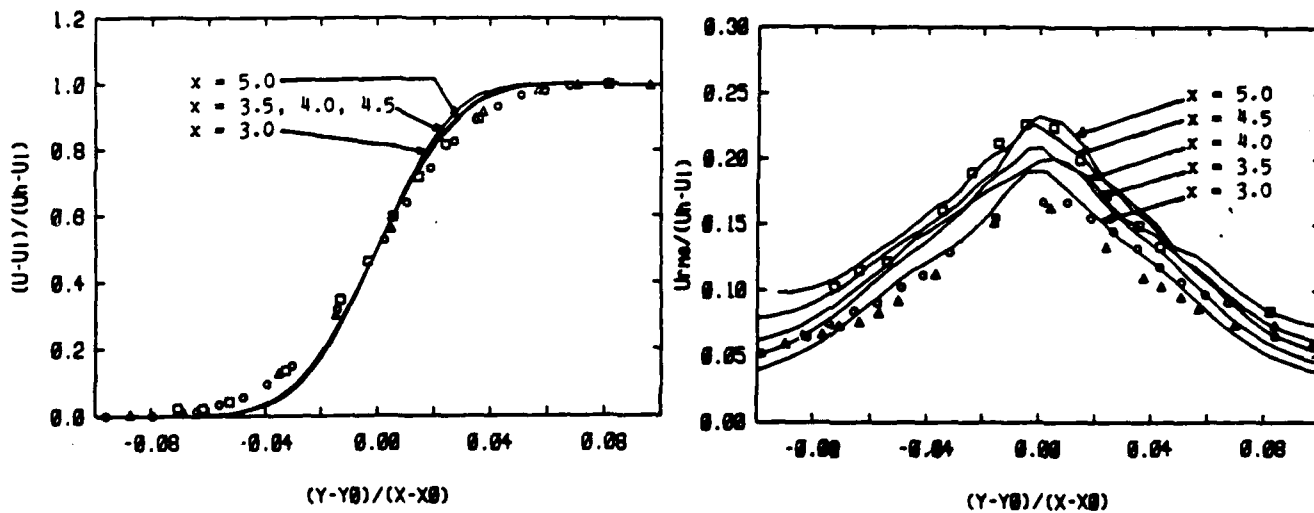

Figure 3. The average velocity profiles, left, and root mean square fluctuations, right, for a free shear layer shown on the top of Fig. 2. Here the velocity ratio is 2:1. Open symbols are experimental data and solid lines are numerical results. x and y are the streamwise and cross-stream directions.

III. VORTEX METHODS IN THREE DIMENSIONS

For an incompressible, three-dimensional, inviscid flow, the vorticity transport equation is:

$$\frac{\partial \omega}{\partial t} + u \cdot \nabla \omega = \omega \cdot \nabla u \qquad (5)$$

where $\omega = \nabla \times u$, and $\nabla = (\partial/\partial x, \partial/\partial y, \partial/\partial z)$. In this case, $u = (u,v,w)$ and $x = (x,y,z)$. The Lagrangian form of Eq. (5) is $d\omega(\chi(X,t),t)/dt = \omega(\chi(X,t),t) \cdot \nabla u$, where as before $\chi(X,t)$ is a particle path and X is the Lagrangian coordinate, while ∇u is the strain tensor $\partial u_i/\partial x_j$. An equivalent expression which can be used to determine the vorticity directly is: $\omega(\chi(X,t),t) = \nabla \chi(X,t) \cdot \omega(X,0)$, where $\nabla \chi$ is the Jacobian of the flow map $\partial \chi_i/\partial X_j$ (Helmholtz theorem). Moreover, $u(x,t) = \int K(x-x') \times \omega(x') dx'$, where $K(x) = -1/4\pi \, x/r^3$. This Lagrangian formulation is the basis for the construction of three-dimensional vortex methods. For reviews, see Chorin [11] and Leonard [12].

Similar to the two-dimensional case, the vorticity field is discretized among elements initially located within volume elements h^3. The vortex elements are then moved along particle path, $\chi_i(X_i,t)$, while their vorticity is changed according to the right-hand side of Eq. (5). Thus:

$$\omega(x,t) = \sum_{i=1}^{N} \omega_i(t) \, h^3 \, f_\delta(x - \chi_i(X_i,t)) \qquad (6)$$

where in this case, $f_\delta(x) = 1/\delta^3 \, f(r/\delta)$ and the rest of the parameters are defined as before. Note that here one defines vortex balls or spheres of diameter δ, and that the core function is spherically symmetric, while the vorticity vector associated with an element is ω_i.

The "total" vorticity vector of an element, $\omega_i h^3$, can be expressed in terms of more natural variables $\Gamma_i \delta l_i$ where $\Gamma_i = \omega_i h^2$ is the circulation of the element which remains constant along a particle path, and δl_i is the length of the material element along the vortex line, $\delta l_i = h_i \, \omega_i/\omega_i$, that changes as the material lines stretchs. The equivalence between $\omega_i h^3$ and $\Gamma_i \delta l_i$ is established by the Helmholtz theorem, while the permanence of Γ_i along a particle path is confirmed by Kelvin's theorem. The formulation in terms δl allows the construction of a natural regridding method which can be used when the stretch along the vortex lines becomes severe. In this case, as $\delta l > \beta h$, an element in divided into two elements along the vector δl, while preserving the total magnitude of Γ.

All the conditions necessary for the accurate discretization of the initial vorticity field in two dimensions apply to vorticity in three dimensions. Here, we stress that Eq. (6) is equivalent to the expansion of the function $\omega(x,0)$ in terms of a number of core functions $f_\delta(x-X_i)$ of similar shapes and located at X_i. For accurate discretization, it was found that $\delta > h$ and that the distribution of X_i must allow this condition

to be satisfied everywhere in the field. Both conditions must be satisfied at all times during the evolution of the vorticity field. Although we found that failure to satisfy these conditions around areas of small concentration of vorticity may not lead to catastrophic numerical instabilities, accuracy cannot be guaranteed.

The velocity field produced by the vorticity distribution expressed by Eq. (6) is:

$$u(x,t) = \sum_{i=1}^{N} \Gamma_i \, \delta l_i(t) \, K_\delta(x - \chi_i(X_i,t)) \qquad (7)$$

and

$$\frac{dX_i}{dt} = u(\chi_i(X_i,t),t) \qquad (8)$$

while

$$\delta l_i(t) = \frac{1}{2} \left(\chi_{i+1}(X_{i+1},t) - \chi_{i-1}(X_{i-1},t) \right) \qquad (9)$$

where $K_\delta(x) = K(x) \, \kappa(r/\delta)$ and $\kappa(r) = 4\pi \int_0^r f(r') r'^2 \, dr'$. Equation (9) utilizes the fact that in an inviscid flow vortex lines are material lines to reduce the computations. However, it requires maintaining data on the immediate neighbors in the direction of vorticity. Thus, one dimensional Lagrangian grids are utilized to describe individual vortex lines as arrays of vortex elements listed by near neighbors. Note that the conditions that a vorticity field in a three dimensional free space is solenoidal, $\nabla \cdot \omega = 0$, is implicitly satisfied in Eq. (9).

The accuracy of the three-dimensional vortex method was extensively investigated in Ghoniem et al. [13] and Knio and Ghoniem [14,15] by applying the scheme to investigate the propagation and stability of vortex rings, and the formation of streamwise vorticity in a shear layer. It has analytically been found that the self-induced velocity of a thin vortex ring, $\sigma \ll R$ where σ is the core radius and R is the ring radius, is a function of σ/R, and the vorticity distribution within the core, $\Omega(r/\sigma)$. In this representation, $\delta = \sigma$ and $\delta/h = 1.5-2.0$. The dependence of the self-induced velocity on σ/R was properly recovered form the numerical solution when the overlap between neighboring vortex elements arranged along the ring axis was strong enough to allow an accurate representation of the ring vorticity. When strong overlap was achieved, the velocity of propagation of the ring reached a constant value independent of the numerical parameters.

The long wavelength azimuthal instability of a thin vortex ring, with a wavelength $\lambda \gg \sigma$, was observed when the ring was perturbed along its axis with a number of wave $n = 2\pi R/\lambda$. The mechanism of this instability depends on the interactions between neighboring sections of the perturbed vortex ring and thus requires accurate discretization of vorticity along its axis. We found that the requirements of accurate prediction of the ring self-induced velocity are sufficient to allow accurate computation of the long wave instability. The computed unstable wavenumber k^* = $2\pi/n^*$, and its growth rate in the linear range were found to agree with the prediction of the linear theory. The growing standing waves at k^*, contrary to the spinning stable waves at all other

6

values of k, expend the energy of the flow in stretching the waves in the direction opposite to the direction of propagation of the ring. Numerical results reveal that initially, and within the linear range of growth of perturbation, the waves grow at an angle of $3\pi/4$ with respect to the direction of propagation of the ring.

In the non-linear range, the growing waves form almost closed loops of vorticity behind the original ring. These loops are connected to the original ring via very narrow passages, or necks, that can be pinched off by the action of viscosity. Each loop is formed of two vortex rings of opposite signs of vorticity which are separated by a very small distance. The separation of these loops from the "parent" ring may lead to the formation of off-spring vortex rings with a smaller diameter than that of the original ring, leading to an interesting cascading to smaller sizes and to a faster decay of the original ring. On the other hand, the fact that these off-springs form in pairs of opposite sings of vorticity, they may diffuse into each other causing their vorticity to decay at a fast rate. In both cases, the formation of these off-springs due to the growth of the azimuthal instability provide a mechanism that may lead to the reduction of the original circulation of the ring. For a graphics presentation, see Fig. (4).

The study was extended further to investigate the growth of small wavelength instabilities, $\lambda \approx \sigma$, within the core of the ring and around its axis. In this case, one must allow the core of the ring to deform under the action of the growing perturbation. Analysis of variations within the core requires adequate resolution of its vorticity field by utilizing vortex elements with a core radius $\delta < \sigma$, i.e. several elements must be used to describe the vorticity field within the core
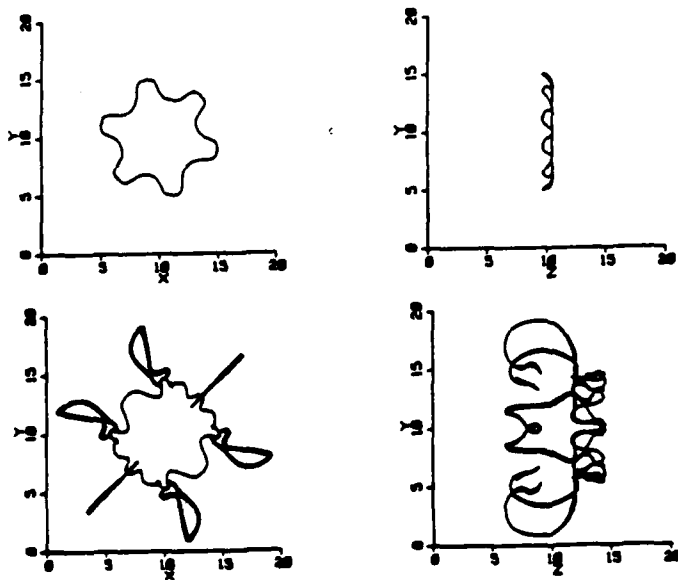
accurately. We found that the grid used to discretize the initial vorticity must be chosen carefully to provide enough overlap between neighboring elements in all direction to guarantee long time accuracy. Several choices have been proposed to satisfy these conditions and limit the number of computational elements.

Computations were performed to find the most unstable mode, or modes, in this case. The values of k^* was found to be in close agreement with that predicted by the linear theory for short wavelength instability in deformable vortex rings. The exact value of k^* is, as expected, dependent on the vorticity distribution within the ring core, $\Omega(r/\sigma)$. The value of k^* predicted from this analysis is much closer to the experimental data that that predicted by the previous long wavelength analysis. This short wave instability indicates that vortex rings are more unstable to small perturbations. The value of k^* increases almost linearly with the normalized self-induced velocity of the ring, which is inversely proportional to σ/R in a logarithmic form. Thus, thin rings, as they become unstable, deform with a larger number of waves around their perimeters that thick rings. See Fig. 5.

Spectral analysis of the results at the later stages show that as the fundamental instability reaches a saturation state, its harmonic becomes unstable and starts to grow. The mechanism of excitation of this frequency is not yet clear. Examining the vorticity field after the saturation of the first instability reveals various interesting features. The most important dynamical change is the presence of a strong streamwise vorticity component which changes its sign as one move along the axis of the ring. This component results from the tilting of the original vortex lines, initially aligned in the direction of the ring axis, due to the growth of the instability. Within each azimuthal wave, two vortices of opposite signs are formed. It should be noted that while the perturbation is along the radial direction, in the final equilibrium state most of the off-axis vorticity is in the streamwise direction.


Figure 4. The growth of long azimuthal waves on a this vortex rings at the end of the linear range, top, and long into the non-linear range, bottom, shown in the plane and normal to the plane of the ring.
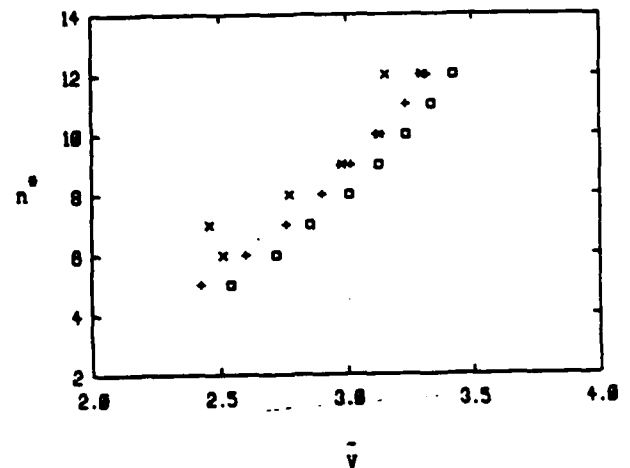
Figure 5. The most unstable wave vs. the self-induced velocity of a vortex ring. (x) experimental data, (*) numerical results, (+) and (□) and results of analytical stability theories.

The formation of the streamwise vorticity component seems to stabilize the ring, indicating that a new equilibrium state is reached. At this stage, the core of the ring exhibits helical deformation around its undisturbed axis. The form of the vortex ring, as exhibited by the plot of the vortex lines, strongly resembles experimental pictures of unstable vortex rings. In particular, the motion of the inner and outer radii can be out of phase, especially at the late stages, and vorticity start to "leak" from the back side. This leak takes the form of loops of vortex filaments which extend far behind the ring in a form that resembles the simpler picture observed in the simulations of a thin ring. See Fig. 6.

The formation of streamwise vorticity was also examined in the temporal shear layer problem. Here, the shear layer described in Section II is initially perturbed in the streamwise and the spanwise directions at the same wavelength and the same amplitude. Thus, the shear layer, which has a finite thickness, is experiencing waviness in the primary flow direction and in the direction of vorticity. Results show that during the growth of the streamwise perturbation, the spanwise mode is completely suppressed, and the flow maintains almost perfect two-dimensionality. The growth rate of the streamwise instability matches that of a two-dimensional flow until the point of maximum growth of this instability which corresponds to the formation of a spanwise, large scale, cylindrical-shaped vortex structure whose axis in perpendicular to the mean flow. See Fig. 7.

The formation of this structure is accompanied by what we labelled before as a secondary flow whose streamlines are almost circular. Beyond the point of maturation of the streamwise instability, the spanwise instability starts to grow causing this large structure to deform into the streamwise direction. This deformation leads to the establishment of a streamwise vorticity component with an alternating sign along the axis of the cylindrical structure. Within each spanwise wavelength, two streamwise vortices of opposite signs form. This feature looks very much like the azimuthal instability of the vortex ring if the latter is viewed along its axis. One more similarity is in the magnitude of absolute value of the streamwise vorticity which reaches an oscillatory stage at the point of maximum growth of the secondary flow instability.

Figure 6. Late stages of development of short wavelength instability on a thick vortex ring.

Figure 7. Late stages of development of a combined streamwise and spanwise perturbations in a periodic shear layer. The middle section shows the translative instability of the core and the sides show the formation of streamwise vorticity within the braids. Vortex lines are shown looking down on the shear layer from the top stream where the flow is from left to right.

IV. THE TRANSPORT ELEMENT METHOD

Given that s is a passive, non-diffusive scalar, the conservation equations for s and $g = \nabla s$ are:

$$\frac{ds}{dt} = 0 \qquad (10)$$

and

$$\frac{dg}{dt} = -g \cdot \nabla u - g \times \omega \qquad (11)$$

Thus, s remains constant along a particle path, while g changes due to the straining and rotation of the material lines by the local strain field and vorticity. We restrict attention to the transport of scalars in two dimensions. If the material is exposed to a strong strain in the direction normal to the gradient, the value of g must increase by the same amount as the stretch in the material element. This can be seen by deriving an equation that governs $g = |g|$. To do this, Eq. (11) must be expnded in terms of g n, implementing kinematical relations that describe the variations of $n = g/g$, the unit normal vector to the iso-scalar line. After some lengthy manipulations, we get:

$$\frac{dg}{dt} n = -g(n \cdot \nabla u + \frac{1}{2} n \times \omega - (1 \cdot (n \cdot \nabla u^s))1) \qquad (12)$$

where ∇u^s is the symmetric part of the strain tensor ∇u and 1 is the unit vector normal to n. Moreover, $g = (ds/dn) n \sim (\delta s/\delta n) n$, where δs is the variation of s across a small material line δn. The variation of a material vector element δl can be shown to be governed by the same equation as Eq. (12) with g replaced by δl. Thus, it follows that $g/\delta l =$ constant along a particle path, and that the scalar gradient can be computed from the following relations:

$$g(x,t) = \sum_{i=1}^{N} g_i(t) h^2 f_\delta(x - \chi_i(X_i,t)) \qquad (13)$$

where

$$g_i(t) = \frac{\delta s_i \ \delta l_i(t)}{h^2} n_i(t) \qquad (14)$$

where $\chi_i(X_i,t)$ is, as before, a particle path. Equation (13) is based on the expansion of g in terms of the core function f_δ. All the comments made before regarding the accuracy of such representation apply to Eq. (13). Since an iso-scalar line is a material line in a non-diffusive field, δl_i can be updated as:

$\delta l_i(t) = (\chi_{i+1} - \chi_{i-1})/2$, while $n_i \cdot l_i = 0$. Thus, it suffices to move the centers of the transport elements, while remembering the near neighbors at $t = 0$, to compute the scalar flux. When an element is inserted between two neighboring elements, the values of δl_i are redistributed between the three elements and h^2 and δ^2 are adjusted so that the total material area is conserved, while δs_i is conserved. See Section II for more detail on the refinement of the accuracy as strong strain fields grow and the material lines becomes strongly curved.

For a compressible flow, the above analysis should be modified to reflect the fact that, in this case, an equation similar to Eq. (12) can be derived with g replaced by ρ δl. Thus, in this case, the expression of g_i changes to:

$$g_i(t) = \frac{\delta s_i \ \delta l_i(t) \ \rho_i(t)}{\rho_i(0) \ h^2} n_i(t) \qquad (15)$$

The value of ρ is computed using the relation ρ T = constant in the low Mach number approximation, or ρ T = p at high Mach number (se Section V). Given the location and strength of the transport elements, the scalar concentration are computed by direct integration over the fields of the transport elements

$$s(x,t) = \sum_{i=1}^{N} g_i(t) h^2 \cdot \nabla G_\delta(x - \chi_i(X_i,t)) \qquad (16)$$

where $\nabla G_\delta(x) = (x,y)/2\pi r^2 \ \kappa(r/\delta)$. Note that this formulation is fully compatible with the vortex method since all the information needed to compute the scalar transport are already a part of the vortex computations, including all the expressions for the Green functions. For extended derivations and discussions, see Ghoniem et al. [7,16].

The effect of molecular diffusion can be modeled by expanding the cores of the elements according to the following relation,

$\delta^2(t+\Delta t) = \delta^2(t) + 2 \ \alpha \ \Delta t$, where Δt is the time step and α is the molecular diffusivity. This relation is obtained by direct substitution of Eq. (11) into the diffusion equation. A limit should be imposed on the maximum allowable value of δ to maintain the spatial accuracy of the calculations. Beyond δ_{max}, an element should be subdivided into a number of smaller elements. Another scheme for implementing the effect of diffusion without expanding the cores was proposed by Raviart [17]. However, we have not pursued this matter further.

The transport element method was used to study the transport of species in a heterogeneous shear layer. Here, we do not have analytical solutions to verify the numerical accuracy as in the case of the vorticity calculations. However, one can use the condition of conservation of species along particle path, $ds/dt = 0$, to check on the consistency of the results. We found that, provided that the field is accurately discretized at the initial step, this condition is satisfied if the core radii of the elements are allowed to decrease at the rate described in Section II, i.e. h^2/δ^2 remains constant as the elements are deofrmed. This process guarantees that the scheme can capture the large scalar gradient that arise due to the strong deformations in the flow that accompany the evolution of the instability without introducing a source of numerical diffusion. Note that a minimum value must be imposed on the smallest δ to limit the number of computational elements and to avoid dealing with the singularity at $\delta = 0$.

The computations of the mean concentration and the root mean square of the fluctuations of concentrations were compared with experimental results for a two dimensional mixing layer. Results were obtained for a range of Peclet number between 1000 and 10000, i.e. intermediate to high,

9

so that the dominant transport process was convection. The effect of species diffusion was incorporated to study mixing. Results show that the resulys of teh numerical simulations agree closely with the experimental measurements in the two dimensional shear layer. The effect of diffusion on the mean scalar distribution is very small since the overall concentration field is established by the convective currents, which are called the entrainment currents. Due to the roll-up of the vorticity layer, fluid from both sides are engulfed into the large structure and, on the average, mean values, between the two extremes, can be encountered.

The root mean square of the fluctuations exhibit stronger dependence on the Peclet number. Its maximum value, 0.5, can only be achieved at very high Peclet number, O(5000 - 10000), where strong unmixedness is present inside the cores of the eddies. As the effect of molecular diffusion increases, it homogenizes the core where the fluctuation drops below 0.5. In this case, the profiles show an area of constant value of fluctuation. In all values of Peclet number which we have used, O(100 - 10000), the fluctuations never reached zero inside the cores, indicating that the fluid did not reach complete homogeneity. Another interesting feature of these mixing flows, which has also been observed experimentally, is the presence of more high speed fluid than low speed fluid inside the cores. Numerical results show that this "mixing asymmetry" is a direct consequence of the unequal velocities across the interface of the layer. See Fig. 8.

The transport element method was extended to reacting flow and, as briefly mentioned, to flows with variable density, in Krishnan and Ghoniem [18] and Ghoniem and Krishnan [19], respectively.
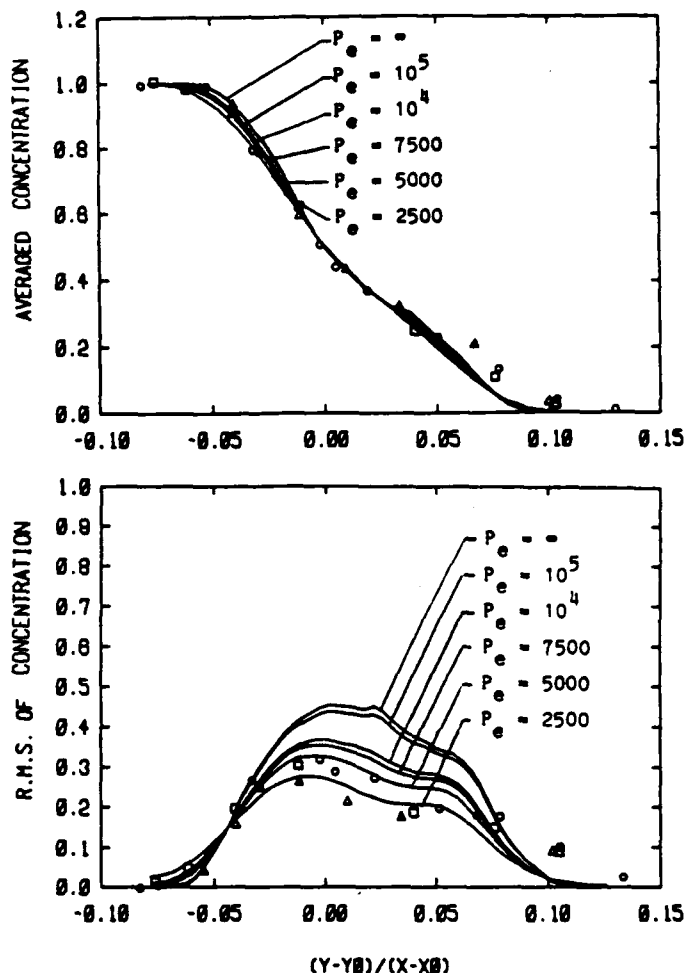
Figure 8. Average concentration, top, and R.M.S of fluctuations for the mixing layer shown in Figs. 2 and 3. Solid lines are numerical results and open symbols are experimental data. P_e is the Peclet number. Boundary conditions at the inlet section correspond to $c = 0$ in top stream and $c = 1$ in bottom stream.

V. COMPRESSIBLE VORTEX METHODS

We now show how to extend the formulations *developed so far to compressible flow at high Mach number.* We present the derivation for an isentropic flow in two dimensions. The governing equations in this case are:

$$\frac{1}{\rho}\frac{D\rho}{Dt} + \nabla \cdot u = 0 \qquad (17)$$

$$\frac{Du}{Dt} = -\frac{1}{\rho}\nabla p \qquad (18)$$

$$\frac{Ds}{Dt} = 0 \qquad (19)$$

where p and s are the pressure and entropy, respectively. The equation of state can be written as $p = C(s)\,\rho^\gamma$, where $C(s)$ is a known function of entropy and γ is the specific heat ratio

To derive a compressible vortex scheme which utilizes the developments described in Sections III and V, the velocity is identically decomposed into three components: (1) a solenoidal component $\nabla \times \phi$, where $\phi = \psi\,e_z$, e_z is the unit vector normal to the x-y plane and ψ in a stream function governed by $\nabla^2\psi = -\omega$; (2) an irrotational component $\nabla\phi$, where ϕ is a velocity potential governed by $\nabla^2\phi = d\ln\rho/dt$; and (3) a potential component $\nabla\phi_p$, governed by $\nabla^2\phi_p = 0$. The total velocity is $u = \nabla\times\phi + \nabla\phi + \nabla\phi_p$. The three velocity components can be obtained in terms of the known distributions of vorticity, $\omega(x,t)$, volumetric dilatation, $d\ln\rho/dt(x,t)$, and the boundary conditions, respectively, by utilizing the Green function solution of the Poisson equations governing the various components. Note that the forcing functions can all be represented in terms distributions of cores as before.

Next, we cast the momentum equation in a form that will allow the evaluation of the pressure distribution from the acceleration, $\nabla p = - \rho\,du/dt$. The acceleration can be computed from the time-derivative of the particle velocity, $a = (du/dt)_\chi$. The pressure can be obtained from the Green function of the corresponding Poisson equation. The entropy transport equation indicates that $s(\chi(X,t),t) = $ constant. Knowing the pressure and the entropy, the density can be computed from the equation of state: $\rho = (p/C(s))^{1/\gamma}$, where for a perfect gas $C(s) = \exp(s/c_v)$, and c_v is the specific heat at constant volume.

The dilatation field is the time derivative of density along the particle path, which can be computed by numerically differentiating the density along the particle path. The entropy gradient, needed to evaluate the baroclinic term in the vorticity transport equation, is obtained using the transport element method applied to Eq. (19). For this purpose, the method developed in Section V can be used. Finally, the vorticity transport equation:

$$\frac{d}{dt}\left(\frac{\omega}{\rho}\right) = \frac{-1}{\gamma\rho^2 C(s)}\frac{dC}{ds}\,\nabla s\times\nabla p \qquad (20)$$

is integrated. The vorticity of an element is updated each time step according to the value of the source term in Eq. (20). This completes the compressible vortex method. Numerical experiments are underway to evaluate the performance of this scheme.

VI. CLOSURE

One important extension of this work is the application of vortex methods to internal, wall bounded flows in which the growth of boundary layers along solid walls plays a dominant role in the dynamics of the flow. This extension has largely been based on the random vortex method in which the effect of molecular viscosity is taken into account by adding a Gaussian random component to the convective motion of the vortex elements (Chorin [21].) Extensive work has been done on the validation of the method (Ghoniem and Gagnon [22] and Sethian and Ghoniem [23]), showing that solutions for steady, low Reynolds number flows, and unsteady, hgih Reynolds number flows converge to appropriate limits as numerical parameters are *refines. In the first case, low Reynolds number* results were in close agreement with experimenatl measurements on velocity distributions within the flow. In the second case, results weree shown to converge to oscillatory flow that can be characterized by a cluster og large scale vorticies.

The random vortex method was also used to study recirculating flows at high Reynolds numbers (Najm and Ghoniem [24]). Of particular interest in these flows is the frequency of vortex shedding and how it depends on the geometry of the channel and the inlet condition. Here, strong organization of the flow structure was observed, and frequency of shedding as well as mean velocity distribution were found in agreement with experimental measurements.

REFERENCES

1. Clark, R.A., "Compressible Lagrangian hydrodynamics without Lagrangian cells," in Numerical Methods for Fluid Dynamics II, ed by K.W. Morton and M.J. Baines, Claredon Press, Oxford, 1986, pp. 255-272.

2. Chorin, A.J. and Bernard, P., "Discretization of a vortex sheet with an example of roll-up," J. Comput Phys., 13, 1973, pp. 423-428.

3. Hald, O., "Convergence of vortex methods fro Euler's equations," SIAM J. Num. Anal., 16, 1979, pp. 726-755.

4. Beale, J.T. and Majda, A. "Higher order vortex methods with explicit velocity kernels," J. Comput. Phys., 58, 1985, pp. 188-209.

5. Ghoniem, A.F., Heidarinejad, G. and Krishnan, A. "Numerical simulation of a thermally-stratified shear layer using the vortex element method ," J. Comput. Phys., 75, 1988, in press.

6. Anderson, C. and Greengard, C., "On vortex methods," SIAM. J. Numer. Anal., 22, 1985, pp. 413-440.

7. Ghoniem, A.F., Heidarinejad, G. and Krishnan, A. "Turbulence-combustion interactions in a reacting shear layer," Lecture Notes in Engineering, Proceedings of the France-U.S.A. Joint Workshop on Turbulent Reactive Flows, July 1987, Rouen, France, Springer-Verlag, 1988, in press.

8. Chorin, A.J., "Vortex sheet approximation of boundary layer equations," J. Comput. Phys., 27, 1978, pp. 423-442.

9. Teng, Z.-H., "Elliptic vortex method for incompressible flow at high Reynolds number," J. Comput. Phys., 45, 1982, pp. 54-68.

10. Ghoniem A.F., and Ng K.K. "Numerical study of a forced shear layer," Phy. Fluids, 30, 1987, pp. 706-721.

11. Ghoniem, A.F., Aly, H.M. and Knio, O.M., "Three dimensional vortex simulations with application to axisymmetric shear layers," AIAA 25the Aerospace Sciences Meeting, Reno, NV, January 1987, AIAA-87-0379.

12. Knio, O. M. and Ghoniem, A. F. "On the formation of streamwise vorticity in turbulent shear flows," the AIAA 26th Aerospace Sciences Meeting, January 11-14, 1988/ Reno, Nevada, AIAA-88-0728.

13. Knio, O.M. and Ghoniem, A.F. "Numerical study of a three-dimensional vortex method," submitted for publication at J. Comput. Phys., April 1988.

14. Leonard, A., "Computing three-dimensional incompressible flows with vortex elements," Ann. Rev. Fluid Mech., 17, 1985, pp. 523-559.

15. Chorin, A.J., "Vortex models and boundary layer instability," SIAM J. Sci. Stat. Comput., 1, 1980, pp.1-20.

16. Ghoniem, A.F., Heidarinejad, G., and Krishnan, A., "Numerical simulation of a reacting shear layer using the transport element method," AIAA/SAE/ASME/ASEE Joint Propulsion Conference, San Diago, CA, July 1987, AIAA-87-1718.

17. Raviart, P.A., "Particle numerical models in Fluid Dynamics," in Numerical Methods for Fluid Dynamics II, ed by K.W. Morton and M.J. Baines, Claredon Press, Oxford, 1986, pp. 231-254.

18. Ghoniem, A.F., Heidarinejad, G. and Krishnan, A. "On mixing, baroclinicity and the effect of strain in a chemically reacting shear layer," the AIAA 26th Aerospace Sciences Meeting, January 11-14, Reno, Nevada AIAA-88-0729.

19. Krishnan, A. and Ghoniem, A.F. "Origin and manifestation of flow-combustion interaction in a premixed shear layer," for presentation at the 22nd Symposium (International) on Combustion, 8-13 August, 1988, Seattle, Washington.

20. Ghoniem, A.F., and Krishnan, A. "Mixing patterns and the generation of vorticity in a density-stratified shear layer," for presentation at the Workshop on Physics of Compressible Turbulent Mixing, Princeton University, October 24-27 1988.

21. Chorin, A.J., "Numerical study of slightly viscous flow," J. Fluid Mech., 57, 1973, 785-7794.

22. Ghoniem, A.F. and Gagnon, Y., "Vortex simulation of laminar recirculating flow," J. Comput. Phys., 68, 1987, pp. 346-377.

23. Sethian, J.A. and Ghoniem, A.F., "Validation study of vortex methods," J. Comput. Phys., 74, 1988, pp. 283-317.

24. Najm, H. and Ghoniem, A.F., "Numerical simulation of the convective instability in a dump," AIAA/SAE/ASME/ASEE 23rd Joint Propulsion Conference, San Diago, CA, 1987, AIAA-87-1874.

For presentation at
the 22nd Symposium (International) on Combustion
University of Washington
Seattle, WA, August 15-19, 1988

ORIGIN AND MANIFESTATION OF FLOW-COMBUSTION INTERACTIONS
IN A PREMIXED SHEAR LAYER

Ahmed F. Ghoniem and Anantha Krishnan
Department of Mechanical Engineering
Massachusetts Institute of Technology
Cambridge, MA 02139

ABSTRACT

The interactions between the flow field and the combustion process in a premixed shear layer are investigated using the results of numerical simulation. The reaction is governed by a finite-rate Arrhenius kinetics, the flow is compressible and at high Reynolds number, heat release is moderate and molecular heat and mass diffusivities are finite. The thickness of the reaction zone and that of the vorticity layer are approximately the same. Lagrangian simulations are obtained using the vortex and transport element methods.

Results indicate that at the early stages, a reacting shear layer behaves like a laminar flame. During the growth of the roll-up eddy, the rate of burning is strongly enhanced by the entrainment fluxes that lead to the swelling of the reaction zone, and the total rate of product formation can be approximated by the unstrained laminar burning velocity times the flame length measured along the line of maximum reaction rate. Following the burning of the eddy core, the strain field along the eddy boundaries causes a noticeable thinning of the reaction zone and reduces the rate of burning.

Baroclinic vorticity generation due to the acceleration of fluid elements in the density gradient is the most important mechanism by which combustion affects the flow field. It augments the overall volumetric entrainment into the eddy core, and causes an entrainment asymmetry with a bias towards the products. The generated vorticity extends the growth period of the eddy and imparts on it an extra mean convective motion.

I. INTRODUCTION

Turbulent combustion is a closed-loop feedback system in which turbulence augments the mixing process and exposes the reaction zone to stretch and convolution, while combustion modifies the turbulent field through the effects of heat release including volumetric expansion and baroclinic vorticity production. These interactions, introduced to control the combustion process or arising due to intrinsic flow and chemical instabilities, represent a complex challenge to analysis and modeling. With an ever increasing need to boost the power, to curb the emission and to improve the efficiency of combustion, it is imperative that we improve our understanding of turbulent combustion.[1]

As a model of turbulent combustion, we have been studying, using numerical simulations, the fluid dynamics and chemical reaction in a premixed shear layer (for experimental realization of this flow, see [2].) This field contains all the elements composing the feedback loop: the mixing via large-scale entrainment and small-scale diffusion, the strain field due to the roll-up of vorticity, the convolution of the streamlines within the evolving eddies, and the generation of strong density and pressure gradients. Numerical simulation offers a powerful tool for probing this complicated flow field. The time-dependent evolution of the spatially-resolved gas dynamic field can be obtained for a range of physical parameters, and the results can then be analyzed to study the origin and outcome of the interactions. Using Lagrangian methods, such as the vortex and the transport element methods,[3,4] allows the study of high Reynolds and Peclet numbers flows since numerical diffusion is small. Numerical simulations have been conducted for a reacting shear layer with non-premixed reactants.[5,6,7]

Numerical models utilizing the concepts of wrinkled laminar flames have been used to study the interaction between a thin flame and the large scales of turbulence[8]. These models were based on the assumption that the laminar burning

velocity was a constant,[9] or a weak function of the flame geometry,[10,11] and that the effect of combustion on the turbulent field was limited to the volumetric expansion. However, analytical studies show that flow stretch may play an important role in determining the laminar burning velocity.[12] Moreover, recent numerical work confirms that baroclinic vorticity generation plays an important role on the flame dynamics.[11]

In this article, we obtain and analyze numerical results for the evolution of combustion in a perturbed, premixed shear layer. The flame structure, governed by the chemical and diffusion parameters of the mixture, is described by the appropriate conservation equations. The flame thickness and the flow gradients are of the same order of magnitude. Thus, results are expected to show strong interactions between the flow field and the combustion process. The analysis of the results will attempt to relate the behavior of this "thick" flame to the properties of a wrinkled flame model.

II. GOVERNING EQUATIONS

The model we use to investigate turbulence-combustion interactions is that of a temporally-growing shear layer in which all the conditions are periodic across the boundaries of the domain. The reactant, R, and product, P, have concentrations c_{Ro} and c_{Po}, velocities U_1 and U_2, and temperatures T_1 and T_2, in the top and bottom streams, $y \rightarrow +\infty$ and $y \rightarrow -\infty$, respectively. We set $U_2 = -U_1$, and $T_2 = T_f$, where T_f is the adiabatic flame temperature. The following idealizations are used to simplify the analysis: (1) the flow is two-dimensional and compressible; (2) chemistry is governed by a single-step, first-order, Arrhenius reaction, $R \rightarrow P$, and the rate of reaction is $A_f W$, where $W = c_R \exp(-T_a/T)$; (3) the Mach number is small, and hence, the pressure is constant (however, $\nabla p \neq 0$ in the momentum equation); (4) the reactant and product behave

as perfect gases with equal molecular weights and specific heats; and (5) the thermal and mass diffusivities are constants, but not necessarily equal, while viscous effects are neglected. The equations governing a two-dimensional, unsteady, unconfined reacting flow, written in non-dimensional form, are:[4]

$$\nabla^2 \phi = \frac{1}{T} \frac{dT}{dt} \tag{1}$$

$$\frac{d}{dt}(\frac{\omega}{\rho}) = \frac{1}{\rho^3} \nabla\rho \times \nabla p \tag{2}$$

$$\frac{dT}{dt} = \frac{1}{P_e} \nabla^2 T + A_f Q W \tag{3}$$

$$\frac{ds}{dt} = \frac{1}{P_e L_e} \nabla^2 s \pm A_f W \tag{4}$$

where the velocity is $u = (u,v) = \nabla\phi + \nabla\times\psi + u_p$, $d/dt = \partial/\partial t + u.\nabla$, $x = (x,y)$ while x and y are the streamwise and the cross-stream directions respectively, t is time, ϕ is a velocity potential, $\psi = \psi e_z$ is a stream function, where e_z is the unit vector normal to the x-y plane, $u_\omega = \nabla\times\psi = (\partial\psi/\partial y, -\partial\psi/\partial x)$, $\omega e_z = \nabla\times u$ is vorticity, $\nabla^2 \psi = -\omega(x,t)$, u_p is a potential velocity, $\nabla.u_p = 0$, added to satisfy the boundary conditions around the domain, T is temperature, c is concentration per unit mass, ∇ and ∇^2 are the gradient and Laplacian operators, respectively. For the reactant $s = c_R$ and the source term is negative, while for the product s $= c_P$ and the source is positive. $T_a = E_a/(R_g T_1)$, where E_a is the activation energy and R_g is the gas constant, $Q = Q_h/(C_p T_1)$, where $Q_h = C_p(T_f - T_1)$ is the enthalpy of reaction and C_p is the specific heat, $P_e = U_1 \Delta_\omega/\alpha$ is the Peclet number, where $\alpha = k/(\rho C_p)$ is the thermal diffusivity, $A_f = A \Delta_\omega/\Delta U$, where A is the frequency factor of the chemical reaction rate constant, and $L_e = \alpha/D$ is the Lewis number. Note that $\nabla p = -\rho du/dt$. Variables are non-dimensionalized with

respect to the appropriate combination of $\Delta U/2$, $\Delta_\omega/2$, c_{Ro}, and T_1, where $\Delta U = (U_1-U_2)$ and Δ_ω is the vorticity thickness.

III. NUMERICAL METHODS

III.1. THE VORTEX ELEMENT METHOD

In this Lagrangian, grid-free scheme, the vorticity field is discretized among finite elements, Γ_i, that move along particle paths, $\chi_i(t)$, such that: $\omega(x,t) = \Sigma \Gamma_i f_\delta(x-\chi_i(t))$. The vorticity of an element is distributed according to a radially-symmetric core function, f_δ, with a characteristic radius, δ, such that most of the vorticity is concentrated within $r < \delta$, where $r^2 = x^2+y^2$. Vortex elements are distributed over the area where $|\omega| > 0$ such that the distance between neighboring elements is h in the two principal directions. A Gaussian core, $f_\delta(r) = 1/(\pi \delta^2) \exp(-r^2/\delta^2)$, leads to a second-order accuracy, and $\delta/h \sim 1.3$ is sufficient to provide strong overlap between neighboring elements. The equations describing the vortex scheme are:[3]

$$\frac{d\chi_i}{dt} = u(\chi_i(t),t) \tag{5}$$

$$u_\omega(x,t) = -\sum_{i=1}^{N} \Gamma_i \frac{(y, -x)}{r^2} \kappa(\frac{r}{\delta}) \tag{6}$$

where $\chi_i(0)=x_i$, and $\kappa(r) = {}_0\int^r r'f_\delta(r')dr'$.

Vortex elements move at the local velocity at their centers. As time progresses, the distance between neighboring elements increases in the direction of maximum strain rate such that $\Delta\chi > h$, where $\Delta\chi$ is the distance in the direction of maximum strain defined as $\Delta\chi = (\Delta u.\Delta\chi)/|\Delta u|$ and Δ is the difference operator between neighboring elements. This leads to a deterioration of the discretization accuracy since accurate discretization requires that $\delta > \Delta\chi$.

Thus, an algorithm must be used such that when $\Delta\chi > h_{max}$, where $h_{max}/h \sim 1.5$, a computational element is inserted at the midpoint between the original elements. The circulation of the new element, and that of the original two neighboring elements, is one third the sum of the circulations of the original two elements.

III.2. THE TRANSPORT ELEMENT METHOD

In this scheme, the gradient of the scalar field is discretized into a a number of finite elements: $g(x,t) = \Sigma \; \Delta g_i(t) \; f_\delta(x-\chi_i(t))$, where $g = \nabla s$ Like vortex elements, transport elements are distributed where $|g| > 0$ and are moved with the local velocity field. Scalar gradients are not conserved along particle path, and should be modified according to the local straining and tilting of the material elements. Moreover, the evolution of the chemical reaction changes the local concentration of the interacting species. The following equations describe the transport element scheme:[4]

$$s(x,t) = \sum_{i=1}^{N} \delta s_i(t) \; \delta l_i(t) \; n_i(t) . \nabla G_\delta(x-\chi_i(t)) \tag{7}$$

$$\delta^2 = \delta_o^2 + 4 \; \alpha \; t \tag{8}$$

$$\frac{d}{dt} \; \delta s_i = \sum_{j=1}^{k+1} D_s \; \frac{dw}{ds_j}(s_j) \; \delta s_j \tag{9}$$

where δ_o is the core radius at $t = 0$, and $\nabla G_\delta = (x,y)/r^2 \; \kappa(r/\delta)$. $D_s = \pm A_f$ for c_P and c_R, respectively, while $D_s = A_f \; Q$ for T. δl_i is updated according to $\delta l_i(t) = (\chi_{i+1}(t)-\chi_{i-1}(t))/2$, while $n.\delta l = 0$. If the distance between neighboring elements in the direction of principal strains exceeds a maximum distance, h_{max}, an element is inserted half-way between the two elements and the values of δl_i and h_i are redistributed among the three elements. Elements are combined at areas of compression to curb the growth of their number.

When $\nabla\rho \times \nabla p \neq 0$, the circulation of each vortex element must be updated each time step. Since $\Gamma = \Sigma \ \Gamma_i \kappa(x-\chi_i)$ and, and $\nabla\rho/\rho = - \nabla T/T$, then:

$$\frac{d\Gamma_i}{dt} = \frac{\Delta T_i}{T_i} \times (\frac{du}{dt})_i \qquad (10)$$

$(du/dt)_i$ is computed by numerically differentiating the velocity of the vortex element using a high-order formula. The velocity field produced by volumetric expansion due to heat release is described by the solution of Eq. (1). Written in terms of Lagrangian transport elements, this expansion velocity is:

$$\nabla\phi(x,t) = \sum_{i=1}^{N} \frac{1}{T_i} (\frac{dT}{dt})_i \ h_i^2(t) \ \nabla G_\delta(x-\chi_i(t)) \qquad (11)$$

where h_i^2 is the area associated with the transport element i. For detailed derivation and validation of the transport element method, see [4] and [13].

IV. RESULTS

IV.1. THE GAS DYNAMIC FIELD

Results were obtained for following parameters: A_f = 0.5, T_a= 6.0, P_e= 1000, L_e= 1.0 and Q = 2.0. The choice of the physical parameters that describe the combustion process was limited to cases for which the computer-time and memory requirements could be met economically. Results will be used to study the modes, and outcome of the interaction between the fluid flow and the combustion process.

Figure 1 depicts the vortex elements and their velocity vectors for the non-reacting eddy (NR) and the reacting eddy (R) at t = 10, 15 and 17.5. In both cases, the initial perturbation is a sinewave with an amplitude ε = 0.05 λ, where λ = 6.6 Δ_ω is the wavelength. The initial vorticity thickness corresponds to the most unstable mode of the layer, while the flame thickness is that of a

steady-state laminar flame as defined by the diffusion and chemical parameters of the problem. Results show that the growth of the eddy can be divided into three stages: (1) in the first stage, t < 5, the increase in the length of a typical material layer and the entrainment is small; (2) in the second stage, 5 < t < 15, an eddy, which corresponds to a concentration of vorticity, forms and grows by entraining fluid from both side into its core leading to the stretching of the material lines; and (3) in the third stage, t > 15, entrainment ceases and the eddy collapses, or flattens in the streamwise direction.

Compared with the non-reacting eddy, the reacting eddy expands due to heat release, it moves in the direction of the reactant stream, it exhibits a definite asymmetry, and it starts collapsing at later times. The expansion of the eddy due to heat release occurs primarily in the second stage and within the core, indicating that most of the burning occurs during this stage and inside the eddy core. It is also observed that the reaction prolongs the growth phase, ending at t = 15 in the reacting eddy vs. t = 12 in the non-reacting eddy, and delays the start of the flattening phase suggesting that volumetric entrainment is larger in the reacting eddy. The delayed collapse of of the reacting eddy explains why the angle between the major axis of the eddy and the reactant stream, assuming that the eddy can be represented by an ellipse, is smaller for the non-reacting than for the reacting eddy. This phenomenon was first observed experimentally.[2]

Figure 1 shows that in the reacting eddy, volumetric entrainment is strongly asymmetric with a bias towards the hot fluid. The gulf of hot fluid reaches deeper into the eddy than the gulf of cold fluid. Moreover, they reach deeper/shallower, respectively, than their counterparts in the non-reacting, uniform-density case. To confirm this observation, we plot the temperature contours for NR and for R, at t = 10, 15 and 17.5, in Fig. 2. The plots

indicate that, while the penetration from both sides is symmetric in the non-reacting eddy, more hot fluid than cold fluid has reached into the core of the reacting eddy. Asymmetric entrainment has experimentally been observed in density-stratified flows.[14] It should be noted that the maximum reaction rate occurs at T = 2.19 , decaying to 20 % of the maximum value at T = 1.15 and 2.92 respectively.

Figure 2 indicates that during the growth stage, 5 < t < 15, the flame thickness, with respect to its value at t = 0, is thinner at the braids, the side arms of the eddy, and is thicker in the core. The first is due to the strong strain and the second is due to the enhanced entrainment, both associated with the formation of a coherent vortex core. Flame thinning due to the strain along the braids is moderate since the reduction of the flame thickness due to the strain field is balanced by the increase in the flame thickness due to the enhanced diffusion fluxes. Flame thickening is due to negative strain in the vicinity of the center of the core and the strong entrainment currents which accompany the roll-up.

IV.2. THE BURNING RATE

The total mass of products, M_p, formed since t = 0 is shown in Fig. 3. The total flame length, L_f, approximated by the line of maximum reaction rate, is depicted on the same plot. As a reference case, we also plot the total mass of products formed due to the propagation of a laminar flame, of constant length λ, which has the same initial conditions. For t < 4, the rate of product formation, $\dot{M}_p = dM_p/dt$, is the same as that of a laminar flame and L_f is constant. Within the growth range, and as L_f stretches due to roll-up, $\dot{M}_p$ increases. It is important to point out that the L_f-curve is used only to characterize the stages of growth of the eddy and not to define a unique relationship between $\dot{M}_p$ and L_f. The flame under investigation is a "thick"

flame in which the flame thickness is of the same order of magnitude as the flow gradients, and it is the area of the reaction zone (or its volume in a three-dimensional sense) that determines the total rate of burning.

The rise in the burning rate during the second stage is due to the swelling of the reaction zone within the core region and the formation of a flame fold, or a gulf of reactant that penetrates into the burning core. Within this stage, there is a burning core at the center of the eddy, formed by the entrainment of reactants at the early stages of roll-up, surrounded by one flame zone on the reactant side and two flame zones on the product side. The two flame zones on the product side approach each other, trapping a gulf of reactants in between. Figure 3 shows that, in the range of $5 < t < 10$, $\dot{M}_p$ exhibits a similar increase as in L_f, indicating that the average burning rate per unit flame length, S_{ua}, remains constant. Therefore, within this stage, the total rate of burning can be approximated by the product of the laminar burning velocity of the unstrained flame times the flame length measured along the line of maximum reaction rate, $\dot{M}_p = S_{ua} L_f$. A wrinkled laminar flame model may, thus, be used to approximate the rate of product formation during this stage.

IV.3. THE EFFECT OF STRAIN

Beyond $t = 10$, Fig. 3 shows that $\dot{M}_p$ stays approximately constant while the apparent flame length, measured along the line of maximum reaction rate, L_f, continues to rise. In this stage, the major portion of the flame exists on the outer boundaries of the eddy and is exposed to a strong strain field. Comparison between streamline plots and the temperature contours, the latter is depicted in Fig. 2, reveals that for $t > 10$, the flame is almost aligned with the streamlines and that its thickness is smaller than its value at $t = 0$. Moreover, due to the geometrical convolution of the streamlines and the

formation of cusps and islands, its difficult to rigorously define a flame length, or to associate the flame length with the line of maximum reaction rate. The temperature contours indicate that although the line of maximum reaction rate is increasing, the area of the reaction zone, or the "thick" flame, may not be increasing.

Without any extra entrainment of reactants, the flame becomes strained along the boundaries of the eddy. The reason for the reduction of the flame thickness is the presence of a strong strain along the flame front. This is illustrated by Fig. 4, where the strain rate in the direction of the local streamlines is plotted for t = 10, 15 and 17.5. The figure indicates that, while during the growth stage, 5 < t < 10, most of the burning zone lies on areas of negative strain, at the later stages, t > 10, most of the burning zone coincides with areas of strong positive strain. Clearly, within this range, neither the line of maximum reaction rate is representative of a flame length, nor the laminar burning velocity is the same as the value for the unstrained flame since the flame thickness has been reduced (see [15,16] for an illuminating discussion on the effect of strain on the burning velocity). Thus, a simple wrinkled laminar flame model may not be able to accurately describe the combustion in this stage.

IV.3.BAROCLINIC GENERATION OF VORTICITY

The asymmetric growth of the reacting eddy is accompanied by its displacement in the direction of the reactant stream and the asymmetric volumetric entrainment of more hot fluid than cold fluid. Close inspection reveals that the reacting eddy and the uniform-density, non-reacting eddy are dynamically distinct in two ways: the volumetric expansion associated with heat release which produces an irrotational velocity field expressed by Eq. (1); and the presence of a stratified-density field which generates vorticity at a rate

governed by Eq. (2). It is of interest to isolate the consequences of the two effects.

For this purpose, numerical experiments were conducted for a reacting shear layer in which the baroclinic term in Eq. (2) was set to zero, i.e. $d(\omega/\rho)/dt = 0$. In this case, the developing eddy was perfectly symmetric around its center and the eddy remained at the center of the domain; hence it was concluded that the volumetric expansion cannot produce the action observed in Figs. 1 and 2. On the other hand, numerical experiments were performed for a density-stratified, non-reacting shear layer, i.e. $\nabla\phi = 0$ and $A_f = 0$. In this case, the developing eddy strongly resembled the reacting eddy in Figs. 1b and 2b (volumetric expansion in the reacting case slightly weakens the vorticity by increasing the area of the eddy core). This confirmed the hypothesis that baroclinic vorticity generation represents the most important dynamic role of combustion in this field.

As seen from Eq. (2), fluid elements accelerating in a density gradient generate vorticity whose sign depends on the orientation of $\nabla\rho$ with respect to (du/dt). In the flow field we are investigating, the density gradient is initially positive and the initial vorticity is negative (clockwise). If the wavelength is divided into four quarters, then negative vorticity is produced along the second and third quarters since the acceleration is negative, and positive vorticity is produced along the first and fourth quarters since the acceleration is positive. This is shown in Fig. 6 which depicts the vorticity contours for the uniform-density NR and for R at t = 10, 15 and 17.5. The plots show that the extra negative vorticity gets entrained into the core of the eddy, strengthening the "primary" eddy, while the positive vorticity generated on the reactant side forms a secondary eddy. A stronger primary eddy entrains more fluid, as indicated before. The secondary eddy produces a velocity field which

propels the primary eddy in the direction of the reactant stream, as seen in Fig. 1. The positive secondary eddy on the reactant side reduces the entrainment velocities into the primary eddy from this side, resulting in less volumetric entrainment of the reactants than that of the products.

Thus, we have been able to correlate the two actions, the motion of the primary eddy in the direction of the reactant stream and the asymmetric entrainment, with the formation of a positive secondary eddy due to the baroclinic vorticity generation. Both effects were observed experimentally in a density-stratified flow.[14] The numerical prediction of the convective velocity of the primary eddy agrees well with the values measured experimentally.[13] The close agreement proves that baroclinic vorticity generation is indeed responsible for this asymmetric dynamics, and validates the numerical results.

V. CONCLUSIONS

Numerical simulation, using the vortex and transport element methods, has been used to study the interactions between the flow field and the combustion process in a premixed shear layer. Results are obtained at conditions for which the flame thickness and the flow gradients are of the same order of magnitude and are analyzed to identify the interplay between the flame structure and the flow fields. Major conclusions are:

1. Entrainment associated with the roll-up and the formation of an eddy leads to the swelling of the core and the establishment of a thick reaction zone during the growth period of the eddy. This enhances the rate of burning by the ratio of the instantaneous length of the line of maximum reaction rate to the unperturbed length of the material layer.

2. At later times, a major portion of the reaction zone exists on the boundary of the core where the strain is positive. The convolution of the streamlines

obscures the definition of the flame length, and the thinning of the reaction zone locally reduces the laminar burning velocity below the unstrained value.

3. The wrinkled flame model, which states that $\dot{M}_p = S_u\, L_f$, can be used to approximate the burning rate during the initial growth phase of the eddy provided that L_f is measured along the line of maximum reaction rate. During the later stages, however, S_{ua} is found to decrease if L_f is defined as before.

4. Baroclinic vorticity generation, associated with the interaction between the hydrodynamic pressure gradient and density field, contributes strongly to the dynamics of the shear layer. Stronger entrainment and entrainment asymmetry have been attributed to the formation of vorticity of the same sign as the original vorticity within the core, and vorticity of the opposite sign along the boundary between the eddy and the reactants, respectively. Since entrainment plays an important role in determining the rate of burning, baroclinicity must also affect the rate of burning during roll-up.

REFERENCES

1. Williams, F.A., United States-France Joint Workshop on Turbulent Reactive Flows, Proceedings: Volume III, July 6-10, 1987, Rouen, France, 1:1-57.

2. Keller, J. and Daily, J.W., AIAA Journal, 23, pp. 1937-1945 (1985).

3. Ghoniem, A.F., Heidarinejad, G., Krishnan, A., J. Comput. Phys., to appear (1988).

4. Ghoniem, A.F., Heidarinejad, G., Krishnan, A., AIAA/SAE/ASME/ASEE Joint Propulsion Conference, San Diego, CA, July 1987, AIAA-87-1718, also the United States-France Joint Workshop on Turbulent Reactive Flows, Proceedings: Volume III, July 6-10, 1987, Rouen, France, 10:1-41.

5. Riley, J.J., Metcalfe, R.W. and Orszag, S.A., Phys. Fluids, 29, pp. 406-422 (1986).

6. McMurtry, P.A, Jou, W.H., Riley, J.J. and Metcalfe, R.W., AIAA Journal, 24, pp. 962-970 (1986).

7. Givi, P., Jou, W.H., and Metcalfe, R.W., Proceedings of the 21st Symposium (International) on Combustion, the Combustion Institute, Pittsburg, PA. (1987).

8. Ghoniem, A.F., Combust. Flame, 64, pp. 321-336 (1986).

9. Ghoniem, A.F., Chorin, A.J. and Oppenheim, A.K., Phil. Trans. R. Soc. Lond, A304, pp. 303-325 (1982).

10. Ghoniem, A.F. and Knio, O.M., Proceedings of the 21st Symposium (International) on Combustion, the Combustion Institute, Pittsburg, PA. (1987).

11. Pindera, M.Z. and Talbot, L., Proceedings of the 21st Symposium (International) on Combustion, the Combustion Institute, Pittsburg, PA. (1987).

12. Clavin, P., Prog. Energy Combust. Sci., 11, pp. 1-59 (1985).

13. Ghoniem, A.F., Heidarinejad, G., Krishnan, A., AIAA 26th Aerospace Sciences Meeting, January 11-14, 1988/Reno, NV, AIAA-88-0729.

14. Dimotakis, P., AIAA Journal, 24, pp. 1791-1796 (1986).

15. Libby, P.A. and Williams, F.A., Combust. Flame, 44, pp. 287-303 (1982).

16. Darabiha, N., Candel, S.M. and Marble, F.E., Combust. Flame, 64, pp. 203-216 (1986).

FIGURE CAPTION

Figure 1. Vortex elements and their velocity vectors for: (a) the non-reacting eddy; and (b) the reacting eddy at t = 10, 15 and 17.5 .

Figure 2. Temperature contours for (a) the non-reacting eddy; and (b) the reacting eddy at t = 10, 15 and 17.5. Minimum temperature, top contour, is 1 and maximum temperature, bottom contour, is 3, while increment between two neighboring contours is 0.133.

Figure 3. Total product formation in: a reacting shear layer; and a laminar flame at the same conditions. Shown also is the apparent flame length in the reacting eddy (L_F).

Figure 4. Contours of the strain rate in the direction of streamlines for the reacting eddy at t = 10, 15 and 17.5. Increment between neighboring contours is 0.05.

Figure 5. Vorticity contours for: (a) a non-reacting shear layer; and (b) a reacting shear layer at t = 10, 15 and 17.5. Solid lines indicate negative vorticity and broken lines are for positive vorticity. Increment between two neighboring contours is 0.06 for (a) and 0.12 for (b).
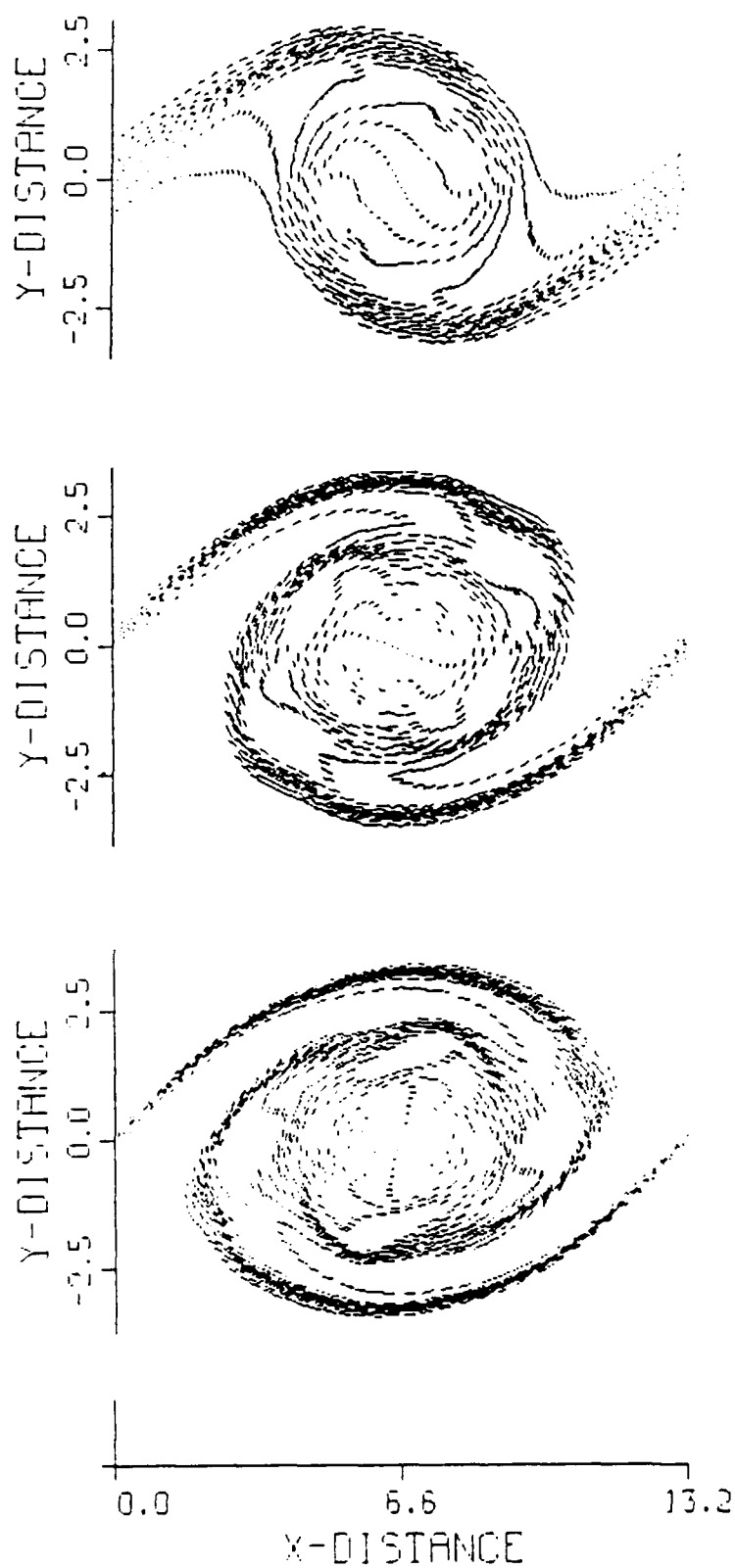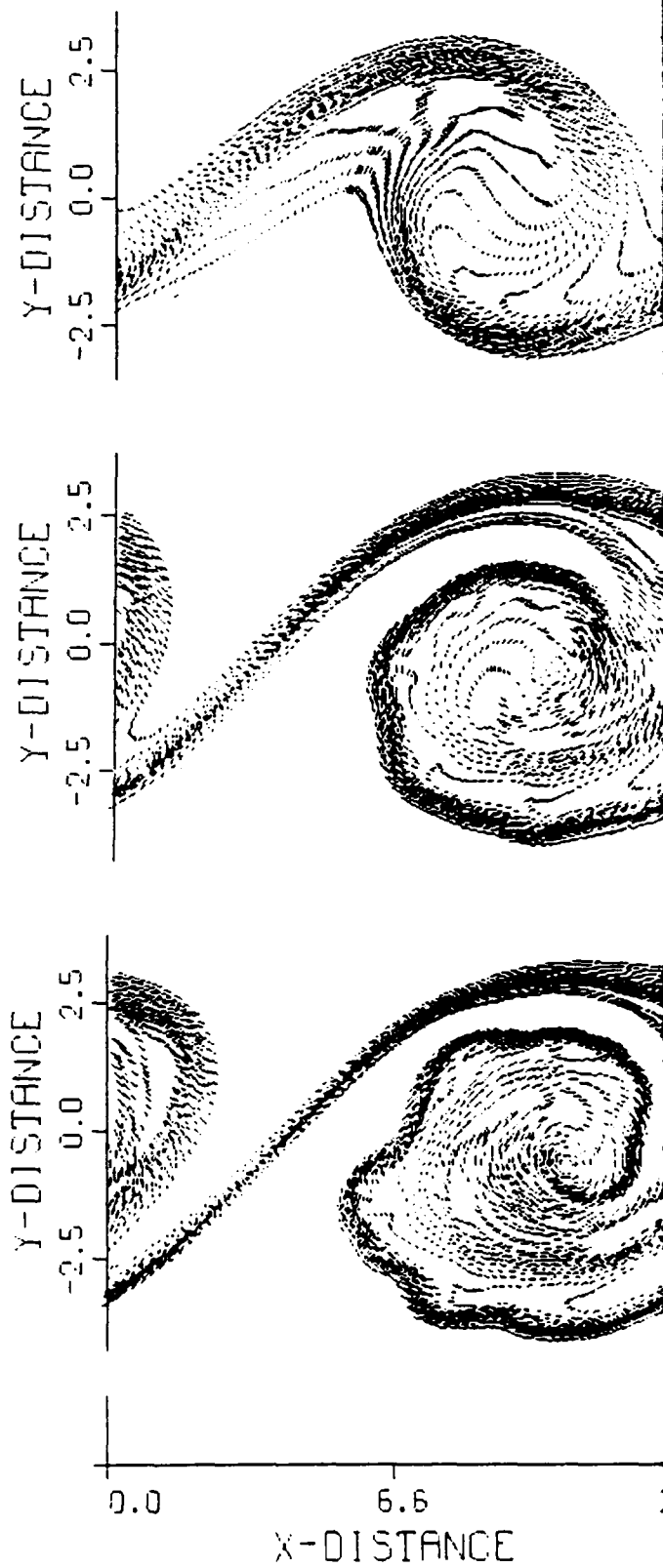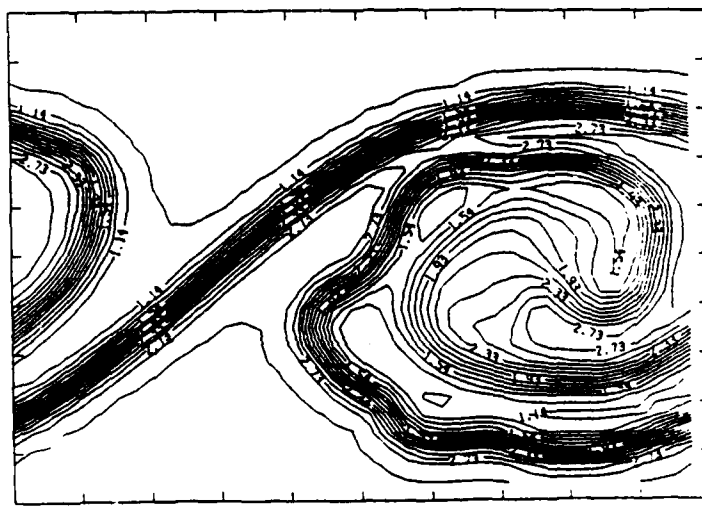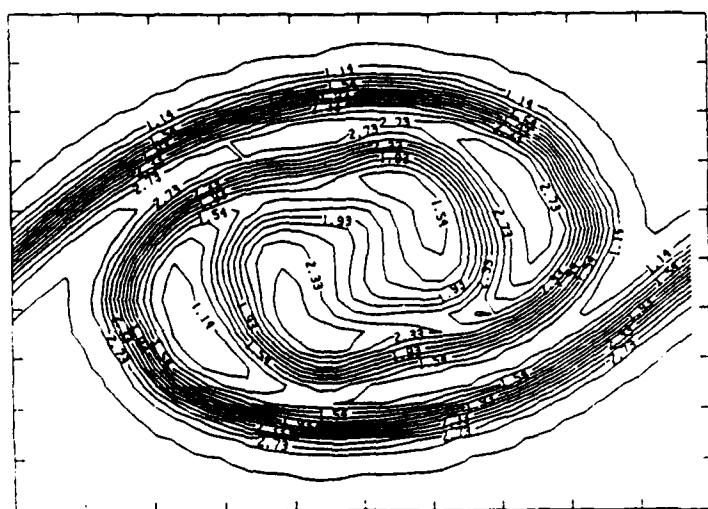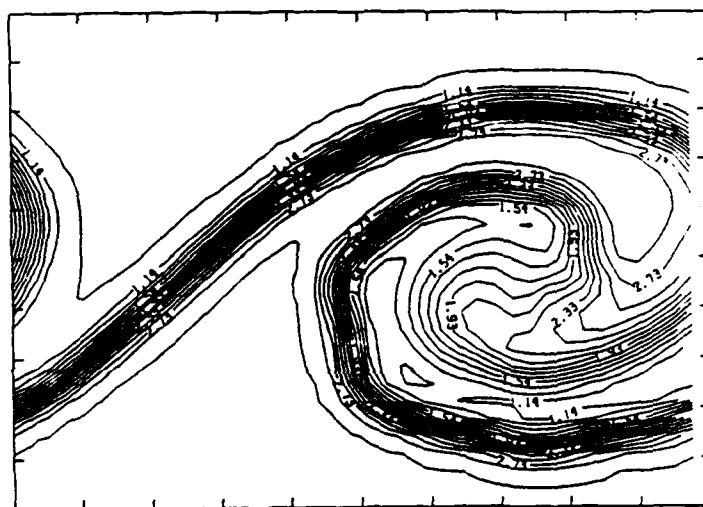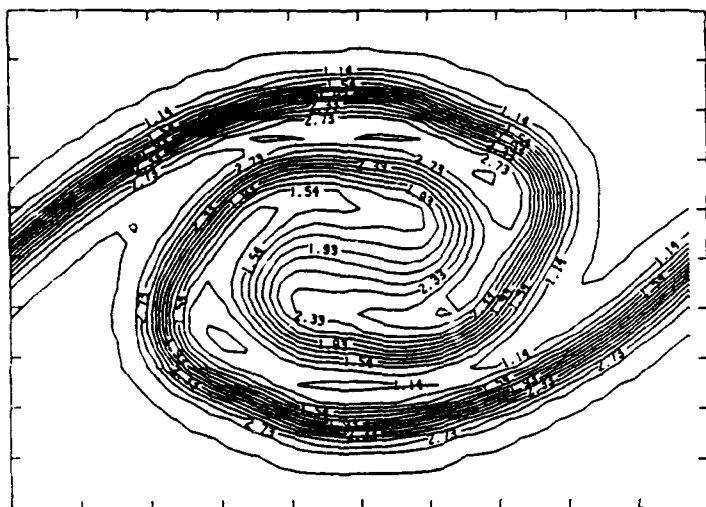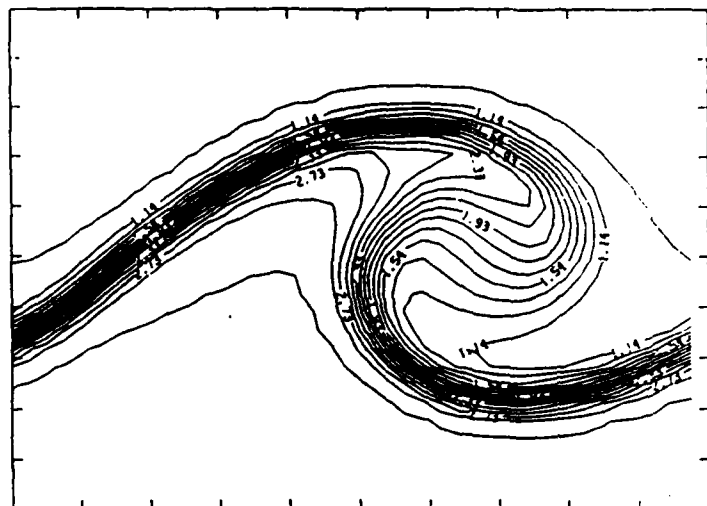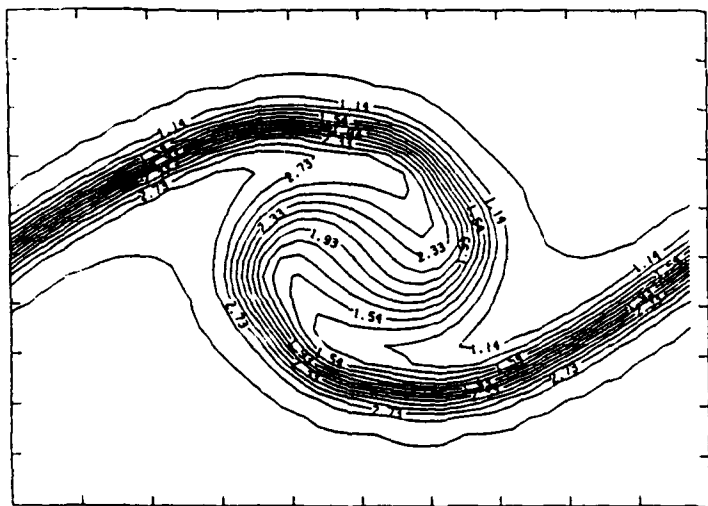
Figure 1.

Fig. 2
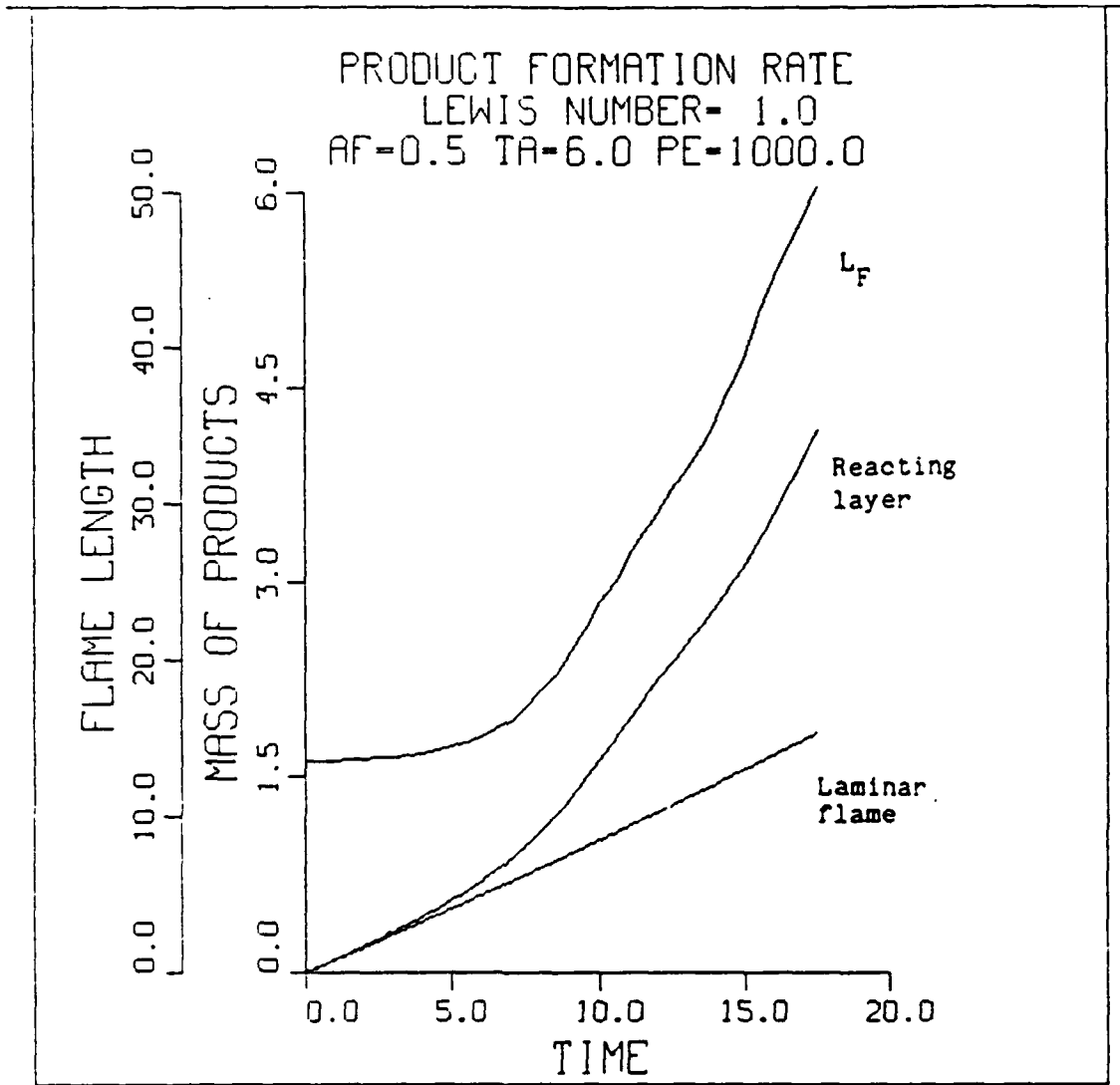
Figure 3.
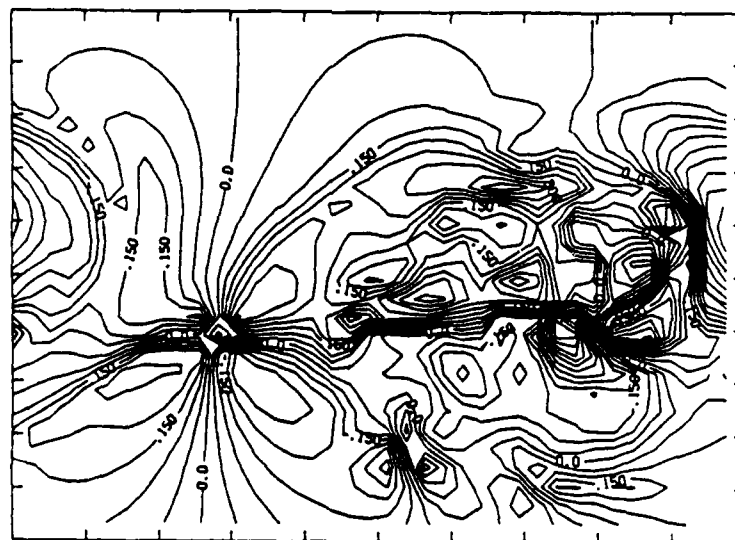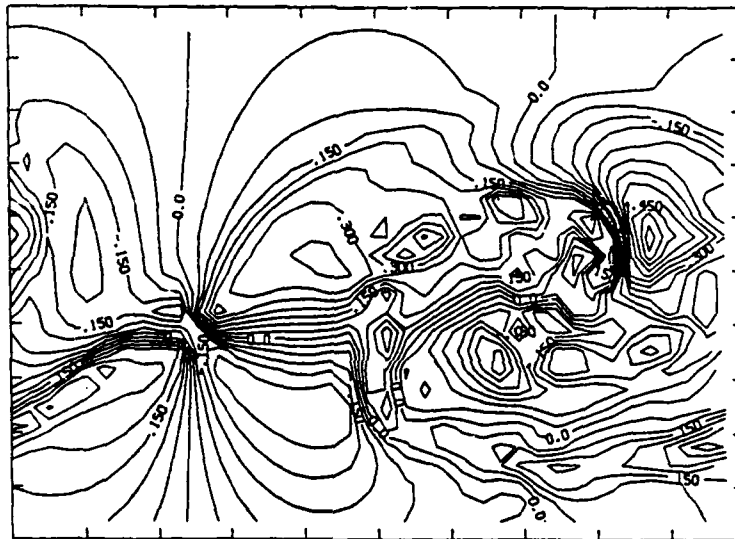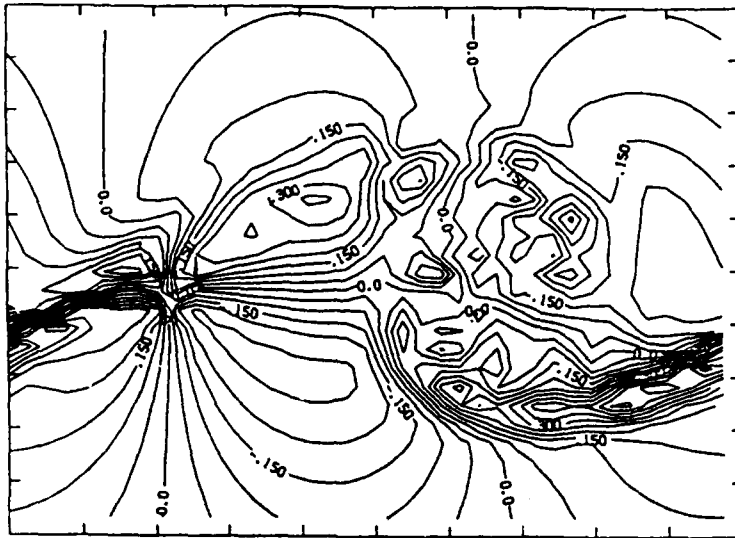
Fig _e 4.
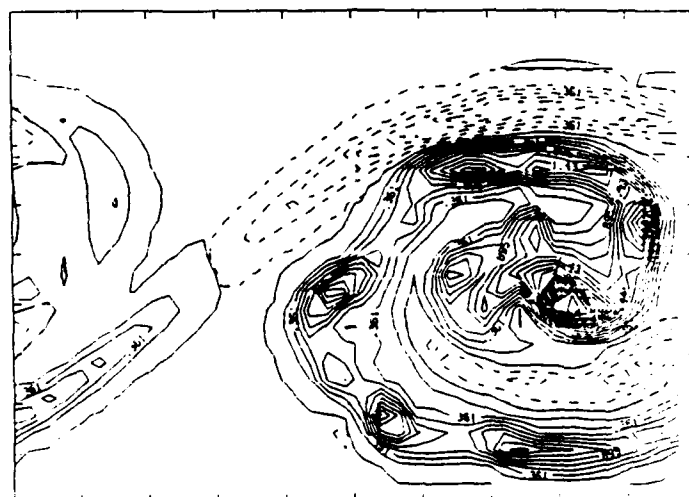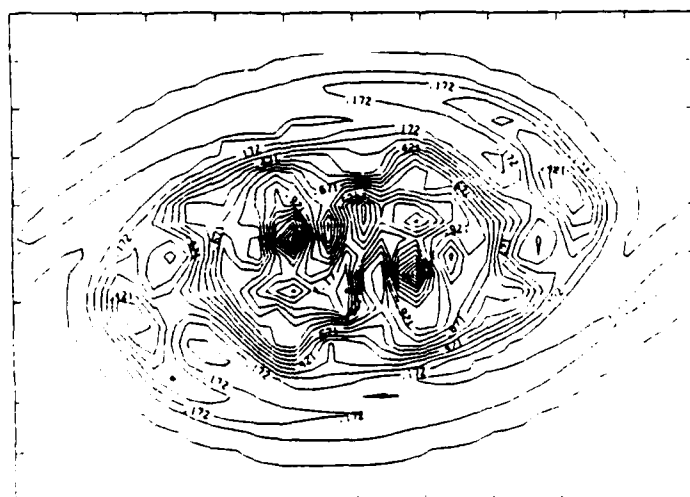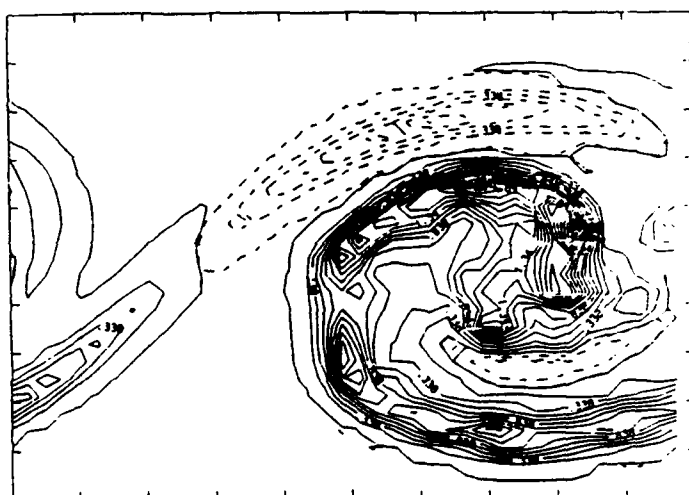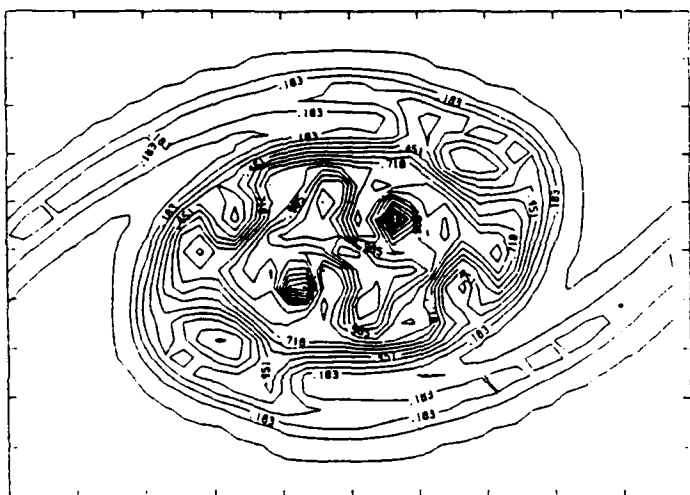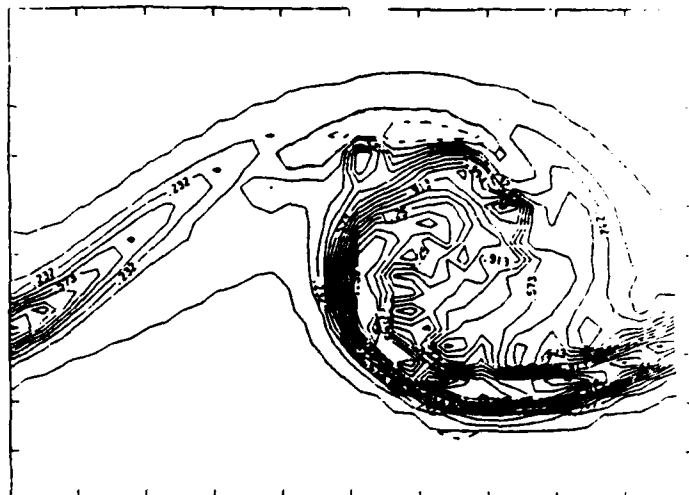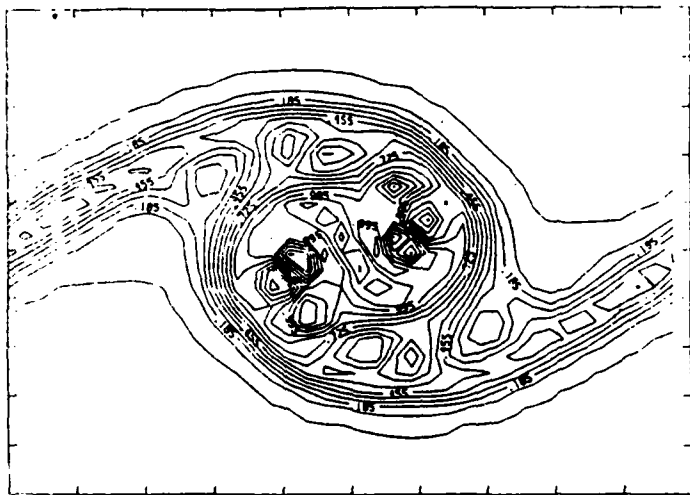
Fig. 5

AIAA-88-0728
On the Formation of Streamwise Vorticity in Turbulent Shear Flows

Omar M. Knio and Ahmed F. Ghoniem
Massachusetts Institute of Technology
Cambridge, MA 02139

AIAA 26th Aerospace Sciences Meeting
January 11-14, 1988/Reno, Nevada

ON THE FORMATION OF STREAMWISE VORTICITY IN TURBULENT SHEAR FLOWS

Omar M. Knio[1] and Ahmed F. Ghoniem[2]
Department of Mechanical Engineering
Massachusetts Institute of Technology
Cambridge, MA 02139

ABSTRACT

The formation of streamwise vorticity is a precursor to self-turbulization and mixing transition in shear flows. In this work, three-dimensional numerical simulation is used to study the formation of streamwise vorticity in turbulent flows which can be characterized by well-defined initial concentrations of vorticity. Two examples are analyzed: an isolated finite-core vortex ring perturbed in the azimuthal direction, and a periodic shear layer simultaneously perturbed in its streamwise and spanwise directions. The numerical scheme is based on the accurate discretization of the vorticity field into a number of finite-core, spherical vortex elements, and the transport of these elements along particle paths. Results show the innate tendency of vorticity, initially aligned in the direction normal to the stream, to form coherent streamwise structures which have alternating vorticity signs in the spanwise direction. The formation of streamwise vorticity follows the "maturation" of the spanwise structure and the evolution of the former is energized by the strain field of the latter. While the streamwise vorticity is responsible for the added "turbulization" of the flow, leading to further mixing enhancement, it does not seem to lead to the disintegration of the two-dimensional structures.

I. INTRODUCTION

Experimental studies of turbulent free shear flows, including shear layers, jets and isolated vortex rings, in non-reacting and reacting flows, have revealed the presence of structures which form as a result of perturbing the initial flow (e.g., for planar shear layers: Roshko [1], Breidenthal [2], Bernal and Roshko [3]; for jets: Crow and Champagne [4], Yule [5] and Roquemore et al. [6]; and for vortex rings: Maxworthy [7]). Elaborate linear stability analyses have been applied to investigate the various modes that contribute to the formation of these structures and their fundamental origin (e.g., Michalke and Hermann [8], Pierrehumbert and Widnall [9], and Widnall and Tsai [10]). Numerical analysis, as applied to model problems, has been used to simulate the non-linear stages of development of these instabilities, and to quantify their state

as they reach "quasi-equilibrium" with the flow (e.g., Corcos and Sherman [11], and Lin and Corcos [12] and Ghoniem et al. [13]).

In shear flows, two types of structures, depending on the orientation of the vorticity with respect to the main flow, have been identified: spanwise (radial in axisymmetric flows) structures and streamwise structures. The former, which most often precedes the latter, has been extensively investigated using the three methods of analysis. It arises as a result of the Kelvin-Helmholtz instability of shear layers and grows to form spanwise coherent structures. These "fundamental" structures pair to form larger structures as they are perturbed by the "subharmonic modes" (Ho and Huerre [14].) Vortex rings issuing at the latter stages of evolution of an axisymmetric jet, are examples of these structures. The streamwise, or secondary structures, arise as the spanwise (azimuthal) perturbation of the two-dimensional flow grows. Analyses of these structures have been elaborated by, e.g., Pierrehumbert and Widnall [9] and Corcos and Lin [15].

Three-dimensional numerical simulations of planar turbulent shear layers have been reported. Couet and Leonard [16], using a vortex-in-cell method, computed the initial stages of development of a temporally-developing shear layer. Riley and Metcalf [17,18], applying a pseudo-spectral method, produced similar results. Ashurst and Meiburg [19], utilizing the vortex filament method of Leonard [20,21], computed the growth of perturbations on a temporally-developing shear layer using one or two rows of vortex elements to represent the vorticity layer. Lowery et al. [22], using a hybrid spectral-finite difference method, extended the calculations to a spatially-growing shear layer. Inoue [23], applying the vortex filament method, reported results for a confined spatially-growing shear layer which starts with a single row of vortex elements.

Results of these calculations have been instrumental in disecting the interesting physics of turbulent shear layers. However, when using grid-based methods [17,18,22] the Reynolds number must be kept at small values, and diffusion is expected to play an important role in determining the strength and dynamics of the growing streamwise vortices. In Lagrangian schemes [19,23], more elements should be used in the cross-stream direction to discretize the initial vorticity accurately. Moreover, the developing strain field, both normal to and in the direction of the vortex lines, extends the distance between neighboring vortex elements, which may deteriorate the long-time accuracy of the scheme (Ghoniem et al. [24].) Thus, more work is needed to improve the accuracy and robustness of these schemes if they are to be used in analyzing the late stages of development of high-Reynolds-number flow fields that develop strong strains and sharp gradients.

---

[1] Graduate student.
[2] Associate professor, associate fellow, AIAA.

In this work, we apply the vortex element method described in Ghoniem et al. [13] to study the stability and formation of streamwise vortices in free shear flows. The method is based on the accurate discretization of the vorticity field in spherically-symmetric vortex vector elements whose cores are large enough to provide strong overlap among neighboring elements. The motion of the elements is followed in a Lagrangian frame of reference. The vortex vector elements change their vorticity according to the local stretch, while their direction is determined by the tilting of the material lines. The velocity is computed as the summation over the fields of the vortex elements, which are evaluated from the integral of the Biot-Savart law over individual vorticity cores. Substantial overlap is maintained by the proper selection of the core radius of the vortex elements, and by increasing the number of vortex elements to capture the small scales which develop due to the strain field.

In our previous article [13], the method was applied to study the instability of a thin-tube model and a torus model of a vortex ring. The results of both models were used to validate the scheme and check on its accuracy. The proper strategy of initializing the strength of the vortex elements and of selecting the numerical parameters to maintain the accuracy for long time was also described. In this work, the vortex element method is used to study the evolution of streamwise vorticity generated as a consequence of the linear instability of a vortex ring, and of a planar periodic shear layer. We direct our attention towards the processes which energize and promote the growth of the streamwise vorticity in both fields.

In Section II, summaries of the physical model and of the numerical scheme are presented. In Section III, results on the early and late stages of instability of the field of a vortex ring are discussed. In Section IV, similar results are obtained and analyzed for the periodic shear layer. In both cases, we concentrate on the formation of streamwise vorticity and investigate its dynamical properties. In Section V, we discuss major conclusions.

II. FORMULATION AND NUMERICAL SCHEME

The problem is formulated in terms of the three-dimensional, unsteady, incompressible, inviscid equations of motion. To use a numerical vortex method, we resort to the vorticity transport form of the equations:

$$\frac{\partial \omega}{\partial t} + u \cdot \nabla \omega = \omega \cdot \nabla u \tag{1}$$

$$u = u_\omega + u_p \tag{2}$$

$$u_\omega = -\frac{1}{4\pi} \int \frac{(x-x') \times \omega'(x')}{|x-x'|^3} dx' \tag{3}$$

where $u = (u,v,w)$ is the velocity in the $x = (x,y,z)$ directions, t is time, $\omega = \nabla \times u$ is the vorticity vector, $\omega = (\omega_x, \omega_y, \omega_z)$, and ∇ is the gradient operator. Equation (1) describes the transport of vorticity along particle path and its concomitant stretch along its own direction by the action of the strain field. Equation (2)

expresses the decomposition of the velocity into a solenoidal and an irrotational component. The first component, u_ω, is obtained from the Biot-Savart integral, Eq. (3), if the vorticity field is known. The second component, u_p, is added to satisfy the potential boundary condition, i.e. if $u_p = \nabla \phi$ then $\nabla^2 \phi = 0$ and $(\nabla \phi + u_\omega) \cdot n_b = U_b$, where n_b is the unit vector normal to the boundary and U_b is the velocity normal to the boundary.

The numerical solution starts by discretizing the initial vorticity field, $\omega(X,0)$, on a grid, which may be non uniform, of sides (h_x, h_y, h_z). At the corners of the grid, vortex elements of finite spherical cores are placed. Each vortex element is characterized by a core radius, δ, a core function, $f_\delta(r) = 1/\delta^3 f(r/\delta)$ where $r = |x-x'|$, a circulation, Γ_i, and a material vector element that describes how the vorticity is distributed along the axis of the element, $\Delta \ell_i$. The core function and core radius are the same for all elements, and are invariant with time. The choice of the f_δ and δ/h_{max} is important for the accurate discretization of the vorticity field, and for preserving the long time accuracy of the computations. Similar schemes were used by Chorin [25,26,27] to study boundary layer transition and the evolution and properties of turbulence, by Mosher [28] to study the interaction between vortex rings and by Shirayama et al. [29] to compute the flow around aerodynamic bodies. For analysis of three-dimensional vortex schemes, see Beale and Majda [30,31,32], Greengard [33], Anderson and Greengard [34], and Beale [35].

From Kelvin's theorem, the circulation of an element is constant as it moves along a particle path. Moreover, from Helmholtz theorem, vorticity changes with the stretch of the material element $\Delta \ell_i(t)$. Thus, the equations governing the discretized vorticity field can be written as:

$$\omega(x,t) = \sum_{i=1}^{N} \Gamma_i \, \Delta \ell_i(t) \, f_\delta(x-\chi_i) \tag{4}$$

$$u_\omega = -\frac{1}{4\pi} \sum_{i=1}^{N} \Gamma_i \frac{(x-\chi_i) \times \Delta \ell_i}{|x-\chi_i|^3} \kappa\left(\frac{|x-\chi_i|}{\delta}\right) \tag{5}$$

$$\chi_i(t+\Delta t) = \chi_i(t) + \Sigma_{\Delta t} u_i \, \Delta t \tag{6}$$

$$\Delta \ell_i(t+\Delta t) = \Delta \ell_i(t) + \Sigma_{\Delta t} \Delta \ell_i(t) \cdot \nabla u_i \, \Delta t \tag{7}$$

where $\chi_i(0) = X_i$, X_i is the Lagrangian coordinate of a vortex element and χ_i is the particle path. The $\Sigma_{\Delta t}$ in Eqs. (6) and (7) indicates a numerical, single-step integration formula, and $\kappa(r) = 4\pi \int_0^r f(r')r'^2 dr'$. The value of $\Delta \ell_i \cdot \nabla u_i$ in Eq. (7) is computed by numerically differentiating the velocity field along the vorticity vector.

As the flow develops strong strain along the vortex lines, the local vorticity intensifies and $|\Delta \ell_i| > h_{max}$. To maintain the resolution of the computations, elements experiencing severe stretch

must be split into two in the local direction of the vorticity. For more detail on the vortex element scheme, see Ghoniem et al. [13].

For the isolated vortex ring calculations, u_p = 0. For the calculation of the periodic shear layer, periodicity is assumed in the streamwise and spanwise directions. The velocity field produced by a periodic vorticity field can be computed using a summation over an infinite series in two indices. Since the contribution of a vortex element to the velocity field decays at a rate of $|x-\chi_i|^{-2}$, a cut-off radius can be used to set a limit on the number of terms used from the series. Taking advantage of the smoothness of the solution of $\nabla^2\phi$ = 0 within the computational domain, more saving can be achieved by computing the contribution of the series on a grid. The solution at an arbitrary location can then be found by interpolation.

III. RESULTS: ISOLATED VORTEX RING

III.1. INSTABILITY OF A VORTEX RING

The first flow field which we use to study the mechanism of formation and the evolution of streamwise vorticity is that of an isolated vortex ring. The radius of the ring, where the vorticity reaches a maximum, is R, the core radius is σ (σ can be chosen as a nominal radius where the vorticity reaches a well-defined fraction of its maximum), and the circulation of the ring is Γ. The vorticity of the ring is represented by several vortex elements whose cores, δ, are smaller than that of the ring, $\delta < \sigma$. The vortex ring is thus modeled by a number of elementary, overlapping vortex rings arranged within its core. The motion of the vortex elements throughout the cross section of the ring allows substantial deformation of its core at different radial stations. Therefore, higher-order radial modes associated with the instability of vortex rings are expected to be properly captured.

The vorticity of the ring, initially in the azimuthal direction, $\omega_\theta(\mathbf{X},0)$, is discretized among the vortex elements by solving a linear system of equations formed by the application of Eq. (4) to a three-dimensional radial mesh covering the ring core. In this case, it is more convenient to use cylindrical coordinates (ρ,θ,z) where ρ is the radial direction measured from the center of the ring, θ is the azimuthal direction and z is the direction of propagation of the ring. Using Eq. (4) to compute the strength of the vortex elements ensures that the numerical value of the vorticity at the mesh corner , $\Sigma\ \Gamma_i\Delta\ell_if_\delta(\mathbf{x}-\mathbf{X}_i)$, is equal to that of the initial vorticity of the ring, $\boldsymbol{\omega}(\mathbf{X}_i,0)$. Note that the vorticity associated with an elementary vortex is $\boldsymbol{\omega}_i = \Gamma_i\Delta\ell_i/\Delta V_i$, where ΔV_i is the volume of the material element.

The mesh is constructed using N_c cross sections of the ring, separated by angle $\Delta\theta=2\pi/N_c$, and N_r points within each cross section. Within the core of the ring, the elements are arranged on circles, starting with one element at the center of the core ρ = R, and separated by a radial distance Δr. The vorticity of the ring is assumed to be uniform in the azimuthal direction, and hence, we only solve N_r equations for the

vorticity of the elements within a particular cross section. The ring core vorticity distribution is taken as third-order Gaussian, σ being the standard deviation.

The effect of the discretization parameters on the accuracy of the simulation has extensively been investigated in Knio and Ghoniem [36]. In the following, we present a brief summary of the results. Three different meshes are used to discretize the vorticity of the ring within its core: a uniform radial mesh, a staggered radial mesh (in both the radial stations within the core have the same number of elements), and an equi-spaced radial mesh in which the number of elements increases as we move outwards to maintain the distance between neighboring elements approximately the same. The mesh coordinates and the core radius of the elements are varied to satisfy the following conditions: (a) the core radius, δ, should be large enough to provide overlap between neighboring elements; (b) the order of magnitude of the vorticity of the elements at different radial stations is the same; and (c) the total circulation of the vortex elements equals the circulation of the ring.

Tests for the discretization accuracy of the vorticity field are performed for a ring with σ/R = 0.25 for the following cases: (1) a uniform mesh with N_r = 9, 17, 25 and 33; (2) a staggered mesh with N_r = 17, 25 and 33; and (3) an equi-spaced mesh with N_r = 19 and 37. Results of the computations are shown in Table I for the nine cases. The normalized self-induced velocity is $\tilde{V}$ = $V/(\Gamma/4\pi R)$. The accuracy of the discretization is measured in terms of: $E_1 = \int|\omega(\mathbf{X},0)-\Sigma\omega_if_\delta|dx$. In light of these results, the following conclusions can be made:
(1) To satisfy the above conditions, (a)-(c), the core radius of the vortex elements must decrease at a slower rate than the separation between elements. This is in agreement with the convergence results of Beale and Majda [31,32];
(2) The computed values of the propagation velocity, $\tilde{V}$ = 3.387, and the total circulation of the ring, Γ = 2.0, are within less than 0.5% for all cases;
(3) E_1 decreases substantially when an equi-spaced mesh, which guarantees maximum overlap among neighboring elements, is used.

To study the effect of the discretization parameters on the time-dependent solution, we apply the method to investigate the evolution of the instability of the ring. Seven cases are computed for a ring with σ/R = 0.275, whose self-induced velocity is $\tilde{V}$ = 3.30. Vorticity discretization is performed using the uniform mesh with N_r = 9, 17 and 33, the staggered mesh with N_r = 17 and 25, and the equi-spaced mesh with N_r = 19 and 37. To start within the linear range of instability, the ring is perturbed in the radial direction by a number of sinewaves, n, around its axis. The amplitude of the wave is ϵ/R = 0.02. In all cases, the unstable mode is found at n^* = 12, except for the case with N_r = 9 in which n^* = 10. Figure 1 shows the evolution of the amplitude of the excited wavenumber for the seven cases. The results are in close agreement with the

3
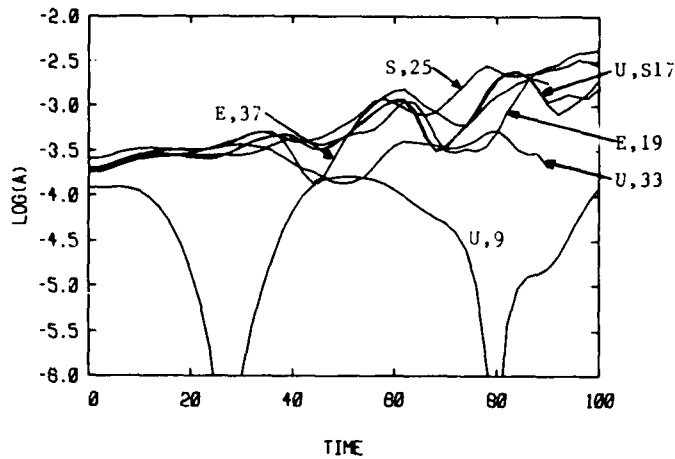
Figure 1. Amplitude of the excited wavenumber, n =
n* = 12, for a vortex ring with σ/R = 0.275 using
a uniform mesh (U) with N_r = 9, 17 and 33, a
staggered mesh (S) with N_r = 17 and 25, and an
equi-spaced mesh (E) with N_r = 19 and 37. ·

exception of the first mesh with N_r = 9 which

shows a stable mode at this wavenumber. Results
on evolution of the instability for the seven
cases lead to the following conclusions:
(1) For accurate simulations using the vortex
method, overlap between the vortex elements must
be maintained at all times. When this condition
is violated, convergence of the results may not be
achieved. We have reached the same conclusion
before by analyzing the accuracy of the
discretization, and by analyzing the stability of
the thin tube approximation [13];
(2) At least two radial stations in the mesh are
needed to ensure accurate prediction of the
unstable mode in vortex rings. This is expected
since the instability observed here corresponds to
the second radial mode which should be properly
represented by the vorticity mesh. A single
radial station within the core is not sufficient
for proper resolution of this mode;
(3) A sufficiently small time step, Δt, must be
used in Eqs. (6) and (7).
    Results indicate that the growth of the
unstable mode can excite its higher harmonics.
The amplitudes of the exciting frequency and its
first harmonic, are plotted in Fig. 2 for the five
cases for which conditions (a)-(c) hold: the
uniform mesh with N_r = 17, the staggered mesh with

N_r = 17 and 25, and the equi-spaced mesh with N_r =

19 and 37. Note that the growth of the amplitude
of the unstable mode and its first harmonic are in
close agreement for the five cases. This confirms
our conclusions regarding the convergence of the
simulation.
    The unstable mode number, n*, was computed
for two more rings: σ/R = 0.325 and 0.375, with
corresponding normalized self-induced velocities

Ṽ = 3.13 and 2.98. For this purpose, the
vorticity was discretized on a uniform mesh with
two radial stations within the ring core and with

N_r = 17. Results show that for the two rings, n*

= 10 and 9, respectively. Comparison between the

predictions of Widnall and Tsai [10], Widnall,
Bliss and Tsai [37], the experimental measurements
of Widnall and Sullivan [38] and our computed
results is shown in Fig. 3.
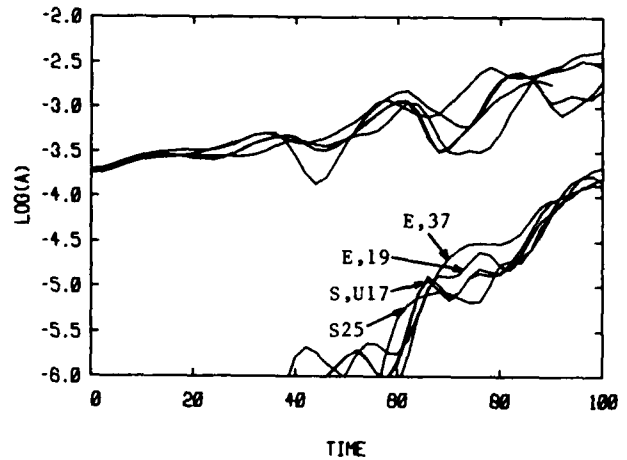
Figure 2. The growth of the excited wavenumber, n
= n* = 12, and its harmonic, n = 24, for the ring
of Fig. 1 using a uniform mesh (U) with N_r = 17, a
staggered mesh (S) with N_r = 17 and 25, and an
equi-spaced mesh (E) with N_r = 19 and 37.
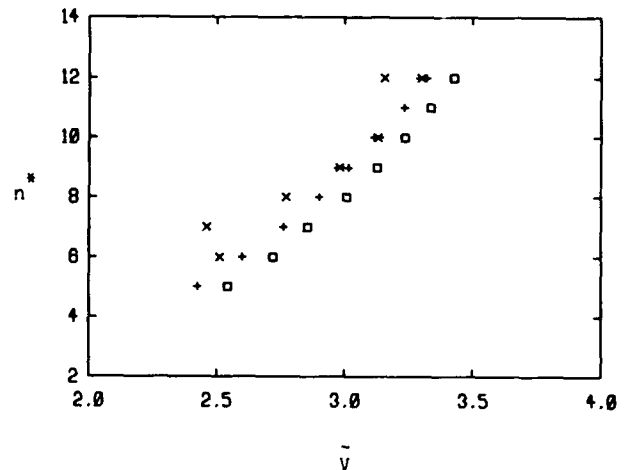
Figure 3. The computed unstable wavenumber (*)
plotted against the normalized velocity of

propagation Ṽ. The results are compared to the
analytical prediction of Widnall, Bliss and Tsai
[37] for a ring with constant vorticity (□), a
ring with fourth order vorticity distribution (+)
and with the experimental results of Widnall and
Sullivan [38] (x).

4

TABLE I
SUMMARY OF DISCRETIZATION RESULTS
$\sigma/R = 0.25$, $\Gamma = 2.0$

N_r	σ	Δr	Γ	$\overline{V}/25.13$	$E_1 \times 100$
UNIFORM MESH					
9	0.67	0.630	2.01806	0.13572	6.646
17	0.56	0.397	2.01296	0.13567	7.697
25	0.52	0.300	2.00073	0.13599	6.988
33	0.50	0.240	2.01686	0.13563	6.877
STAGGERED MESH					
17	0.56	0.397	2.0033	0.13518	7.252
25	0.55	0.300	2.0005	0.13370	4.340
33	0.50	0.245	1.9925	0.13447	4.190
EQUI-SPACED MESH					
19	0.56	0.393	2.0093	0.13474	7.782
37	0.56	0.320	1.9941	0.13477	0.996

III.2. FORMATION OF STREAMWISE VORTICITY

To study the evolution of streamwise vorticity on an isolated vortex ring, we plot perspective views of a ring with $\sigma/R = 0.275$ in Fig. 4. The ring is initially perturbed at the unstable mode, $n^* = 12$, and results are plotted at $t = 30, 60, 90$ and 120. The perturbation grows in both the radial and streamwise directions causing substantial non-uniform deformation around the axis of the ring, and the generation of streamwise vorticity. The amount of deformation can be measured by the growth of the total number of vortex elements used in the discretization of the vorticity field. While this number stays constant in all the stable cases, for $n < n^*$, it increases as soon as the instability grows beyond the linear range for $n = n^*$. For this ring, the number of elements grew from 2040 to 6396 for $t = 0$ to 140.

In the initial stages, and within the linear range $t < 20$, waves do not rotate around the axis of the ring, while their amplitudes grow exponentially, as shown in Figs. 1 and 2. This is in agreement with the numerical results of Ghoniem et al. [13], and the analytical results of Widnall and Tsai [10]. For $t > 20$, non-linear effects grow, extending the outer part of each wave radially outwards while tilting it in the direction opposite to the direction of propagation of the ring. The inner part of the wave moves radially inwards while it is tilted in the direction of propagation of the ring. For $t > 90$, Fig. 4 shows that the vorticity of the ring is redistributed around the azimuthal direction into a number of sectors equal to the number of waves. The outer part of each sector stretches opposite to the direction of propagation of the ring, while the inner part elongates forwards.

It is interesting to note that at the later stages, $t > 90$, the core deformation is different at different radial locations and that the inner and outer radii may not follow the same pattern. The figure indicates that the inner and outer edges of the vorticity core may move in anti-phase, and that deformations at a scale smaller than that of the perturbing wave are observed. This suggests that frequencies different than the perturbation frequency may be present at later times. The first harmonic was observed to grow in the non-linear range in Fig. 2.
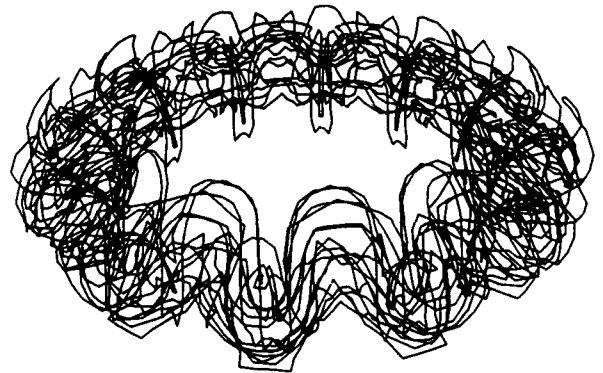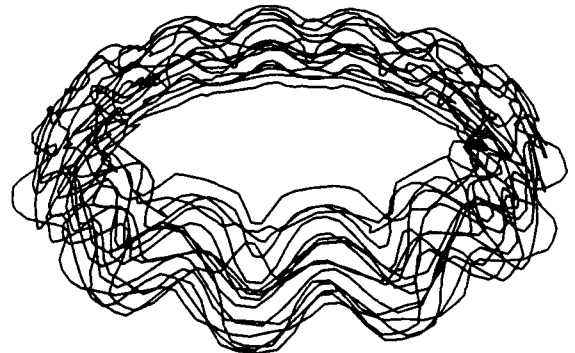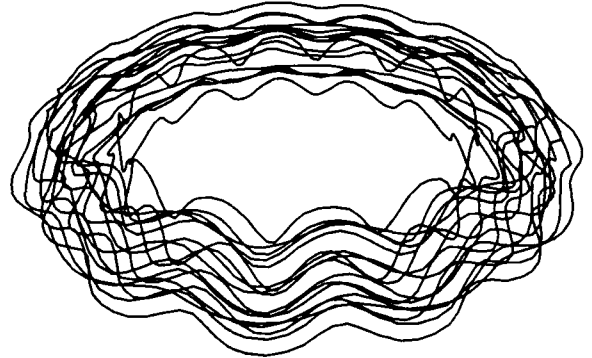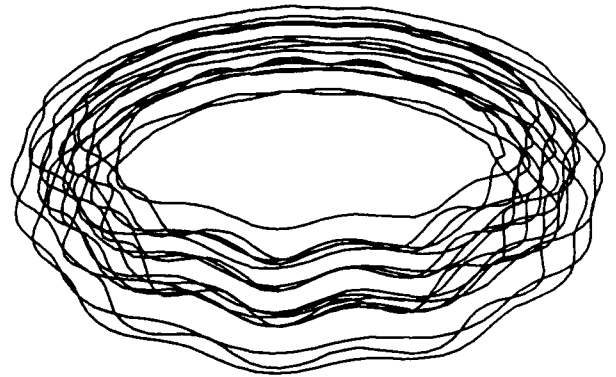

Figure 4. Perspective views of a vortex ring with $\sigma/R = 0.275$, excited at the linearly unstable mode, $n = n^* = 12$, depicted at $t = 30, 60, 90$ and 120, and taken from the point of view of an observer standing ahead of the ring and looking at an angle of $\phi = 60°$ with respect to the direction of propagation. The ring is represented by all the vortex tubes used in the computations, and it propagates upwards.

The growth of streamwise vorticity, measured by the value of $\int |\omega_z|\, dA$ computed in the z_a-plane where z_a is the average value of z within the ring, is shown in Fig. 5. At $t = 0$, $\omega_z = 0$ since the initial vorticity of the ring, ω_θ, is perturbed by moving the vortex elements in the radial direction only. The growth of ω_z is negligibly small within the linear range, rises fast for $20 < t < 80$, and tends to stabilize for $t > 80$. The oscillation of the curve for later times is an indication that parts of the core of the vortex ring experience some rotation even after the "maturation" of the azimuthal instability.

Three perspective views of the vortex ring are shown in Fig. 6 at $t = 140$. Vortex lines elongate in the streamwise direction on the outer radii of the ring, reaching a maximum extension opposite to the direction of propagation of the ring and then fold backwards towards the ring centerline. On the other hand, vortex lines on the inner radii of the ring stretch in the direction of propagation of the ring, reaching a maximum extension and then fold back and move towards the ring center line. The mechanism of vortex line folding maintains the ring coherent.

Figure 7 shows the streamwise vorticity contours, ω_z, at three sections in the direction of propagation of the ring at $t = 140$. Within each sector, the core of the vortex rings experiences a displacement into and out of the direction of propagation of the ring, resulting in the formation of alternating signs of streamwise vorticity. Note that the sections of the core that move radially outwards produce streamwise vorticity opposite to the direction of propagation of the ring, and vice versa.

To complete the picture of the vorticity distribution within a perturbed ring, we plot ω_θ at four azimuthal sections within the ring core in Fig. 8. The vorticity contours show clearly how the core moves forwards and backwards in the direction of propagation of the ring as we move along the ring axis.

Figure 6. Three perspective views of the vortex ring shown in Fig. 4 taken at $t = 140$. $\phi = 0°$, $60°$ and $90°$. The ring propagates upwards (and out of the page.)
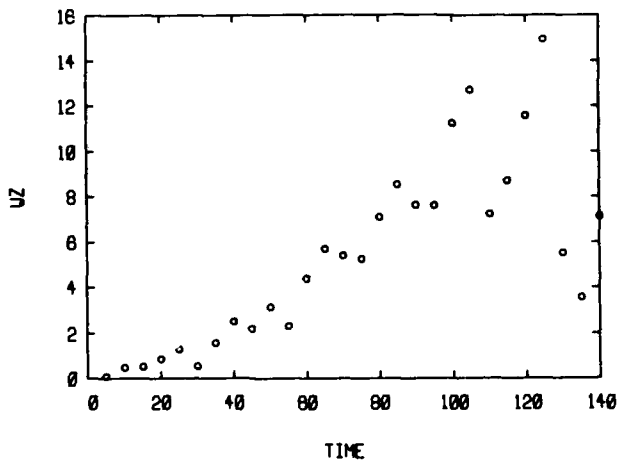
Figure 5. Evolution of the streamwise vorticity $\int |\omega_z|\, dA$ across the midsection of the ring, $z = z_a$, of the vortex ring shown in Fig. 4.

6
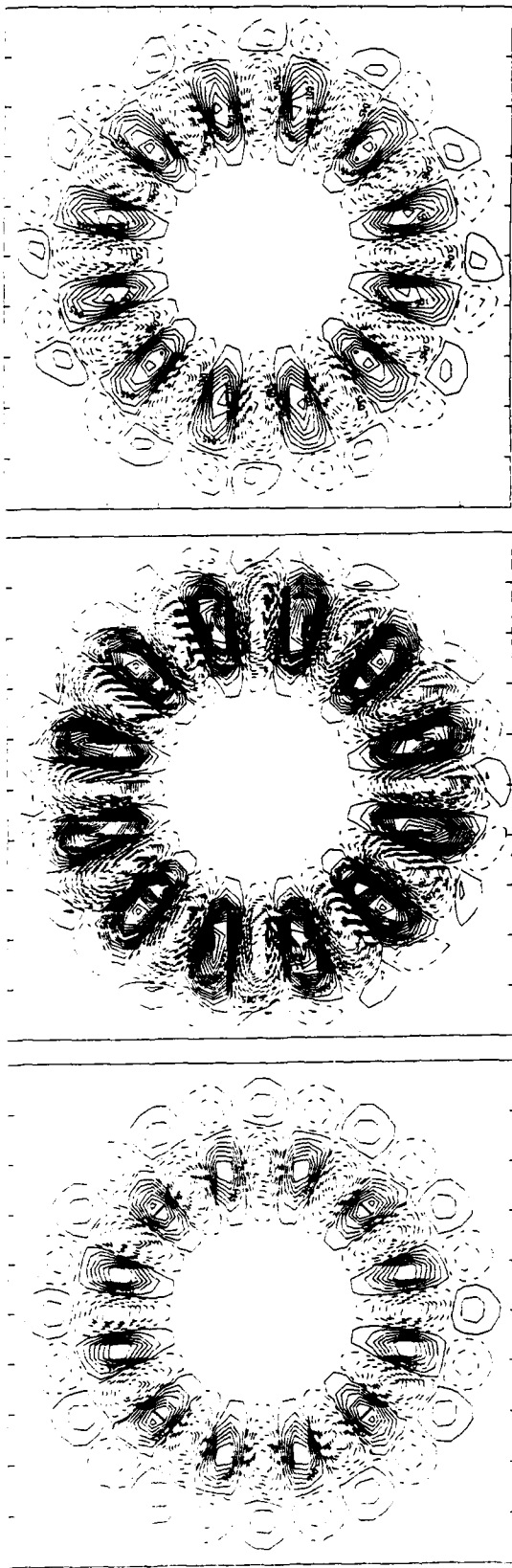
Figure 7. Contours of streamwise vorticity, ω_z, for the vortex ring shown in Fig. 4, in the ρ-θ planes located at $z = z_a - 0.5$, $z_a + 0.5$ and $z_a + 1.5$, at $t = 140$. Continuous/broken lines indicate -ve/+ve vorticity
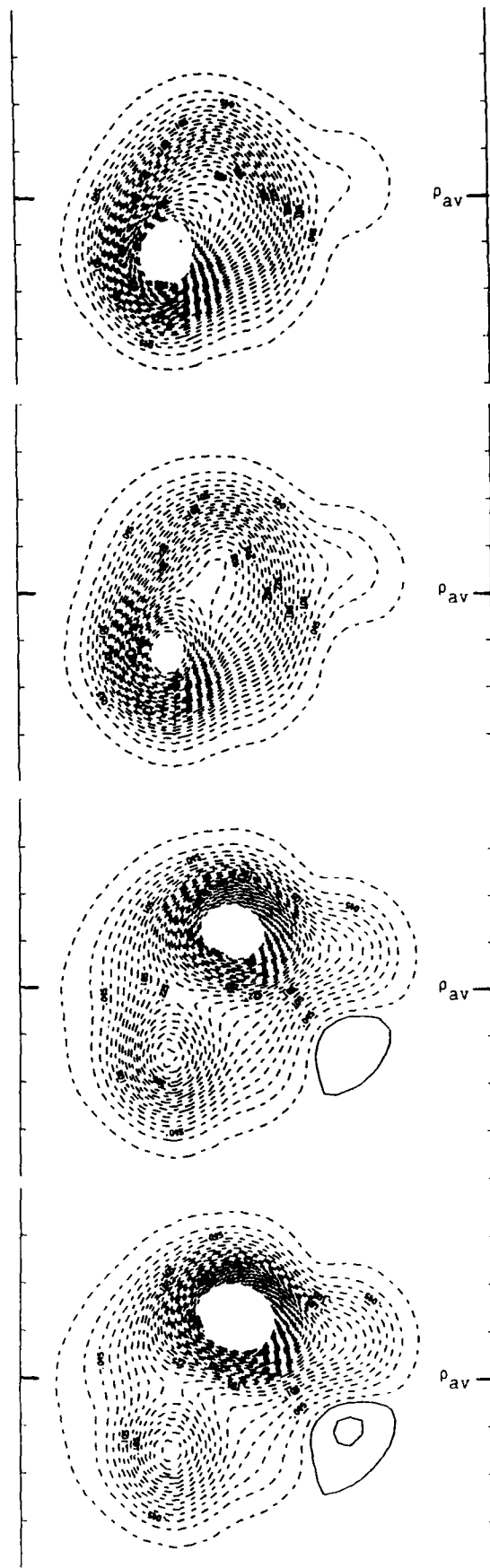
Figure 8. Distribution of ω_θ in four azimuthal sections lying within a single wavelength of perturbation 2π: $\theta = 2\pi/5$, $4\pi/5$, $6\pi/5$ and $8\pi/5$. The ring propagates towards the left.

7

IV. RESULTS: PERIODIC SHEAR LAYER

IV.1. INSTABILITY OF A SHEAR LAYER

The second flow field which we use to study the formation of streamwise vorticity due to the evolution of a perturbation in a two-dimensional flow is that of a periodically excited, planar shear layer. In this case, the initial state is that of a vorticity layer with a finite thickness, measured by 2σ where σ is the standard deviation of the second-order Gaussian that describes the vorticity distribution within the layer, and finite streamwise velocity jump, ΔU. Initially, the spanwise vorticity, ω_y, is uniform in the streamwise x-direction, and spanwise y-direction.

Thus, $\omega_y(\mathbf{X},0) = \Delta U/(\sqrt{\pi}\ \sigma)\ \exp(-z^2/\sigma^2)$ where z is the cross-stream direction. The corresponding velocity distribution is $u(\mathbf{x},0) = \Delta U/2\ \mathrm{erf}\ (y/\sigma)$, where erf is the error function. The layer is perturbed by sinewaves in both the streamwise and the spanwise directions. The wavelength of the perturbation, λ, in both directions corresponds to the two-dimensional most unstable mode. The amplitude of the perturbation is kept small, $\varepsilon = 0.02\ \lambda$, to capture the linear stages of growth of both perturbations. The perturbation is applied by moving the vortex elements in the cross-stream direction according to the sinewaves.

We start by presenting a sample of results for the two-dimensional case. In Fig. 9, we show the location and velocity of all vortex elements used in the computation of a strictly two-dimensional shear layer, i.e. without allowing any changes in the spanwise directions. At time $t = 0$, the vorticity is discretized among elements distributed on a grid of 5 x 20 points in the z-direction and the x-direction, respectively. Extensive analysis of this flow field has been documented in Ghoniem et al. [24], and will not be repeated here. Results show the different stages of development of the layer: the linear stage, the formation of a spanwise core, and the flattening, or collapse of the core. The computed linear growth of the perturbation, $\dot{I} = d\ \ln I/dt = 0.215$ where $I = \int |u(\mathbf{x},t)-U(\mathbf{x})|d\mathbf{x}$, integrated over the entire domain. The value predicted by the linear theory is 0.22. Thus, the simulation is capable of accurately capturing the growth of the perturbation through the linear stages (an accurate initialization of the strength of the vortex elements is, however, very important for predicting the growth rate of the instability).

In the non-linear phase, which starts as soon as the central layer reaches a vertical position around $t = 6$, a strong, planar strain field accompanies the formation of a coherent core at the center of the wavelength of the perturbation. The strain field is strongest at the center of the core, where vorticity is accumulating, and near the boundaries of the domain, where vorticity is pulled towards the center. In the meantime, the structure of the vorticity field changes from a uniform distribution into a concentrated region of elliptical-like shape. The average diameter of this structure is almost $\lambda/2$, and the vorticity distribution within the structure decays radially-outwards away from its center, as shown by the vorticity contours depicted in Fig. 10.

When the vorticity is perturbed in both the streamwise and spanwise directions, its growth develops a three-dimensional flow. In this case, the vorticity layer is discretized using a grid of 5x20x25 elements in the z-, the x-, and the y-direction, respectively. Figures 11 and 12 depict the projection of the location of the vortex elements on the x-z plane and the x-y plane, respectively. In each figure, vortex elements which were initially aligned in the spanwise direction are connected to show the axial stretch of vorticity and the areas of deformation of the vortex lines. Three-dimensional perspectives of the shear layer are shown in Fig. 13. The relative displacement of vortex elements show the magnitude and direction of the local velocity. The figures indicate that the initial growth rate of the streamwise perturbation far exceeds that of the spanwise perturbation, leading to the formation of a spanwise eddy, as in the strictly two-dimensional case.
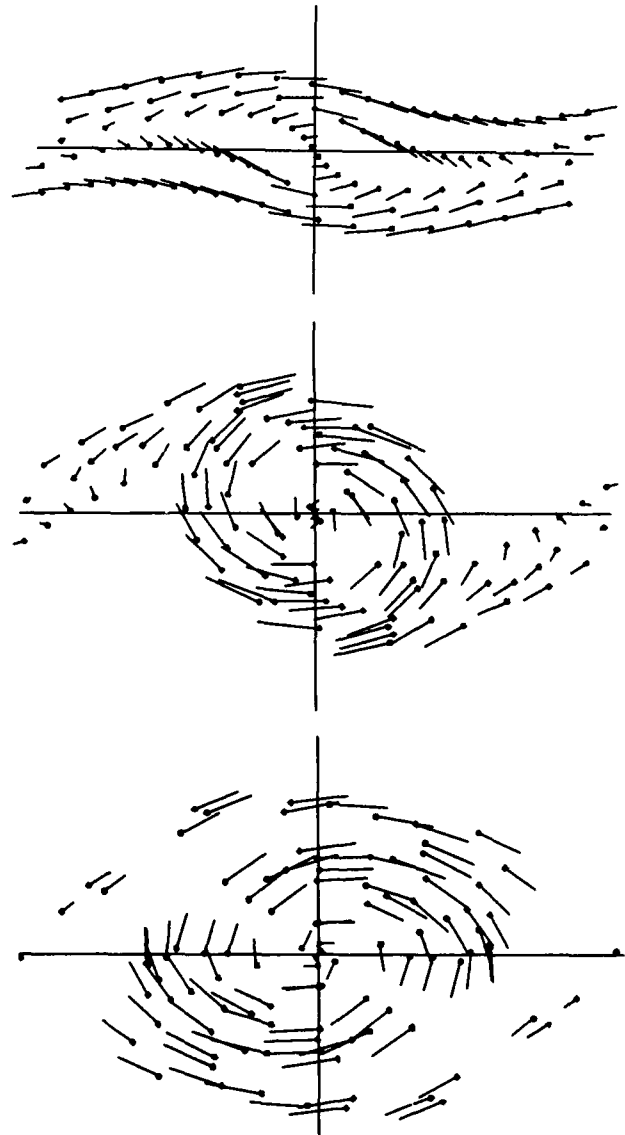

Figure 9. Location and velocity vector of the vortex elements for the two-dimensional shear layer. $t = 6$, 12 and 18.
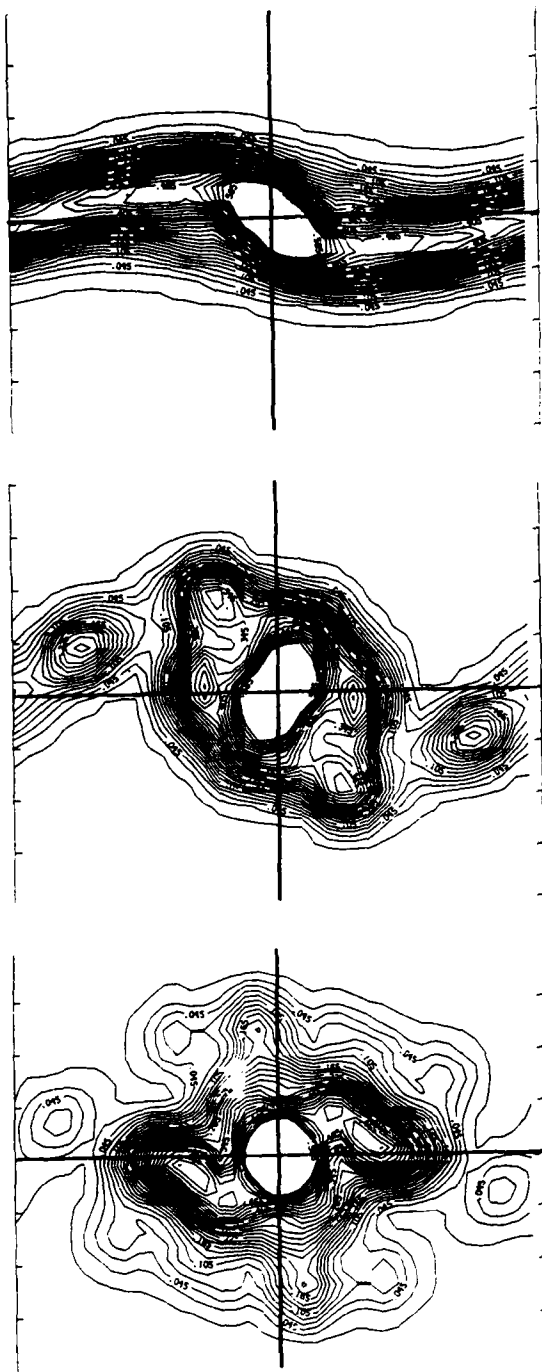
Figure 10. Contours of spanwise vorticity, ω_y, for the two-dimensional shear layer. $t = 6, 12$ and 18. In this, and the following figures, continuous/broken line indicate +ve/-ve vorticity, respectively.
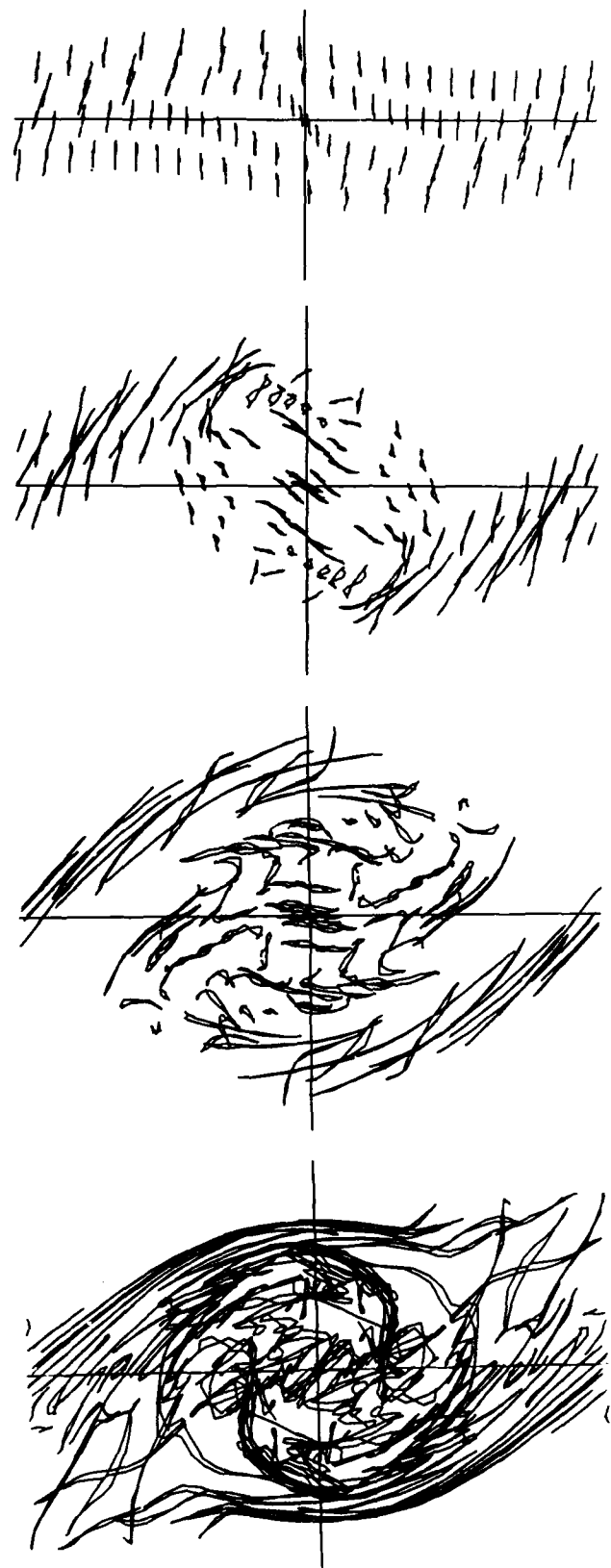

Figure 11. The location of the vortex elements for the three-dimensional shear layer projected on the x-z plane. $t = 6, 12, 18,$ and 24.
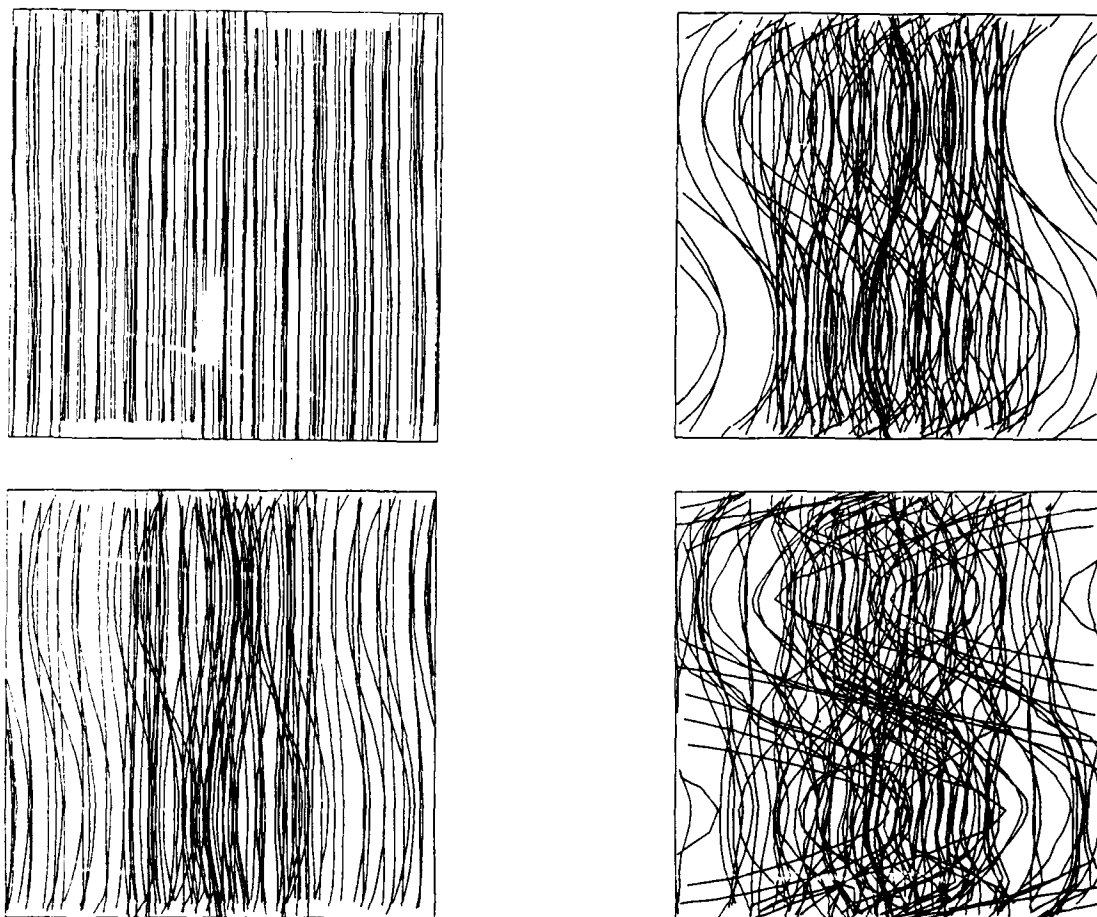
Figure 12. The location of the vortex elements for the three-dimensional shear layer projected on the x-y plane. t = 6, 12, 18 and 24.

Within the linear stage, the vorticity remains aligned with the spanwise direction, as seen from Fig. 12. Vortex lines do not experience any noticeable stretch, only some tilting as the material lines deform. The linear growth of the streamwise component of the perturbation suppresses that of the spanwise component. Around t = 10.0, and with the inception of a strong spanwise eddy along the center of the domain, the wiggles in the spanwise direction start to grow. The rate of growth of these wiggles is highest within the braids, where the strain field is strongest, indicating that the presence of a strong strain field is necessary for the development of a streamwise component of vorticity within the braids.

During the formation of the spanwise eddy, the strain field is strongest near the center and the boundaries of the domain. The vorticity within the braids suffers the strongest stretch along its axis while the vorticity which is accumulating within the core remains, to a large extent, aligned with the spanwise direction. The axial stretch of the braid vorticity is tied up to the strain field produced by neighboring spanwise eddies and the formation of stagnation points, or saddle points, near the boundaries of the domain. While the stagnation points act to anchor the vortex lines at both ends in the spanwise

direction, the strain field created by the cores pulls the mid-section of the vortex lines inwards.

As depicted by Fig. 11, the vorticity within the braids is continuously entrained into the cores in the form of "hair-pin" vorticity lines, around both the top side and the bottom side of the large eddy. In a strictly two-dimensional flow, this process will deplete the braids of their initial vorticity. However, as was observed experimentally, some streaks of streamwise vorticity can be detected between the spanwise eddies [2]. The formation of these streamwise vortex rods is not expected to affect the flow within the shear layer in a prominent way since the vorticity that remains in the braids at the later stages is a very small fraction of the initial vorticity. However, it is still important in areas between the spanwise cores since it tends to form, as will be shown next, zones of counter-rotating vortex rods that characterize the braids.

In the second stage, and while the eddy is reaching its maximum size by entraining vorticity from the shear layer, the strain field acting on the spanwise core promotes the growth of the perturbation along its spanwise axis. The growth of the perturbation along the spanwise core can be first detected at t = 11 - 12, where the projected lengths of the vortex lines on the x-z plane start to grow beyond their values at t = 0. Moreover,

10
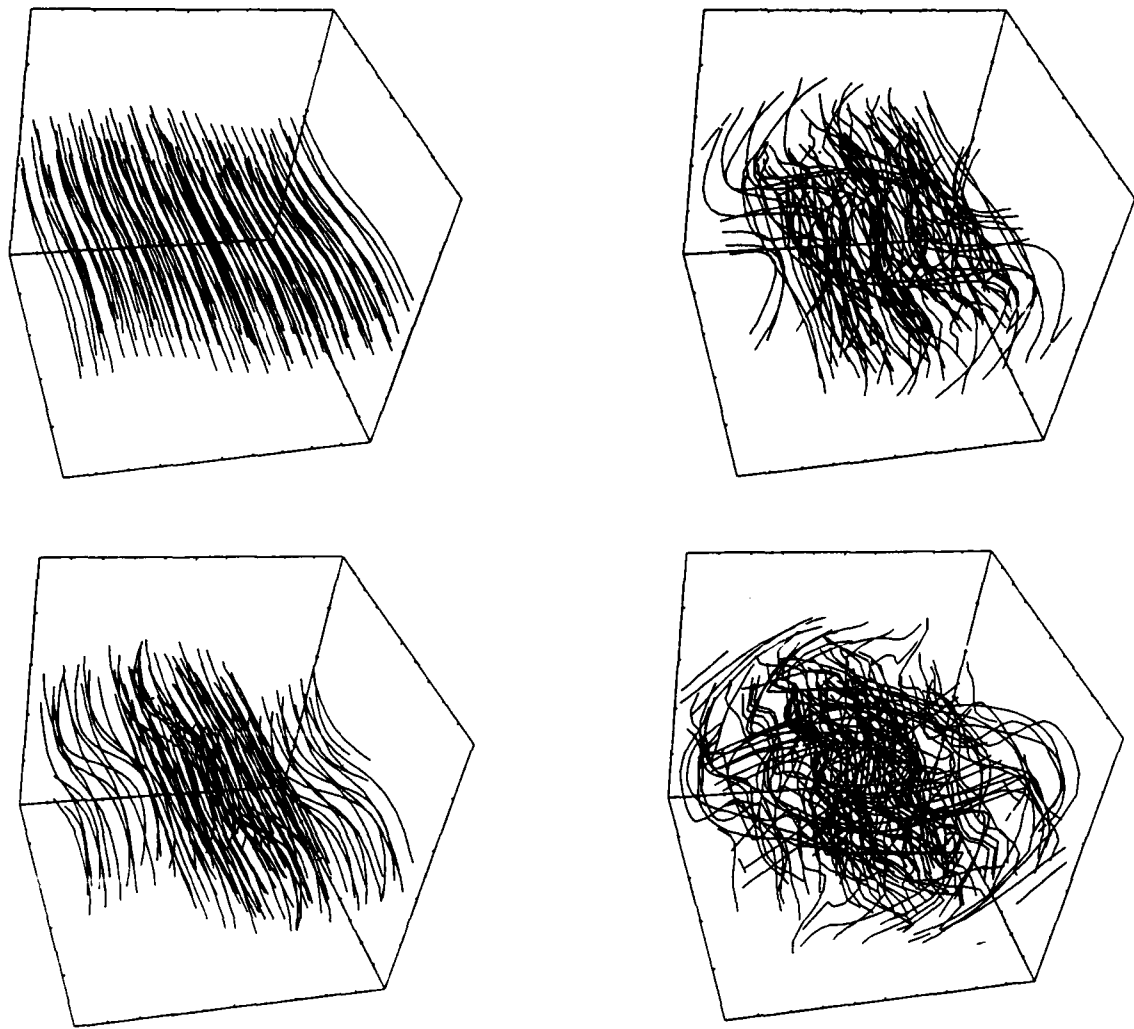
Figure 13. A perspective view of the development of the three-dimensional layer,
shown in terms of all the vortex tubes used in the computations. t = 6, 12, 18
and 24.

Fig. 12 shows that, near the center of the plane, wiggles start to grow non uniformly along the spanwise direction. It is interesting to point out that the growth of the wiggles inside the core and within the braids is out of phase.

The vorticity within the core experiences most of its axial stretching during the second and third stages of growth, i.e. for t > 10. During the second stage, and while the core is reaching its maximum size, only those vortex lines that are close to the axis get strained. With the spanwise straining of the vortex lines within the core, its spinning becomes slower than that of a strictly two-dimensional flow. Beyond t = 14, and within the third stage, the perturbation grows on more vortex lines within the core, generating a stronger streamwise vorticity component. The displacement of the vortex lines, originally aligned with the spanwise direction, into the streamwise direction continues until the entire vorticity core has been partly deformed.

Between t = 10 ~ 18, and when the spanwise eddy exhibits most coherence, the wiggle spreads throughout the entire core. After the third stage, t > 18, and while the cross section of the core is slowly flattening, the vorticity approaches a state of semi-equilibrium. At this stages, two modes of spanwise instability are observed: the braid instability leading to the formation of the "hair-pin" vortices, or vortex rods which become lined up between the large cores, and the core instability which deforms the spanwise eddy in the spanwise direction.

11

IV.2. FORMATION OF STREAMWISE VORTICITY

Figure 14 depicts the development of the spanwise vorticity, ω_y, on an x-z plane at y = 6.6. The figures show strong resemblance to the vorticity field in the strictly two-dimensional case, indicating that the growth of the spanwise perturbations does not alter substantially the two-dimensional underlying flow. The amplitude of the wiggle that grows along the spanwise eddy is small with respect to the wavelength.

Figures 15 and 16 exhibit the evolution of the streamwise vorticity, ω_x, in two y-z planes: x = 2.0 and x = 6.6. The first plane shows a cut through the braids and the second plane shows a cut through the core. The streamwise vorticity distribution within the braids, as mentioned before, results from the straining of the vortex lines near the boundaries of the domain during the roll-up of the core. Since most of the vorticity within the braids is depleted during roll-up, ω_x is relatively weak. There is a remarkable similarity between these vorticity contours and those produced by Lin and Corcos [12] using a simplified model for the evolution of the vorticity eddies within the braids. More detailed comparisons will be presented in the future.

Figure 15 reveals that there is only one row of streamwise eddies within the braids during roll-up. Within one spanwise wavelength, the layer forms two eddies of opposite signs. Thus, the sign of vorticity within the braids alternates as we move in the spanwise direction, indicating that this vorticity is actually the ω_x component of the elongating vortex lines as they are strained by the spanwise cores. At the early stages, these large streamwise eddies possess elliptical cores with their major axes aligned with the spanwise direction. At later stages, around t = 20, the two eddies become more rounded and somewhat more "compact". This is due to the extreme elongation of the braids between two neighboring spanwise eddies, leading to the extension of a vortex line that may exceed the perturbation wavelength. At the latest stages, t = 24, the two eddies collapse to form two distinct vortex rods separated by a distance less that $\lambda/2$.

The streamwise vorticity contours, shown in Fig. 16, indicate that, per wavelength in the spanwise direction, there are six main eddies arranged in two columns and three rows. The two eddies on the top and the two eddies on the bottom are extensions of the braid eddies; they have the same signs and the same coordinates, but they have twice the vorticity of the braid eddies when intersected at x = 2. The vorticity distribution can be explained by the inspection of the geometry of the vortex tubes shown in the sketch in Fig. 17. This sketch was generated by examining the geometry of individual vortex tubes and identifying their contribution to the vorticity field at several streamwise and spanwise cross-sections. The sketch shows only the vortex tubes which contribute to the vorticity distribution in the x=6.6 plane. The six main eddies depicted in Fig. 16 can be decomposed into ten elementary eddies: eight eddies from the braids which join to form four cores at the central plane x =6.6 and two eddies resulting from the streamwise displacement of the spanwise core.

The two central eddies which appear in the vorticity contours on the x = 6.6 plane are the intersections of this plane with the spanwise
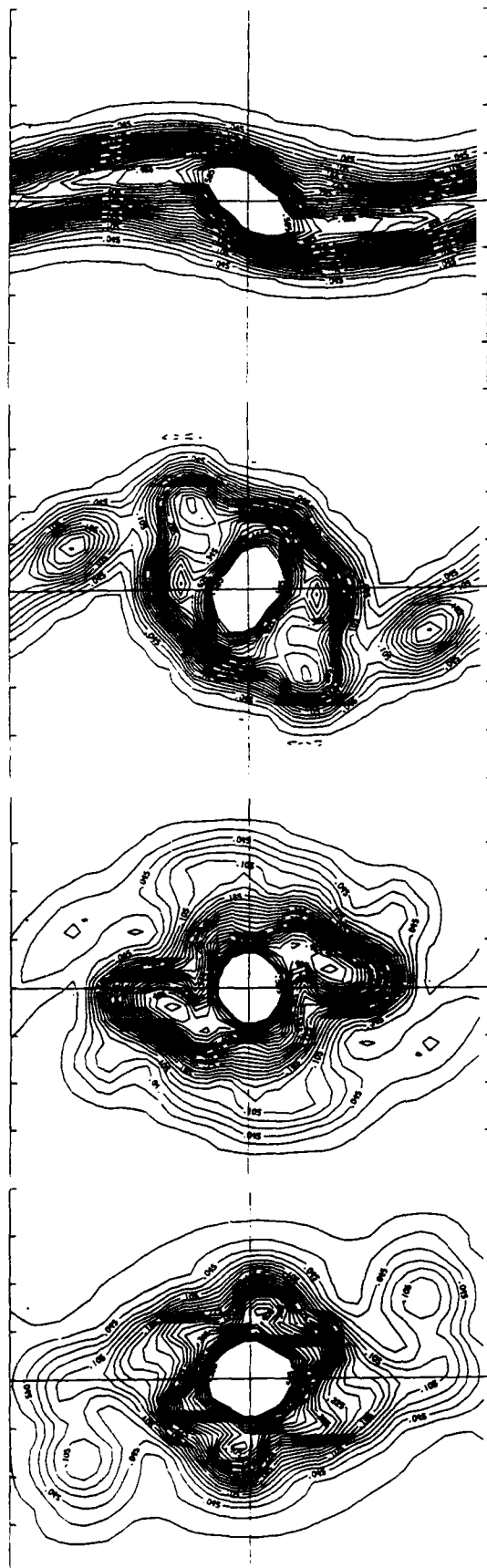

Figure 14. Contours of the spanwise vorticity, ω_y, shown in the x-z plane located at y = 6.6. t = 6, 12, 18 and 24.

12
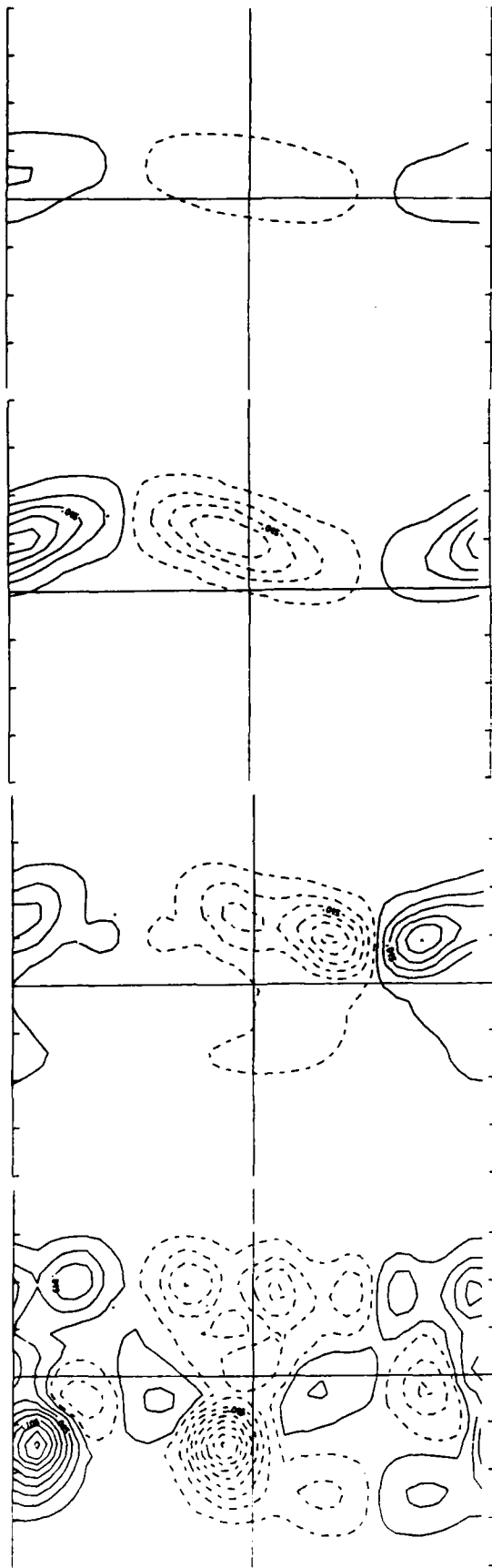
Figure 15. Contours of the streamwise vorticity, ω_x, shown in the y-z plane located at x = 2.0. t = 6, 12, 18 and 24.
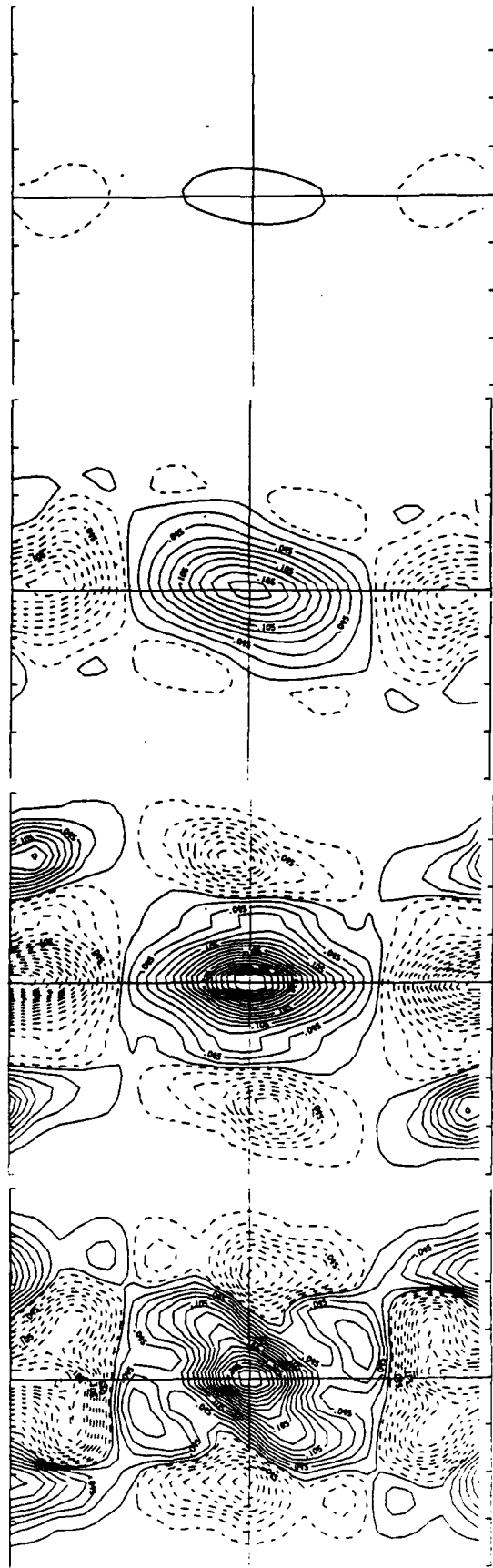
Figure 16. Contours of the streamwise vorticity, ω_x, shown in the y-z plane located at x = 6.6. t = 6, 12, 18 and 24.
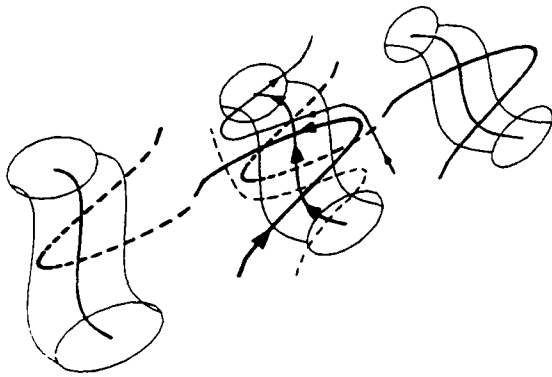
Figure 17. Sketch of the geometry of the vortex lines showing the location of the spanwise core and the axial deformation of the braids.

eddy. Clearly the spanwise eddy experiences bending along the spanwise direction which moves the vortex lines forwards and backwards in the streamwise direction. This is a manifestation of the "translative" instability which was discovered in the work of Pierrehumbert and Widnall [9]. Figure 18 shows the streamwise vorticity contours plotted on three sections $x = 3.3$, $x = 4.4$ and $x = 5.5$, all computed at $t = 24$. The streamwise vorticity in the spanwise core appears between $x = 3.3$ and 4.4, indicating the streamwise extent of the core. Section $x = 5.5$ shows how two hair-pin vortices join to form the top and bottom eddies observed at $x = 6.6$.

Figure 19 shows the distribution of the velocity components in the y-z plane, v and w, computed on a grid at the $x = 6.6$ plane. The presence of the spanwise vorticity, and its growth with time, are clearly indicated by the direction and magnitudes of the velocity vectors. The growth of the streamwise vorticity, measured by $\int |\omega_x| dA$, computed at the $x = 6.6$ plane, is shown in Fig. 20. As seen in the computations of an isolated vortex ring, ω_x is very small during the linear stages of development of the spanwise core. It grows steadily with the formation of a strong strain field due to the roll-up and the formation of spanwise cores, and approaches a stationary oscillating state during the flattening of the core in the last stage.
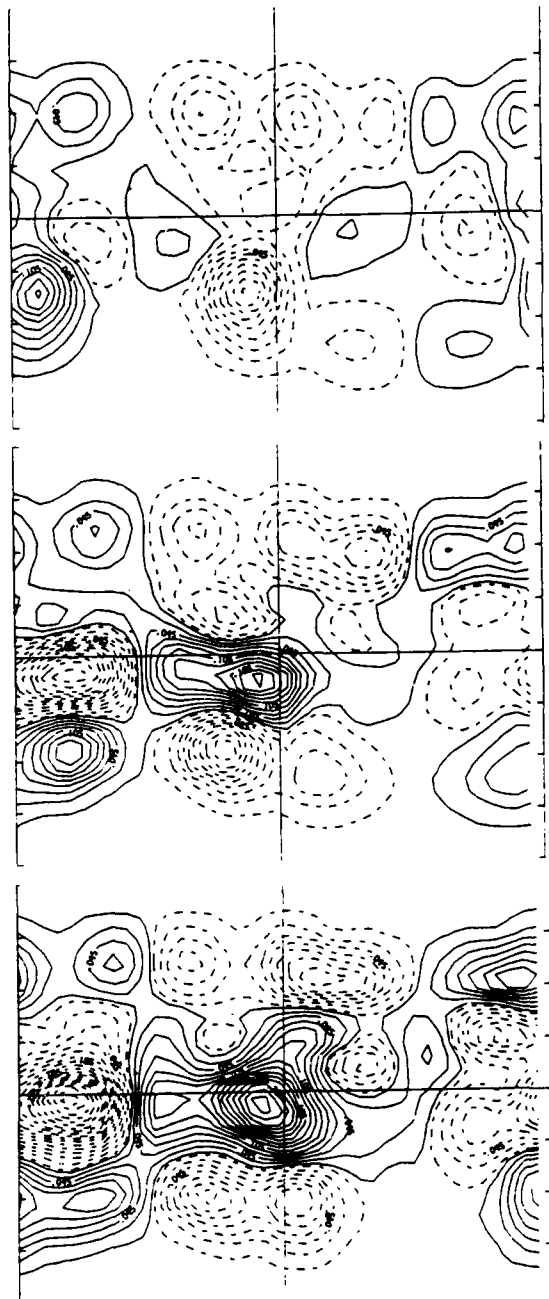
Figure 18. Contours of the streamwise vorticity, ω_x, shown in y-z planes located at $x = 3.3$, 4.4 and 5.5, all at $t = 24$.
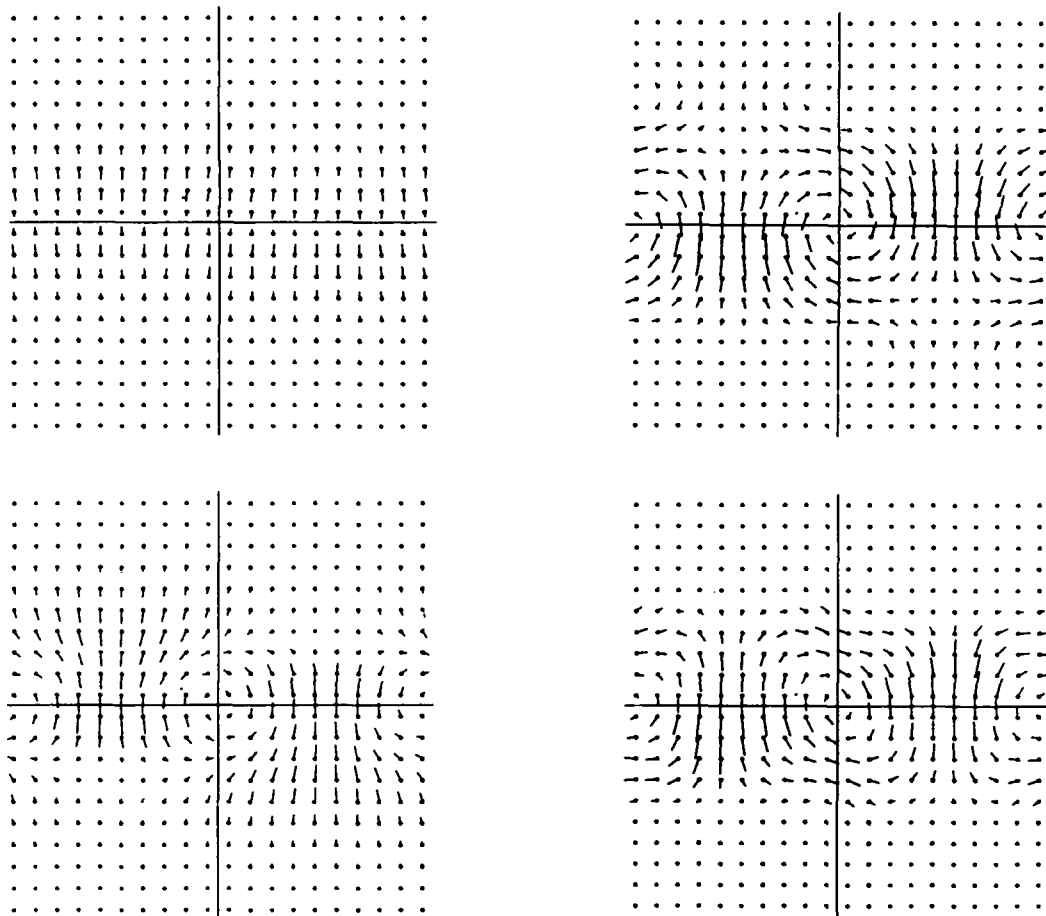
Figure 19. The flow field in the y-z plane located at x = 6.6, represented by velocity vectors computed on a grid of mesh size Δy = Δz = 0.66. t = 6, 12 18 and 24.
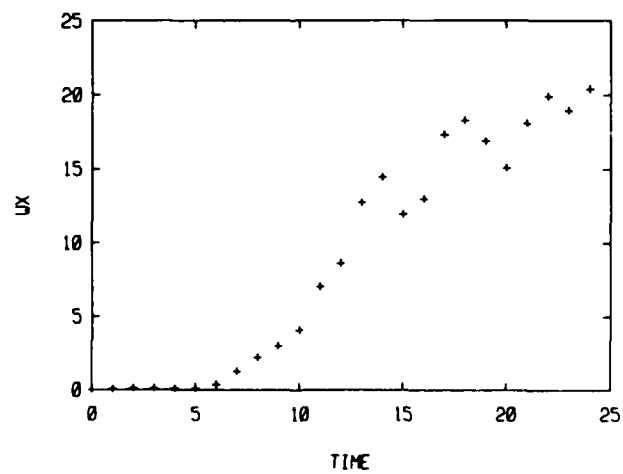

Figure 20. Evolution of the streamwise vorticity $\int |\omega_x| dA$ computed in the y-z plane located at x = 6.6.

15

V. CONCLUSIONS

Three-dimensional numerical simulation using the vortex element method has been used to study the instability and the evolution of streamwise vorticity in two commonly-encountered flow fields: an isolated vortex ring and a perturbed shear layer. The convergence of the numerical scheme is investigated by a detailed study of the effect of the numerical parameters on the prediction of the unstable mode which grows on a vortex ring. The non-linear growth of this mode leads to the formation of a streamwise vorticity component with an alternating sign along the axis of the ring. A study of the structure of the ring core after the growth of this azimuthal instability reveals that the core deforms on a conical surface, bending the vortex line forwards and backwards in the direction of propagation of the ring, while they are moving radially inwards and outwards, respectively. In spite of the growth of the streamwise vorticity, the ring stays coherent and the flow remains, on the average, two-dimensional.

In the shear layer, the initial growth rate of the streamwise component of the perturbation exceeds that of the spanwise component, resulting in the formation of spanwise vorticity cores, wrapped with streamwise vorticity rods. Similar to the vortex ring, the spanwise cores are subject to a spanwise instability that bends the core forwards and backwards in the streamwise direction, forming a strong streamwise vorticity component of alternating sign in the spanwise direction. The braids, on the other hand, are formed of vortex rods that, during their excursion into the free stream, bend into and out of the streamwise direction. Here also, the flow remains, on the average two-dimensional and the vortex cores maintain their coherence.

REFERENCES

1. Roshko, A., "Structure of turbulent shear flows: a new look," AIAA Journal, Vol. 14, 1976, pp. 1349-1357.

2. Breidenthal, R., "Structure in turbulent mixing layers and wakes using a chemical reaction," J. Fluid Mech., Vol. 109, 1981, pp. 1-24.

3. Bernal, L.P. and Roshko, A., "Streamwise vortex structure in plane mixing layers," J. Fluid Mech., Vol. 170, 1986, pp. 499-525.

4. Crow, S.C. and Champagne, F.H., "Orderly structure in jet turbulence," J. Fluid Mech., Vol. 48, 1971, pp. 547-591.

5. Yule, A.J., "Large-scale structures in the mixing layer of a round jet," J. Fluid Mech., Vol. 89, 1978, pp. 413-432.

6. Roquemore, W.M., Bradley, R.P., Jackson, T.A., Kizirnis, S.W., Gross, L.P., Switzer, G.L., Trump, D.D., Sarka, B., Ballal, D.R., Lightman, A.J., Yaney, P.P. and Chen, T.H., "Development of laser diagnostics for combustion research," Central States Section/The Combustion Institute, 1986 Spring Meeting.

7. Maxworthy, T., "Some experimental studies of vortex rings," J. Fluid Mech., Vol. 81, 1977, pp. 465-495.

8. Michalke, A. and Hermann, G., "On the inviscid instability of a circular jet with external flow," J. Fluid Mech., Vol. 114, 1982, pp. 343-359.

9. Pierrehumbert, R.T. and Widnall, S.E., "The Two- and Three-Dimensional Instabilities of a Spatially Periodic Shear Layer," J. Fluid Mech., Vol. 114, 1982, pp. 59-82.

10. Widnall, S.E. and Tsai, C.-Y., "The instability of the thin vortex ring of constant vorticity," Philos. Trans. R. Soc. Lond., Series A, Vol. 287, 1977, pp. 273-305.

11. Corcos, S.J. and Sherman, F.S., "The mixing layer: deterministic models of a turbulent flow. Part 1. Introduction and two-dimensional flow," J. Fluid Mech., Vol. 139, 1984, pp. 29-65.

12. Lin, S.J. and Corcos, G.M., "The mixing layer: deterministic models of a turbulent flow. Part 3. The effect of plane strain on the dynamics of streamwise vortices," J. Fluid Mech., Vol. 141, 1984, pp. 139-176.

13. Ghoniem, A.F., Aly, H.M. and Knio, O.M., "Three-dimensional vortex simulation with application to axisymmetric shear layer," AIAA 25th Aerospace Sciences Meeting, January 12-15, 1987/Reno, Nevada, AIAA Paper 87-0379.

14. Ho, C.-M., and Huerre, P., "Perturbed free shear layers," Ann. Rev. Fluid Mech., Vol. 16, pp. 365-424.

15. Corcos, G.M. and Lin, S.J., "The mixing layer: deterministic models of a turbulent flow. Part 2. The origin of the three-dimensional motion," J. Fluid Mech., Vol. 139, 1984, pp. 67-95.

16. Couet, B. and Leonard, A., "Mixing layer simulation by an improved three-dimensional vortex-in-cell algorithm," 7th Int. Conf. Num. Meth. Fluid Dynamics, Stanford 1980.

17. Riley, J.J. and Metcalfe, R.W., "Direct numerical simulation of a perturbed turbulent mixing layer," AIAA Paper 80-0274, 1980.

18. Riley, J.J. and Metcalfe, R.W., "Direct numerical simulation of a chemically reacting turbulent mixing layer," AIAA Paper 85-0321, 1985.

19. Ashurst, W.T. and Meiburg, E., "Three-dimensional shear layers via vortex dynamics," Sandia National Laboratory report, SAND85-8777, 1985.

20. Leonard, A., "Vortex methods for flow simulation," J. Comput. Phys., Vol. 37, 1980, pp. 289-335.

21. Leonard, A., "Computing three dimensional incompressible flows with vortex elements," Ann. Rev. Fluid Mech., Vol. 17, 1985, pp. 525-559.

22. Lowery, P.S., Reynolds, W.C., and Mansour, N.N., "Passive scalar entrainment and mixing in a forced, spatially developing mixing layer," AIAA Paper 87-0132, 1987.

23. Inoue, O. "Vortex simulation of three dimensional mixing layers," AIAA 19th Fluid Dynamics, Plasma Dynamics and Lasers Conference, June 8-10, 1987/Honolulu, Hawaii. AIAA Paper 87-1311.

24. Ghoniem, A.F., Heidarinejad, G., and Krishnan, A., "Numerical simulation of a thermally stratified shear layer using the vortex element method," J. Comput. Phys., accepted for publication (1987).

25. Chorin, A.J., "Vortex models and boundary layer instability," SIAM J. Sci. State. Comput., Vol. 1, 1980, pp. 1-21.

26. Chorin, A.J., "Estimates of intermittency, spectra and blow-up in developed turbulence," Commun. Pure Appl. Math., Vol. 34, 1981, pp. 853-866.

27. Chorin, A.J., "The evolution of a turbulent vortex," Commun. Math. Phys., Vol. 83, 1982, pp. 517-535.

28. Mosher, M.C., "A method for computing three-dimensional vortex flows," translated from Z. Fluwiss, Waltraumtorsch, Vol. 9, 1985, Heft 3.

29. Shirayama, S. Kuwahara, K. and Mendez, R.H., "A new three-dimensional vortex method," AIAA Paper 85-1488 (1985).

30. Beale, J.T. and Majda, A., "Vortex methods I: Convergence in three dimensions," Math. Comput., Vol. 39, 1982, pp. 1-27.

31. Beale, J.T. and Majda, A., "Vortex methods II: Higher order accuracy in two and three dimensions," Math. Comput., Vol. 39, 1982, pp. 29-52.

32. Beale, J.T. and Majda, A., "Vortex methods II: Higher order accurate vortex methods with explicit velocity kernels," J. Comput. Phys., Vol. 58, 1985, pp. 188-208.

33. Greengard, C., Three Dimensional Vortex Methods, Ph.D. thesis, University of California, Berkeley, 1984.

34. Anderson, C. and Greengard, C., "On vortex methods," SIAM J. Numer. Anal., Vol. 22, 1985, pp. 413-440.

35. Beale, J.T., "A convergent 3-D vortex method with grid-free stretching," Math. Comput., Vol. 46, 1986, pp. 401-424.

36. Knio, O.M. and Ghoniem, A.F., "Three dimensional vortex simulation using spherical, finite-core vortex elements," J. Comput. Phys., to be submitted for publication.

37. Widnall, S.E., Bliss, D.B. and Tsai, C.-Y., "The instability of short waves on a vortex ring", J. Fluid Mech., Vol. 60, 1974, pp. 35-47.

38. Widnall, S.E. and Sullivan, J.P., "On the stability of vortex rings", Proc. R. Soc. Lond., Series A, Vol.332, 1973, pp. 335-353.

NUMERICAL STUDY OF A THREE-DIMENSIONAL VORTEX METHOD

Omar M. Knio and Ahmed F. Ghoniem

Department of Mechanical Engineering
Massachusetts Institute of Technology
Cambridge, MA   02139

ABSTRACT

A three-dimensional vortex method based on the discretization of the vorticity field into vortex vector elements of finite spherical cores is constructed for the simulation of inviscid incompressible flow. The velocity is obtained by summing the contribution of individual elements using the Biot-Savart law desingularized according to the vorticity cores. Vortex elements are transported in Lagrangian coordinates, and vorticity is redistributed, when necessary, among larger number of elements arranged along its direction. The accuracy and convergence of the method are investigated by comparing numerical solutions to analytical results on the propagation and stability of vortex rings. Accurate discretization of the initial vorticity field is shown to be essential for the prediction of the linear growth of azimuthal instability waves on vortex rings. The unstable mode frequency, growth rate and shape are in agreement with analytical results. The late stages of evolution of the instability show the generation of small scales in the form of hair-pin vortex structures. The behavior of the turbulent vortex ring is in good qualitative agreement with experimental data.

I INTRODUCTION

The subject of this paper is the construction and validation of a Lagrangian, grid-free vortex method for the simulation of three-dimensional, unsteady, inviscid, incompressible flow. In these flows, as exemplified by shear layers, jets and wakes, vorticity remains confined to a small fraction of the total volume of the field while experiencing rapid and large distortion. Kinematically, vorticity is transported along particle paths while its magnitude is modified according to the strain field. Moreover, if the vorticity field and boundary conditions are specified, the velocity field can be computed by direct integration. Thus, a complete simulation scheme of the flow can be built on the tracking of the vorticity field in Lagrangian coordinates. These facts make vortex methods in which the vorticity field is represented by a finite number of localized vortex elements particularly attractive. Using these methods, accurate numerical simulation of complex non-linear flows can be achieved at a limited computational effort.

In a three-dimensional flow, several forms of instability may arise sequentially or simultaneously. As a result of these multiple instabilities, rapid and strong distortions of the flow map and the vorticity field are observed. The changes in the vorticity field can pose serious challenges to computational methods that attempt to capture the late stages of development using grids of fixed coordinates. Moreover, the changes in the vorticity distribution are associated with the formation of length scales which are smaller than those that existed at early times by the action of the strain field in the direction of the vortex lines. This makes it necessary to employ a scheme of local grid refinement as time progresses.

The desire to resolve small scale, streamwise structures in turbulent shear flows constitutes the motivation behind the task of constructing three-dimensional vortex methods. While the ultimate goal of this work is the

development of numerical solutions of the Navier-Stokes equations at high Reynolds number in complex geometry, we limit our attention in this paper to the construction and validation of a vortex method for the solution of the incompressible Euler equations in free space. The scheme is based on the discretization of the vorticity field into a number of vortex vector elements with finite point-symmetric cores, and following the motion of these elements in Lagrangian coordinates. The vortex vector elements change their vorticity according to the local stretch, while their direction is determined by the tilting of the material lines. The velocity is computed by summing over the fields of individual vortex elements which is evaluated from the desingularized Biot-Savart integral.

The evolution of vortex rings in an inviscid flow is selected as a case study for the validation of the proposed vortex method. The choice of this problem was motivated by the following reason. There exist two different linear stability theories, based on a non-deforming core model and a more accurate deforming core model, indicating that a vortex ring is unstable to azimuthal bending waves around its perimeter [1-4]. Experimental data which support the results of the linear theory of the deforming core model are also available [5-9]. Another attractive feature of vortex rings at high Reynolds numbers lies in the fact that the finite-amplitude wave breaking of the azimuthal instability does not lead to a substantial increase in the size of the support of the vorticity field. Instead, the process leads to the formation of a turbulized vortex ring, a ring of approximately the same dimensions as the original ring but with a highly turbulent core [3]. The volume over which computational elements should be distributed is thus not expected to increase substantially under the action of the strain field. Meanwhile, the growth of the number of computational elements, if necessary, will be mainly due to vortex stretching.

The paper is organized as follows. The formulation of the vortex method is described in Section II. The study of propagation and stability of vortex rings are tackled using two different physical models for their structure. In Section III, we use the thin tube model in which the core of the ring is assumed to be small and non-deformable. A more accurate model, where the dynamics of the flow within the core of the physical vortex are properly taken into account, is used in Section IV. Computations are performed for rings with different core-to-radius ratios and results of both models are compared to analytical expressions for the propagation velocity, to the predictions to the linear theory of vortex ring instability, and to experimental data. The simulations are then extended beyond the linear range of growth of the azimuthal instability to study the formation of a turbulent vortex ring. In Section V, we present conclusions regarding the convergence of the scheme and a discussion of the properties of vortex rings.

II FORMULATION AND NUMERICAL SCHEME

II.1. EQUATIONS OF MOTION

The motion of an incompressible, inviscid fluid is governed by the Euler equations:

$$\nabla \cdot u = 0 \tag{1}$$

$$\frac{\partial u}{\partial t} + u \cdot \nabla u = -\nabla p \tag{2}$$

expressing the conservation of mass and momentum, respectively. In these equations, $x = (x,y,z)$ is the position vector, $u = (u,v,w)$ is the velocity, t is time, $\nabla = (\partial/\partial x, \partial/\partial y, \partial/\partial z)$ is the gradient operator and p is pressure. Variables are non–dimensionalized with respect to the appropriate combination of a characteristic length, a characteristic velocity and the density. The governing equations can be rewritten in terms of the vorticity ω, defined as:

$$\omega = \nabla \times u \tag{3}$$

by taking the curl of Eq. (2). Using Eq. (1) and the fact that, by definition, the vorticity forms a solenoidal vector field, we obtain the vorticity transport equation:

$$\frac{\partial \omega}{\partial t} + u \cdot \nabla \omega = \omega \cdot \nabla u \tag{4}$$

Equation (4) indicates that the vorticity moves along a particle path while it is being tilted and stretched with the evolving strain field, ∇u. This can be seen by comparing the vorticity transport equation with the equation governing the evolution of a differential material element $\delta \chi$:

$$\frac{\partial}{\partial t} \delta \chi + u \cdot \nabla \delta \chi = \delta \chi \cdot \nabla u \tag{5}$$

This comparison yields the well-known Helmholtz theorem.

If the vorticity distribution is known, the velocity can be evaluated from the integration of Eqs. (1) and (3). Based on the uniqueness of the decomposition of a vector field, the velocity can be split into two components as follows:

$$u = u_\omega + u_p \tag{6}$$

where u_ω is a solenoidal field and u_p is an potential field. Furthermore, we assume the existence of a vector stream function ψ satisfying:

$$u_\omega = \nabla \times \psi \tag{7}$$

By construction, u_ω satisfies the continuity equation since $\nabla \cdot \nabla \times \psi$ vanishes identically. Substituting Eq. (6) into Eq. (3) and assuming that ψ itself is divergence-free, we get:

$$\nabla^2 \psi = -\omega \tag{8}$$

The solution of this equation is given by:

$$\psi(x) = \int G(x-x')\, \omega(x')\, dx' \tag{9}$$

where x' is the position of the volume element dx', and

$$G(x) = \frac{1}{4\pi\, r} \tag{10}$$

is the Green function of the Poisson equation in three dimensions, where $r = |x|$. As shown by Batchelor [10], the vector stream function ψ given by the above expression is solenoidal, as previously assumed, if the boundaries of the domain extend to infinity. Equation (6) states that the velocity can be written as the sum of a rotational component induced by the vorticity field in an unbounded space and a potential component required to satisfy the boundary conditions. For an unbounded domain with no interior boundaries, u_p vanishes identically.

The velocity component u_ω can be evaluated from Eqs. (7) and (9), yielding the well-known Biot-Savart law:

$$u(x) = \int K(x-x') \times \omega(x') \, dx' \tag{11}$$

where

$$K(x) = -\frac{1}{4\pi} \frac{x}{r^3} \tag{12}$$

Next, we show how to use Eqs. (4), (5) and (11) to construct a vortex scheme.

II.2. NUMERICAL SCHEME

The construction of the numerical method starts with the discretization of the initial vorticity field into a number of vortex vector elements, each with vorticity ω_i, on a three-dimensional mesh. The support of the initial vorticity is divided into volume elements dV_i, $i = 1, 2, \ldots, N$, and the vorticity is written as:

$$\omega(x,0) = \sum_{i=1}^{N} \omega_i(0) \, dV_i \, f_\delta(x-X_i) \tag{13}$$

where X_i is the center of the volume element dV_i, and ω_i is the vorticity associated with the element i. The vorticity associated with each element is smoothed in a small neighborhood of X_i according to a spherical core function f_δ with a core radius δ. The core function f_δ is chosen to satisfy the following conditions: (1) $\int f_\delta(x) \, dx = 1$ and f_δ converges to the Dirac delta function $\delta(.)$ in the sense of distributions as $\delta \to 0$; (2) the induced velocity field away from the core is the same as that induced by a concentrated vortex element, i.e., the core function decays at a fast rate; and (3) the velocity field of a finite vortex element is non-singular at its center. Let:

$$f_\delta = \frac{1}{\delta^3} f(\frac{r}{\delta}) \tag{14}$$

where f > 0 for r < δ and vanishes rapidly for r > δ, so that δ represents the radius of the shpere where most of the vorticity is concentrated. Note that if f_δ was chosen to be the Dirac delta function, Eq. (13) would represent the distribution of singular vortex elements. In what follows, a core function will always be used and δ will be taken as a positive number larger than the distance between the centers of neighboring elements. The accuracy of the discretization in Eq. (13) depends on: (1) the ratio δ/h, where h is the distance between neighboring elements; (2) the choice of the core function, f_δ; and (3) the scheme used to determine of the values of ω_i.

From the analysis of the computational results, we found that best accuracy is obtained for values of δ larger than the distance between neighboring elements. This last requirement, δ > h, will ensure that the core functions associated with neighboring elements are highly overlapping. This condition has been widely used in the analysis of the convergence properties of vortex algorithms [11-14], and it has been enforced in two-dimensional vortex simulations to improve the accuracy of the results [15,16]. In the computations, this condition will be satisfied even when the use of cubic volume elements is not practical. In this case, $dV = h_x h_y h_z$, and δ > h is replaced by δ > max $\{h_x, h_y, h_z\}$.

The accuracy of the discretization also depends on the shape of the core function f. The analysis of Beale and Majda [17] outlines a procedure that describes the construction of core functions which satisfy the above conditions and yield schemes of arbitrary high spatial order. In this work, the third order Gaussian core function:

$$f(r) = \frac{3}{4\pi} e^{-r^3} \tag{15}$$

is used. This core function, which was proposed by Leonard [18], has been shown to yield a second order discretization by Beale and Majda [17].

The accuracy of the computation also depends on the method used to find $\omega_i(0)$. Three methods have been proposed: (1) using a point measure of the vorticity, $\omega_i(0) = \omega(X_i,0)$; (2) using an average of the vorticity, $\omega_i(0) \, dV_i = \int \omega(X,0) \, dX$; and (3) solving the system of linear equations resulting from the application of Eq. (13) to the mesh points X_i, $i = 1, 2, \ldots, N$. In the two-dimensional version of the scheme, we found that the last algorithm yields the most accurate results for the initial vorticity discretization and for the initial development of the flow field. Thus, in the following computations, we use the last scheme to distribute the initial vorticity among the vortex elements.

Equation (13) remains unchanged if the quantity $\omega_i \, dV_i$ is replaced by $\Gamma_i \, \delta X_i$, where $\delta X_i = (X_{i+1} - X_{i-1})/2$ is a small material line segment in the direction of the local vorticity vector at X_i and Γ_i is the circulation. This substitution becomes unambiguous if the centers of the vortex elements are carefully chosen to lie on the vortex lines of the initial vorticity field so that both Γ_i and δX_i are well defined according to the initial vorticity distribution, and if the index i increases incrementally in the direction of ω. In this representation, δX_i is associated with a material line segment and Γ_i remains constant along a particle path, in accordance with Kelvin's theorem. As a consequence of the Helmholtz theorem, derived by comparing Eqs. (3) and (4), the evolution of δX_i, which will be denoted by $\delta X_i(t)$, can be related to the vorticity ω_i can be related as follows:

$$\omega_i(t) = \frac{|\omega_i(0)|}{|\delta X_i|} \, \delta X_i(t) \tag{16}$$

Using Eq. (16), the vorticity distribution expressed by Eq. (13) evolves according to:

$$\omega(x,t) = \sum_{i=1}^{N} \Gamma_i \, \delta\chi_i(t) \, f_\delta(x-\chi_i(t)) \tag{17}$$

In this expression, $\chi_i(t)$ is the coordinate of the material particle initially at X_i so that $\chi_i(0) = X_i$ is the Lagrangian coordinate of this point, and $\delta\chi_i(0) = \delta X_i$. A vortex element is thus described by $(\Gamma, \chi, \delta\chi)_i$. The evolution of the material line element, and the vortex vector element, $\delta\chi_i$ is governed by Eq. (5). Since χ_i is the position of a material particle and $\delta\chi_i$ is the material line, their evolution is governed, respectively, by:

$$\frac{d\chi_i}{dt} = u(\chi_i(t),t) \tag{18}$$

$$\frac{d}{dt}\delta\chi_i = \delta\chi_i \cdot \nabla u(\chi_i(t),t) \tag{19}$$

The solution of Eq. (4) is thus replaced by Eq. (17) and the solutions of Eqs. (18) and (19).

The velocity field u in Eqs. (18) and (19) can be obtained by substituting Eq. (17) into Eq. (11) and performing the integration. The result of the integration, which represents a discrete desingularized version of the Biot-Savart law, Eq. (11), is given by:

$$u_\omega = -\frac{1}{4\pi} \sum_{i=1}^{N} \Gamma_i \frac{(x-\chi_i) \times \delta\chi_i}{|x-\chi_i|^3} \, \kappa(\frac{r_i}{\delta}) \tag{20}$$

where $\kappa(r) = 4\pi \int_0^r f(r') \, r'^2 \, dr'$ and $r_i = |x-\chi_i|$. For the core function given in Eq. (15), the corresponding expression of κ is:

$$\kappa(r) = 1 - e^{-r^3} \tag{21}$$

Using a first-order time integration of Eqs. (18) and (19), the vortex element center, χ_i, and the vortex vector, $\delta\chi_i$, can be approximated, respectively, by:

$$\chi_i(t+\Delta t) = \chi_i(t) + u(\chi_i(t),t) \ \Delta t \tag{22}$$

and

$$\delta\chi_i(t+\Delta t) = \delta\chi_i(t) + \delta\chi_i(t) \cdot \nabla u(\chi_i(t),t) \ \Delta t \tag{23}$$

The velocity gradient ∇u_i can be evaluated analytically by differentiating the velocity expression in Eq. (19), as proposed by Anderson and Greengard [19]. However, in order to reduce the computational effort, the following approach is adopted. The velocity gradient along the vorticity vector can be approximated by:

$$\delta\chi_i \cdot \nabla u(\chi_i(t),t) = \frac{u(\chi_{i+1}(t),t) - u(\chi_{i-1}(t),t)}{2} \tag{24}$$

Substituting Eq. (24) into Eq. (23) and using Eq. (22), we get,

$$\delta\chi_i(t+\Delta t) = \frac{\chi_{i+1}(t+\Delta t) - \chi_{i-1}(t+\Delta t)}{2} \tag{25}$$

This approach explicity enforces the soleniodality of the vorticity field. The vortex filament scheme of Leonard [18,20] and the vortex stick scheme of Chorin [21-23] employ similar, but not identical devices to account for the change of vorticity as material lines are strained. In our computations, a second-order time integration is used to move the points χ_i:

$$\chi_i^* = \chi_i(t) + u(\chi_i,t) \quad \Delta t$$

and $\qquad\qquad\qquad\qquad\qquad\qquad\qquad\qquad\qquad\qquad\qquad\qquad$ (26)

$$\chi_i(t+\Delta t) = \chi_i(t) + \frac{u(\chi_i,t) + u^*(\chi_i^*,t)}{2} \Delta t$$

As mentioned before, this scheme implicitly enforces the connectivity of the vortex lines. It, thus, ensures that the vorticity field remains solenoidal, $\nabla\cdot\omega = 0$, irrespective of how accurate time integration or discretization of the vorticity field are.

As the flow develops strong stretch along the vortex lines, the value of $\delta\chi_i$ increases and the amount of vorticity carrie. by each vortex element grows. To maintain a uniform resolution, a vortex element is split into two elements each with $\delta\chi = \delta\chi_i/2$ and $\Gamma = \Gamma_i$, whenever the magnitude of $|\delta\chi_i|$ exceeds $2h_{max}$. This amounts to redistributing the vorticity field among a larger number of elements to prevent the deterioration of the accuracy of the discretization as the distance between neighboring elements increases due to the strain field.

To study the accuracy and convergence of this scheme, we compute the propagation and the linear stability of a vortex ring using two models: the thin tube model and the vortex torus model. Results of each model are compared with the corresponding linear theory of stability. We continue the computations beyond the linear range to illustrate the dynamics of the vorticity field at the later stages of development of the flow.

III RESULTS FOR THE THIN TUBE MODEL

This is a simplified model of a vortex ring. In this model, the cross section of the ring, with core radius σ, is represented by one vortex element with core radius $\delta = \sigma$. This "thin tube" model, while resembling the thin filament approximation proposed by Leonard [18], differs by the following. In the filament approximation, the core maintains its vorticity distribution as the filament is deformed. In the thin tube model, the relative motion of neighboring elements can affect the local vorticity distribution within the tube. Although this is not expected to cure the limitations of the thin vortex ring approximation, especially in determining the stability behavior of the vortex ring, we start with this case for its simplicity and computational efficiency. The model is used as a test case to examine the effect of the vortex element length, h, and the time step, Δt, on the accuracy of the computations.

III.1. SELF-INDUCED VELOCITY

The physical ring, of radius R, is divided along its axis into N vortex elements, each of length $h = \delta X_i = 2\pi R/N$, $i = 1, 2, \ldots, N$. To ensure overlap between neighboring elements, we use $\delta > h$ so that the vorticity within the core can be accurately discretized by the vortex elements. The vorticity distribution across the section of the ring, $\Omega(X)$, is best approximated by a second-order Gaussian distribution with a standard deviation σ. Equation (20) is used to evaluate the self-induced velocity, V, by summing the contribution of the elements around the ring. Results are compared with the analytical expression of Saffman [24] for a thin vortex ring: $\tilde{V} = \ln(8R/\sigma) - C$, where $\tilde{V} = 4\pi RV/\Gamma$ is the normalized velocity and C is a constant which depends on the vorticity distribution within the core. For a second-order Gaussian distribution $C = 0.558$ and σ is the standard deviation of the Gaussian curve.

A comparison between the computed value of $\tilde{V}$, using different values of N, and the analytical value is shown in Fig. 1 for $\sigma/R = 0.1$, 0.2 and 0.3. The results indicate that strong overlap between neighboring vortex elements, $\delta \sim 2h$, is necessary for the accurate prediction of $\tilde{V}$. It also shows that, as the ring becomes thinner, more elements are required to achieve accurate discretization, i.e. N grows as R/σ increases. Therefore, for a fixed core size, the number of elements required for accurate discretization grows with the curvature of the ring. The computed self-induced ring velocities are in good agreement with the values evaluated from the analytical expression for thin rings, while they are somewhat higher for thick rings. This is expected since the analytical expression was derived under the assumption that $\sigma/R \ll 1.0$.

III.2. STABILITY OF A THIN RING

A more interesting problem, which provides a test for the accuracy of the time-dependent calculations, is the growth of small perturbations on the vortex ring. There exists a rigorous linear theory for the stability of vortex rings in two forms: (1) for a ring with a non-deformable core, performed by Widnall and Sullivan [1]; and (2) a more elaborate theory where the dynamics of the flow within the core and its deformation are taken into account, reported in Widnall et al. [2], Widnall [25] and Widnall and Tsai [3]. The results of the current thin tube model will be compared to the predictions of the first analysis. In Section IV, the results of the vortex torus calculations, in which a number of elements are used to represent the ring cross section, will be compared with the theory of the deformable core.

To study the linear stability of thin rings using the thin tube model, a radial perturbation, with amplitude $\varepsilon = 0.02R$ and wavenumber n, is imposed on the axis of the vortex ring. The wavenumber is the number of waves that are fitted along the entire length of the ring axis. The size of the perturbation

varies in the azimuthal direction as $\Delta\rho = \varepsilon \sin(n\theta)$, where ρ denotes the radial direction in the plane of the ring and θ is the azimuthal angle. At t = 0, the ring lies in the x-y plane, the z-direction being the streamwise direction, and the vortex elements are displaced so that $\rho = R + \Delta\rho$. We start with n = 1 and increase the wavenumber by an increment of one. The time step used is $\Delta t = 0.10$ and the selected value of circulation is $\Gamma = 2.0$. Results are obtained for rings with $\sigma/R = 0.10$, 0.15, 0.20 and 0.25, and are analyzed in terms of the growth of the perturbation in the radial and streamwise directions. In the following, only the case of $\sigma/R = 0.1$ is discussed in detail.

For $n < n_n$, where n_n is the wavenumber of the neutrally stable mode, the ring spins around its unperturbed axis at a frequency λ_r that depends on the value of n. The motion described by any point on the ring, with respect to the unperturbed axis of the ring, is that of an ellipse whose major axis is in the radial direction and the minor axis is in the streamwise direction (if the perturbed ring is opened to form a rectilinear vortex, it will resemble a corkscrew spinning at a frequency λ_r and, hence, these bending waves are also called helical waves). The sense of rotation of the ring is the same as that of the ring vorticity. The frequency of rotation, λ_r, starts low at small n, grows to a maximum and then decreases again as n moves towards n_n. The amplitudes in the ρ-direction and z-direction are shown in Fig. 2 for n = 2, 5, 8 and 12. The figure shows that the radial perturbation produces a streamwise perturbation of almost the same magnitude. These modes are characterized as being linearly stable since their amplitudes remain bounded.

At $n = n_n$, the wave neither grows nor rotates. For $\sigma/R = 0.1$, and $n_n = 13$ the ring remains in its original plane without bending, as depicted in Fig. 3. For the next mode, $n^* = 14$, the wave grows in the radial direction and then in the streamwise direction so that the total amplitude grows

exponentially in time, i.e., the ring becomes linearly unstable, as shown in Fig. 4. Moreover, wave rotation is not observed. At higher values of n, n > n^*, the ring is stabilized again and the eigenfunctions behave in a similar way to those corresponding to n < n_n, with the exception that the major axis of the ellipse is now in the streamwise direction and the sense of rotation of the wave is reversed. The wave amplitudes in the ρ and z-directions are shown in Fig. 5 for n = 15 and 19.

Similar observations are made for rings with σ/R = 0.15, 0.20 and 0.25. In all cases, the unstable mode n^* is a bifurcation in the eigenfunction that corresponds to λ_r = 0. In Fig. 6, λ_r, normalized with respect to Γ/R^2, is plotted against the non-dimensional wavenumber defined as k = $n\sigma/R$. The unstable mode $k^* = n^*\sigma/R \sim 1.25$ corresponds to a non-rotating mode, λ_r = 0, for all the values of σ/R. This is in agreement with the analytical results of Widnall and Sullivan [1] for the stability of rings with non-deformable cores. They observed that a mode becomes unstable when the self-induced rotation of the wave balances the rotation induced by the ring, and the energy of the perturbation is expent in stretching the wave amplitude.

In order to check on the accuracy of the computations, we varied the discretization parameter h by using more elements around the ring axis. Figure 7 shows the growth of the amplitude of the perturbation $a_p = \sqrt{\Delta\rho^2 + \Delta z^2}$, computed using an increasing number of elements for the unstable mode of a ring with σ/R = 0.2, n^* = 7. Although N = 30 is the smallest number of elements required to satisfy the condition δ > h, we notice that N = 90 is necessary to compute the growth rate accurately. This is the same number of elements required for the accurate prediction of the self-induced velocity of the unperturbed ring, $\tilde{V}$ = 3.1309, as seen in Fig. 2. Using this value of N was also necessary for the discrete vorticity field, $\Omega(X)$, to become independent of N. This is not surprising since the stability of the wave

depends strongly on the velocity and strain field induced by the ring on the perturbation. The growth rate α_x, defined as $\alpha_x = d(\log a_p)/dt$, is computed from Fig. 7 as 0.162. The analytical value of α_x for the same value of $\tilde{V}$ is $\alpha_x = 0.157$ [1].

The effect of the time step, Δt, on the computed results is studied in a similar way. Figure 8 shows the growth of the wave amplitude for $\sigma/R = 0.2$, using $N = 100$, employing decreasing values of Δt. For $\Delta t < 1.0$, the computations are almosty insensitive to the choice of Δt. Results diverge for $\Delta t > 1.0$, showing an accelerated growth of the perturbation accompanied with a high rate of stretch along the ring. For the other cases of σ/R, the computations were repeated using $\Delta t = 0.05$ but yielded no appreciable change in the results. In the following computations, we use $\Delta t = 0.10$ for rings having the same value of circulation.

In Fig. 9, we plot the critical wave number n^* against the self-induced velocity $\tilde{V}$, used to characterize the ring, for the four cases of σ/R. We have reproduced on the same figure the analytical results of Widnall and Sullivan [1] for the non-deformable core model, and their experimental results. The results agree well with the results of the stability theory of vortex rings with non-deformable cores. The model, as expected, is unable to describe the stability characteristics of a vortex ring with a deformable core. The computed results are, however, closer to the experimental data than those obtained by the long wave stability analysis. This seems to support earlier speculation that the use of vortex elements allows small first order deformation in the vorticity core of the ring which causes the computed results to behave slightly better than those of the corresponding linear theory.

III.3. SHAPE OF INSTABILIY

The growth of the perturbation is now examined by observing the deformation it develops along the vortex ring, i.e. the eigenfunction of the instability. Figure 10 depicts two views of the vortex elements, connected along the direction of vorticity, for a ring with $\sigma/R = 0.25$, at $t = 140$, 180, 210 and 230. The ring is initially perturbed at $n^* = 6$ with $\epsilon/R = 0.02$. According to the results, the evolution of the instability can be divided into three stages. In the linear stage, $t < 140$, the perturbation grows as a standing wave, as predicted by the linear theory and verified by the analysis of the numerical results in the previous section. The growth of the number of vortex elements, and concomitantly the vorticity, is negligibly small.

In the non-linear stage, $140 < t < 190$, the amplitude of the instability continues to grow, but the condition of zero rotation is no longer satisfied. Due to this growth, the peaks of the waves extend radially outwards, while they are stretching in the direction opposite to the direction of propagation of the ring. The peaks suffer a strong stretch that sends them away from the original axis of the ring, generating counter-rotating vortex rods, or hairpin vortices. In the meantime, the valleys of the wave rotate slowly, forming flat connections between neighboring hairpins.

At the later stages, $t > 190$, violent stretching of the hairpin vortices, with an exponential growth of the total arclength of the ring, is observed. However, the outward-reaching, inverted U-shaped vortices, the hairpin vortices, do not continue to move outwards. Instead, they fold backwards, stretching towards the original axis of the ring. In the meantime, the number of elements used to discretize the ring continues to increase, growing from N $= 90$ at $t = 0$ to $N = 802$ at $t = 230$. This catastrophic growth of the number of elements forced us to stop the computations at this time. Similar exponential growth of vorticity has been observed before in models that employ thin filament approximations of vorticity structures, e.g., [26,27].

As has been shown before, the thin tube model does not allow enough changes within the core of vorticity to capture higher order radial bending modes that support the short wave instability observed experimentally. To overcome this limitation, a more detailed description of the ring in which the core vorticity is discretized into a number of vortex elements with $\delta < \sigma$, is used in Section IV. We call this model the vortex torus.

IV RESULTS FOR THE VORTEX TORUS

This is a more elaborate model of a vortex ring. The terminology is motivated by the way the physical ring is discretized. The core of the vortex ring is represented by several vortex elements whose cores are smaller than that of the enclosing torus, $\delta < \sigma$. The vortex ring is thus modeled by a number of thin vortex tubes arranged within its core, forming a vortex torus. Note that we still call the physical object a ring, while the model is labelled as torus. The motion of the elements throughout the cross section of the torus allows substantial deformation of its core at different radial and azimuthal stations. Therefore, higher-order radial modes associated with the instability of vortex rings, as observed in the linear stability analysis, are expected to be properly simulated. The larger the number of elements arranged in the radial direction within the torus core, the higher the order of the radial instability which can be captured by the simulations.

IV.1. DISCRETIZATION OF THE VORTICITY CORE

The initial vorticity of the vortex elements, $\omega_i(0)$, is computed by solving a linear system of equations formed by applying Eq. (17) to a three-dimensional radial mesh within the torus. The centers of the vortex elements are located at the centers of the mesh cells, and the left hand side of Eq. (17) is set equal to the total vorticity of the vortex ring at the center of the vortex element. This ensures that the numerical value of the vorticity at the mesh center is equal to that of the initial vorticity of the ring. The mesh is constructed using N_c cross sections of the torus separated by an angle $\Delta\theta = 2\pi/N_c$, and N_r points within each cross section. The elements within each cross section of the ring are arranged on N_s radial locations. Initially, the vorticity of the ring, Ω_θ, is aligned with the azimuthal θ-direction and is independent of θ. The coordinate system which is used to describe the ring is shown in Fig. 11a. Thus, N_r equations are solved for the initial vorticity of

the elements within a particular cross section. The initial vorticity within the core of the ring is taken as as third-order Gaussian distribution:

$$\Omega_\theta(r) = \frac{1}{a\sigma^2} \exp(-\frac{r^3}{\sigma^3})\, e_\theta \tag{27}$$

where e_θ is the unit vector along the unperturbed ring axis, r is measured from the center of the vorticity core, as shown in Fig. 11a, $a = \pi/3\,\gamma(2/3)$, σ is the standard deviation of the Gaussian and γ denotes the Gamma function. The constant a is chosen so that the normalized circulation of the vortex ring is 2, and Ω_θ is positive so that the ring moves in the positive z-direction in a right-handed reference frame.

Three different meshes are used to discretize the vorticity of the ring, as shown in Fig. 11b. Mesh I is a uniform radial mesh; mesh II is a staggered radial mesh; and mesh III is an equi-spaced radial mesh. In meshes I and II, all the radial stations within the core have the same number of elements. In mesh I, the elements are aligned on radial rays, while in mesh II, they are radially staggered. In both cases, the radial distance between neighboring elements increases as we move outwards. In mesh III, the number of elements increases as we move outwards to maintain the radial distance between neighboring elements approximately the same. In all cases, the number of elements in the θ-direction for each radial location, N_c, was chosen such that the self-induced velocity of individual thin tubes were accurately predicted according to the analysis in the previous section.

Many choices of the mesh and of the core of the vortex elements would satisfy Eq. (13). The locations of the centers of the vortex elements, and the core radius of the elements, δ, are chosen to satisfy the following conditions: (a) the element core radius should be large enough to ensure overlap between neighboring elements; and (b) the order of magnitude of the

vorticity of the elements at different radial stations is the same to optimize the utilization of the elements; and (c) the total circulation of the elements is as close as possible to the circulation of the ring. When it was not possible to satisfy the three conditions simultaneously, a compromise which favored the enforcement of condition (c) was used.

Tests for the accuracy of the discretization of the vorticity field were performed for a ring with $\sigma/R = 0.275$ for the following cases: (1) mesh I with $N_r = 9$, 17, 25 and 33; (2) mesh II with $N_r = 17$, 25 and 33; and (3) mesh III with $N_r = 19$, 37 and 61, all shown in Fig. 11b. The results of the computations are summarized in Table I. The accuracy of the discretization is measured in terms of: (1) the deviation of the computed value of Γ from the intended value of 2; (2) the predicted value of the self-induced velocity; (3) the error in the vorticity field $E_1 = 1/\Gamma \int_A |\Omega_\theta(r) - \omega_\theta(r,0)| dA$, where A is the cross-sectional area of the vortex torus; and (4) the predicted most unstable mode n^*. In light of the results of the first three quantities, the following observations can be made:

(1) To satisfy the conditions for accurate discretization, the core radius of the vortex elements, δ, must decrease at a slower rate than the separation between elements, h. In each case, the results show that δ decreased slightly while the number of elements was doubled. This is in agreement with the convergence results of Beale and Majda [12,13];

(2) The computed values of the self-propagation velocity, $\tilde{V}$, are within less than 0.5% variation for all cases. This is despite the larger error in the vorticity discretization, E_1. A similar trend is shown in the values of Γ. The fact that both $\tilde{V}$ and Γ are integrals, or averages, of the vorticity field explains why the error diminishes.

(3) E_1 decreases substantially when an equi-distance mesh, which guarantees the maximum overlap among the vortex elements at the outer

radial stations, is used. Note that when using mesh I with N_r = 25 and 33 and mesh II with N_r = 33, it was not possible to satisfy condition (a) at the outermost radial location of the elements, which resulted in a non-diminishing E_1. Using almost the same number of elements in mesh III resulted in an order of magnitude drop in the error.

IV.2. STABILITY OF A VORTEX TORUS

To investigate the effects of the discretization parameters on the evolution of the instability of the ring, the torus with σ/R = 0.275 was initially perturbed by fitting n sinewaves with an amplitude ε/R = 0.02 along the perimeter. The number of cross sections along the θ-direction was chosen so that at least 10 elements were used to fit a single sinewave. The integration time step Δt = 0.10, and the computations were carried for 1000 time steps. To obtain an accurate measure for the evolution of the perturbation around the torus, the computed energy spectrum of the ring was examined. The energy spectrum was evaluated by computing the discrete Fourier transform of the energy calculated at 200 points evenly distributed along a circle of radius ρ = R, located at z = z_a, z_a being the average streamwise location of the vortex elements. In the following section, we will investigate the growth of the perturbation in the physical plane.

Figure 12 shows the evolution of the amplitude of the excited wavenumbers n = 7, 8, 9, 10, 11 and 12 using mesh I with N_s = 1 and N_r = 9. At n = 7 and 8, the amplitudes oscillate without growth, indicating that the ring is stable to these waves. For n = 9 and 10, the amplitudes grow exponentially at the early stages, t < 30, and continue to grow at a more moderate rate at later times. The rate of growth is higher for n = 10, indicating that this is the fastest growing mode n^*. For n > n^*, the amplitudes of the waves oscillate and a stable behavior is observed. The computations were repeated using mesh I with N_s = 2 and N_r = 17, and the results are plotted in Fig. 13 showing the

evolution of the amplitudes of the waves $n = 9$, 10, 11, 12 and 13. These results show that $10 \geq n \leq 13$ are stable waves, while $n = 11$ and 12 are unstable waves. Here, $n^* = 12$ corresponds to the most unstable perturbation.

By repeating the computations for $N_r = 25$ and 33 using mesh I, we confirmed that $n^* = 12$. As shown in Table I, the same value for the most unstable wavenumber was obtained using mesh II with $N_r = 17$ and 25, and using mesh III with $N_r = 19$ and 37. A more detailed account of the results of these computations is shown in Fig. 14. These results indicate that mesh I with $N_r = 9$ did not provide enough resolution to capture the correct unstable mode. More careful inspection of Fig. 14 reveals that while the early behavior of the results of mesh I with $N_r = 25$ and 33 agree with those obtained using the other discretization parameters at early time, they diverge at later times.

Comparison of the evolution of the instability, when computed using the eight discretization meshes, reveal the following:

(1) At least two radial locations within the core are needed to ensure accurate prediction of the unstable mode in vortex rings. When we used mesh I with $N_s = 1$, the resolution of the vorticity field could not capture the correct wavenumber of the unstable mode. This is expected since the instability observed here, according to the results of the linear theory, corresponds to the second radial mode which should be properly represented. A single radial station within the core is not sufficient for proper resolution of this mode. Note that using more than two locations did not affect the value of n^*.

(2) For accurate simulations using the vortex method, overlap between the elements must be maintained at all times. When this condition is not observed, convergence of the results may not be achieved. Note that the loss of overlap is responsible for large error in the estimate of the

initial amplitude of the perturbation for mesh I with N_r = 25 and 33, as seen from Fig. 14.

(3) The prediction of the unstable mode and the evolution of the instability are independent of the initial location and number of vortex elements when: (a) overlap between neighboring elements is ensured, (b) at least two radial stations within the core are present and (c) a sufficiently small time step Δt is used.

These conclusions were further confirmed by inspecting the long time energy spectrum for the five cases for which conditions (a)-(c) hold, mesh I with N_r = 17, mesh II with N_r = 17 and 25, and mesh III with N_r = 19 and 37. Figure 15 shows the behavior of the unstable wavenumber, n^* = 12, and its first harmonic, n = 24, for the five cases. The response of the unstable mode and that of its harmonic are in close agreement for the five cases. For cases where overlap was not maintained, the generation of the first harmonic was not observed.

To derive the relationship between $\tilde{V}$ and n^*, the computations were repeated for rings with σ/R = 0.325, 0.375 and 0.45. The corresponding self-induced velocity was $\tilde{V}$ = 3.13, 2.98 and 2.79. The tori were discretized on mesh I using N_r = 9 and 17, and were perturbed as for the σ/R = 0.275 case. Results are summarized in Table II, and plotted on Fig. 16. These results indicate that the relationship between the unstable wavenumber and normalized self-induced velocity derived by using a single radial station within the core is not accurate. The computed results obtained by using <u>two or more radial</u> stations are in excellent agreement with the results of the linear theory, and in very good agreement with experimental data. It is interesting to note that using two radial locations for vorticity discretization, we find two amplified wavenumbers. This indicates that the ring is unstable to a narrow frequency band and that, in reality, both modes may grow simultaneously [3].

IV.3. SHAPE OF INSTABILITY

The shape of a vortex ring undergoing deformation due to the growth of azimuthal instability is now analyzed using the results of numerical simulation based on the vortex torus model. We study the evolution of a ring perturbed at the most unstable wavenumber and compare the results with observations made by the linear stability theory, starting with analysis of the evolution of the flow field of a ring perturbed at a stable wavenumber.

Figure 17 depicts two views of the vortex torus with $\sigma/R = 0.275$ when perturbed by a stable wavenumber $n = 9$, at time $t = 10, 40, 70, 100$, computed using mesh II with $N_r = 17$. These views are generated by projecting the lines connecting the vortex elements initially aligned along vortex lines on the planes normal and parallel to the direction of propagation of the ring. The figure shows that the vorticity core experiences a mild deformation due to the motion of individual vortex elements around the original axis of the torus. However, the amplitude of the perturbation remains bounded while the waves rotate around the axis of the ring, as seen by the exchange of peaks and valleys at the same azimuthal location around the ring. The frequency of rotation of the waves is the same as that predicted by the curve in Fig. 13. The number of vortex elements used to discretize the vorticity field of the ring remains constant during the entire run, $N = 2040$, indicating that the corresponding vorticity stretch is negligibly small.

Figure 18 shows perspective views of the same vortex torus when perturbed at the most unstable wavenumber, $n^* = 12$, depicted at time $t = 30, 60, 90, 120$. During the initial stages, and within the linear range of the instability, the waves do not rotate around the axis on the ring while their amplitudes grow at an exponential rate. The growth of the perturbation as standing waves has been predicted by the linear stability theory. The perturbation grows in the radial and streamwise directions causing substantial

non uniform deformation around the ring. At $t > 30$, while the rate of growth subsides due to the onset of non-linear dynamics, the deformation of the ring continues to reshape the vorticity structure. The figure shows that the outer sections of the standing waves continue to extend radially outwards while they are being tilted in the direction opposite to the direction of propagation of the ring. On the other hand, the inner parts of the waves extend inwards towards the center of the ring while they are being tilted opposite to the direction of propagation of the ring. During this stage, the entire cross section of the core moves almost in phase. This process leads to a redistribution of the ring vorticity into a number of sectors equal to the number of waves.

At later stages, $t > 90$, the core experiences more deformation due to the motion of different radial locations at different speeds. The figure shows that the inner and outer radii of the ring move in anti-phase, leading to deformations at scales smaller than the scale of the initial perturbation. The formation of small scales can be examined by looking at the long time energy spectrum. Figure 19 displays the time-change of the amplitude of the perturbation wavenumber, n^*, and of its higher harmonics, $2n^*$ and $3n^*$, showing how higher harmonics are energized after the saturation of the fundamental frequency. It is interesting to observe that the generation of small scales takes the form of an energy cascade in which successively excited wavenumbers are higher harmonics of the most unstable wavenumber. This is also associated with severe stretching of the vortex lines, as indicated by the growth of the number of vortex elements from $N = 2040$ at $t = 0$ to $N = 6936$ at $t = 140$ where we had to terminate the computations.

Three perspective views of the vortex ring at $t = 140$ are shown in Fig. 20. The figure shows that vortex lines at the outside radii elongate along the negative z-direction reaching a maximum in the direction opposite to that

of propagation of the ring and then fold forwards towards its center. On the other hand, vortex lines at the inside radii of the ring stretch along the positive z-direction reaching a maximum in the direction of propagation of the ring and then fold backwards towards its center. The mechanism of vortex line folding maintains the ring coherent and is responsible for the formation of the hairpin vortices. The shape of the ring at the later stages is in agreement with experimental observation [8,9]. This suggests that these hairpin vortex structure, which were also observed in the late stages of development of the thin tube model, represent fundamental forms for vortex lines in turbulent flows.

TABLE I

SUMMARY OF DISCRETIZATION RESULTS FOR A RING WITH $\sigma/R = 0.275$

UNIFORM MESH I

N_r	N_s	δ/R	$\Delta r/R$	Γ	$\tilde{V}$	E1x100	$n^{\star}$
9	1	0.1875	0.1700	2.0033	3.277	3.5047	10
17	2	0.1550	0.1087	1.9993	3.291	3.4472	12
25	3	0.1425	0.0900	2.0089	3.285	2.8073	12
33	4	0.1425	0.0650	1.9988	3.297	3.4559	12

STAGGERED MESH II

17	2	0.1550	0.1090	2.0027	3.290	3.4250	12
25	3	0.1512	0.0825	2.0011	3.265	2.1934	12
33	4	0.1250	0.0762	2.0014	3.303	2.3219	—

EQUI-SPACED MESH III

19	2	0.1550	0.1080	2.0007	3.281	3.1814	12
37	3	0.1550	0.0910	1.9992	3.296	0.4120	12
61	4	0.1500	0.0705	1.9999	3.297	0.3480	—

TABLE II

SUMMARY OF THE COMPUTED UNSTABLE WAVENUMBER USING MESH I

$\sigma/R = 0.275$	n	$N_r = 9$	$N_r = 17$
	7	stable	——————
	8	stable	——————
	9	unstable*	stable
	10	unstable*	stable
	11	stable	unstable*
	12	stable	unstable*
	13	——————	stable

$\sigma/R = 0.325$	n	$N_r = 9$	$N_r = 17$
	6	stable	—————
	7	neutral *	—————
	8	unstable*	stable
	9	stable	unstable*
	10	stable	unstable*
	11	——————	stable

$\sigma/R = 0.375$	n	$N_r = 9$	$N_r = 17$
	5	stable	—————
	6	unstable*	—————
	7	unstable*	stable
	8	stable	unstable*
	9	stable	unstable*
	10	——————	stable

$\sigma/R = 0.45$	n	$N_r = 9$	$N_r = 17$
	4	stable	—————
	5	unstable*	stable
	6	unstable*	unstable*
	7	stable	unstable*
	8	——————	stable
	9	——————	stable

* indicates the most unstable

V DISCUSSION AND CONCLUSIONS

In this work, a three-dimensional vortex method for the solution of the unsteady, inviscid, incompressible flow equations is constructed, and its convergence and accuracy are investigated. The method is applied to the study of the evolution of unstable vortex rings in an unbounded fluid. Two models for the vorticity core of the ring are introduced, a thin tube model where the vorticity of the core is concentrated into a single vortex element, and a vortex torus model where several elements are used to represent the core cross-section. Computed results for both models are compared to analytical predictions of the number of waves of the unstable mode and the properties of the corresponding eigenfunction of the linear stability problem.

The following numerical parameters have been shown to play an important role in the accuracy and convergence of vortex methods: the smoothing core, f; the ratio of core radius to separation between neighboring elements, δ/h; the numerical integration procedure; the time step Δt; and the vorticity initialization procedure. In our numerical study of the scheme, the approach we followed was to view the three-dimensional vortex method as an extension of its two-dimensional counterpart. In doing that, and due to the expensive nature of the computations, we have implicitly taken advantage of results which had already been established in the two-dimensional case and have not experimented with those areas where analytical analysis is more revealing. In particular, the effect of the smoothing function, which has been shown to control the spatial convergence order of scheme [17], was not studied. A single second-order time integration scheme was adopted for all the computations and we were content to verify that the results were insensitive to decreasing the time step.

This study has revealed two crucial ingredients in the application of three-dimensional vortex methods, namely the procedure of discretization of

the initial vorticity field and the method of maintaining overlap between neighboring elements. Accurate discretization of the vorticity field into overlapping elements is found necessary for convergence of the results. The accuracy of the discretization, which is shown to depend on the mesh and the core radius of the elements, can be measured by the deviation from the target profile. The initialization procedure has to be further constrained by the condition that neighboring elements must have overlapping cores. When this last condition was not satisfied, results were found to diverge rapidly. Best results were obtained when the initial mesh is chosen so that the distance between neighboring elements is almost the same in all directions. Finally, it is also shown that maintaining overlap between neighboring elements at all times is necessary. This is achieved through the redistribution of the vorticity field into a larger number of elements when the strain field causes separation between neighboring elements to exceed the core radius. An analogous situation is encountered in the two-dimensional case [16] where overlap can be lost due to strain normal to the direction of the local vorticity vector. We have not experienced such a problem in the case of the vortex ring since the instability did not cause substantial growth of the core itself.

Results of the thin tube model are found to be in good agreement with the results of the corresponding linear theory. In this model, the dynamics of the vorticity core are neglected, and the instability of the vortex ring is spuriously predicted [2]. The model is in poor agreement with experimental data, however, the behavior of real unstable vortex rings is qualitatively obtained. The study shows that the unstable wave number corresponds to a non-rotating mode and that the unstable wavenumber increases with the normalized self-induced velocity of the ring. Results for the vortex torus model are in excellent agreement with theoretical results on the stability of real vortex

rings and in good agreement with experimental data. They suggest that the numerical constraints discussed above have to be supplemented with the condition that the initial mesh where the vorticity is discretized should be appropriate for the physics of the problem to be properly represented. The vortex ring is found unstable to perturbations lying in a small overlapping band around the critical wavenumber.

The evolution of the instability beyond the linear range indicates that the onset of the turbulization of the core of vorticity is associated with harmonics of the unstable mode, excited in succession in the form of a discrete energy cascade. The ring is substantially deformed around the azimuth and hairpin vortices are generated at the edges of the vorticity core. While a qualitatively similar behavior was obtained by using the thin tube model, the shape of the vortex torus is more realistic and in much better agreement with experimental observation.

REFERENCES

1. Widnall, S.E. and Sullivan, J.P. "On the stability of vortex rings," Proc. Roy. Soc. London A332, 1973, pp. 335-353.

2. Widnall, S.E., Bliss, D.B. and Zalay, A. "The instability of short waves on a vortex ring," J. Fluid Mech., 66, 1974, pp. 35-47.

3. Widnall, S.E. and Tsai, C.-Y. "The instability of the thin vortex ring of constant vorticity," Proc. Roy. Soc. London A1334, 1977, pp. 273-305.

4. Saffman, P.G. "The number of waves on unstable vortex rings," J. Fluid Mech., 84, 1978, pp. 625-639.

5. Maxworthy, T. "The structure and stability of vortex rings," J. Fluid Mech., 51, 1972, pp. 15-32.

6. Maxworthy, T. "Turbulent vortex rings," J. Fluid Mech., 64, 1974, pp. 227-239.

7. Maxworthy, T. "Some experimental studies of vortex rings," J. Fluid Mech., 81, 1977, pp. 625-639.

8. Lugt, H. Vortex Flow in Nature and Technology, Wiley, 1983.

9. Van Dyke, M. An Album of Fluid Motion, Parabolic, 1982.

10. Batchelor, G.K. An Introduction to Fluid Dynamics, Cambridge University Press, 1967.

11. Beale, J.T. and Majda, A. "Vortex methods I: Convergence in three dimensions," Math. Comput., 39, 1982, pp. 1-27.

12. Beale, J.T. and Majda, A. "Vortex methods II: Higher order accuracy in two and three dimensions," Math. Comput., 39, 1982, pp. 29-52.

13. Hald, O. "The convergence of vortex methods II," SIAM J. Num. Anal, 16, 1979, pp. 726-755.

14. Hald, O. and Del Prete, V.M. "Convergence of vortex methods for Euler equations," Math. Comput., 32, 1978, pp. 791-809.

15. Ghoniem, A.F., Heidarinejad, G. and Krishnan, A. "Numerical simulation of a reacting shear layer using the transport element method," AIAA Paper 87-1718, 1987.

16. Ghoniem, A.F., Heidarinejad, G. and Krishnan, A. "Numerical simulation of a thermally stratified shear layer using the vortex element method," J. Comp. Phys., in press, 1988.

17. Beale, J.T. and Majda, A. "Vortex methods II: Higher order accurate vortex methods with explicit velocity kernels," J. Comp. Phys., 58, 1985, pp. 188-208.

18. Leonard, A. "Computing three-dimensional incompressible flows with vortex elements," Ann. Rev. Fluid Mech., 17, 1985, pp. 525-559.

19. Anderson, C. and Greengard, C. "On vortex methods," SIAM J. Num. Anal., 22, 1985, pp. 413-440.

20. Leonard, A. "Vortex methods for flow simulation," J. Comp. Phys., 37, 1980, pp. 289-335.

21. Chorin, A.J., "Vortex models and boundary layer instability," SIAM J. Sci. State. Comput., Vol. 1, 1980, pp. 1-21.

22. Chorin, A.J., "Estimates of intermittency, spectra and blow-up in developed turbulence," Commun. Pure Appl. Math., Vol. 34, 1981, pp. 853-866.

23. Chorin, A.J. "The evolution of a turbulent vortex," Comm. Math. Phys., 83, 1982, pp. 517-535.

24. Saffman, P.G. "The velocity of viscous vortex rings," Stud. Appl. Math., 49, 1970, pp. 371-380.

25. Widnall, S.E. "The structure and dynamics of vortex filaments," Ann. Rev. Fluid Mech., 8, 1976, pp. 141-165.

26. Siggia, E.D. "Collapse and amplification of a vortex filament," Phys. Fluids, 28, 1985, pp. 794-805.

27. Pumir, A. and Siggia, E.D. "Vortex dynamics and the existence of solutions to the Navier-Stokes equations," Phys. Fluids, 30, 1987, pp. 1606-1626.

FIGURE CAPTIONS

Figure 1. Normalized self-induced velocity of the ring, $\tilde{V} = V/(\Gamma/4\pi R)$, vs. the number of vortex elements around the perimeter, N. The analytical results of Saffman [23] are represented by straight lines. $\sigma/R = 0.1 \rightarrow$ o; $\sigma/R = 0.2 \rightarrow$ +; $\sigma/R = 0.3 \rightarrow$ v.

Figure 2. Evolution of the amplitude of the perturbation in the radial ρ- and streamwise z-direction for a vortex ring with $\sigma/R = 0.1$, computed using the thin tube approximation. Both amplitudes are normalized with respect to the initial perturbation, $\varepsilon/R = 0.02$, and time is normalized with respect to R^2/Γ. The wavenumber n = 2, 5, 8 and 12 as indicated.

Figure 3. Amplitude of the perturbation for the ring of Fig. 2 and $n = n_n = 13$.

Figure 4. Amplitude of the perturbation for the ring of Fig. 2 excited at the unstable wavenumber $n^* = 14$.

Figure 5. Amplitude of the perturbation for the ring of Fig. 2 perturbed at n = 15 and 19 arranged from the top.

Figure 6. Frequency of rotation λ_r, normalized with respect to R^2/Γ, vs. non-dimensional wavenumber K, defined as $K = n\sigma/R$. $\sigma/R = 0.1 \rightarrow$ v; $\sigma/R = 0.15 \rightarrow$ *; $\sigma/R = 0.2 \rightarrow$ \; $\sigma/R = 0.25 \rightarrow$ (diamond).

Figure 7. The growth of the natural logarithm of the unstable mode amplitude, $n^* = 7$, for the ring with $\sigma/R = 0.2$, computed using N = 30-140 with increments of 10.

Figure 8. The growth of the unstable wavenumber for the ring of Fig. 7 using $\Delta t = 2.0, 1.0, 0.5, 0.4, 0.3, 0.2,$ and 0.1, all using N = 100.

Figure 9. The computed wavenumber of the most unstable mode n^* (Δ) vs. the normalized self-induced velocity, $\tilde{V}$, compared with the analytical (o) and experimental (x) results of Widnall and Sullivan [1].

Figure 10. The form of the vortex ring with $\sigma/R = 0.25$ excited at the unstable wavenumber $n^* = 6$. The plots are obtained by projecting the ring on planes

parallel and normal to its direction of propagation at t = 140, 180, 210 and 230, respectively, arranged from the top.

Figure 11. (a) The geometry of the vortex tortus, (b) Schematic cross-sections of the vortex torus showing the location of the vortex elements for various meshes used in the computations.

Figure 12. Evolution of the natural logarithm of the amplitude of the excited modes for the vortex ring with σ/R = 0.275 using mesh I and N_r = 9.

Figure 13. Natural logarithm of the amplitude of the excited modes for the ring of Fig. 13 using mesh I and N_r = 17.

Figure 14. Evolution of the natural logarithm of the most unstable mode n^* = 12 for the ring of Fig. 12 using: mesh I with N_r = 9, 17, 25 and 33; mesh II with N_r = 17 and 25; and mesh III with N_r = 19 and 37.

Figure 15. Natural logarithm of the amplitude of the unstable mode, n^*, and its first harmonic, $n = 2n^*$, for the ring of Fig. 12 using mesh I with N_r = 17, mesh II with N_r = 17 and 25; and mesh III, with N_r = 19 and 37.

Figure 16. The wavenumber of the most unstable mode, n^*, computed using mesh I with N_r = 9 (diamond) and N_r = 17 (*), plotted against the normalized self-induced velocity, $\tilde{V}$, compared with the analytical results of Widnall et al. [2] for a ring with constant (square) and quadratic (+) vorticity distributions. The results of Fig. 9 are also included.

Figure 17. The form of the vortex torus with σ/R = 0.275 perturbed at n = 9 at t = 10, 40, 70 and 100, respectively, arranged from the top. The results are obtained using mesh I with N_r = 17, and shown in terms of the lines connecting neighboring vortex elements arranged in the vorticity direction.

Figure 18. Perspective views of the vortex torus of Fig. 17 excited at n^* = 12 depicted at t = 30, 60, 90 and 120, taken from the point of view of an observer standing ahead of the ring and looking at an angle β = 60° with respect to the direction of propagation. The ring is represented by all vortex

tubes used in the computations, connected in the direction of vorticity, and the ring is propagating in the upward direction.

Figure 19. Natural logarithm of the amplitude of perturbation wavenumber, n^*, and of its higher harmonics, $2n^*$ and $3n^*$ for the the ring of Fig. 18.

Figure 20. Three perspective views of the vortex ring of Fig. 18 at $t = 140$. The plots are generated as in figure 18 with $\beta = 0^o$, 60° and 90°.
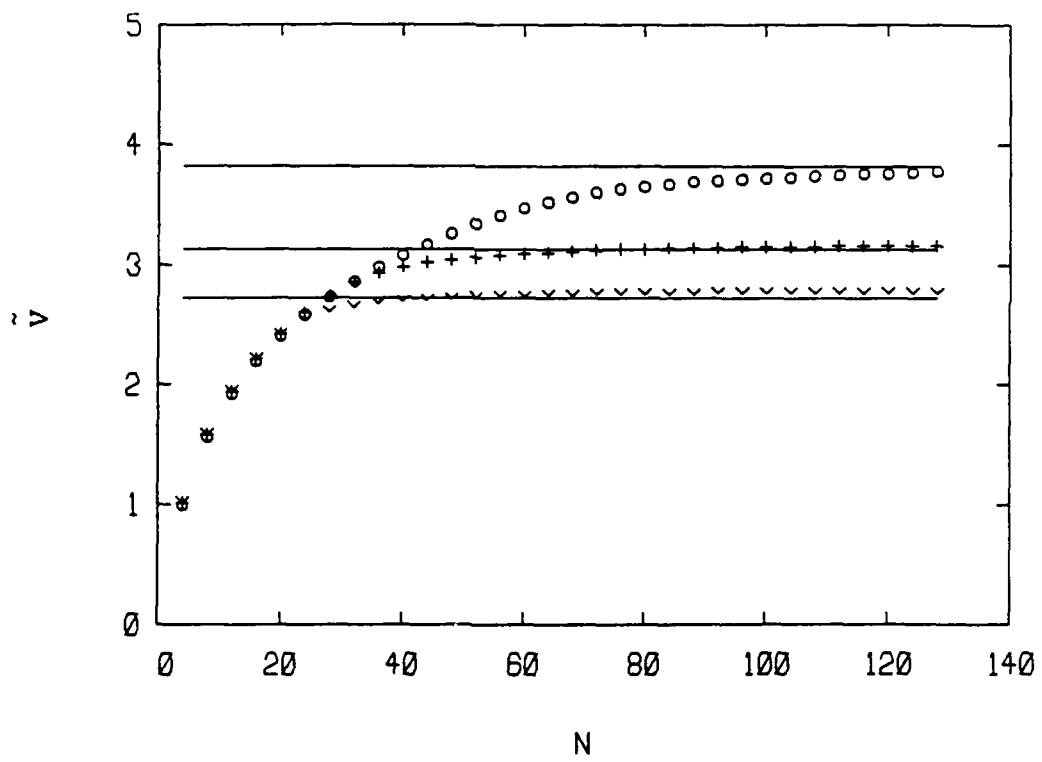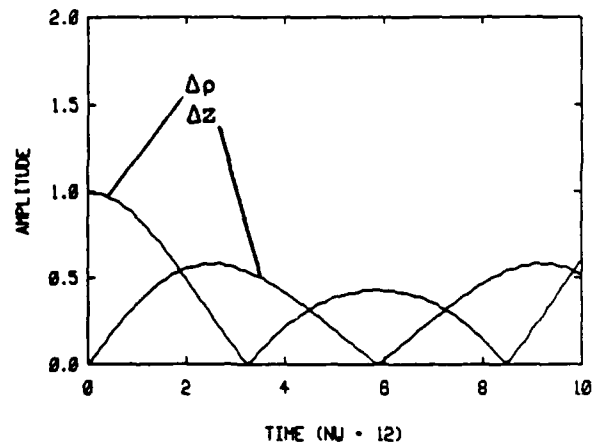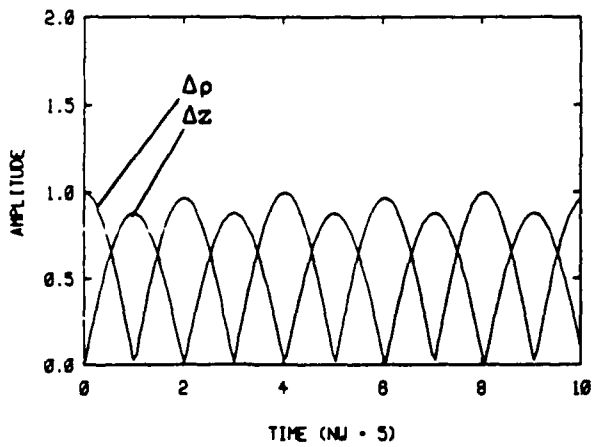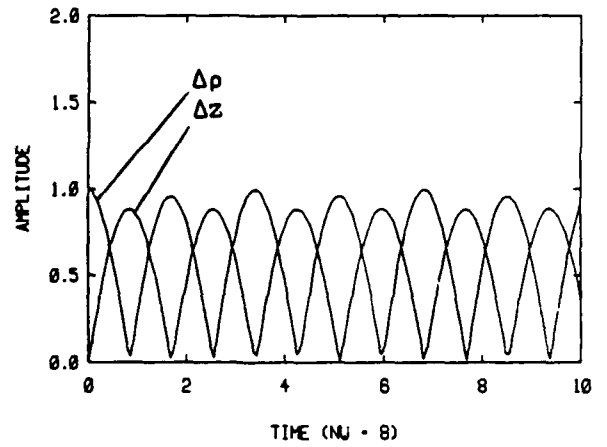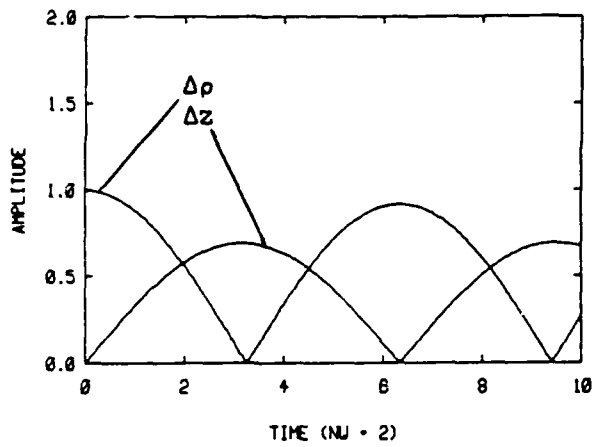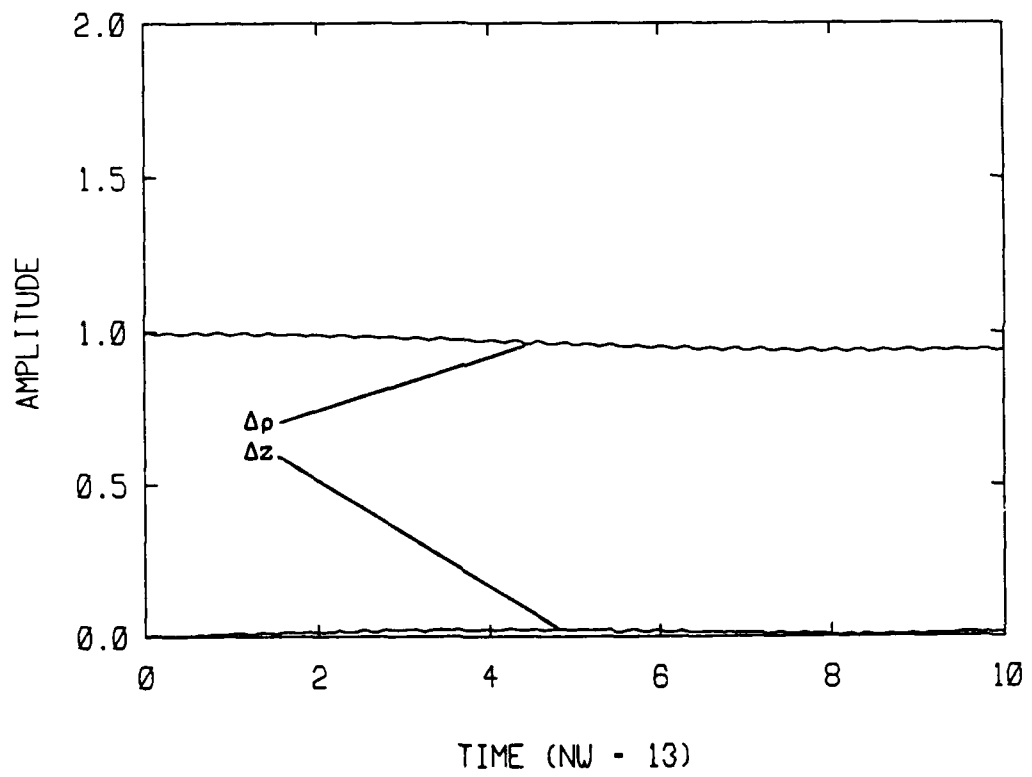
Figure 1.

Figure 2.

Figure 3.
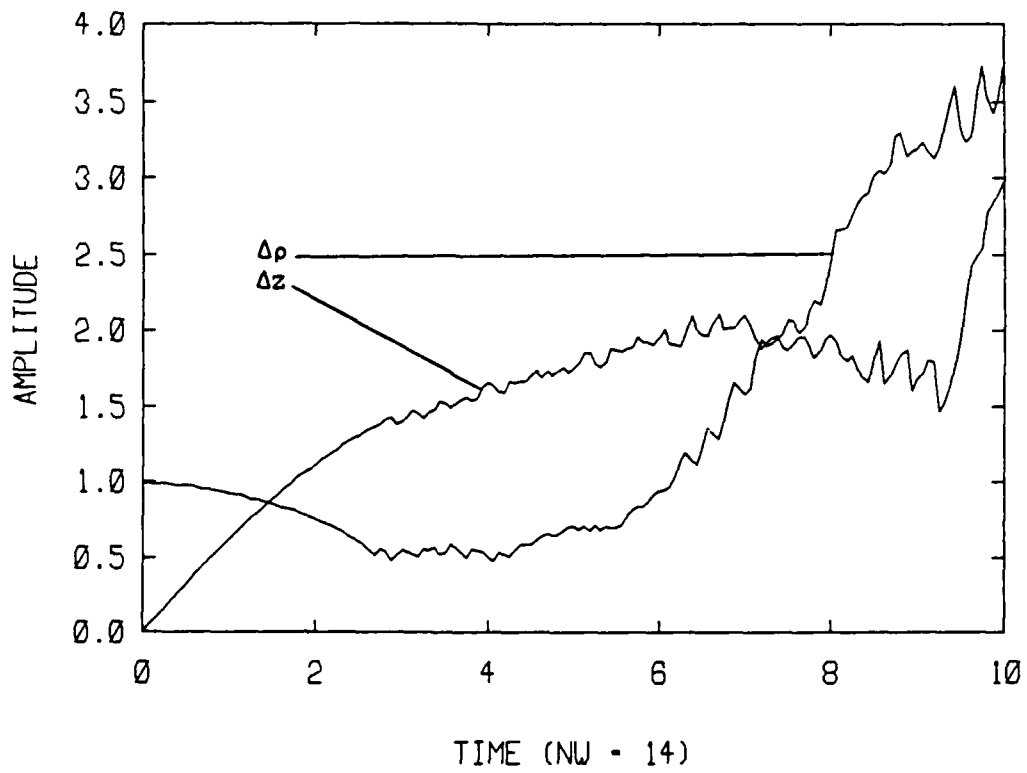
Figure 4.
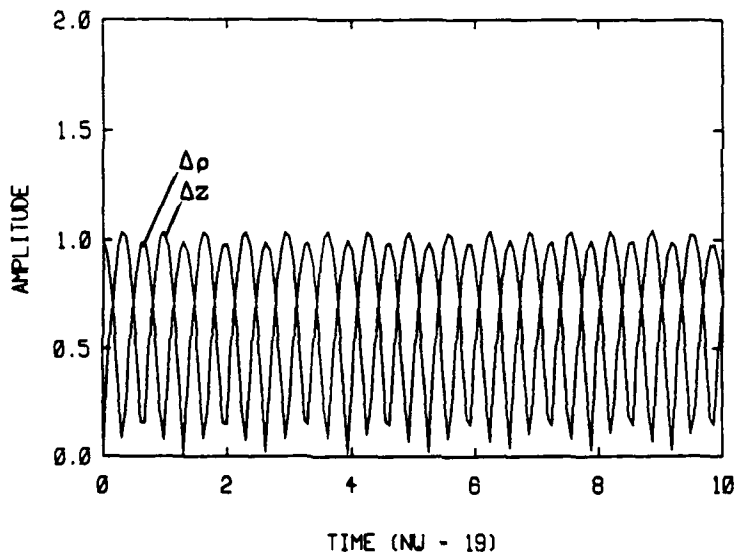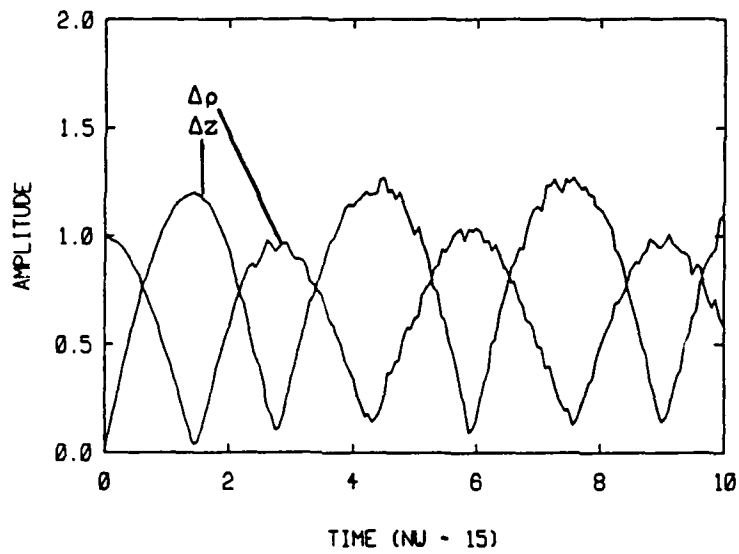
Figure 5.
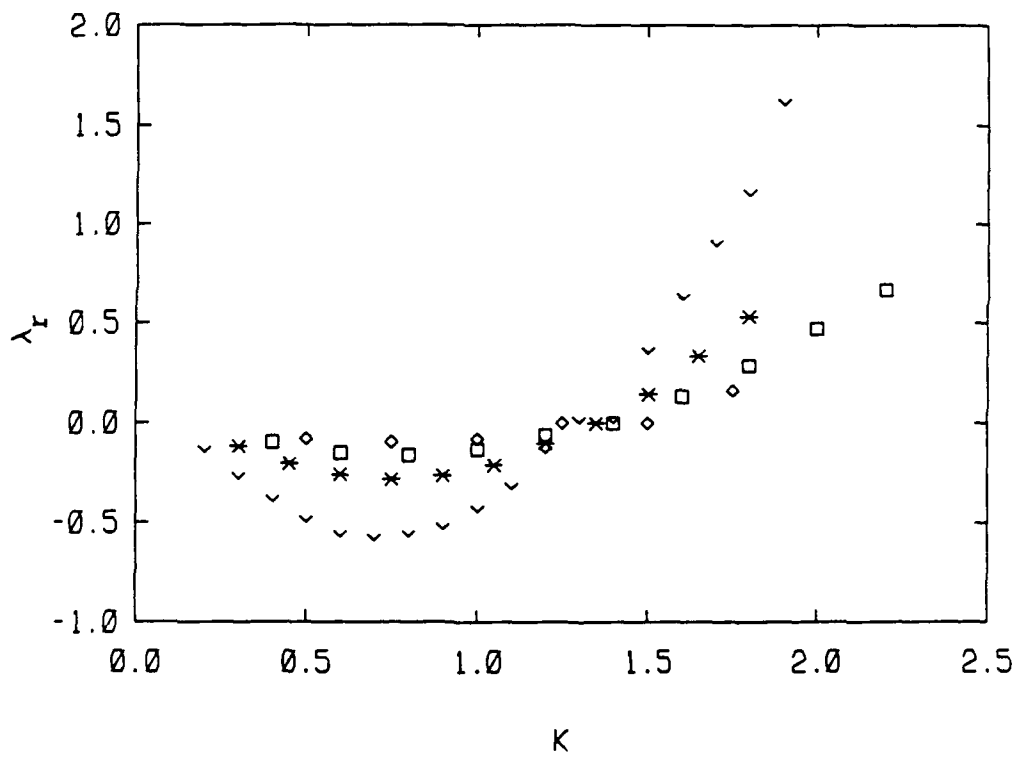
Figure 6.
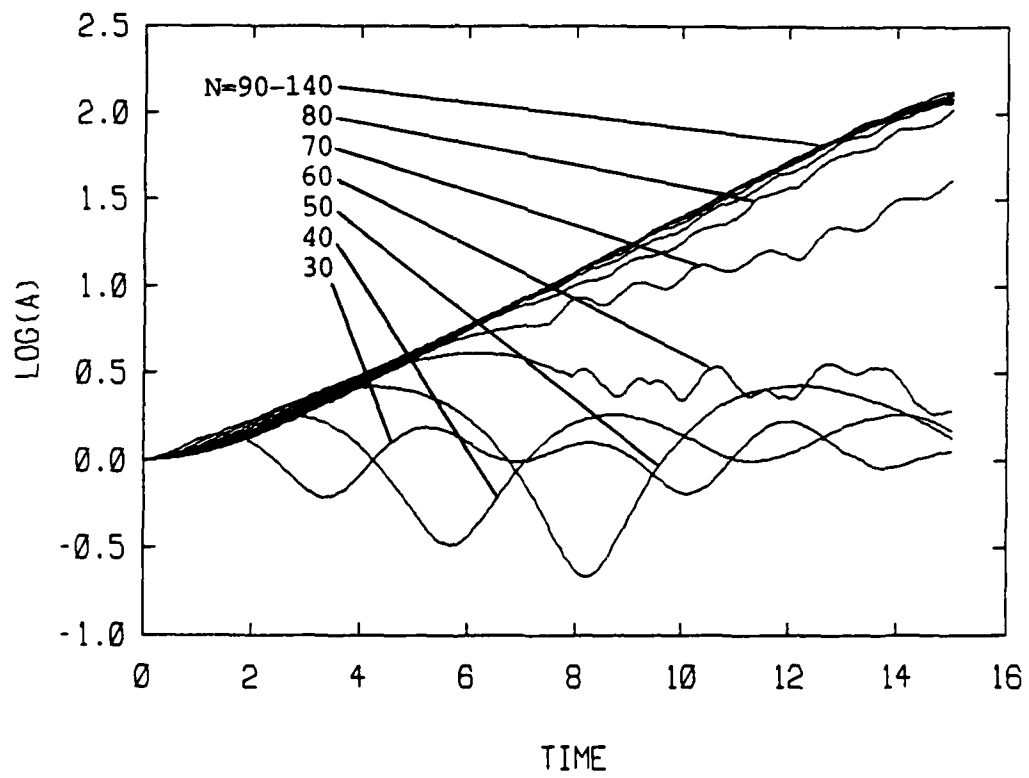
Figure 7.
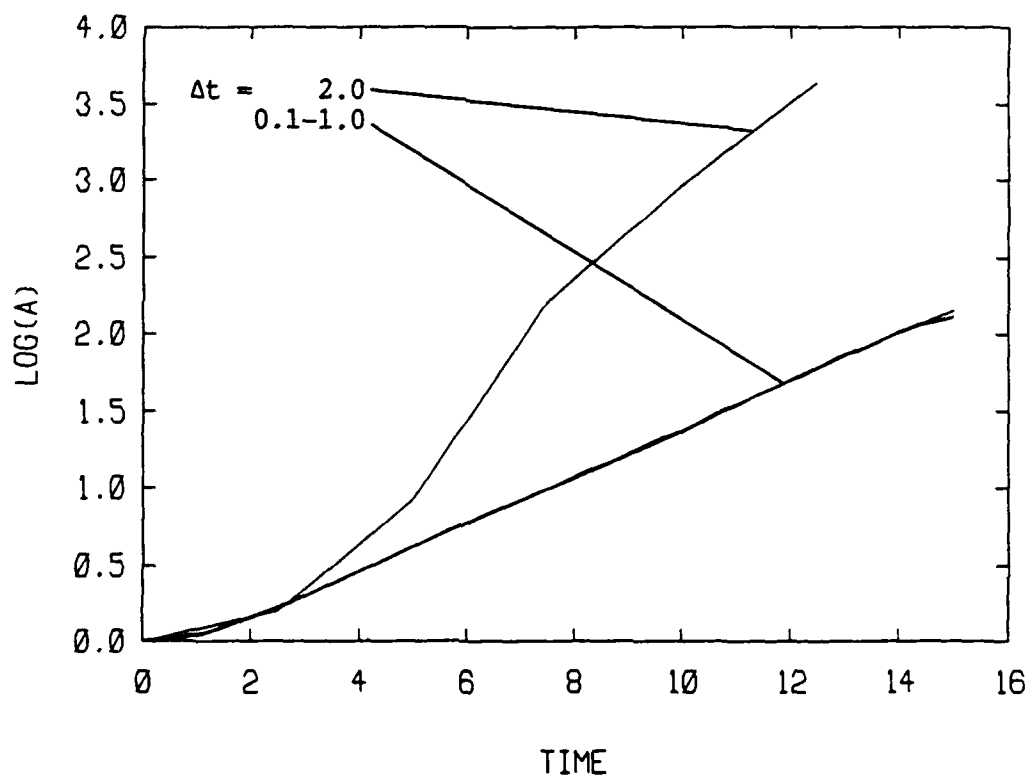
Figure 8.
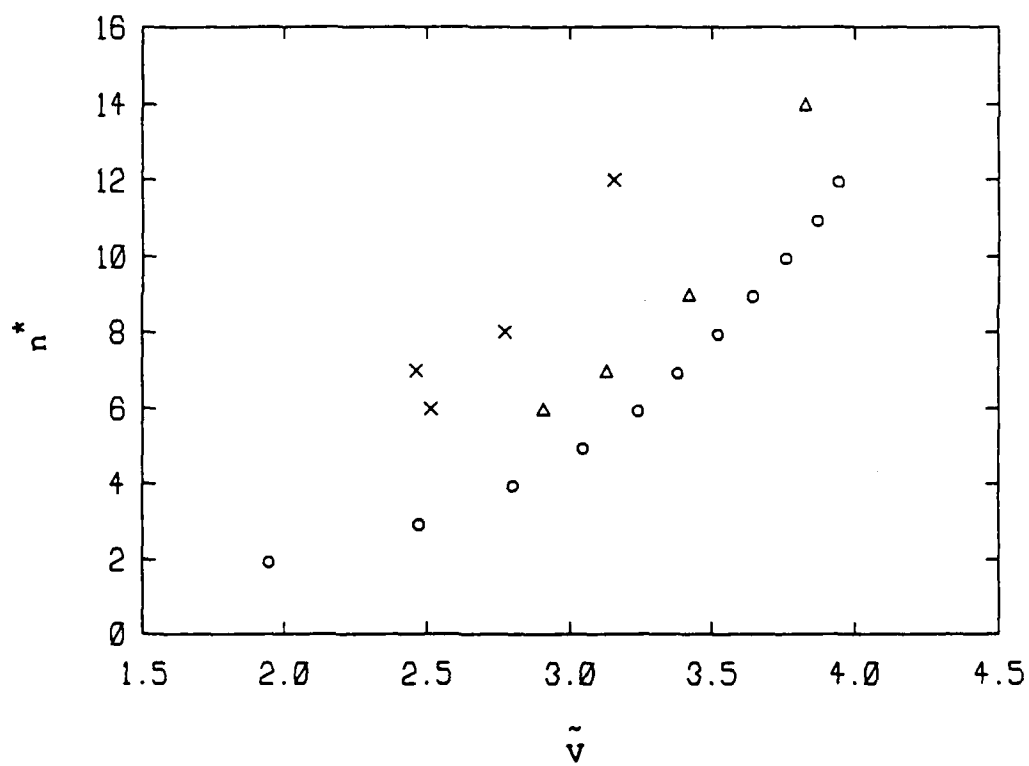
Figure 9.

Figure 10.

Figure 11a.

Figure 11b.

Mesh	I	II	III

$N_s = 1$

$N_r = 9$

$N_s = 2$

$N_r = 17$ $N_r = 17$ $N_r = 19$

$N_s = 3$

$N_r = 25$ $N_r = 25$ $N_r = 37$

$N_s = 4$

$N_r = 33$ $N_r = 33$ $N_r = 61$
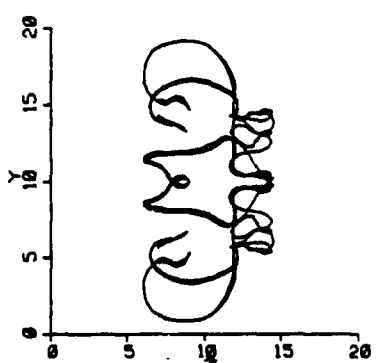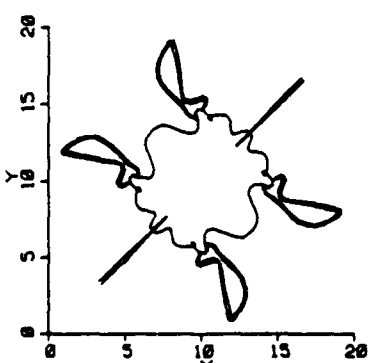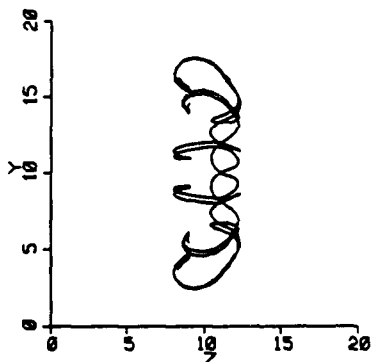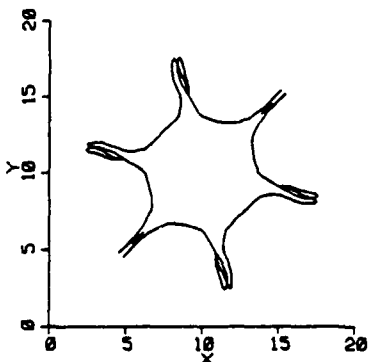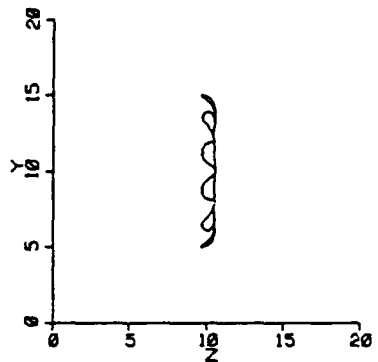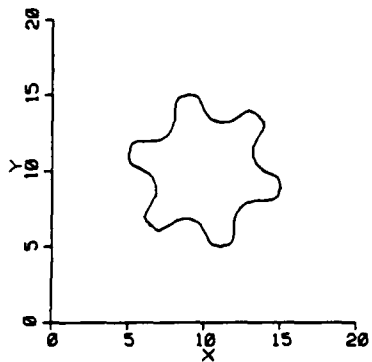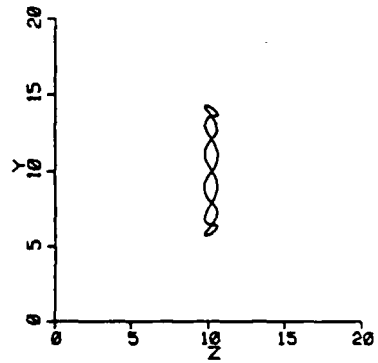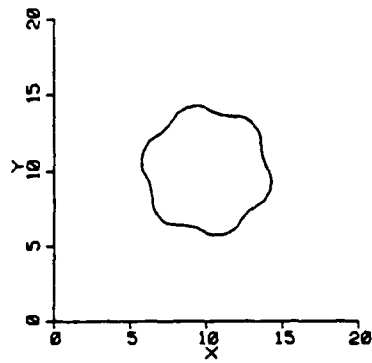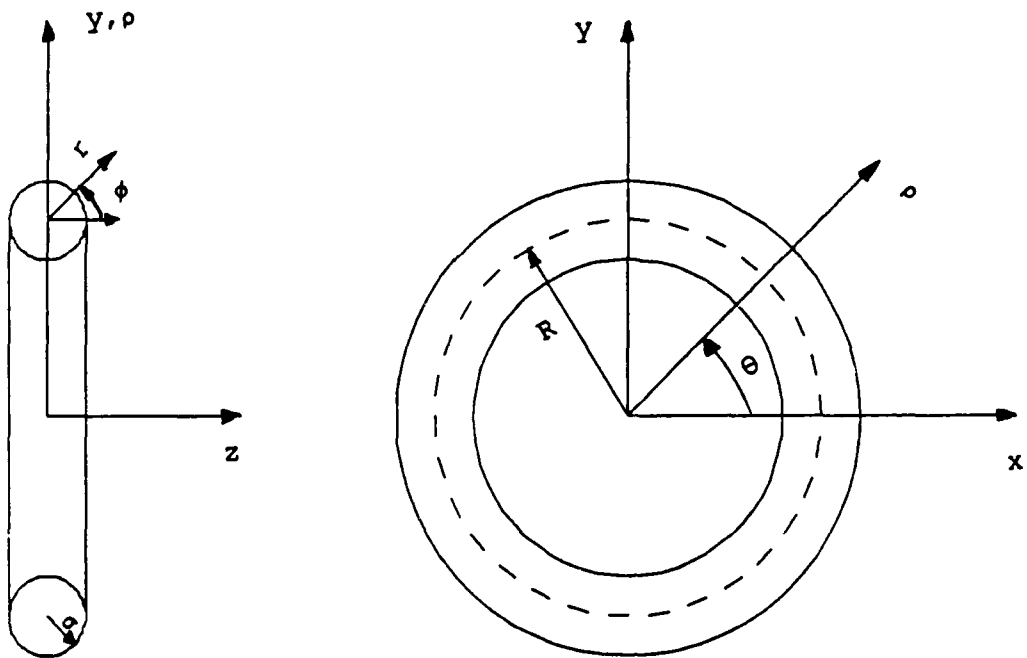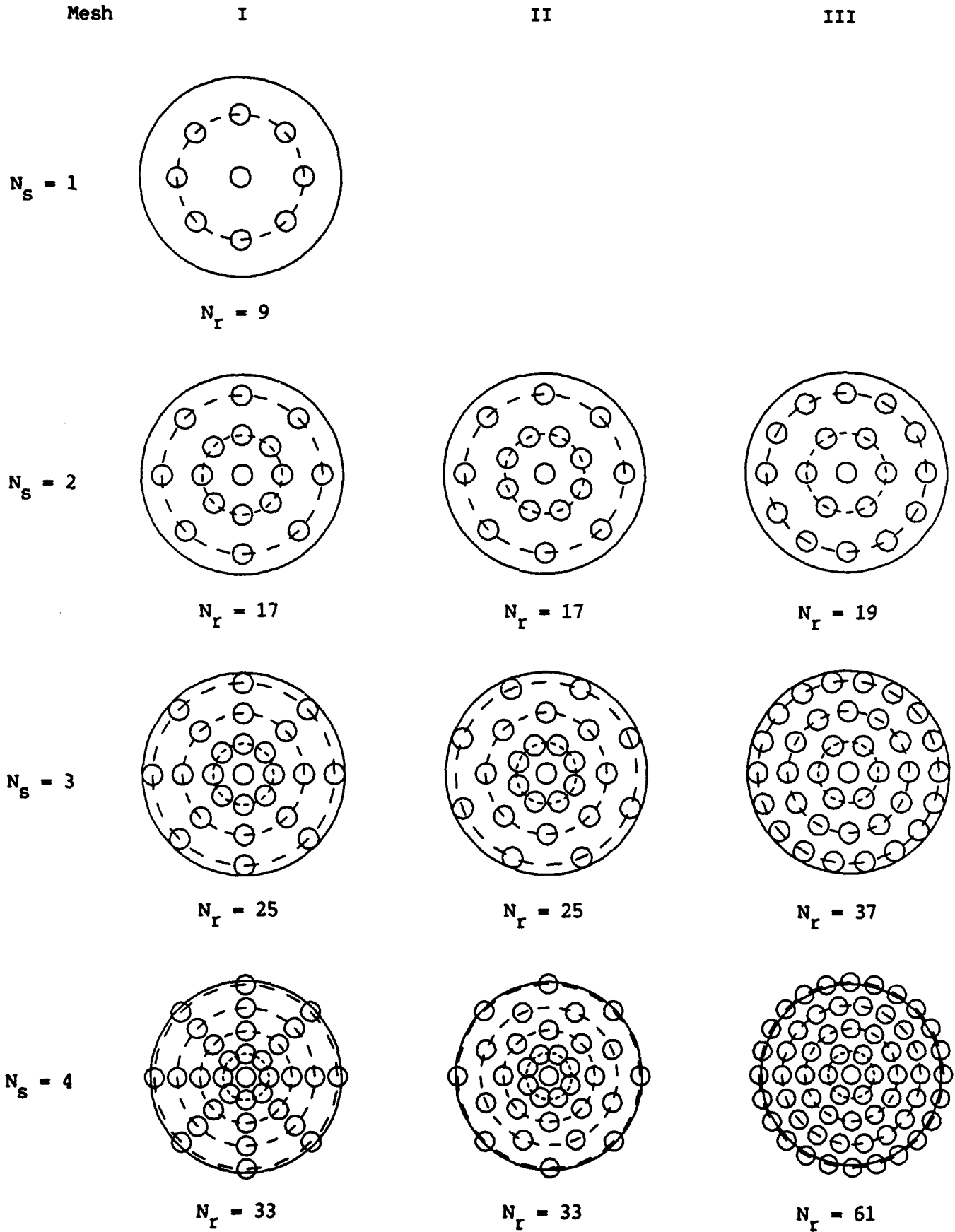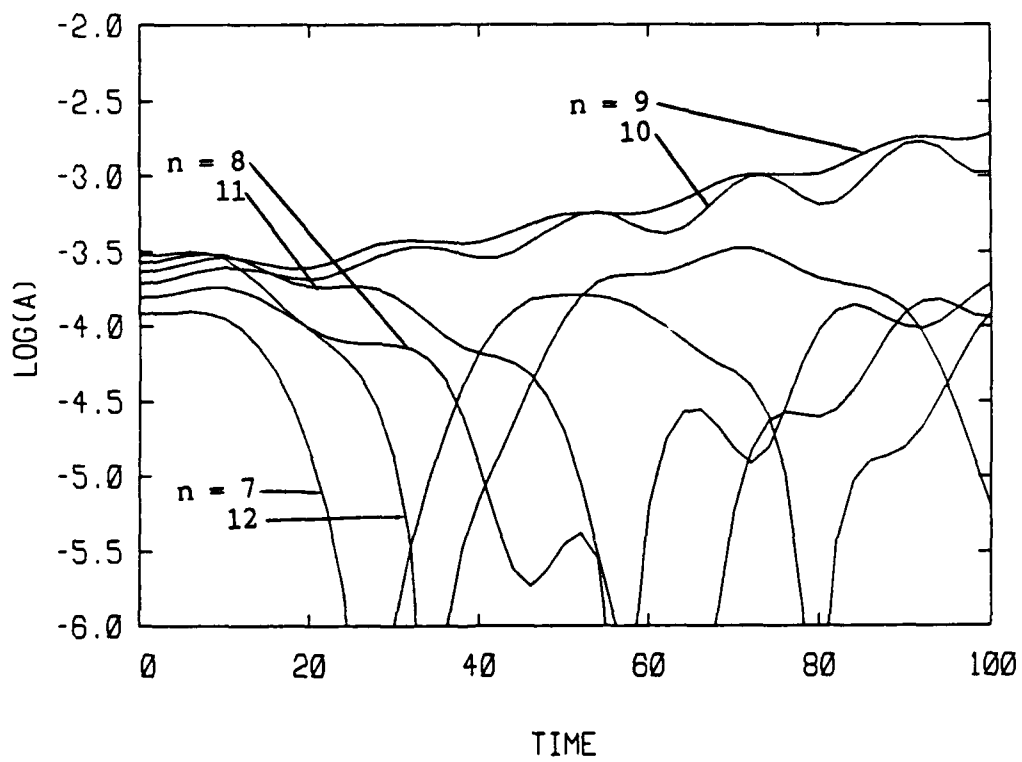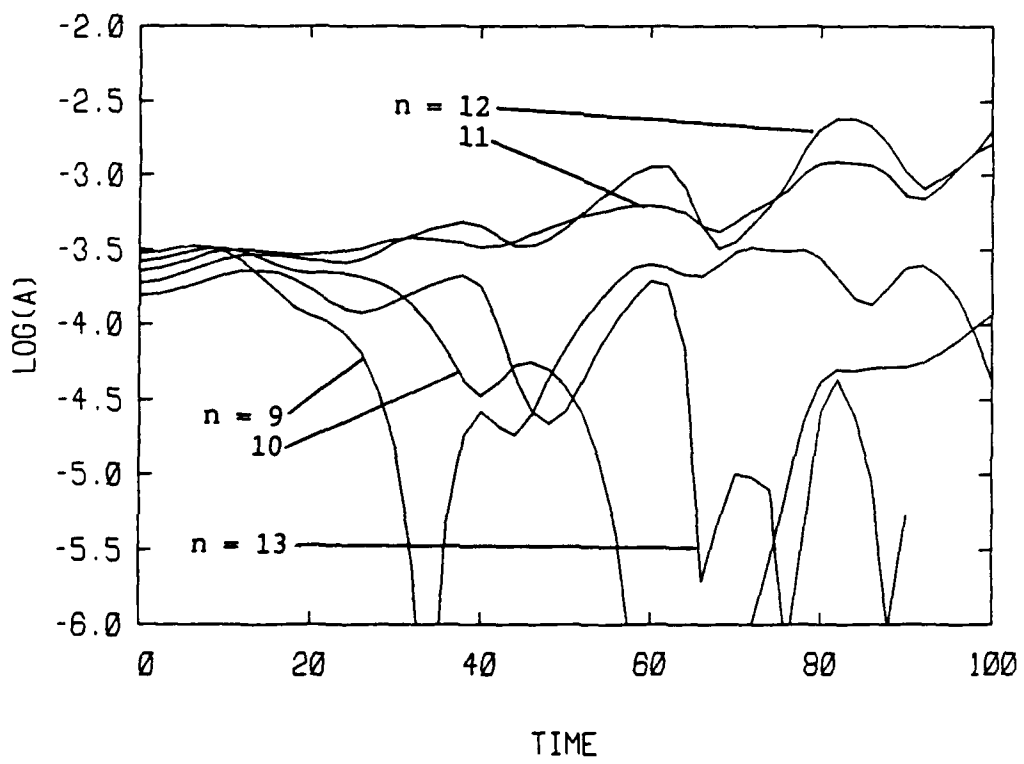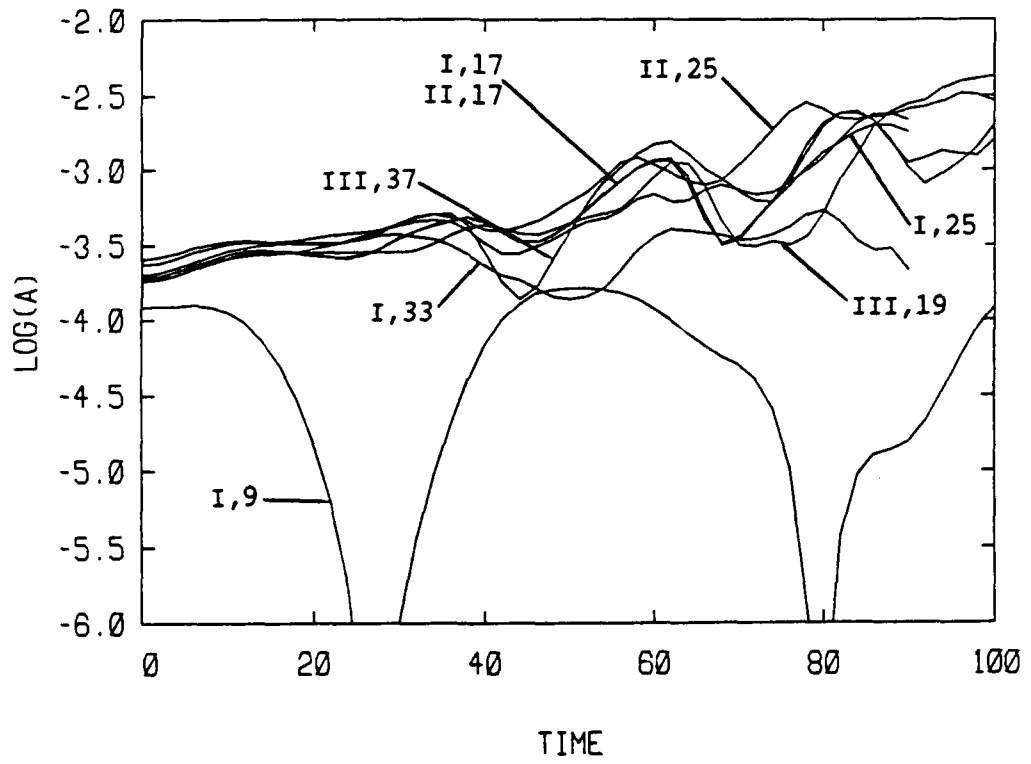
Figure 12.

Figure 13.

Figure 14.
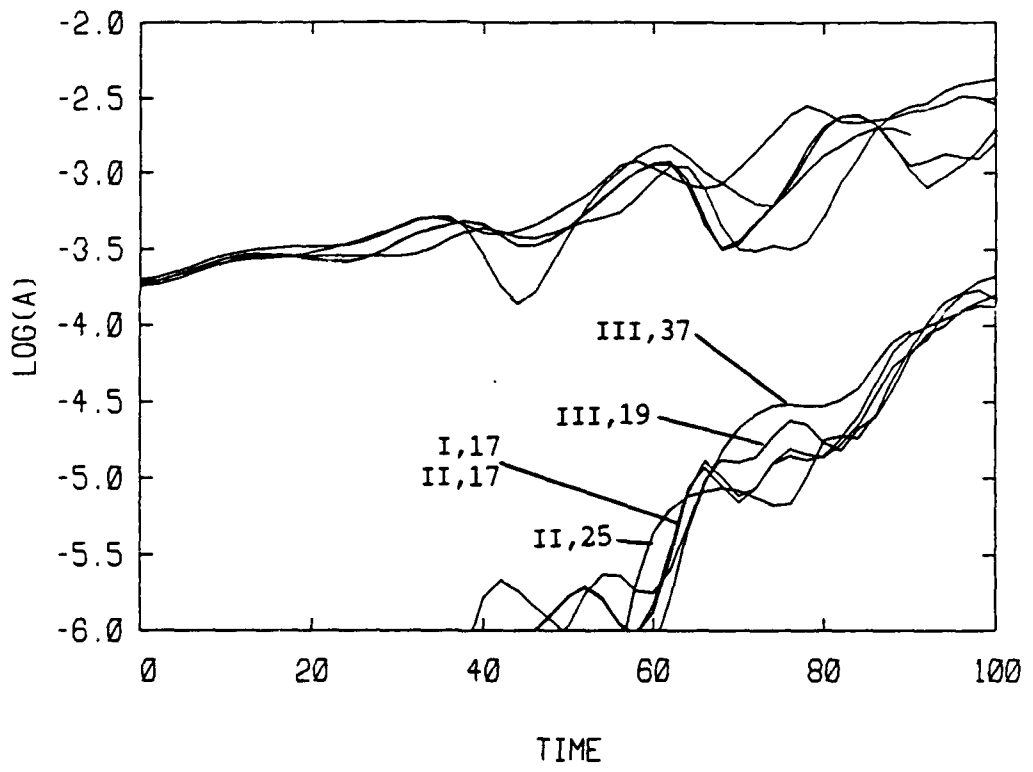
Figure 15.
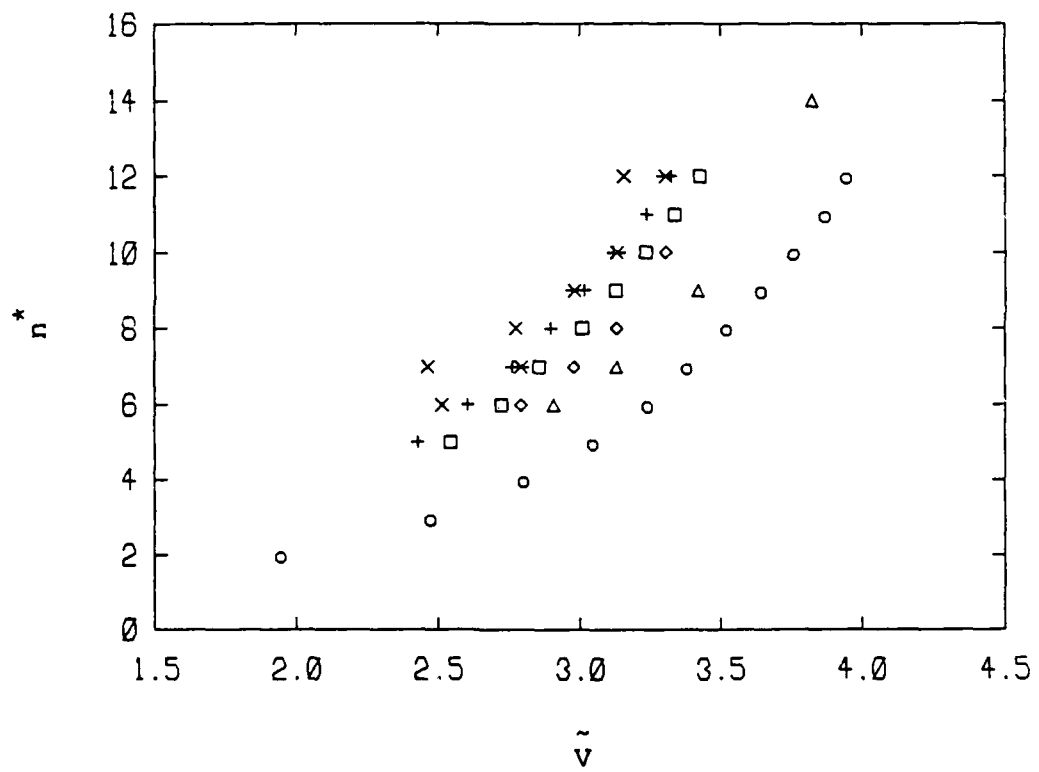
Figure 16.

Figure 17.
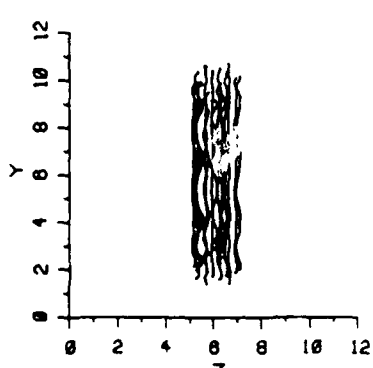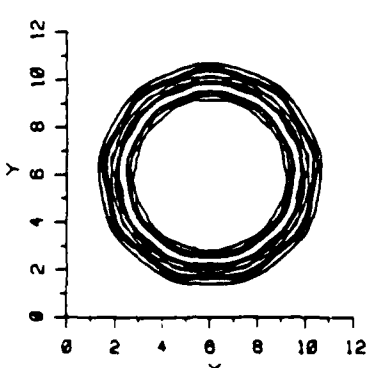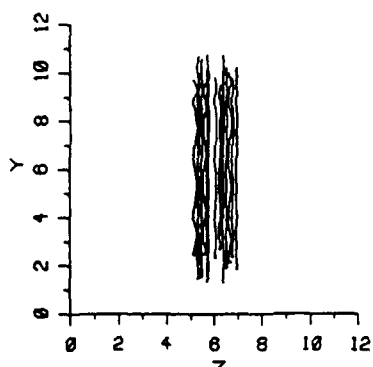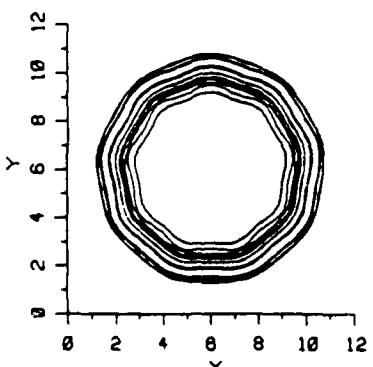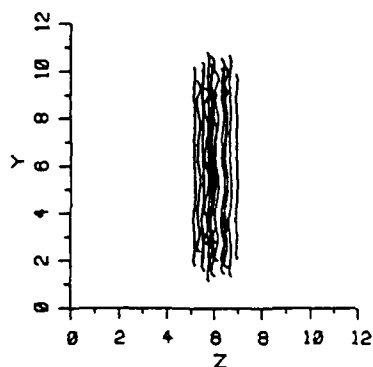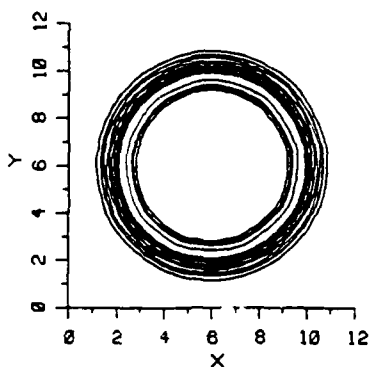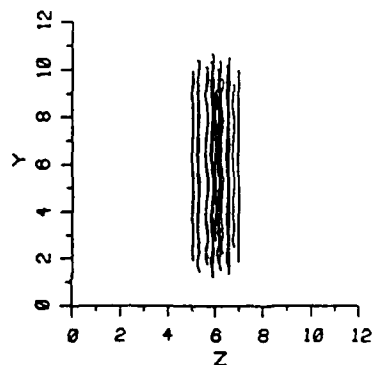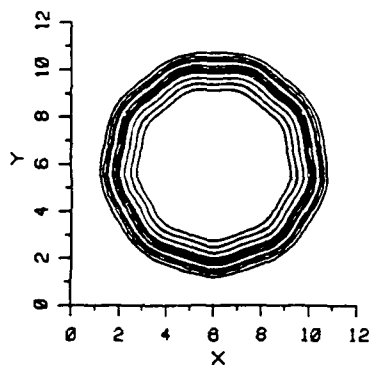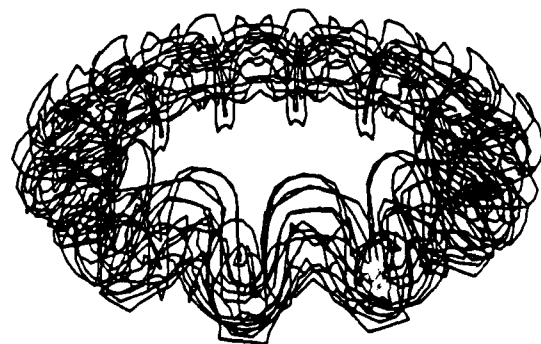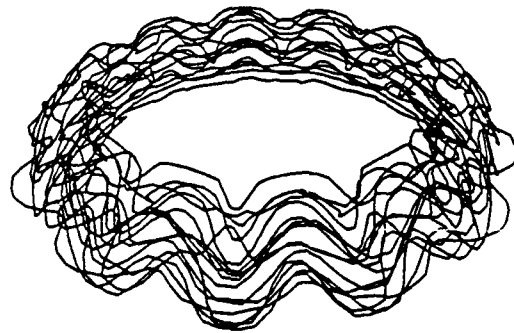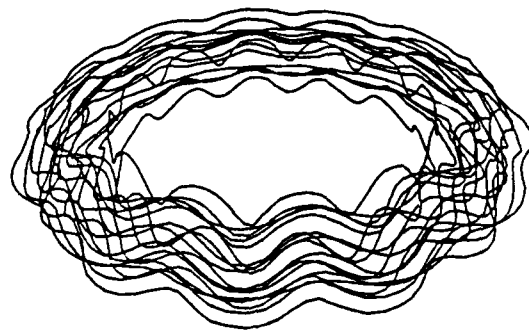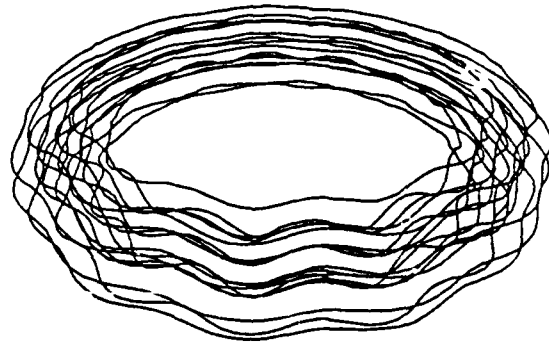
Figure 18.

Figure 19.

Figure 20.